NEW ORGANIC AND ORGANOMETALLIC PLATFORMS FOR LUMINESCENCE AND CATALYSIS APPLICATIONS

A Dissertation Presented to

the Faculty of the Department of Chemistry

University of Houston

In Partial Fulfillment

of the Requirements for the Degree of

Doctor of Philosophy

By

Ku Sun Choung

May 2019

NEW ORGANIC AND ORGANOMETALLIC PLATFORMS FOR LUMINESCENCE AND CATALYSIS APPLICATIONS

_____

Ku Sun Choung

APPROVED:

_____

Dr. Thomas S. Teets, Chairman

_____

Dr. Olafs Daugulis

_____

Dr. Don Coltart

_____

Dr. Steven Baldelli

_____

Dr. Gregory Cuny

_____

Dean, College of Natural Sciences and Mathematics

Dedicated to my parents,

and my younger brother,

Jin Yong Choung, Mi Yeol Lee, and Ku Hoon Choung

For the love and constant support during my academic period

ACKNOWLEDGMENTS

I wish to express my gratitude to my advisor, Dr. Thomas S. Teets, for his enthusiastic guidance and mentorship, as he has encouraged and supported me to pursue my research in his research group during my Ph.D. journey. I appreciate his continuous patience, motivation, and keen insight, which have helped and guided me for all the time of research projects. Especially, Dr. Teets always gave me valuable directions and patient advices when I encountered some problems of my research work.

I want to further extend my appreciation toward all of my committee members Dr. Thomas S. Teets, Dr. Olafs Daugulis, Dr. Don Coltart, Dr. Steven Baldelli, and Dr. Gregory Cuny, for their time, dedication, and commitment to review my Ph.D. dissertation.

I also would like to specially thank all current Teets research group members for their support, relationship, kindness, and for all the good times we have had in the last five years. Without their helpful advices for my research work in the either office or laboratory, it is even not possible for me to complete my Ph.D. academic course.

Finally, I would always like to thank my parents, family, and especially my fiancée Jahyun Kate Lee for their love, constant support, extraordinary encouragement, and sacrifice throughout my academic endeavor.

NEW ORGANIC AND ORGANOMETALLIC PLATFORMS FOR LUMINESCENCE AND CATALYSIS APPLICATIONS

An Abstract of a Dissertation

Presented to

the Faculty of the Department of Chemistry

University of Houston

In Partial Fulfillment

of the Requirements for the Degree of

Doctor of Philosophy

By

Ku Sun Choung

May 2019

ABSTRACT

This dissertation describes the development of organometallic compounds, including cyclometalated platinum and iridium complexes and iridium pincer complexes, and organic chromophores, applied to dehydrogenation of alkanes, Lewis-acid-modulated luminescence, and ratiometric O_2 sensing. Chapter 1 describes a series of cyclometalated platinum complexes with two different fluorinated β-diketiminate (NacNac) ligands, with the nuclearity of the product depending on the temperature of the reaction. The two types of complexes are characterized by X-ray crystallography, UV-vis absorption and emission spectroscopy, and by cyclic voltammetry, which shows a reversible reduction at mild potentials. All of these properties are suggested to involve NacNac-centered frontier orbitals. Chapter 2 describes two pyridyl-substituted BODIPY compounds and one aza-BODIPY, which can interact with the strong Lewis acid $B(C_6F_5)_3$. The interactions of BODIPYs with borane Lewis acids induce significant changes in the photophysical properties of these chromophoric molecules. Chapter 3 introduces a new class of ratiometric O_2 sensors for hypoxic environments. Two-component structures composed of phosphorescent cyclometalated Ir(III) complexes and the well-known organic fluorophore BODIPY exhibit dual emission, with significant phosphorescence from the iridium site and fluorescence from the BODIPY, and thus function as ratiometric oxygen sensors. Finally, Chapter 4 describes the synthesis of two type iridium pincer complexes (CCC- and CNC types) as precatalysts for the dehydrogenation of cyclooctane.

TABLE OF CONTENTS

LIST OF FIGURES

LIST OF SCHEMES

LIST OF TABLES

Chapter 1. Monometallic and Bimetallic Platinum Complexes with Fluorinated β-Diketiminate Ligands

1.1. Introduction

The coordination chemistry of β-diketiminates, often referred to as "NacNac" ligands, has a rich history covering many decades and many transition and main-group metals.[1] The general structure of the β-diketiminate ligand is shown in **Figure 1.1**, and with many potential avenues to tune their steric and electronic properties these ligands have emerged in a number of important areas in synthetic chemistry and catalysis. Most NacNac ligands are derived from 2,4-pentanedione, with $R^2 = R^3$= Me in **Figure 1.1**, and sterically hindered NacNac analogues, i.e. with bulky substituents at the 2- and 6-positions of the phenyl rings (R^1) have become especially prominent in stabilizing low-coordinate complexes for small-molecule activation[2–4] and polymerization catalysis.[5–7] Other well-known analogues include sterically encumbering *tert*-butyl groups at the backbone R^2 and R^3 positions,[8–10] and it is also possible to add alkyl[11] or cyano[12] substituents to the central R^4 backbone position. More significant electronic modification is possible via backbone fluorination of the NacNac, and a series of electron-deficient β-diketiminates derived from 1,1,1-5,5,5-hexafluoroacetone have emerged,[13–19] where $R^2 = R^3 = CF_3$, as well as an asymmetric version where R^2 = Me and $R^3 = CF_3$.[12] These analogues have been especially prominent in the coordination chemistry of coinage metals like Cu(I) and Ag(I), where by making the NacNac less electron-rich the low-valent, electro-negative transition

---

Chapter 1 was reproduced with permission from Choung, K. S.; Islam, M. D.; Guo, R. W.; Teets, T. S. *Inorg. Chem.* **2017**, *56*, 14326–14334.

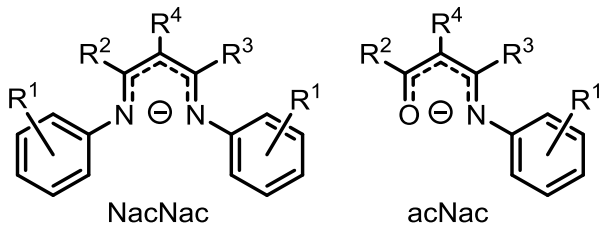

Figure 1.1. General structure of β-diketiminate (NacNac) and β-ketoiminate (acNac) ligands.

elements can be accommodated.

With all of these precedents in mind, until now there have been considerably fewer examples of coordination compounds of β-diketiminates with third-row transition metals when compared to main group metals and first-row transition metals.[1,20] Previous well-known accounts include iridium hydride/olefin complexes[21,22] and platinum complexes, which have been platforms for studying fundamental reactivity like C–H activation,[23–25] O_2 activation,[26,27]and other organometallic transformations.[28–30] More recently, our group has discovered a series of bis-cyclometalated iridium complexes with ancillary β-diketiminate and related β-ketominate (acNac) ancillary ligands and demonstrated the profound effects of the ancillary ligands on the electrochemical and photophysical properties of these organometallic phosphors, unveiling a new application for this richly-studied ligand platform. We have partnered bis-cyclometalated iridium(III) both with electron-rich (N)acNac (R^2 = Me) variants[31] and with differentially fluorinated versions where R^2 and/or R^3 = CF_3 and R^1 = H or 3,5-$(CF_3)_2$.[32] Relative to isoelectronic acetylacetonate (acac) analogues we have noted a significant destabilization of the Ir dπ HOMO in complexes with unsubstituted (R^2 = R^3 = Me) (N)acNac ligands, and in some cases large enhancements in phosphorescence quantum yields.[31] The Ir^{IV}/Ir^{III} redox

potentials and corresponding HOMO energies are exquisitely sensitive to the extent of fluorination on the ancillary ligand, particularly on the backbone, such that complexes with maximally fluorinated NacNac ligands (R^1 = 3,5-$(CF_3)_2$; $R^2 = R^3 = CF_3$) exhibit oxidation potentials that are shifted by over 0.75 V relative to the unsubstituted versions. In addition, NacNac complexes with backbone CF_3 substituents luminesce in the deep red to near-infrared regions from a NacNac-centered triplet state when cooled to 77 K; this low-energy phosphorescence is a previously unrecognized feature of fluorinated β-diketiminates and depends minimally on the cyclometalating (C^N) ligand the NacNac is paired with.

In this work, we describe a series of platinum complexes of fluorinated NacNac ligands. In addition to establishing the previously unexplored coordination chemistry of this ligand class with platinum, this series of compounds allows us to evaluate the effect of the metal center and the coordination geometry on NacNac-derived optical properties. A series of eight complexes were prepared by treating cyclometalated platinum precursors with two different fluorinated NacNac ligands. With milder reaction conditions we isolate a halide-bridged diplatinum complex which also features a η^2 bridging NacNac ligand, a previously unobserved β-diketiminate binding mode. These diplatinum complexes show low-energy visible absorption bands attributed to the NacNac ligand but are not luminescent even when cooled to 77 K. Two examples of monoplatinum complexes with a conventional κ^2 NacNac were also prepared, and these complexes are luminescent at low temperature, exhibiting vibronically structured, NacNac-centered luminescence that is slightly perturbed from the previously described cyclometalated iridium complexes, indicating that interactions with the metal center play a small role in determining the energies of NacNac-centered triplet excited states. All of the complexes display rich re-

dox chemistry attributed to NacNac-centered frontier orbitals, adding to the growing body of literature on cyclometalated platinum complexes with redox-active ancillary ligands.[33–35]

1.2. Experimental Section

1.2.1. Materials

Dry solvents were obtained from a Grubbs Solvent Purification System and degassed with argon. Starting materials and reagents, unless otherwise specified, were obtained from commercial sources and used without further purification. The precursors $[Pt(C^N)(\mu\text{-}Cl)]_2$ (C^N = ppy, F_2ppy) were prepared with conventional heating as previously described.[36] The precursor $[Pt(ppy)(\mu\text{-}Br)]_2$ was prepared either by following the literature procedure for anion exchange of $[Pt(ppy)(\mu\text{-}Cl)]_2$[37] or by direct reaction of K_2PtBr_4 with 2-phenylpyridine using the same conditions employed in the synthesis of the chloride analogues. $NacNac^{F6}H$[15,38] and $NacNac^{F18}H$[13] were prepared following established methods, and deprotonated with *n*-BuLi as previously described by our group.[31,32] Tetrabutylammonium hexafluorophosphate ($TBAPF_6$) was recrystallized from hot ethanol and ferrocene was sublimed at ambient pressure before use in electrochemical experiments.

1.2.2. Physical Methods.

^1H and ^{19}F NMR spectra were recorded at room temperature using a ECA-600 NMR spectrometer. UV-vis absorption spectra were recorded in screw-capped 1 cm quartz cuvettes using an Agilent Carey 8454 UV-vis spectrophotometer. Steady-state emission spectra were recorded using a Horiba FluoroMax-4 spectrofluorometer. To exclude air,

samples for emission spectra were prepared in a nitrogen-filled glove-box using dry, deoxygenated toluene. The samples were contained in a custom quartz EPR tube with high-vacuum valve and immersed in liquid nitrogen using a finger Dewar. Cyclic voltammetry (CV) experiments were performed with a CH Instruments 602E potentiostat using a three-electrode system in a nitrogen-filled glove-box. A 3 mm diameter glassy-carbon electrode, Pt wire, and silver wire were used as working electrode, counter electrode, and pseudoreference electrode, respectively. Measurements were carried out at concentrations of ca. 10^{-3} M in acetonitrile or THF solution with 0.1 M $TBAPF_6$ as a supporting electrolyte at scan rate of 0.1 V/s. Ferrocene was used as an internal standard, and potentials were referenced to the ferrocene/ferrocenium couple. Bulk purity for all complexes is established by elemental analysis, performed by Atlantic Microlab, Inc. (Norcross, GA). ^{1}H and ^{19}F NMR spectra of all compounds are also shown in **Appendix 1**, **Figures A1.15**–**A1.28**, and provide additional evidence for sample purity.

1.2.3. General procedure for the synthesis of diplatinum complexes 1–5.

$[Pt(C^N)(\mu\text{-}Cl)]_2$ and the lithium salt of the respective NacNac ligand (1–1.5 equivalents) were weighed out in the glovebox, suspended together in 6 mL of toluene, and sealed in a thick-walled, Teflon-capped glass vessel. The contents were heated to 80 °C with constant stirring for 16 h, giving a dark purple solution. The solution was allowed to cool to room temperature and filtered through a short plug of silica to remove the LiCl byproduct. The solvent was removed under vacuum, and the crude product was purified by silica gel column chromatography (hexane/ethyl acetate gradient eluent) and recrystallization (dichloromethane/hexane).

$Pt_2(ppy)_2(\mu\text{-}NacNac^{F6})(\mu\text{-}Cl)$ (1). Prepared by the general method using $[Pt(ppy)(\mu\text{-}Cl)]_2$ (132 mg, 0.172 mmol) and $NacNac^{F6}Li$ (90 mg, 0.25 mmol, 1.5 equiv). Yield: 27 mg (14%). ^1H NMR (600 MHz, CD_2Cl_2) δ: 8.78 (d, *J* = 5.8 Hz, 2H, Ar*H*), 7.91–7.86 (m, 2H, Ar*H*), 7.75 (d, *J* = 8.1 Hz, 4H, Ar*H*), 7.52 (dd, *J* = 5.9, 3.0 Hz, 2H, Ar*H*), 7.24 – 7.16 (m, 8H, Ar*H*), 7.12 (s, 2H, Ar*H*), 7.04 (m, 2H, Ar*H*), 7.01 – 6.98 (m, 2H, Ar*H*), 6.62 (s, 2H, Ar*H*), 5.64 (s, 1H, $PhNC(CF_3)CHC(CF_3)NPh$). ^{19}F NMR (564 MHz, CD_2Cl_2) δ: –60.00 (s, 6F, CF_3). Anal. Calcd for $C_{39}H_{27}ClF_6N_4Pt_2$: C, 42.92; H, 2.49; N, 5.13. Found: C, 43.00; H, 2.72; N, 5.03.

$Pt_2(ppy)_2(\mu\text{-}NacNac^{F6})(\mu\text{-}Br)$ (2). Prepared by the general method using $[Pt(ppy)(\mu\text{-}Br)]_2$ (72 mg, 0.084 mmol) and $NacNac^{F6}Li$ (31 mg, 0.084 mmol, 1.0 equiv). Yield: 5 mg (5%). Due to the low isolated yield this compound was not submitted for elemental analysis, but ^1H and ^{19}F NMR spectra (**Figures A1.17 and A1.18**) indicate suitable bulk purity. ^1H NMR (600 MHz, $CDCl_3$) *δ*: 8.83 (d, *J* = 5.7 Hz, 2H, Ar*H*), 7.85 (t, *J* = 7.9 Hz, 4H, Ar*H*), 7.72 (d, *J* = 8.1 Hz, 2H, Ar*H*), 7.49 (d, *J* = 7.3 Hz, 2H, Ar*H*), 7.22 – 7.15 (m, 8H, Ar*H*), 7.10 (s, 2H, Ar*H*), 7.00 – 6.96 (m, 4H, Ar*H*), 6.58 (s, 2H, Ar*H*), 5.71 (s, 1H, $PhNC(CF_3)CHC(CF_3)NPh$). ^{19}F NMR (564 MHz, $CDCl_3$) δ: –59.62 (s, 6F, CF_3).

$Pt_2(F_2ppy)_2(\mu\text{-}NacNac^{F6})(\mu\text{-}Cl)$ (3). Prepared by the general method using $[Pt(F_2ppy)(\mu\text{-}Cl)]_2$ (128 mg, 0.152 mmol) and $NacNac^{F6}Li$ (56 mg, 0.15 mmol, 1.0 equiv). Yield: 27 mg (15%). ^1H NMR (600 MHz, CD_2Cl_2) δ: 8.76 (dd, *J* = 5.8, 0.8 Hz, 2H, Ar*H*), 8.11 (d, *J* = 8.4 Hz, 2H, Ar*H*), 7.96 – 7.89 (m, 2H, Ar*H*), 7.74 (s, 2H, Ar*H*), 7.23 (s, 2H, Ar*H*), 7.05 (ddd, *J* = 28.3, 11.0, 4.3 Hz, 6H, Ar*H*), 6.75 – 6.68 (m, 2H, Ar*H*), 6.55–6.66 (m, 4H, Ar*H*), 5.71 (s, 1H, $PhNC(CF_3)CHC(CF_3)NPh$). ^{19}F NMR (564 MHz, CD_2Cl_2) δ: –60.02 (s, 6F,

CF_3), –106.37 (q, *J* = 9.2 Hz, 2F, F_2ppy). –110.96 (t, *J* = 11.3 Hz, 2F, F_2ppy). Anal. Calcd for $C_{39}H_{23}ClF_{10}N_4Pt_2$: C, 40.27; H, 1.99; N, 4.82. Found: C, 40.52; H, 2.14; N, 4.68.

Pt_2(ppy)$_2$(μ-NacNac^{F18})(μ-Cl) (4). Prepared by the general method using [Pt(ppy)(μ-Cl)]$_2$ (30 mg, 0.039 mmol) and NacNac^{F18}Li (25 mg, 0.039 mmol, 1.0 equiv). Yield: 34 mg (64%). ^{1}H NMR (600 MHz, $CDCl_3$) δ: 8.78 – 8.65 (m, 2H, Ar*H*), 8.27 (s, 2H, Ar*H*), 7.87 (ddd, *J* = 8.2, 7.6, 1.5 Hz, 2H, Ar*H*), 7.73 (d, *J* = 7.9 Hz, 2H, Ar*H*), 7.66 (s, 2H, Ar*H*), 7.50 (dd, *J* = 6.2, 2.9 Hz, 4H, Ar*H*), 7.22 – 7.19 (m, 4H, Ar*H*), 7.08 – 7.03 (m, 4H, Ar*H*), 5.86 (s, 1H, PhNC(CF_3)CHC(CF_3)NPh). ^{19}F NMR (564 MHz, $CDCl_3$) δ: −59.51 (s, 6F, CF_3), –62.61 (s, 6F, CF_3), –62.96 (s, 6F, CF_3). Anal. Calcd for $C_{43}H_{23}ClF_{18}N_4Pt_2$: C, 37.88; H, 1.70; N, 4.11. Found: C, 38.88; H, 1.86; N, 4.08.

Pt_2(F_2ppy)$_2$(μ-NacNac^{F18})(μ-Cl) (5). Prepared by the general method using [Pt(F_2ppy)(μ-Cl)]$_2$ (135 mg, 0.160 mmol) and NacNac^{F18}Li (103 mg, 0.162 mmol, 1.01 equiv). Yield: 79 mg (34%). ^{1}H NMR (600 MHz, $CDCl_3$) δ: 8.69 (d, *J* = 5.8 Hz, 2H, Ar*H*), 8.19 (s, 2H, Ar*H*), 8.13 (d, *J* = 8.5 Hz, 2H, Ar*H*), 7.92 (t, *J* = 7.8 Hz, 2H, Ar*H*), 7.58 (s, 2H, Ar*H*), 7.53 (s, 2H, Ar*H*), 7.08 (t, *J* = 6.7 Hz, 2H, Ar*H*), 6.70–6.78 (m, 2H, Ar*H*), 6.53 (dd, *J* = 8.7, 2.1 Hz, 2H, Ar*H*), 5.90 (s, 1H, PhNC(CF_3)CHC(CF_3)NPh) ^{19}F NMR (564 MHz, $CDCl_3$) δ: –59.51 (s, 6F, CF_3), –62.64 (s, 6F, CF_3) –63.05 (s, 6F, CF_3), –104.52 (q, *J* = 8.9 Hz, 2F, F_2ppy), –109.66 (t, *J* = 10.3 Hz, 2F, F_2ppy). Anal. Calcd for $C_{43}H_{19}ClF_{22}N_4Pt_2$: C, 35.99; H, 1.33; N, 3.90. Found: C, 35.78; H, 1.28; N, 3.91.

Pt(ppy)(NacNac^{F6}) (6). [Pt(ppy)(μ-Cl)]$_2$ (30 mg, 0.039 mmol) and NacNac^{F6}Li (31 mg, 0.085 mmol, 2.2 equiv) were combined in 5 mL of toluene in a Teflon-capped glass vessel inside the glovebox. The mixture was heated to 100 ℃ with constant stirring for 16 h. After cooling, the solution was filtered through a short alumina column and concentrated in

vacuo. The crude product was purified by column chromatography, using an alumina stationary phase and 1:3 (v:v) ethyl acetate/hexane as the eluent. The compound was recrystallized from Et_2O/hexane and dried in vauo. Yield: 52 mg (94%). ^{1}H NMR (600 MHz, CD_2Cl_2) δ: 7.65 – 7.59 (m, 1H, Ar*H*), 7.51 (d, *J* = 7.8 Hz, 1H, Ar*H*), 7.45 (d, *J* = 8.1 Hz, 2H, Ar*H*), 7.42 – 7.38 (m, 1H, Ar*H*), 7.35 (dd, *J* = 7.5, 1.4 Hz, 1H, Ar*H*), 7.30 – 7.23 (m, 4H, Ar*H*), 7.21 – 7.13 (m, 3H, Ar*H*), 7.08 – 7.01 (m, 2H, Ar*H*), 6.96 (dtd, *J* = 22.4, 7.3, 1.4 Hz, 2H, Ar*H*), 6.65 (ddd, *J* = 7.4, 6.0, 1.5 Hz, 1H, Ar*H*), 6.02 (s, 1H, PhNC(CF_3)CHC(CF_3)NPh). ^{19}F NMR (564 MHz, CD_2Cl_2) δ: –58.46 (s, 3F, CF_3), –59.11 (s, 3F, CF_3). Anal. Calcd for $C_{28}H_{19}ClF_6N_3Pt$: C, 47.60; H, 2.71; N, 5.95. Found: C, 47.47; H, 2.61; N, 5.92.

Pt(F_2ppy)(NacNac^{F6}) (7). Prepared analogously to complex **6**, using [Pt(F_2ppy)(μ-Cl)]$_2$ (35 mg, 0.042 mmol) and NacNac^{F6}Li (32 mg, 0.088 mmol, 2.1 equiv). Yield: 13 mg (21%). ^{1}H NMR (600 MHz, $CDCl_3$) δ: 7.87 (d, *J* = 7.9 Hz, 1H, Ar*H*), 7.61 (dd, *J* = 14.6, 6.8 Hz, 2H, Ar*H*), 7.43 (d, *J* = 7.6 Hz, 2H, Ar*H*), 7.29 (d, *J* = 7.6 Hz, 2H, Ar*H*), 7.23 (dd, *J* = 11.0, 4.7 Hz, 4H, Ar*H*), 7.12 (dt, *J* = 14.8, 7.2 Hz, 2H, Ar*H*), 6.65 (t, *J* = 6.6 Hz, 1H, Ar*H*), 6.52 – 6.46 (m, 1H, Ar*H*), 6.43 (d, *J* = 9.7 Hz, 1H, Ar*H*), 6.05 (d, *J* = 1.5 Hz, 1H, PhNC(CF_3)CHC(CF_3)NPh). ^{19}F NMR (564 MHz, $CDCl_3$) δ: –58.54 (s, 3F, CF_3), –58.91 (s, 3F, CF_3) –106.70 (br, m, 1F, F_2ppy), –111.61 (br, s, 1F, F_2ppy). Anal. Calcd for $C_{28}H_{17}ClF_8N_3Pt$: C, 45.29; H, 2.31; N, 5.66. Found: C, 45.34; H, 2.74; N, 5.24.

1.2.4. X-ray Crystallography Procedures.

Single crystals were grown by vapor diffusion of pentane into concentrated CH_2Cl_2 solutions or by slow evaporation of Et_2O solutions. Crystals were mounted on a Bruker Apex II three-circle diffractometer using MoKα radiation (λ = 0.71073 Å). The data was

collected at 123(2) K and was processed and refined within the APEXII software. Structures were solved by direct methods in SHELXS and refined by standard difference Fourier techniques in the pro-gram SHELXL.[39] Hydrogen atoms were placed in calculated positions using the standard riding model and refined isotropically; all non-hydrogen atoms were refined anisotropically. The structure of complexes **1** and **3** contained disordered THF solvent molecules and the structures of **4** and **5** each included one rotationally disordered CF_3 groups. Distance restraints (SADI) were used for all 1,2 and 1,3 distances within the disordered parts, and rigid bond restraints SIMU and DELU were employed for the thermal displacement parameters. Crystallographic details are summarized in **Tables A1.1–A1.3**.

1.3. Results and Discussion

1.3.1. Synthesis and Structural Characterization.

Scheme 1.1 describes the synthesis of the seven NacNac complexes that will be described here. When cyclometalated platinum dimers $[Pt(C\hat{}N)(\mu\text{-}X)]_2$ (C^N = 2-phenylpyridine (ppy), 2-(2,4-difluorophenyl)pyridine (F_2ppy); X = Cl, Br) are treated with lithium salts of the respective β-diketiminate ligand and heated in toluene, the insoluble halide-bridged dimer is gradually drawn into solution and the yellow color of the precursors gives way to deep purple. At milder temperatures of ca. 80 ℃, NacNac-bridged diplatinum complexes **1** and **3**–**5** are isolated as the major product following chromatographic purification. Bromide analogue **2** is formed under similar conditions, but is seemingly more reactive and has a higher propensity to cleave and form monoplatinum complexes (see below). Integration of the ^{1}H NMR spectra of **1**–**5** or the ^{19}F NMR spectra of **3** and **5** indicate a ratio of one NacNac ligand per two C^N ligands.

Scheme 1.1. Synthesis of fluorinated β-diketiminate platinum complexes.

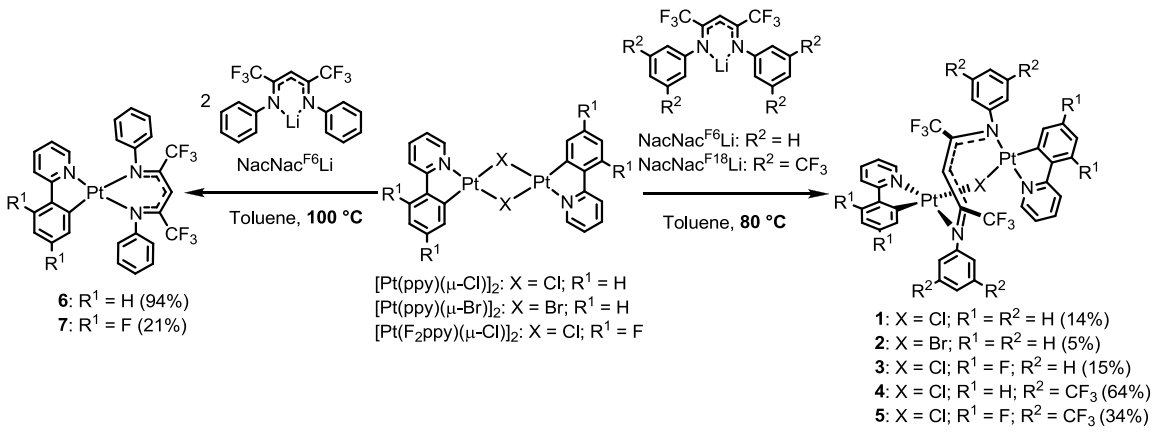

Furthermore, the ^{19}F NMR spectra of all complexes show a single resonance for the backbone CF_3 groups (ca. −59.6 ppm vs. $CFCl_3$), indicating chemical equivalency of the two "halves" of the NacNac ligand, and for NacNac^{F18} complexes **4** and **5** the two aryl CF_3 resonances are inequivalent (ca. –62.6 and –63.0 ppm), suggesting hindered rotation of the *N*-aryl groups at room temperature.

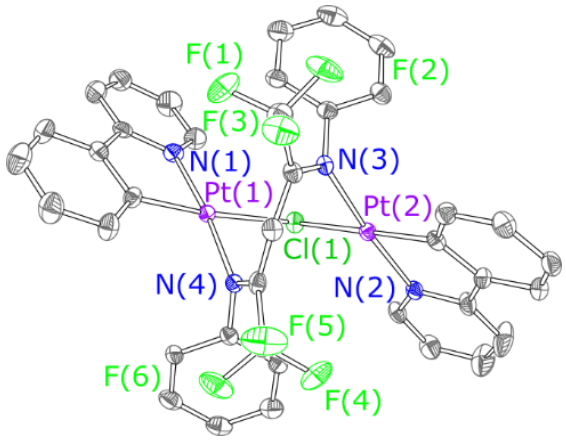

Figure 1.2. X-ray crystal structure of complex **1**. Ellipsoids are drawn at the 50% probability level with solvent molecules and hydrogen atoms omitted.

The structures of complexes **1**–**5** were ascertained by single-crystal X-ray diffraction, and that of complex **1** is shown in **Figure 1.2** as a representative example. Diffraction data and refinement details for all complexes are summarized in Tables **A1.1**–**A1.3** of **Appendix 1**, and the structures of **2**–**5** are collected in **Figures A1.1–A1.4**. The structures of **1**–**5** are essentially identical, with no substantial differences except the longer Pt–Br distances in complex **2** when compared to chloride complexes **1** and **3**–**5**. In each case the two platinum centers possess a planar geometry, symmetrically bridged by the halide. In **4** and **5** the bridging chloride resides on a special position and the two Pt–Cl distances are identical by symmetry, whereas for **1**–**3** the two distances are only minimally inequivalent. There are no apparent Pt---Pt interactions in any of the structures; the two nuclei are separated by at least 3.65 Å , and the two platinum coordination planes are twisted by 58–63° in each case. The nitrogen atoms of the NacNac ligand are trans to the nitrogen atoms of the C^N ligands, and the NacNac backbone is significantly twisted. Backbone N–C–C–C torsion angles of the NacNac range from 25–33°, much larger than the corresponding angles in crystallographically characterized cyclometalated iridium complexes with the same NacNac ligands in a chelating mode (< 11° in each case).[32] This type of binding mode for the NacNac is unprecedented. There are some bimetallic silver complexes where a fluorinated NacNac ligand simultaneously chelates one metal center and bridges to the other, but the pure η^2 binding mode in complexes **1**–**5** has not been previously observed in any crystallographically characterized transition metal complexes.

Heating $[Pt(C^N)(\mu\text{-}Cl)]_2$ with >2 equivalents of the NacNacLi salts at a higher temperature of 100 °C leads to formation of mononuclear complexes Pt(C^N)(NacNac) as major products. In separate experiments heating complexes **1** and **3**–**5** in the presence of 1

equivalent of NacNac salts also forms the same complexes, suggesting that the diplatinum complexes are intermediates in the formation of the bis-chelate Pt(C^N)(NacNac) species. Two such complexes, Pt(ppy)($NacNac^{F6}$) (**6**) and Pt(F_2ppy)($NacNac^{F6}$) (**7**) can be isolated in pure form. NMR spectra are consistent with the structures shown in **Scheme 1.1**. Integration of ^{1}H NMR spectra of both complexes and the ^{19}F NMR spectrum of **7** now indicate a 1:1 ratio of $NacNac^{F6}$ to the C^N ligand. Furthermore, the ^{19}F signals for the backbone CF_3 groups become inequivalent, appearing as two closely spaced singlets at ca. –58.5 and –59.0 ppm, consistent with the NacNac ligand being opposed by the asymmetric C^N ligand.

Structures of complexes **6** (**Figure 1.3**) and **7** (**Figure A1.5**) were confirmed by X-ray crystallography. The NacNac ligand chelates the platinum center with two slightly different Pt–N distances. The stronger trans influence of the aryl group imposes a longer distance (ca. 2.18 Å) for the bond opposite the Pt–C bond, with the other NacNac Pt–N bond shorter by over 0.1 Å (ca. 2.02–2.04 Å). The chelated NacNac is not planar however, and a puckered structure is observed, as evident from the side view shown in **Figure 1.3**. This conformation presumably exists to avoid unfavorable steric interactions between the N-phenyl rings and the C^N ligand, and is markedly similar to the conformation observed in structurally related cyclometalated platinum formazanate complexes also described by our group.[40] The structures of **6** and **7** are nearly identical, with no notable changes in bond lengths or angles caused by fluorination of the C^N ligand in the latter.

$NacNac^{F18}$ analogues of complexes **6** and **7** were pursued, and they were identified in crude NMR spectra of the reaction mixtures. However, attempted chromatographic purification of these complexes, with silica or alumina adsorbent and either on the benchtop

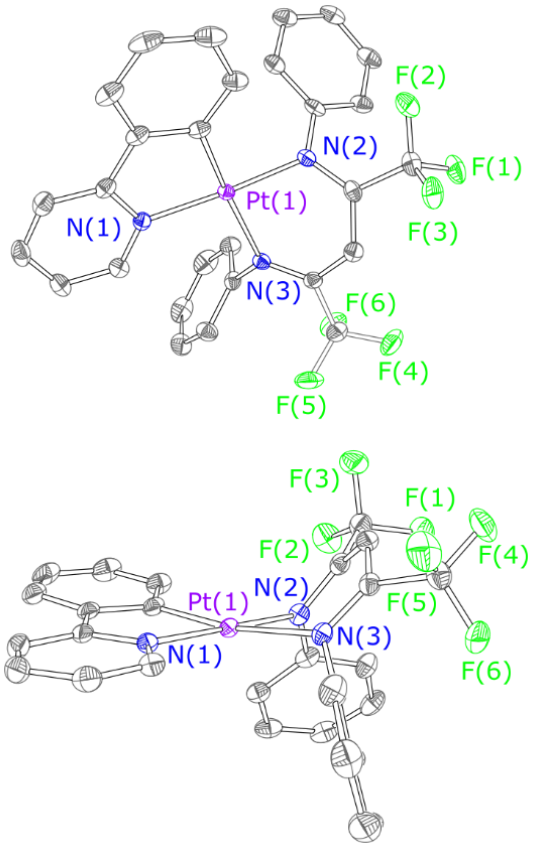

Figure 1.3. Two different views of the X-ray crystal structure of complex **6**. Ellipsoids are drawn at the 50% probability level with hydrogen atoms omitted. Only one of the two crystallographically independent molecules is shown.

Scheme 1.2. Hydrolysis of Pt(ppy)(NacNac^{F18}).

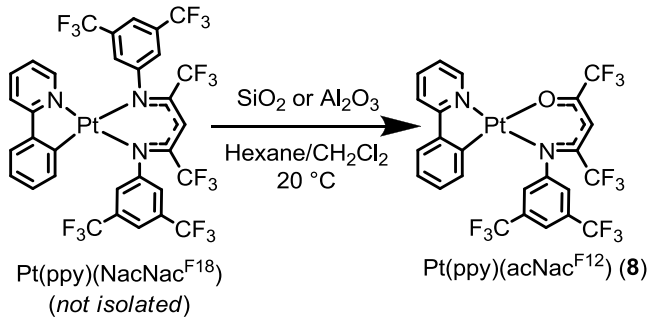

or in the glovebox with anhydrous solvents, resulted in hydrolysis of the NacNac^{F18} ligand to the corresponding acNac^{F12} ligand. In the case of the ppy analogue, the identity of the hydrolysis product was conclusively identified to be Pt(ppy)(acNac^{F12}), as shown in **Scheme 1.2**. The formation of the acNac product is clearly evident from the crude ^{19}F NMR spectrum, where a new resonance at ca. −75 ppm grows in following filtration of the crude product through alumina, assigned to the backbone CF_3 group adjacent to the oxygen (**Figure A1.6**). The structure of **8** was ascertained by X-ray crystallography and is shown in **Figure 1.4**. Our group has previously prepared bis-cyclometalated iridium complexes with fluorinated acNac ligands,[32] but these complexes were not luminescent. For this reason, rational syntheses of platinum complexes with fluorinated acNac ligands or further purification and study of the ones formed by hydrolysis were not pursued.

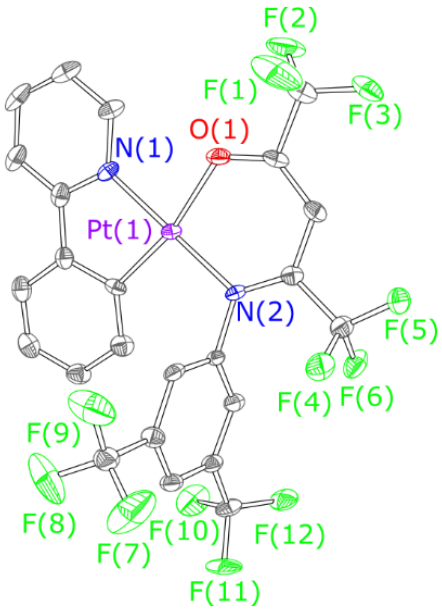

Figure 1.4. X-ray crystal structure of complex **8**. Ellipsoids are drawn at the 50% probability level with hydrogen atoms omitted.

1.3.2. Electrochemistry.

Redox properties of the complexes were characterized by cyclic voltammetry. For the diplatinum complexes anodic sweeps result in a series of closely spaced irreversible oxidations, as shown **Figure A1.7**. The onset of oxidation is responsive to the fluorination of the NacNac ligand, with NacNac^{F6} complexes **1** and **3** significantly easier to oxidize than NacNac^{F18} complexes **4** and **5**. Chloride-bridged complexes **1** and **3**–**5** exhibit reversible reduction waves that are strongly dependent on the identity of the NacNac ligand minimally dependent on the C^N ligand.

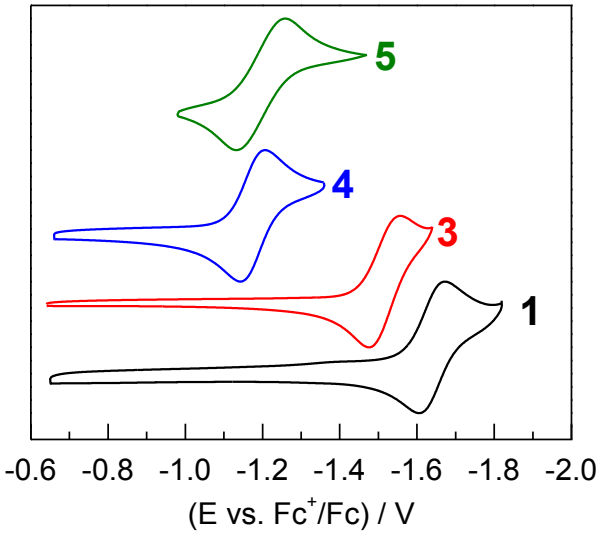

Figure 1.5. Overlaid cyclic voltammograms of chloride-bridged diplatinum complexes **1**, **3**, **4**, and **5**, showing cathodic (negative) sweeps only. The voltammograms were recorded in MeCN (**1**, **3**, and **4**) or THF (**5**) with 0.1 M $TBAPF_6$ supporting electrolyte, a glassy carbon working electrode, a platinum wire counter electrode, and a silver wire pseudo-reference electrode. Potentials are referenced to the ferrocenium/ferrocene couple. Currents are normalized to bring the plots onto the same scale.

The CVs of these four complexes, showing the reversible reduction wave, are overlaid in **Figure 1.5**, and the data is summarized in **Table 1.1** along with UV-vis data described

below. $Pt_2(ppy)_2(\mu\text{-}NacNac^{F6})(\mu\text{-}Cl)$ (**1**) is reduced at –1.64 V (all potentials are quoted relative to the ferrocenium/ferrocene couple), and this value shifts to –1.52 V when ppy is replaced with F_2ppy in complex **3**. The reduction potential is much more strongly perturbed in $NacNac^{F18}$ complexes, anodically shifting by > 300 mV to –1.17 V for **4** (C^N = ppy) and –1.20 V for **5** (C^N = F_2ppy; recorded in THF due to low solubility in MeCN). The similar responses of the oxidation and reduction waves to fluorination of the NacNac ligand suggests that the frontier orbitals include substantial contribution from NacNac-centered orbitals, and also that the HOMO–LUMO gaps for **1**, **3**, **4**, and **5** are all approximately equal. To determine the effect of replacing the bridging chloride with a bromide, complex **2** was prepared, and its electrochemical features (**Figure A1.8**) are minimally different than

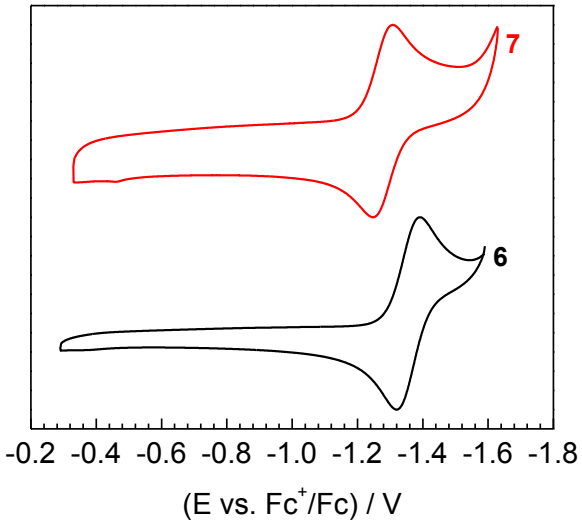

Figure 1.6. Overlaid cyclic voltammograms of monoplatinum complexes **6** and **7**, showing cathodic (negative) sweeps only. The voltammograms were recorded in MeCN with 0.1 M $TBAPF_6$ supporting electrolyte, a glassy carbon working electrode, a platinum wire counter electrode, and a silver wire pseudo-reference electrode. Potentials are referenced to the ferrocenium/ferrocene couple. Cur-rents are normalized to bring the plots onto the same scale.

complex **1**, with a reversible reduction observed at –1.68 V.

The electrochemistry of monoplatinum complexes **6** and **7** was also investigated, and there are many similarities to the diplatinum complexes. Oxidations for these compounds are likewise irreversible, as shown in **Figure A1.9**, with onset potentials fairly similar to the diplatinum complexes. Complexes **6** and **7** are also reduced at mild potentials, with reversible reduction waves observed at –1.36 V (**6**) and –1.28 V (**7**), again depending only slightly on the C^N ligand (**Figure 1.6**). All of complexes **1**–**7** are much easier to reduce than other well-known cyclometalated platinum complexes. For example, the complexes $Pt(C^N)_2(acac)$ are reduced at potentials of –2.4 V (C^N = ppy) and –2.3 V (C^N = F_2ppy), and this reduction corresponds to addition of an electron to a C^N-centered

Table 1.1. Summary of electrochemical and photophysical data.

	(E_{red} vs. Fc^+/Fc) / V[a]	λ_{abs} / nm ($\varepsilon \times 10^{-3}$ / $M^{-1}cm^{-1}$)[b]	λ_{em} / nm[c]
1	–1.64	325 (sh) (7.2), 376 (4.3), 531 (5.6)	[d]
2	–1.68	325 (sh) (7.6), 373 (4.3), 529 (5.1)	[d]
3	–1.52	308 (14), 323 (14), 361 (6.4), 527 (8.6)	[d]
4	–1.17	312 (sh) (15), 326 (13), 365 (sh) (8.2), 373 (8.3), 535 (10)	[d]
5	–1.20	308 (18), 321 (20), 351 (9.2), 361 (9.2), 530 (12)	[d]
6	–1.36	313 (sh) (6.0), 400 (3.3), 475 (2.1), 527 (sh) (1.8)	646, 704, 770 (sh)
7	–1.28	311 (6.5), 322 (6.6), 398 (3.2), 464 (2.3), 522 (sh) (1.7)	632, 688, 747(sh)

[a] Recorded in MeCN, except complex **5** (THF). [b] Recorded in CH_2Cl_2 at 293 K. [c] Recorded in toluene at 77 K. [d] Not luminescent.

π* orbital.[41] Reduction potentials of Pt(C^N)(NacNac^{F6}) complexes **6** and **7** are anodically shifted by over 1 V relative to their acac analogues, and the reduction potentials for the diplatinum complexes depend most strongly on the fluorination of the NacNac ligand. For these reasons, the one-electron reversible CV waves depicted in **Figures 1.5** and **1.6** are attributed to NacNac-centered reductions. NacNac^{F6}-bridged diplatinum complexes **1** and **3** are more difficult to reduce by ca. 250 mV when compared to monoplatinum complexes featuring the same NacNac and C^N ligands (**6** and **7**), suggesting that the energy of the NacNac-centered LUMO is strongly dependent on the ligand binding mode (bridged vs. chelated).

1.3.3. UV-vis absorption and emission.

Further confirmation for the large contribution of the NacNac-centered π system to the frontier orbitals comes from studies of the UV-vis absorption and emission spectra of complexes **1**–**7**. All of the complexes described here are highly colored, appearing red to purple in the solid state and solution. Overlaid UV-vis absorption spectra of diplatinum complexes **1**–**5** are shown in **Figure 1.7**. Spectra are displayed in the range of 300–700 nm; for $\lambda < 300$ nm the absorption monotonically increases. Like other platinum complexes with cyclometalated ppy or F_2ppy ligands[41] **1**−**7** display absorption bands ~360 − 370 nm which are attributed to Pt(d) → C^N(π *) metal-to-ligand-charge transfer (MLCT) transitions. When comparing complexes with C^N = ppy (**1**, **2**, and **4**) to complexes with C^N = F_2ppy (**3** and **5**), these MLCT transitions are typically about 10–15 nm (~1000 cm^{-1}) blue-shifted in the latter.

The most prominent feature in the absorption spectra of **1**–**5** is an intense absorption band ($\varepsilon \sim 5–12 \times 10^3\ M^{-1}cm^{-1}$) near 530 nm, which varies little in wavelength throughout

the series. There are no Pt---Pt interactions in the crystal structures (see **Figures 1.2** and **A1.1 – A1.4**) and the low-energy absorption band obeys Beer's Law and is not concentration dependent, eliminating the possibility of this band being assigned to

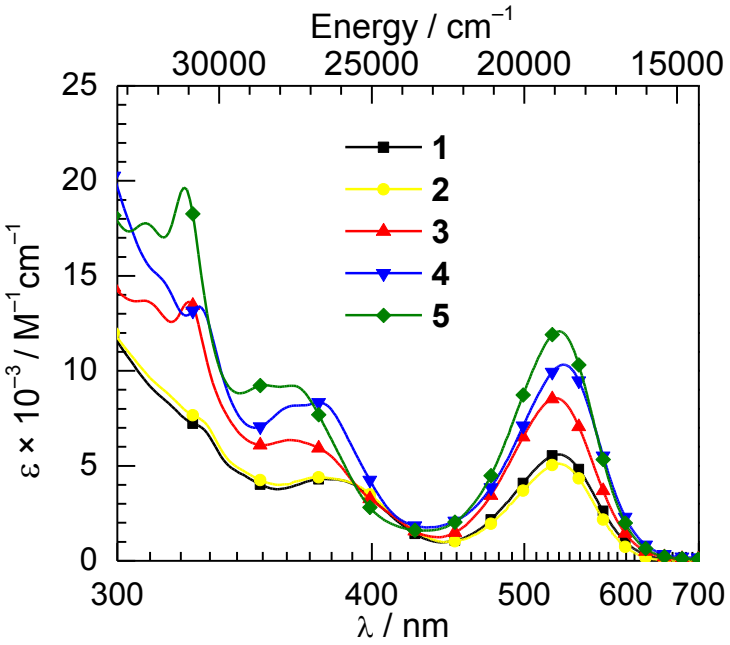

Figure 1.7. Overlaid UV-vis absorption spectra of complexes **1**–**5**, recorded in CH_2Cl_2 at room temperature.

a $d\sigma^* \rightarrow p\sigma$ transition frequently observed in diplatinum complexes or in solutions of aggregated Pt(II) complexes.[42] We can also rule out any contribution from ligand-to-metal charge transfer (LMCT) transitions involving the bridging halide, both to the low-energy band or any other absorption features, as the spectra of **1** (X = Cl) and **2** (X = Br) overlay perfectly. Instead, we attribute this band to a low-energy, NacNac-centered $\pi \rightarrow \pi^*$ transition. Free NacNac^{F6}H and NacNac^{F18}H ligands dissolved in CH_2Cl_2 are yellow in color with absorption bands near 350 nm,[32] and these transitions are greatly perturbed in diplatinum complexes **1**–**5**, suggesting that interactions of the NacNac π system with Pt(dπ)

orbitals and/or the structural distortion caused by the η^2 binding mode disrupt the frontier orbital energies. Further support for this assignment comes from solvatochromic studies, recording the absorption spectra in solvents of different polarity.

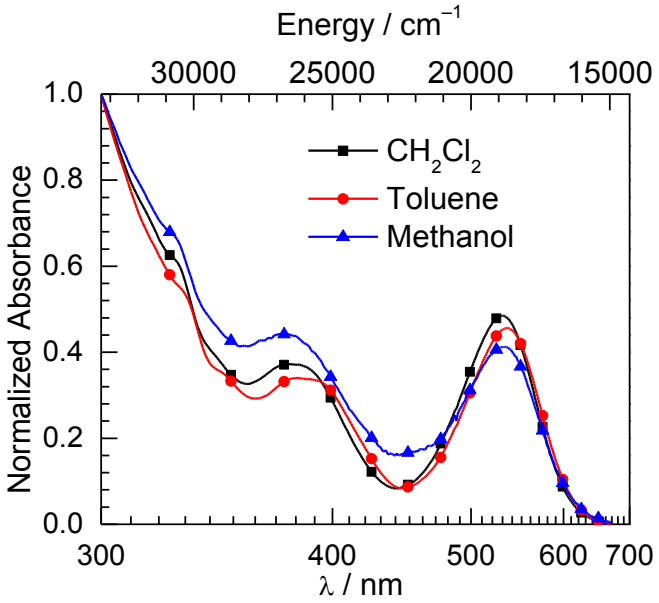

Figure 1.8. Overlaid, normalized UV-vis absorption spectra of complex **1** recorded in CH_2Cl_2, toluene, and methanol at room temperature.

Figure 1.8 overlays the spectra of complex **1** in the solvents toluene (ε = 2.38), dichloromethane (ε = 8.93) and methanol (ε = 33.0)[43], with analogous plots for the remaining chloride-bridged complexes (**3**–**5**) shown in **Appendix 1**, Figures **A1.10**–**A1.12**. The visible absorption bands in these complexes show negligible solvatochromism, differing by no more than 4 nm (140 cm^{-1}) as the solvent polarity is varied. This supports the contention that this low energy-band is primarily a ligand-centered, $\pi \rightarrow \pi^*$ transition with minimal charge transfer character.

The UV-vis absorption profiles of monoplatinum complexes **6** and **7** are markedly different, with several broad, overlapping bands that cover most of the visible range.

Overlaid spectra of these two compounds are depicted in **Figure 1.9**. There are minimal differences between the absorption spectra of complexes **6** and **7**, and again very little solvatochromism is observed (**Figures A1.13** and **A1.14**). These observations indicate that the low-energy absorption features in the monoplatinum complexes with chelated NacNac ligands likewise are not influenced by the cyclometalating ligand and derive from NacNac-centered, $\pi \rightarrow \pi^*$ excited states. Complexes **6** and **7** do not luminesce at room temperature, but unlike the diplatinum complexes these monometallic analogues are luminescent when cooled to 77 K. The lack of emission at room temperature obviates an accurate determination of quantum yield.

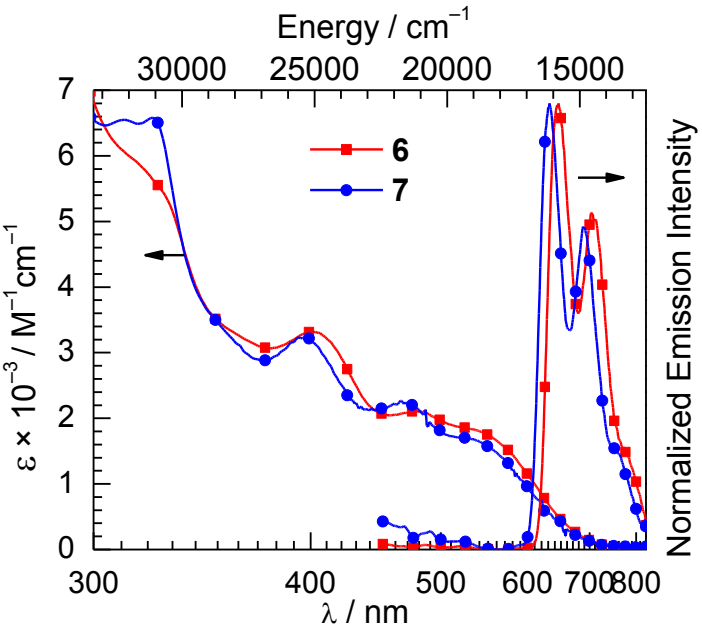

Figure 1.9. Overlaid UV-vis absorption and emission spectra of complexes **6** and **7**. Absorption spectra were recorded at room temperature in toluene, whereas emission spectra were recorded at 77 K in toluene glass with λ_{ex} = 420 nm.

Structured emission is observed in the red and near-infrared regions of the visible spectrum, with emission wavelengths that depend slightly on the C^N ligand (see **Table 1.1**). For the

complex Pt(ppy)(NacNac^{F6}) (**6**) vibronic spacing of 1275 cm^{-1} is observed between the two highest-energy maxima, and in the F_2ppy analogue **7** the vibronic structure is nearly identical but the maxima are blue-shifted by ca. 340 cm^{-1}. The emission is assigned to a NacNac-centered $^3(\pi\rightarrow\pi^*)$ excited state, and the overlap of the emission spectrum with the low-energy absorption features suggests that one or more of the low-energy absorption bands in complexes **6** and **7** may arise from direct triplet excitation. Furthermore, the spectra of **6** and **7** are strikingly similar to those of cyclometalated iridium complexes bearing fluorinated NacNac ligands, previously described by our group.[32] Comparing complex **6** with Ir(ppy)$_2$(NacNac^{F6}), which has the same C^N and NacNac ligands, we observe that the emission from the platinum complex occurs at higher energy, by about 600 cm^{-1}, and that the vibronic structure is compressed by 100 cm^{-1}. These comparisons demonstrate that the low-energy, NacNac-centered excited state is influenced to a small but measureable extent by the nature of the heavy metal and/or the coordination geometry, opening up the possibility that other designs could further perturb the emission in fluorinated NacNac phosphors.

1.4. Conclusions

In this work we disclosed a series of platinum complexes of fluorinated β-diketiminate ligands, and noted two different coordination modes for the NacNac ligand. The two types of complexes are prepared by slight variation of the reaction temperature. A series of bimetallic complexes with a bridging NacNac were structurally characterized, a previously unobserved binding mode for the typically chelating NacNac moiety. By increasing the reaction temperature and adding more NacNac precursor, these bimetallic

complexes are cleaved and converted into simple monometallic Pt(C^N)(NacNac) bis-chelate species. In addition to the structural diversity that is revealed by this work, all of the complexes described here exhibit redox and optical proper-ties derived from the NacNac ligand. Reversible reductions at mild potentials (E > –1.65 V vs. Fc+/Fc), intense visible absorptions covering much of the visible spectrum, and luminescence in the red and near-infrared regions in the monoplatinum complexes are all posited to involve NacNac-centered frontier orbitals. These observations motivate continued pursuit of these emerging applications of fluorinated β-diketiminates as redox-active, chromophoric ligands with tunable triplet luminescence.

1.5. References

1. Bourget-Merle, L.; Lappert, M. F.; Severn, J. R. The Chemistry of β-Diketiminatometal Complexes. *Chem. Rev.* **2002**, *102*, 3031–3066.
2. Cui, C.; Roesky, H. W.; Schmidt, H.-G.; Noltemeyer, M.; Hao, H.; Cimpoesu, F. Synthesis and Structure of a Monomeric Aluminum(I) Compound [{HC(CMeNAr)$_2$}Al] (Ar=2,6-^{i}Pr$_2$C$_6$H$_3$): A Stable Aluminum Analogue of a Carbene. *Angew. Chem.* **2000**, *39*, 4274–4276.
3. Smith, J. M.; Sadique, A. R.; Cundari, T. R.; Rodgers, K. R.; Lukat-Rodgers, G.; Lachicotte, R. J.; Flaschenriem, C. J.; Vela, J.; Holland, P. L. Studies of Low-Coordinate Iron Dinitrogen Complexes. *J. Am. Chem. Soc.* **2006**, *128*, 756–769.
4. Basuli, F.; Bailey, B. C.; Tomaszewski, J.; Huffman, J. C.; Mindiola, D. J. A Terminal and Four-Coordinate Titanium Alkylidene Prepared by Oxidatively Induced α-Hydrogen Abstraction. *J. Am. Chem. Soc.* **2003**, *125*, 6052–6053.
5. Chisholm, M. H.; Gallucci, J.; Phomphrai, K. Coordination Chemistry and Reactivity of Monomeric Alkoxides and Amides of Magnesium and Zinc Supported by the Diiminato Ligand CH(CMeNC$_6$H$_3$-2,6-^{i}Pr$_2$)$_2$. A Comparative Study. *Inorg. Chem.* **2002**, *41*, 2785–2794.

6. Feldman, J.; McLain, S. J.; Parthasarathy, A.; Marshall, W. J.; Calabrese, J. C.; Arthur, S. D. Electrophilic Metal Precursors and a β-Diimine Ligand for Nickel(II)- and Palladium(II)-Catalyzed Ethylene Polymerization. *Organometallics* **1997**, *16*, 1514–1516.
7. Chamberlain, B. M.; Cheng, M.; Moore, D. R.; Ovitt, T. M.; Lobkovsky, E. B.; Coates, G. W. Polymerization of Lactide with Zinc and Magnesium β-Diiminate Complexes: Stereocontrol and Mechanism. *J. Am. Chem. Soc.* **2001**, *123*, 3229–3238.
8. Vela, J.; Smith, J. M.; Yu, Y.; Ketterer, N. A.; Flaschenriem, C. J.; Lachicotte, R. J.; Holland, P. L. Synthesis and Reactivity of Low-Coordinate Iron(II) Fluoride Complexes and Their Use in the Catalytic Hydrodefluorination of Fluorocarbons. *J. Am. Chem. Soc.* **2005**, *127*, 7857–7870.
9. Badiei, Y. M.; Dinescu, A.; Dai, X.; Palomino, R. M.; Heinemann, F. W.; Cundari, T. R.; Warren, T. H. Copper-Nitrene Complexes in Catalytic C−H Amination. *Angew. Chem. Int. Ed.* **2008**, *47*, 9961–9964.
10. Zhao, G.; Basuli, F.; Kilgore, U. J.; Fan, H.; Aneetha, H.; Huffman, J. C.; Wu, G.; Mindiola, D. J. Neutral and Zwitterionic Low-Coordinate Titanium Complexes Bearing the Terminal Phosphinidene Functionality. Structural, Spectroscopic, Theoretical, and Catalytic Studies Addressing the Ti−P Multiple Bond. *J. Am. Chem. Soc.* **2006**, *128*, 13575–13585.
11. Rodriguez, M. M.; Bill, E.; Brennessel, W. W.; Holland, P. L. N_2 Reduction and Hydrogenation to Ammonia by a Molecular Iron-Potassium Complex. *Science* **2011**, *334*, 780–783.
12. Byrne, C. M.; Allen, S. D.; Lobkovsky, E. B.; Coates, G. W. Alternating Copolymerization of Limonene Oxide and Carbon Dioxide. *J. Am. Chem. Soc.* **2004**, *126*, 11404–11405.
13. Laitar, D. S.; Mathison, C. J. N.; Davis, W. M.; Sadighi, J. P. Copper(I) Complexes of a Heavily Fluorinated β-Diketiminate Ligand: Synthesis, Electronic Properties, and Intramolecular Aerobic Hydroxylation. *Inorg. Chem.* **2003**, *42*, 7354–7356.

14. Hong, S.; Hill, L. M. R.; Gupta, A. K.; Naab, B. D.; Gilroy, J. B.; Hicks, R. G.; Cramer, C. J.; Tolman, W. B. Effects of Electron-Deficient β-Diketiminate and Formazan Supporting Ligands on Copper(I)-Mediated Dioxygen Activation. *Inorg. Chem.* **2009**, *48*, 4514–4523.
15. Carey, D. T.; Cope-Eatough, E. K.; Vilaplana-Mafé, E.; Mair, F. S.; Pritchard, R. G.; Warren, J. E.; Woods, R. J. Structures and Reactions of Monomeric and Dimeric Lithium Diazapentadienyl Complexes with Electrophiles: Synthesis of α-C,C′-Dialkyl-β-Diimines, and Dissolution-Reversible Synthesis of an α-Alkoxylithium-β-Diimine. *Dalton Trans.* **2003**, *6*, 1083–1093.
16. Barrett, A. G. M.; Crimmin, M. R.; Hill, M. S.; Hitchcock, P. B.; Procopiou, P. A. Trifluoromethyl Coordination and C−F Bond Activation at Calcium. *Angew. Chem. Int. Ed.* **2007**, *46*, 6339–6342.
17. Kernbichl, S.; Reiter, M.; Adams, F.; Vagin, S.; Rieger, B. CO_2-Controlled One-Pot Synthesis of AB, ABA Block, and Statistical Terpolymers from β-Butyrolactone, Epoxides, and CO_2. *J. Am. Chem. Soc.* **2017**, *139*, 6787–6790.
18. Kundu, S.; Kim, W. Y.; Bertke, J. A.; Warren, T. H. Copper(II) Activation of Nitrite: Nitrosation of Nucleophiles and Generation of NO by Thiols. *J. Am. Chem. Soc.* **2017**, *139*, 1045–1048.
19. Chiong, H. A.; Daugulis, O. Monomeric Silver(I) β-Diketiminate Complexes. *Organometallics* **2006**, *25*, 4054–4057.
20. Zhu, D.; Budzelaar, P. H. M. *N*-Aryl β-Diiminate Complexes of the Platinum Metals. *Dalton Trans.* **2013**, *42*, 11343–11354.
21. Bernskoetter, W. H.; Lobkovsky, E.; Chirik, P. J. Synthesis of a β-Diiminate Iridium Tetrahydride for Arene C–H Bond Activation. *Chem Commun* **2004**, *7*, 764–765.
22. Bernskoetter, W. H.; Lobkovsky, E.; Chirik, P. J. Ancillary Ligand Effects on C−H Bond Activation Reactions Promoted by β-Diiminate Iridium Complexes. *Organometallics* **2005**, *24*, 6250–6259.
23. Fekl, U.; Kaminsky, W.; Goldberg, K. I. A Stable Five-Coordinate Platinum(IV) Alkyl Complex. *J. Am. Chem. Soc.* **2001**, *123*, 6423–6424.

24. Fekl, U.; Goldberg, K. I. Five-Coordinate Platinum(IV) Complex as a Precursor to a Novel Pt(II) Olefin Hydride Complex for Alkane Activation. *J. Am. Chem. Soc.* **2002**, *124*, 6804–6805.
25. Fekl, U.; Kaminsky, W.; Goldberg, K. I. β-Diiminate Platinum Complexes for Alkane Dehydrogenation. *J. Am. Chem. Soc.* **2003**, *125*, 15286–15287.
26. Scheuermann, M. L.; Fekl, U.; Kaminsky, W.; Goldberg, K. I. Metal−Ligand Cooperativity in O_2 Activation: Observation of a 'Pt−O−O−C' Peroxo Intermediate[§]. *Organometallics* **2010**, *29*, 4749–4751.
27. Scheuermann, M. L.; Luedtke, A. T.; Hanson, S. K.; Fekl, U.; Kaminsky, W.; Goldberg, K. I. Reactions of Five-Coordinate Platinum(IV) Complexes with Molecular Oxygen. *Organometallics* **2013**, *32*, 4752–4758.
28. West, N. M.; White, P. S.; Templeton, J. L. Facile Dehydrogenation of Ethers and Alkanes with a *β* -Diiminate Pt Fragment. *J. Am. Chem. Soc.* **2007**, *129*, 12372–12373.
29. West, N. M.; White, P. S.; Templeton, J. L. Alkyne Insertion into the Pt−H Bond of Pt(H)(1-Pentene)(β-Diiminate) Initiates a Reaction Cascade That Results in C−H Activation or C−C Coupling. *Organometallics* **2008**, *27*, 5252–5262.
30. West, N. M.; White, P. S.; Templeton, J. L.; Nixon, J. F. Cycloaddition Reactions of Terminal Alkynes and Phosphaalkynes with an Isolable 5-Coordinate β-Diiminate Platinum(IV) Dihydrosilyl Complex. *Organometallics* **2009**, *28*, 1425–1434.
31. Radwan, Y. K.; Maity, A.; Teets, T. S. Manipulating the Excited States of Cyclometalated Iridium Complexes with β-Ketoiminate and β-Diketiminate Ligands. *Inorg. Chem.* **2015**, *54*, 7122–7131.
32. Maya, R. A.; Maity, A.; Teets, T. S. Fluorination of Cyclometalated Iridium β-Ketoiminate and β-Diketiminate Complexes: Extreme Redox Tuning and Ligand-Centered Excited States. *Organometallics* **2016**, *35*, 2890–2899.
33. Moussa, J.; Cheminel, T.; Freeman, G. R.; Chamoreau, L.-M.; Williams, J. A. G.; Amouri, H. An Unprecedented Cyclometallated Platinum(II) Complex

Incorporating a Phosphinine Co-Ligand: Synthesis and Photoluminescence Behaviour. *Dalton Trans* **2014**, *43*, 8162–8165.

34. Sesolis, H.; Moussa, J.; Gontard, G.; Jutand, A.; Gullo, M. P.; Barbieri, A.; Amouri, H. A Unique Class of Neutral Cyclometalated Platinum(II) Complexes with π-Bonded Benzenedithiolate: Synthesis, Molecular Structures and Tuning of Luminescence Properties. *Dalton Trans.* **2015**, *44*, 2973–2977.
35. Moussa, J.; Loch, A.; Chamoreau, L.-M.; Degli Esposti, A.; Bandini, E.; Barbieri, A.; Amouri, H. Luminescent Cyclometalated Platinum Complexes with π-Bonded Catecholate Organometallic Ligands. *Inorg. Chem.* **2017**, *56*, 2050–2059.
36. Godbert, N.; Pugliese, T.; Aiello, I.; Bellusci, A.; Crispini, A.; Ghedini, M. Efficient, Ultrafast, Microwave-Assisted Syntheses of Cycloplatinated Complexes. *Eur. J. Inorg. Chem.* **2007**, *2007*, 5105–5111.
37. Black, D.; Deacon, G.; Edwards, G. Observations on the Mechanism of Halogen-Bridge Cleavage by Unidentate Ligands in Square Planar Palladium and Platinum Complexes. *Aust. J. Chem.* **1994**, *47*, 217–227.
38. Tang, L.-M.; Duan, Y.-Q.; Li, X.-F.; Li, Y.-S. Syntheses, Structure and Ethylene Polymerization Behavior of β-Diiminato Titanium Complexes. *J. Organomet. Chem.* **2006**, *691*, 2023–2030.
39. Sheldrick, G. M. A Short History of *SHELX*. *Acta Crystallogr. A* **2008**, *64*, 112–122.
40. Kabir, E.; Wu, C.-H.; Wu, J. I.-C.; Teets, T. S. Heteroleptic Complexes of Cyclometalated Platinum with Triarylformazanate Ligands. *Inorg. Chem.* **2016**, *55*, 956–963.
41. Brooks, J.; Babayan, Y.; Lamansky, S.; Djurovich, P. I.; Tsyba, I.; Bau, R.; Thompson, M. E. Synthesis and Characterization of Phosphorescent Cyclometalated Platinum Complexes. *Inorg. Chem.* **2002**, *41*, 3055–3066.
42. Roundhill, D. M.; Gray, H. B.; Che, C. M. Pyrophosphito-Bridged Diplatinum Chemistry. *Acc. Chem. Res.* **1989**, *22*, 55–61.

43. *CRC Handbook of Chemistry and Physics: A Ready-Reference Book of Chemical and Physical Data*, 84th ed.; Chemical Rubber Company, Lide, D. R., Eds.; CRC Press: Boca Raton, 2003.

Chapter 2. Lewis Acid Modulation of aza-BODIPY and *meso*-Pyridyl BODIPY Chromophores

2.1. Introduction

Boron dipyrromethene (BODIPY) derivatives of the general structure A have been intensely researched for their intense absorption and strong fluorescence.[1,2] In recent years BODIPY compounds have been developed and applied in a variety of contexts including photodynamic therapy[3–5], fluorescent probes for biological imaging[6,7], emitter materials in organic light-emitting diodes (OLEDs),[8] and dye-sensitized[9] or organic[10] solar cells. Additionally, changing BODIPY (A) to aza-BODIPY (B) can lead to large bathochromic shifts in absorption and emission, via substitution of the methine bridge carbon to nitrogen (**Figure 2.1**). As a result, aza-BODIPY chromophores have emerged in a number of solar cell and sensing applications, where the red-shifted absorption and emission create desirable advantages.[4,11–15]

When tailoring the properties of a BODIPY-based chromophore for a particular application, synthetic modifications typically involve introduction of covalent substituents to the periphery of the BODIPY core,[16,17] which is achieved either by complete synthesis from the appropriate pyrrole precursors or through coupling reactions that modify pre-formed BODIPY precursors. In sensing applications, the optical properties of BODIPY and aza-BODIPY fluorophores are modulated through specific interactions with the analyte, often involving peripheral Lewis bases on the chromophore which interact with

Chapter 2 was reproduced with permission from Choung, K. S.; Teets, T. S. *ChemPhotoChem*. **2019**, *3*, 86–92.

environmental additives like cationic Lewis acids.[18–21] These sensors are typically designed to have "on/off" responses, meaning it is the intensity of emission, and not the color, that is primarily altered by the analyte. For certain applications, especially solar cells where the precise absorption profile is critical or OLEDs where the emission color is a key determinant in device performance, the ability to rapidly, systematically, and precisely control the optical properties would be a significant advantage.

Our group has recently introduced the concept that Lewis acid-base interactions in the secondary coordination sphere can modulate the photophysical properties of organometallic phosphors, allowing rapid and facile color-tuning of the emission over a wide range.[22] In this previous work we showed that boranes, which are available with numerous substituents that can engender a wide range of available Lewis acidities, allow precise control over the electronic structure. In essence, the acidity of the borane correlates with how strong of an electron-withdrawing group it is when bound to the phosphor, and the site of binding influences the magnitude and direction (i.e. red-shift or blue-shift) of the effect on the emission profile. In this way, we demonstrated the ability to precisely control the excited-state energy, by changing the strength or amount of the Lewis acid additive and by synthetically controlling the binding site of the chromophore. Around the same time, it was shown that coordination of $B(C_6F_5)_3$ to non-emissive aldehydes could engender intense color-tunable luminescence, further highlighting the ability of Lewis acid-base coordination chemistry to influence photophysical attributes.[23–25]

In this work we expand this concept to BODIPY-based organic fluorophores. Two BODIPY compounds possessing pyridine receptors are presented here. Compounds with

this design should be able to coordinate to virtually any borane Lewis acid, providing versatile platforms for studying the effects of Lewis acid

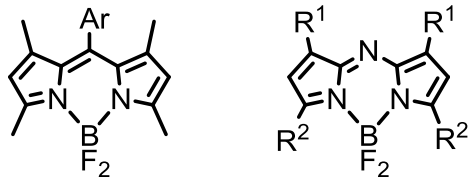

A **B**

Figure 2.1. Structures of BODIPY (A), aza-BODIPY (B).

additives on the optical properties. With these pyridyl-substituted BODIPYs we demonstrate tight binding of $B(C_6F_5)_3$, which results in distinct changes in the UV/Vis absorption and emission, the extent of which depends on how close the bound borane is to the BODIPY core.

In addition, we investigate the effects of coordination of boranes directly to the aza position in a sterically unhindered aza-BODIPY compound. Little is known about the coordination properties of this central nitrogen atom, although there are some examples of metal ion sensors that utilize the bridgehead nitrogen atom to assist coordination of Hg(II), in one case causing a significant red-shift in absorption and emission.[26,27] Furthermore, computational studies on aza-BODIPY chromophores demonstrate significant participation of the bridgehead nitrogen in the LUMO, so it stands to reason that coordination of Lewis acids at this position could influence the absorption and emission spectra.[28,29] With these precedents in mind, coordination of $B(C_6F_5)_3$ to the bridgehead positions of aza-BODIPY is a viable strategy for inducing spectral changes.

2.2. Experimental Section

2.2.1. Materials

Dry solvents were obtained from a Grubbs Solvent Purification System and degassed with argon. Starting materials and reagents, unless otherwise specified, were obtained from commercial sources and used without further purification. 3.3'-Dimethyldiphenylazadipyrromethene was prepared with a previously described the literature procedure.[12] Aza-BODIPY **3** was prepared by a reaction of 3.3'-dimethyldiphenylazadipyrromethene with boron trifluoride etherate using trimethylamine as a base in dichloromethane.

2.2.2. Physical Methods.

^{1}H, $^{13}C\{^{1}H\}$, ^{19}F, and ^{11}B NMR spectra were recorded at room temperature using a JEOL ECA-500 or ECA-600 spectrometer. UV-vis absorption spectra were recorded in screw-capped 1 cm quartz cuvettes using an Agilent Carey 8454 UV-vis spectrophotometer. Steady-state emission spectra were recorded using a Horiba FluoroMax-4 spectrofluorometer. To exclude air, samples for emission spectra were prepared in a nitrogen-filled glovebox using dry, deoxygenated toluene. Emission quantum yields were obtained relative to standards of 4-pyridinyl BODIPY **1** (Φ_F = 0.30 in CH_2Cl_2, λ_{ex} = 475 nm)[30] and aza-BODIPY **3** (Φ_F = 0.41 in $CHCl_3$, λ_{ex} = 560 nm)[12] which have been reported. The emission spectra of the BODIPYs were measured with a range of absorbance between 0.01 and 0.1 at the excitation wavelength mentioned above. The integrated emission intensity was plotted vs. absorbance and the slope of the best-fit line was obtained. The quantum yield of the BODIPYs (Φ_x) was calculated by using the Equation (1) indicated

below (Φ_{st} = the quantum yield of the standard, m_x = the slope for the BODIPYs, m_{st} = standard compound, η_x and η_{st} = the refractive indexes of the solvents).

$$\Phi_x = \Phi_{st}\left[\frac{m_x}{m_{st}}\right]\left[\frac{\eta_x}{\eta_{st}}\right]^2 \quad (1)$$

The high-resolution mass spectrometry (HRMS-ESI) measurements were carried out by Mass Spectrometry Laboratory at University of Houston, using a Thermo Exactive mass spectrometer and operated in positive ionization mode with a spray voltage at 1.5 kV. ^{1}H and ^{19}F NMR spectra of all compounds are also shown in **Appendix 2**, **Figures A2.11**–**A2.17**, and provide additional evidence for sample purity.

2.2.3. General synthetic procedure for *meso*-pyridyl BODIPYs.

2,4-Dimethylpyrrole (2 equiv.) and pyridyl-substituted aldehyde (1 equiv.) were dissolved under N_2 atmosphere in 400 mL of dichloromethane. Trifluoroacetic acid (20 µL) was added and the mixture was stirred for 3 days. Chloranil (1 equiv.) was added and the mixture was stirred for 4 h. The solvent was removed under vacuum, and the crude product was dissolved in dichloromethane, followed by subsequent addition of triethylamine and boron trifluoride. The reaction mixture was further stirred at room temperature for 12 h and the progress of reaction was monitored by TLC. The dark red precipitate was filtered off, and the filtrate was reduced under vacuum. The crude product was purified by silica gel column chromatography (SiO_2) with ethyl acetate/CH_2Cl_2 (1:4 v/v) to get the desired product.

***meso*-4-pyridyl-BODIPY (1).** Prepared by the general method using 2,4-dimethylpyrrole (920 mg, 9.67 mmol), pyridine-4-carboxaldehyde (514 mg, 4.80 mmol), and chloranil (1.14 g, 4.64 mmol). Yield: 375 mg (24.0%). NMR data in $CDCl_3$ agree with the previously

reported data.[31] ^{1}H NMR (500 MHz, C_6D_6) δ: 8.37 (d, J = 5.9 Hz, 2H, Pyridine *H*), 6.28 (d, J = 5.9 Hz, 2H, Pyridine *H*), 5.52 (s, 2H, Pyrrole *H*), 2.53 (s, 6H, CH_3), 1.07 (s, 6H, CH_3). ^{19}F NMR (470 MHz, C_6D_6) δ: –145.29 (q, J = 32.4 Hz, 2F). ^{11}B NMR (160 MHz, C_6D_6) δ: 0.29 (t, J = 32.4 Hz, 1B).

***meso*-4-pyridylphenyl-BODIPY (2).** 4-(Pyridin-4-yl)benzaldehyde was prepared according to the published synthetic procedure[32] using a palladium-catalyzed Suzuki cross-coupling reaction. The title compound was prepared by the general method using 2,4-dimethylpyrrole (650 mg, 6.83 mmol), 4-(pyridin-4-yl)benzaldehyde (549 mg, 3.00 mmol), and Chloranil (0.93 g, 3.8 mmol). Yield: 293 mg (24.3%). ^{1}H NMR (500 MHz, $CDCl_3$) δ: 8.73 (d, J = 4.4 Hz, 2H, Pyridine *H*), 7.86–7.78 (m, 2H, Pyridine *H*), 7.61 (dd, J = 4.5, 1.6 Hz, 2H, Phenyl *H*), 7.50 – 7.35 (m, 2H, Phenyl *H*), 6.01 (s, 2H, Pyrrole *H*), 2.58 (s, 6H, CH_3), 1.43 (s, 6H, CH_3). ^{13}C{^{1}H} NMR (126 MHz, $CDCl_3$) δ: 155.9, 150.5, 147.2, 143.0, 140.8, 138.8, 136.1, 131.4, 129.1, 127.7, 121.7, 121.5, 77.4, 77.1, 76.9, 14.7, 14.7. ^{19}F NMR (470 MHz, $CDCl_3$) δ: –146.18 (q, J = 32.6 Hz, 2F). ^{11}B NMR (160 MHz, $CDCl_3$) δ: –0.18 (t, J = 33.1 Hz, 1B). HRMS (ESI): m/z calcd. for $C_{24}H_{22}BF_2N_3$ $[M + H]^+$: 402.1948, found: 402.2096.

^{1}H NMR (500 MHz, C_6D_6) δ: 8.55 (br, s, 2H, Pyridine *H*), 7.10 (d, J = 8.3 Hz, 2H, Pyridine *H*), 6.86 (d, J = 4.0 Hz, 2H, Phenyl *H*), 6.64 (d, J = 8.4 Hz, 2H, Phenyl *H*), 5.62 (s, 2H, Pyrrole *H*), 2.60 (s, 6H, CH_3), 1.23 (s, 6H, CH_3). ^{19}F NMR (470 MHz, C_6D_6) δ: –145.28 (q, J = 32.6 Hz, 2F). ^{11}B NMR (160 MHz, C_6D_6) δ: 0.46 – 0.35 (m, 1B). ^{11}B NMR (160 MHz, C_6D_6) δ: 0.45 (t, J = 32.7 Hz, 1B).

Dibutylborylazadipyrromethene (4). The precursor 3,3′-dimethyl-5,5′-diphenylaza-dipyrromethene (29 mg, 0.089 mmol) was dissolved in dry CH_2Cl_2 (5.0 mL) and treated

with triethylamine (50 μL, 0.36 mmol). After 1 h dibutylboron trifluoromethanesulfonate (80 μL, 0.36 mmol) was added and the mixture was stirred at room temperature under N_2 for 3 h. The reaction mixture was concentrated under reduced pressure and the residue was purified by silica gel column chromatography (SiO_2) with hexane to give the product as a red solid. Yield: 24 mg (60%). ^{1}H NMR (600 MHz, $CDCl_3$) δ: 7.33 (m, 10H, Ar*H*), 6.29 (s, 2H, Pyrrole *H*), 2.41 (s, 6H, CH_3), 1.01 (q, *J* = 7.4 Hz, 4H, CH_2), 0.84 – 0.75 (m, 4H, CH_2), 0.71 (t, *J* = 7.4 Hz, 6H, CH_3), 0.15 – 0.08 (m, 4H, CH_2). ^{13}C{^{1}H} NMR (151 MHz, $CDCl_3$) δ: 158.6, 144.5, 140.2, 135.0, 128.8, 128.5, 127.5, 122.3, 77.3, 77.1, 76.9, 27.6, 27.3, 26.0, 14.2, 11.2. HRMS (ESI): m/z calcd. for $C_{30}H_{36}BN_3$ $[M + H]^+$: 450.3075, found: 450.3239.

2.2.4. General procedure to prepare $B(C_6F_5)_3$ adducts of 1 and 2.

In the glovebox, a solution of complex **1** or **2** (6 mg) in 0.5 mL of C_6H_6 was treated with 1.0 equiv. of $B(C_6F_5)_3$, also dissolved in 0.5 mL. The solution was transferred to a vial, and stirred at room temperature for 20 min. The solvent was removed under vacuum, and the product was dissolved with C_6D_6 for ^{1}H and ^{19}F NMR study.

1-$B(C_6F_5)_3$. ^{1}H NMR (500 MHz, C_6D_6) *δ*: 8.07 (s, 2H, Pyridine *H*), 6.34 (s, 2H, Pyridine *H*), 5.45 (s, 2H, Pyrrole *H*), 2.45 (s, 6H, CH_3), 0.94 (s, 6H, CH_3). ^{19}F NMR (470 MHz, C_6D_6) δ: –131.79 (br, s, 6F), –145.14 (q, *J* = 32.2 Hz, 2F), –154.62 (t, *J* = 20.6 Hz, 3F), –162.30 (m, 6F). ^{11}B NMR (160 Hz, C_6D_6) δ: 0.11 (t, *J* = 31.8 Hz, 1B, *B*F_2). A second ^{11}B resonance for the $B(C_6F_5)_3$ was not located, presumably due to line broadening caused by rapid on/off equilibrium.

2-$B(C_6F_5)_3$. ^{1}H NMR (500 MHz, C_6D_6) *δ*: 8.05 (s, 2H, Pyridine *H*), 6.85 (d, *J* = 7.6 Hz, 2H, Pyridine *H*), 6.55 (d, *J* = 5.9 Hz, 4H, Phenyl *H*), 5.66 (s, 2H, Pyrrole *H*), 2.60 (s, 6H,

CH_3), 1.18 (s, 6H, CH_3). ^{19}F NMR (470 MHz, C_6D_6) δ: –131.28 (br, s, 6F), –145.39 (m, 2F), –155.18 (t, J = 20.7 Hz, 3F), –162.55 (m, 6F). ^{11}B NMR (160 MHz, C_6D_6) δ: 0.39 (br, s, 1B, *B*F_2). A second ^{11}B resonance for the $B(C_6F_5)_3$ was not located, presumably due to line broadening caused by rapid on/off equilibrium.

2.2.5. X-ray Crystallography Procedures.

Single crystals were grown by vapor diffusion of pentane into concentrated CH_2Cl_2 solutions or by slow evaporation of pentane solutions. Crystals were mounted on a Bruker Apex II three-circle diffractometer using MoKα radiation (λ = 0.71073 Å). The data was collected at 123(2) K and was processed and refined within the APEXII software. Structures were solved by direct methods in SHELXS and refined by standard difference Fourier techniques in the program SHELXL.[33] Hydrogen atoms were placed in calculated positions using the standard riding model and refined isotropically; all non-hydrogen atoms were refined anisotropically. The structure of **2**-$B(C_6F_5)_3$ included a dichloromethane molecule modeled as a two-part disorder. Distance restraints were used to fix the 1,2 and 1,3 distances of the disordered molecules, and rigid bond restraints were used for thermal displacement parameters. An electron-density peak of 1.74 eÅ−3 near the disordered solvent generated a level B checkCIF alert; attempts to model the disordered solvent with more than two disordered components did not improve the refinement statistics. Crystallographic details of BODIPY **2** and **2**-$B(C_6F_5)_3$ structures are summarized in **Table A2.1**. CCDC 1869532 (**2**) and 1869533 (**2**-$B(C_6F_5)_3$) contain the supplementary crystallographic data for this thesis.

2.3. Results and Discussion

2.3.1. Synthesis of pyridyl BODIPYs and aza-BODIPY.

Scheme 2.1 describes the synthesis of pyridyl-substituted BODIPYs **1** and **2** and their borane adducts. The general procedure for the preparation of BODIPYs with pyridyl groups in the *meso*-position followed the strategy outlined by Weare and coworkers.[30,34]

Scheme 2.1. Synthesis of pyridyl-substituted BODIPYs.

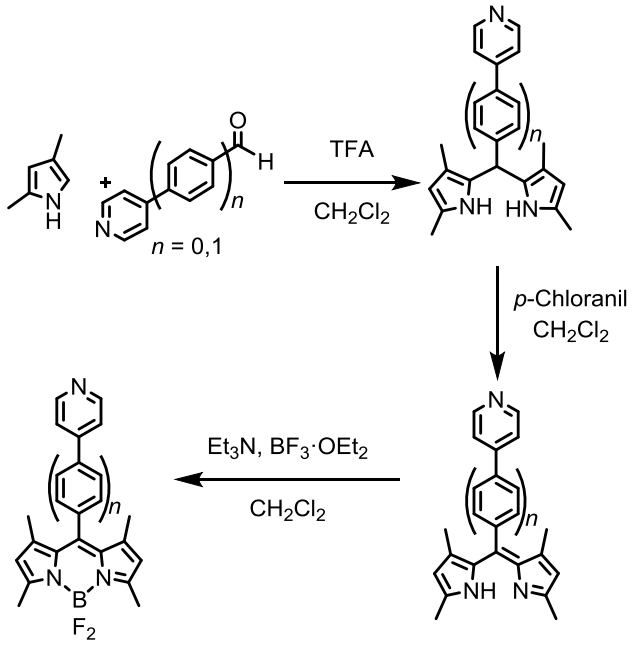

1: *n* = 0 (24.0%)
2: *n* = 1 (24.3%)

This standard protocol involves the condensation of 2,4-dimethylpyrrole with the pyridyl-substituted benzaldehyde derivatives with trifluoroacetic acid in dichloromethane. Commercially available pyridine-4-carboxaldehyde used to prepare BODIPY compound **1**. The dipyrromethane intermediate, not isolated, was oxidized with chloranil, followed by addition of triethylamine and boron trifluoride etherate in dichloromethane under N_2 at

room temperature, producing the desired BODIPY in a one-pot reaction. ^{1}H, ^{19}F, and ^{11}B NMR spectra of 4-Pyridyl BODIPY **1** agree with the previously published data.[30]

The additional phenyl spacer in BODIPY **2** allows us to investigate the effect of increasing the distance between the BODIPY core and the pyridine functional group upon interaction with $B(C_6F_5)_3$. The 4-(pyridin-4-yl)benzaldehyde used in the preparation of **2** was obtained by Suzuki cross-coupling of 4-bromo-pyridine and (4-formylphenyl)-boronic acid, following a previously reported procedure.[31] 4-Phenyl-4-pyridyl BODIPY complex **2** was synthesized by the general procedure using 4-(pyridin-4-yl)benzaldehyde as a starting material with a 24% yield. BODIPY complex **2** has not been previously reported, and its structure and purity were confirmed by the ^{1}H, ^{19}F, and ^{11}B NMR spectra shown in **Figures A2.11**–**A2.15** in **Appendix 2**. BODIPY complex **2** was crystallized by slowly evaporation of dichloromethane solution in air and characterized by single-crystal X-ray diffraction. The structure of complex **2** is shown in **Figure 2.2**, which verifies the extended linker between the BODIPY and the pyridine donor. In the solid state, the phenyl spacer and the pyridine ring are nearly coplanar, with a small dihedral angle of 6.4° between the two planes. The dihedral angle between BODIPY plane and phenyl substituent is 76°, which is slightly smaller than the dihedral angle (84° and 88° for two crystallographically independent molecules) previously reported in BODIPY **1**.[30,32] Diffraction data and refinement details for BODIPY **2** are summarized in **Table A2.1** of **Appendix 2**.

To investigate the interaction of $B(C_6F_5)_3$ with the bridge-head nitrogen of aza-BODIPY, the sterically unhindered 3,3′-dimethyl-5,5′-diphenylazadipyrromethene **3** was chosen as a candidate molecule.

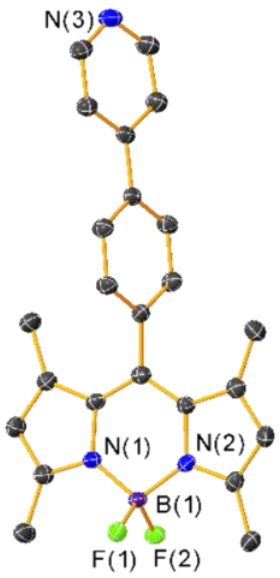

Figure 2.2. X-ray crystal structure of complex **2**. Ellipsoids are drawn at the 50% probability level with hydrogen atoms omitted. All carbon atoms are shown in black and are unlabelled.

We adopted methodology from O'Shea's group[12] to prepare 3,3′-dimethyl-5,5′-diphenylazadipyrromethene as a precursor to aza-BODIPYs. Conversion of the precursor to BF_2 chelate **3** was achieved in 85% yield using BF_3·etherate and triethylamine base in dichloromethane under N_2 gas at room temperature for 24 h (**Scheme 2.2**). In preliminary experiments titrating **3** with $B(C_6F_5)_3$ at NMR scale, we treated a solution of complex **3** (6 mg) in 0.5 mL of CD_2Cl_2 with successively 0.5 equiv. of $B(C_6F_5)_3$, dissolved in 0.5 mL of CD_2Cl_2. After 20 min the ^{1}H NMR spectrum of the resulting solution was analyzed. The ^{1}H NMR spectra showed an intractable mixture of products, suggesting significant decomposition during the titration. Also, a small amount of precipitate was found in the bottom of the NMR tube. It could be possible for F^- from complex **3** be abstracted by $B(C_6F_5)_3$, giving unstable ion pairs that decompose nonspecifically.

Scheme 2.2. Synthesis of BF_2-azadipyrromethene and dibutylborylazadipyrromethene.

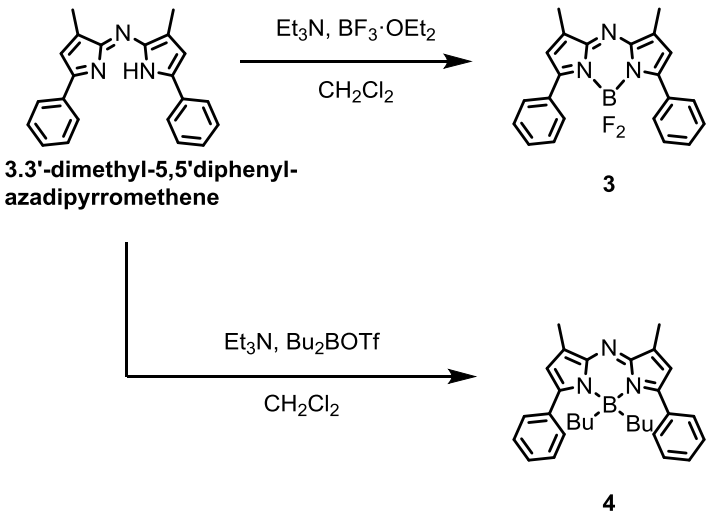

To guard against the possibility of fluoride abstraction, we prepared compound **4** with alkyl substituents on the boron center.[35] The free ligand 3,3′-dimethyl-5,5′-diphenylazadipyrromethene was used to generate complex **4** with a 60% isolated yield following treatment with dibutylboron trifluoromethanesulfonate and triethylamine under N_2 at room temperature for 3 h (**Scheme 2.2**). ^{1}H and ^{13}C NMR spectra of previously unreported complex **4** are shown in **Figures A2.16**–**A2.17** in **Appendix 2**, and they are consistent with the structure shown in **Scheme 2.2** and indicate good purity.

2.3.2. $B(C_6F_5)_3$ Adducts of pyridyl BODIPYs, aza-BODIPY.

While the photophysical effects of protonation and methylation of pyridyl BODIPY **1** have been studied,[36] its coordination chemistry with $B(C_6F_5)_3$ has not been explored. To investigate the interaction of pyridyl BODIPYs with $B(C_6F_5)_3$, we titrated solutions of **1** and **2** with $B(C_6F_5)_3$ in NMR tubes, also shown in **Scheme 2.3**. ^{1}H and ^{19}F NMR spectra

were measured and indicate tight binding of $B(C_6F_5)_3$. **Figures A2.1−A2.3** in **Appendix 2** show stacked NMR spectra for the addition of $B(C_6F_5)_3$ (1 equiv.) to BODIPY **1**.

Scheme 2.3. Reaction of compounds **1** and **2** with $B(C_6F_5)_3$.

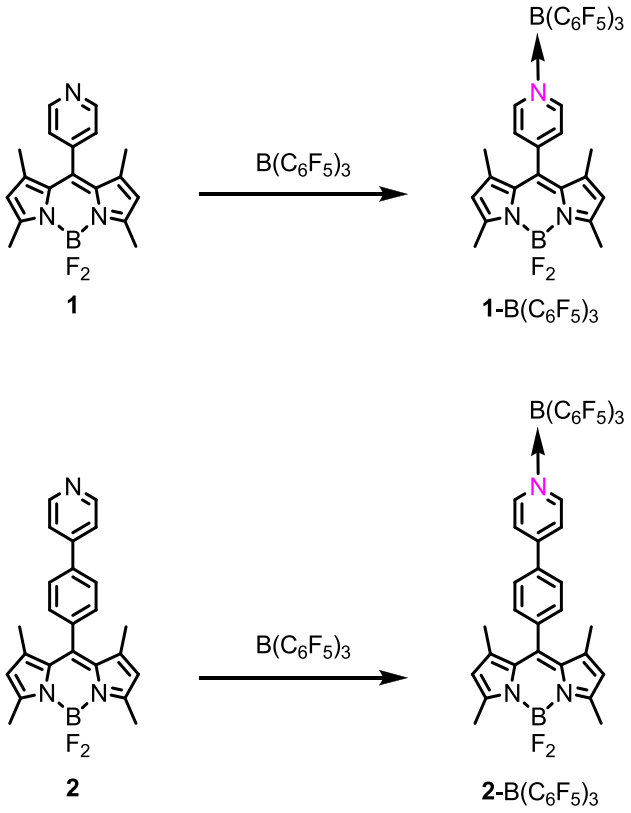

For example, the most downfield pyridyl proton (ortho to nitrogen) resonates at 8.37 ppm in **1**, and is shifted upfield to 8.07 ppm upon binding of $B(C_6F_5)_3$. In contrast, the ^{1}H NMR peak at 6.28 ppm, corresponding to the pyridyl hydrogen atoms remote from the nitrogen, was minimally shifted to 6.34. The pyrrole proton peak was also slightly influenced, shifting from 5.52 ppm in **1** to 5.45 ppm in the borane adduct. The C*H*$_3$ resonances observed at 2.45 and 0.94 ppm are unaffected by addition of the Lewis acid. In addition, the ^{19}F NMR resonances associated with the $B(C_6F_5)_3$ are perturbed substantially relative

to the free borane. Particularly, the resonance associated with the *para* fluorine atom, which occurs near –140 ppm in free $B(C_6F_5)_3$, shifts upfield to −154.6 ppm in **1**-$B(C_6F_5)_3$, consistent with tight binding and formation of a four-coordinate boron.[37]

When $B(C_6F_5)_3$ (1 equiv.) is bound to the pyridyl nitrogen of BODIPY **2** in C_6D_6, the NMR spectra evolve as shown in **Figures A2.4**−**A2.6** in **Appendix 2**. For instance, the most downfield proton peak (ortho to nitrogen) in BODIPY **2** is observed at 8.55 ppm. Addition of $B(C_6F_5)_3$ (1 equiv.) induces a large upfield shift, with this same resonance appearing at 8.05 ppm in the adduct. The remaining aromatic protons overlap into two groups of peaks in the adduct and appear to be shifted upfield from those of **2**. Whereas the pyrrole resonance of BODIPY **1** shifts slightly *upfield* when borane is bound, the pyrrolic proton peak BODIPY **2** undergoes a slight downfield shift, from 5.62 ppm (**2**) to 5.66 ppm (adduct). Again, the C*H*$_3$ resonances in **2** are minimally impacted by borane binding. After addition of more than 1 equiv. of $B(C_6F_5)_3$ to both **1** and **2**, no further changes in the ^{1}H spectra are observed, indicating tight binding at these concentrations.

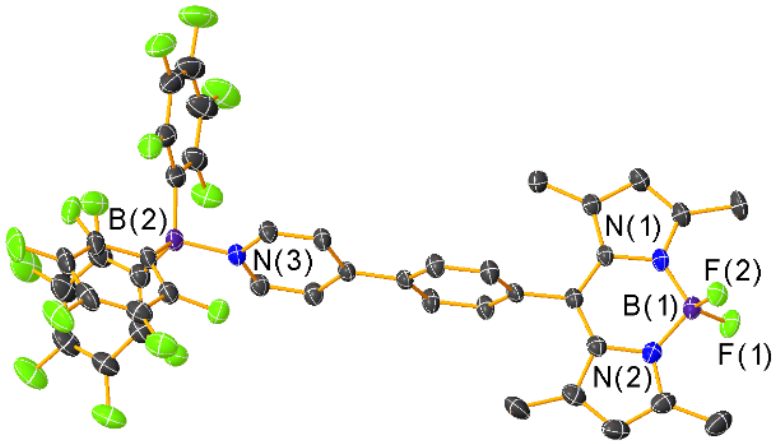

Figure 2.3. X-ray crystal structure of complex **2**-$B(C_6F_5)_3$. Ellipsoids are drawn at the 50% probability level with solvent molecules and hydrogen atoms omitted. All carbon atoms are shown in black and are unlabelled.

The ^{19}F NMR spectrum of **2**-$B(C_6F_5)_3$ is markedly similar to that of **1**-$B(C_6F_5)_3$ and is again consistent with a strong Lewis acid-base interaction and the presence of a tetracoordinated boron.

The $B(C_6F_5)_3$ adduct **2**-$B(C_6F_5)_3$ can be crystallized by slow diffusion of pentane into a concentrated dichloromethane solution in the glovebox and characterized by single-crystal X-ray diffraction. The structure is shown in **Figure 2.3**. The bond length N(3)–B(2) is 1.615(3) Å, very similar to the N(pyridine)−$B(C_6F_5)_3$ bond distances of 1.624(4) and 1.613(4) Å previously observed by our group in adducts of pyridyl-substituted platinum diimine acetylide complexes,[22] and also matching with the bond distance of 1.628(2) Å observed in the simple $C_6H_5N \rightarrow B(C_6F_5)_3$ adduct.[38] This distance indicates a strong bonding interaction between N(3) of pyridine and B(2) of $B(C_6F_5)_3$. The tetrahedral character of the boron atom, determined using all six bond lengths with boron as the vertex,[39] was calculated to be 65.5%, also consistent with a relatively strong boron–nitrogen interaction. The structural metrics of the BODIPY core, namely the skeletal C–C and C–N internuclear distances and the bond distances involving the boron atom B(1) are minimally impacted by the remote borane binding. The dihedral angles in the adduct **2**-$B(C_6F_5)_3$ are slightly perturbed from those of **2**. The angle between the BODIPY plane and the phenyl ring increases from 76° to 88°, and the angle between the pyridine plane and the phenyl plane also increases slightly, from 6.4° to 14°.

The interaction of the bridgehead nitrogen of aza-BODIPY **4** with $B(C_6F_5)_3$ was likewise studied by ^1H NMR. Addition of $B(C_6F_5)_3$ Lewis acid (1 equiv.) to aza-BODIPY **4** in C_6D_6 results in no significant changes in chemical shifts in the ^1H NMR spectrum (**Figures A2.7**−**A2.8** in **Appendix 2**). After addition of more than 2 equiv. of $B(C_6F_5)_3$, the

NMR spectra of resulting materials indicate significant decomposition when excess $B(C_6F_5)_3$ is present. These results suggest that the bridgehead nitrogen in aza-BODIPY **4** is weakly Lewis basic, and the interaction with $B(C_6F_5)_3$ is weak. The weak binding of $B(C_6F_5)_3$ by aza-BODIPY **4** was further verified by UV−vis absorption and emission titrations, although in these experiments evidence for significant decomposition is not as clear. The nonspecific decomposition observed at NMR scale in C_6D_6 ([**4**] ~ 2×10^{-2} M) may arise from the higher concentration, leading to bimolecular decomposition pathways that are not prevalent in UV-vis-scale measurements ([**4**] ~ 8×10^{-5} M).

2.3.3. Effect of $B(C_6F_5)_3$ binding on UV-vis absorption and emission spectra.

Having established that compounds **1** and **2** can cleanly form Lewis acid-base adducts with $B(C_6F_5)_3$, we investigated the effects of borane binding on the UV-vis absorption and photoluminescence. The UV-vis absorption and emission data for compounds **1** and **2** and their borane adducts are summarized in **Table 2.1**.

Table 2.1. Summary of UV-vis absorption and emission data for compounds **1** and **2** and their borane adducts, recorded in benzene at room temperature.

Compound	UV-vis absorption λ_{max} / nm ($\varepsilon \times 10^{-3}/M^{-1}cm^{-1}$)	Photoluminescence λ_{em} / nm	Φ_{PL}
1	507 (79)	521	0.51
1-$B(C_6F_5)_3$	513 (59)	580	0.08
1-BPh_3	510 (66)	528	0.16
2	505 (102)	519	0.68
2-$B(C_6F_5)_3$	508 (90)	528	0.22

Binding of $B(C_6F_5)_3$ to pyridyl-substituted BODIPY **1** in benzene results in significant changes in the UV-vis absorption spectrum, as shown in **Figure 2.4a**.

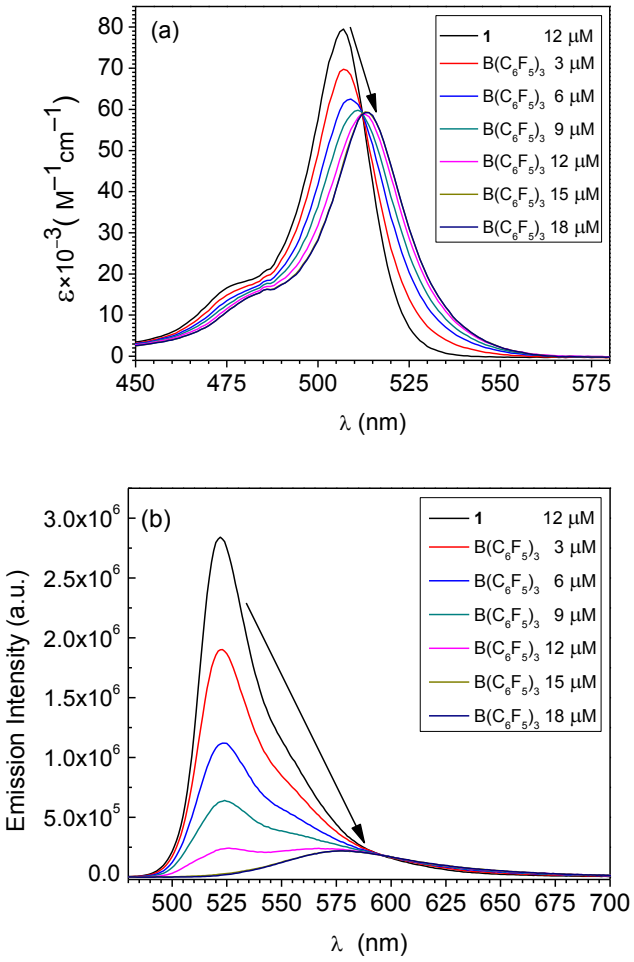

Figure 2.4. Electronic absorption spectra (a) and emission spectra (b) of BODIPY **1** (12 μM) during successive addition of $B(C_6F_5)_3$ up to 18 μM. The arrow shows the direction of spectral evolution as borane is added. Spectra were recorded in C_6H_6 at room temperature. Excitation for the emission spectra was at 460 nm. The molar extinction coefficient (ε) is a measure of how strongly a chemical species or substance absorbs light at a particular wavelength.

Addition of $B(C_6F_5)_3$ (0.25 equiv. aliquots) to a 12 μM solution of BODIPY **1** results in a gradual change in the visible absorption band as the pyridine functional group of BODIPY

1 coordinates to $B(C_6F_5)_3$. There are no further changes after addition of 18 μM $B(C_6F_5)_3$ (1.5 equiv.), consistent with the tight binding that was concluded from the abovementioned NMR studies. The absorption band of BODIPY **1** in C_6H_6 solvent appears at 507 nm (ε = 79,000 M^{-1} cm^{-1}, full width at half-max (fwhm) ~ 700 cm^{-1}). Following addition of 18 μM $B(C_6F_5)_3$, which converts **1** to its borane adduct **1**-$B(C_6F_5)_3$, the absorption maximum shifts slightly to 513 nm and broadens slightly as well (ε = 59,000 M^{-1} cm^{-1}, fwhm ~ 1050 cm^{-1}). From the UV-vis titration data, we estimate a binding constant of ~10^6 M^{-1} for complex **1** and $B(C_6F_5)_3$.

Figure 2.4b displays the effect of Lewis acid binding on the emission spectrum, using the same samples as shown in the UV-vis titration. The emission spectrum of BODIPY **1** (1.2×10^{-5} M) shows λ_{max} at 521 nm and a photoluminescence quantum yield Φ_{PL} of 0.51 at room temperature in C_6H_6. Addition of $B(C_6F_5)_3$ induces a bathochromic shift in the emission spectrum. The trend of the emission spectral changes is similar to that of the absorption spectral changes and the quantum yield also decreases along with the red-shift. When $B(C_6F_5)_3$ (18 μM) is added in BODIPY **1** to completely form **1**-$B(C_6F_5)_3$, the emission maximum red-shifts to 580 nm, with the photoluminescence quantum yield Φ_{PL} = 0.08. Interestingly, the bathochromic shift observed in the photoluminescence upon borane binding (~1950 cm^{-1}) is significantly larger than the shift in absorption λ_{max} (~230 cm^{-1}), on account of the larger Stokes shift in the borane adduct. This increase in Stokes shift suggests larger geometric distortion in the excited state of **1**-$B(C_6F_5)_3$ as compared to unbound BODIPY **1**.

BODIPY **2** includes an elongated linker between the pyridine substituent and the BODIPY core, allowing us to determine the effects of borane binding to a more remote

position in the chromophore. In the absence of borane, the properties of **2** are very similar to those of **1**, as summarized in **Table 2.1**. The spectroscopic properties of BODIPY **2** with added $B(C_6F_5)_3$ were evaluated in an identical fashion to **1**. When $B(C_6F_5)_3$ was added to the solution of BODIPY **2**, the electronic absorption spectra evolved as shown in **Figure 2.5a**.

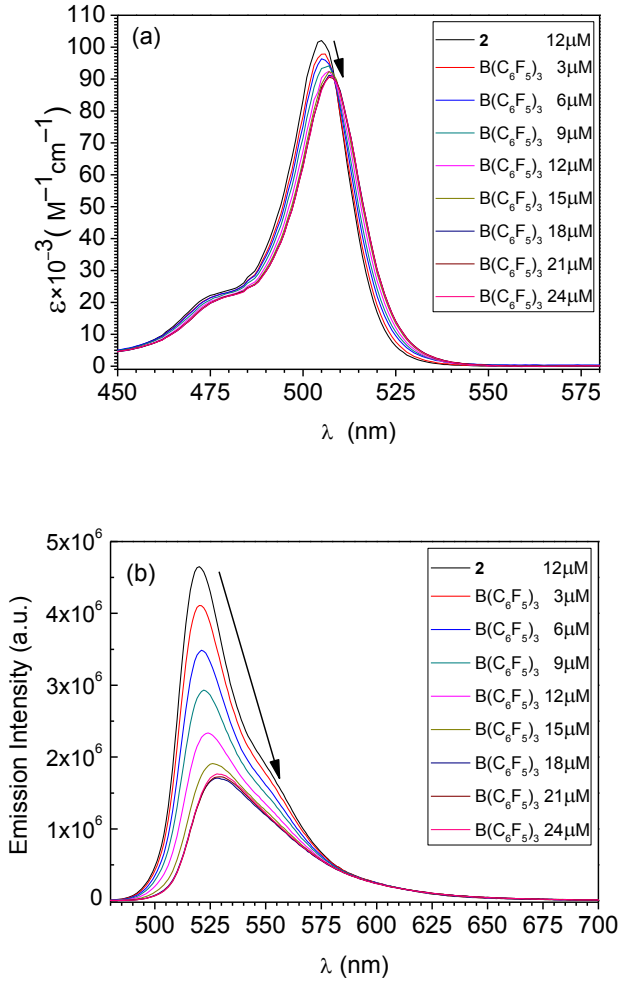

Figure 2.5. Electronic absorption spectra (a) and emission spectra (b) of BODIPY **2** (12 μM) during successive addition of $B(C_6F_5)_3$ up to 24 μM. The arrow shows the direction of spectral evolution as borane is added. Spectra were recorded in C_6H_6 at room temperature. Excitation for emission spectra was at 460 nm.

The additional phenyl ring in **2** has little impact on the UV-vis absorption, with the visible band of BODIPY **2** occurring at 505 nm (ε = 102,000 M^{-1} cm^{-1}) in C_6H_6, assigned to a characteristic S_0 to S_1 transition.[40] Successive additions of $B(C_6F_5)_3$ to a 12 μM solution of **2** results in very modest changes in the UV-vis absorption, and no further changes occur after addition of 24 μM $B(C_6F_5)_3$. A small bathochromic shift and slight decrease in absorptivity are observed, with the new band **2**-$B(C_6F_5)_3$ appearing at 508 nm (ε = 90,000 M^{-1} cm^{-1}). In this case there is no perceptible peak broadening with addition of borane, and the spectral fwhm in **2** (790 cm^{-1}) and **2**-$B(C_6F_5)_3$ (820 cm^{-1}) are nearly identical. Thus, the absorption spectrum of BODIPY **2** is bathochromically shifted upon addition of $B(C_6F_5)_3$, but the magnitude is not nearly as large as in the case of BODIPY **1**. The titration data for complex **2** suggests a slightly smaller binding constant than was observed for **1**, but we still conclude the binding strength to be around the same order-of-magniute (~10^6 M^{-1}).

To investigate the effect of Lewis acid strength on the modulation of photophysical properties, we investigated adducts of **1** with the weaker Lewis acid BPh_3. Complex **1** was chosen for this experiment since its response to the stronger Lewis acid $B(C_6F_5)_3$ was more pronounced than **2**. The adduct **1**-BPh_3 was not fully characterized, but its UV-vis absorption and emission spectra were measured via titration of **1** with BPh_3, as shown in **Figure 2.6**. The weaker Lewis acid does not bind as tightly, and as such when a 12 μM solution of **1** was treated with sequential aliquots of BPh_3 the spectra evolved until 84 μM (7 equiv.) of BPh_3 were added. From this data, we estimate a binding constant ~10^5 M^{-1}, about one order-of-magnitude smaller than observed with $B(C_6F_5)_3$. The perturbations of the photophysical properties are qualitatively similar to those observed with $B(C_6F_5)_3$, but

not as pronounced in magnitude. The UV-vis absorption red-shifts slightly and decreases in intensity, from $\lambda = 507$ nm ($\varepsilon = 79{,}000\ M^{-1}\ cm^{-1}$) to $\lambda = 510$ nm ($\varepsilon = 66{,}000\ M^{-1}\ cm^{-1}$). The photoluminescence, which occurs at 521 nm in **1**, also red-shifts by a small amount to 528 nm in **1**-BPh_3.

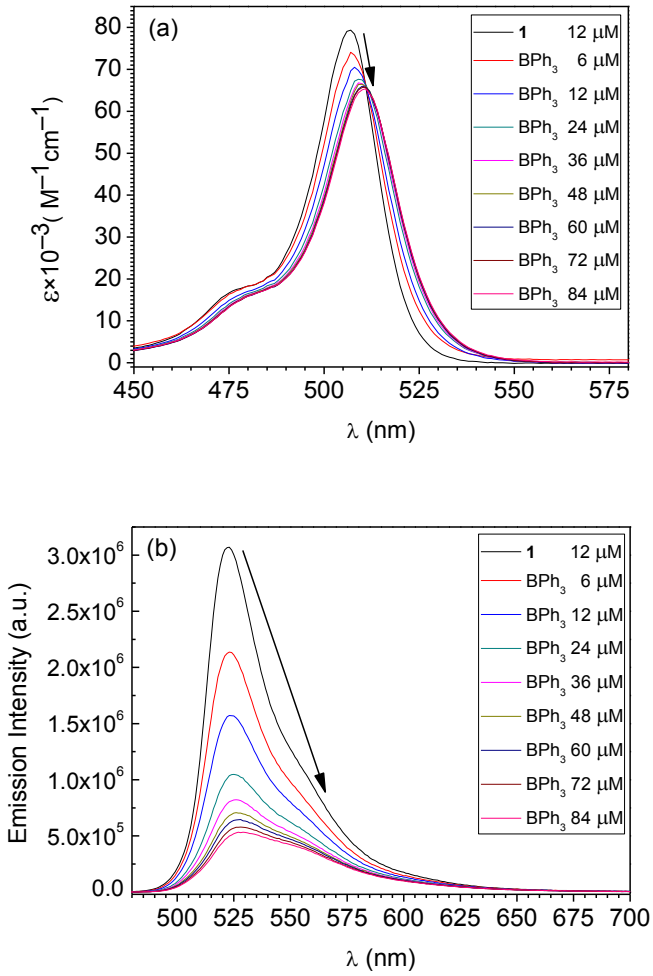

Figure 2.6. Electronic absorption spectra (a) and emission spectra (b) of BODIPY 1 (12 μM) during successive addition of BPh_3 up to 84 μM. The arrow shows the direction of spectral evolution as borane is added. Spectra were recorded in C_6H_6 at room temperature. Excitation for emission spectra was at 460 nm.

In contrast, the shift induced by $B(C_6F_5)_3$ was much larger (see **Table 2.1**). The quantum yield in **1**-BPh_3 is also attenuated, decreasing to 0.16, but this decrease is not as pronounced as that of **1**-$B(C_6F_5)_3$. Taken together, these results indicate that the photophysical properties of **1** are not as strongly perturbed when the weaker Lewis acid BPh_3 is used.

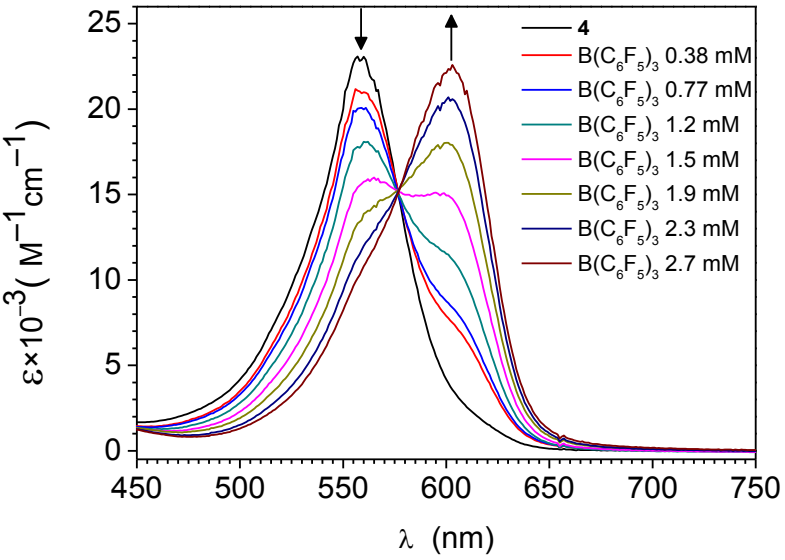

Figure 2.7. Electronic absorption spectra of aza-BODIPY **4** (7.7×10^{-5} M) to the successive addition of $B(C_6F_5)_3$ up to 35 equivalents (2.7×10^{-3} M). Spectra were recorded in C_6H_6 at room temperature.

In spite of the NMR experiments indicating significant decomposition when aza-BODIPY **4** was titrated with $B(C_6F_5)_3$, we investigated changes in UV-vis absorption and emission spectra when this compound was titrated with $B(C_6F_5)_3$. **Figure 2.7** shows the evolution of the absorption spectra when aza-BODIPY **4** (77 μM in benzene) is titrated with $B(C_6F_5)_3$. The $B(C_6F_5)_3$ was added in increments of 1 equiv., with 5 equiv. increments displayed in **Figure 2.7**. The addition results in a gradual change in the spectrum until 35

equiv. (2.7 mM) have been added. The higher concentrations of **4** and $B(C_6F_5)_3$ used in this experiment are necessitated by the weaker Lewis basicity of the bridgehead nitrogen in **4** compared to the pyridyl substituents in **1** and **2**. The non-specific decomposition observed in NMR-scale experiments is not as evident during titration of UV-vis samples. The absorption maximum in **4** appears at 558 nm (ε = 23,000 $M^{-1}cm^{-1}$), and with added borane this band disappears and a new band grows in, significantly red-shifted at 603 nm with the same absorptivity.

During these changes in visible absorption a clear isosbestic point is maintained at 576 nm, suggesting that clean conversion to a new species is occurring, without any significant decomposition as was observed in more concentrated NMR experiments. These experiments do not conclusively reveal the structure of the product that forms when **4** interacts with $B(C_6F_5)_3$, though it is reasonable to suppose that a simple adduct involving coordination of the bridgehead nitrogen to the borane is the primary species. Consistent with this notion, an aza-BODIPY optical sensor was found to exhibit a similar bathochromic shift in absorption upon coordination of Hg(II), which was presumed to involve the bridgehead nitrogen. Thus, much in the same manner as observed in BODIPY compounds **1** and **2**, adding an electron-withdrawing group to the meso position of **4** results in a significant decrease of the HOMO–LUMO gap.

For completeness we include the emission spectra of **4** during addition of borane, although the results are not nearly as straightforward as the UV-vis titration (**Figures A2.9**−**A2.10** in **Appendix 2**). The emission spectrum of aza-BODIPY **4** (7.7×10^{-5} M) displays λ_{max} at 631 nm at room temperature in benzene with Φ_{PL} = 0.044. During the initial addition of $B(C_6F_5)_3$ up to 6 equivalents (4.6×10^{-4} M, see **Figure A2.9**) there is a small

red shift of the maximum to 636 nm a substantial loss of intensity (Φ_{PL} = 0.015 at this borane concentration). Beyond 6 equivalents, continuous titration of aza-BODIPY **4** with $B(C_6F_5)_3$ up to 35 equivalents (2.7×10^{-3} M) enhances significantly the intensity of emission with additional bathochromic shift to 641 nm. One possible explanation for this behavior is that the borane adduct of **4** is weakly luminescent, resulting in an initial decrease in photoluminescence as it forms, but that with a large excess of borane present decomposition to a highly luminescent impurity begins to occur. The clean isosbestic point in the UV-vis titration suggests that decomposition is minor (see **Figure 2.7**), but if one or more decomposition products is highly luminescent the signal could overtake the initial emission of **4**, which is quite weak.

To contextualize the results described above, we point to previous studies on BODIPYs which demonstrate that covalent substitution of the meso phenyl 4-position with electron-withdrawing substituents induces a red-shift in the low-energy absorption and emission maxima.[41] This previous work has shown that fully fluorinating the meso-phenyl ring, i.e. replacing C_6H_5 with C_6F_5, causes a ca. 800 cm^{-1} red shift in the emission maximum. In contrast, coordination of $B(C_6F_5)_3$ by **1** results in a > 1900 cm^{-1} bathochromic shift, which is more than double the effect. This comparison shows that a datively coordinated $B(C_6F_5)_3$ functions as a powerful electron-withdrawing substituent and has an even larger effect on the photoluminescence than fully fluorinating the phenyl ring would. It should also be possible to attenuate this affect by using weaker borane Lewis acids, which offers a much faster and more systematic approach for tuning emission color than is achieved with covalent substituent modification, which typically requires full synthesis of the modified chromophore. That said, an apparent limitation of using borane Lewis acids

to tune photoluminescence is a large decrease in photoluminescence quantum yield. The origins of this decrease in quantum yield are not immediately apparent, although we did observe similar behavior when binding Lewis acids to a phosphorescent platinum complex in our previous work.[22] A decrease in quantum yield is expected when the photoluminescence red-shifts, both because the radiative rate constant (k_r) has a cubic dependence on excited-state energy, and because of the Energy-gap Law which stipulates that the nonradiative rate constant (k_{nr}) has an inverse dependence on excited-state energy. However, in complex **1** the quantum yield decreases by a factor of 6 when the Lewis acid is bound, and this magnitude of decrease cannot be simply explained by the normal dependencies of radiative and nonradiative rate constants. In our previous work on platinum complexes it was k_{nr} that was much more strongly affected than k_r, so one possibility is that the large $B(C_6F_5)_3$, which is likely bound in a dynamic on/off equilibrium, introduces new nonradiative decay pathways that are not present in the unbound state. Additional time-resolved photoluminescence experiments and computations of the low-energy excited states may clarify these details. Regardless of the precise origins, the decrease in quantum yield that occurs with borane binding is a limitation that must be overcome if this approach is to ever become a practical method for tuning emission colors in optoelectronic applications.

2.4. Conclusions

In this work we have synthesized two BODIPY molecules with pendant pyridine donors along with a sterically unhindered aza-BODIPY and studied their interactions with Lewis acids, demonstrating that binding of Lewis acids in the secondary coordination

sphere can result in significant changes to the optical properties. Two different types of pyridyl BODIPYs have been investigated; one has the pyridine directly in the meso position, whereas the second has a phenyl spacer between the meso carbon and the pyridine. In both cases addition of $B(C_6F_5)_3$ to pyridyl substituted BODIPYs results in bathochromic shifts in the UV-vis absorption and emission bands, with the effects much larger when the pyridine Lewis base is closer to the BODIPY core. The Lewis acid functions as an electron-withdrawing group and lowers the S_1 excited-state energy, giving rise to the red-shifted absorption and emission bands. We also investigated the coordination of $B(C_6F_5)_3$ to the bridgehead nitrogen of aza-BODIPY **4**, which is sterically accessible to Lewis acids. Again binding Lewis acids resulted in a substantial red shift in the UV-vis absorption spectrum, although the Lewis basicity of **4** is significantly lower than that of the pyridine donors in **1** and **2**, and adduct formation is accompanied by nonspecific decomposition. The potential appeal of this approach is that coordination of Lewis acids to BODIPYs offers rapid and systematic control of the excited-state energies, which could benefit certain optoelectronic applications where precise control over the absorption wavelengths and/or emission colors is desirable. Future studies include evaluating other borane and non-borane Lewis acids as well as developing aza-BODIPYs with multiple pyridine binding sites, both of which offer the promise of giving even greater control over the optical properties.

2.5. References

1. Loudet, A.; Burgess, K. BODIPY Dyes and Their Derivatives: Syntheses and Spectroscopic Properties. *Chem. Rev.* **2007**, *107*, 4891–4932.
2. Bergström, F.; Mikhalyov, I.; Hägglöf, P.; Wortmann, R.; Ny, T.; Johansson, L. B.-Å. Dimers of Dipyrromethene boron Difluoride (BODIPY) with Light

Spectroscopic Applications in Chemistry and Biology. *J. Am. Chem. Soc.* **2002**, *124*, 196–204.

3. Killoran, J.; Allen, L.; Gallagher, J. F.; Gallagher, W. M.; O′Shea, D. F. Synthesis of BF_2 Chelates of Tetraarylazadipyrromethenes and Evidence for Their Photodynamic Therapeutic Behaviour. *Chem Commun* **2002**, *17*, 1862–1863.
4. Gorman, A.; Killoran, J.; O'Shea, C.; Kenna, T.; Gallagher, W. M.; O'Shea, D. F. In Vitro Demonstration of the Heavy-Atom Effect for Photodynamic Therapy. *J. Am. Chem. Soc.* **2004**, *126*, 10619–10631.
5. McDonnell, S. O.; Hall, M. J.; Allen, L. T.; Byrne, A.; Gallagher, W. M.; O'Shea, D. F. Supramolecular Photonic Therapeutic Agents. *J. Am. Chem. Soc.* **2005**, *127*, 16360–16361.
6. Bröring, M.; Krüger, R.; Link, S.; Kleeberg, C.; Köhler, S.; Xie, X.; Ventura, B.; Flamigni, L. Bis(BF_2)-2,2′-Bidipyrrins (BisBODIPYs): Highly Fluorescent BODIPY Dimers with Large Stokes Shifts. *Chem. - Eur. J.* **2008**, *14*, 2976–2983.
7. Xu, J.; Sun, S.; Li, Q.; Yue, Y.; Li, Y.; Shao, S. A Rapid Response 'Turn-On' Fluorescent Probe for Nitroreductase Detection and Its Application in Hypoxic Tumor Cell Imaging. *The Analyst* **2015**, *140*, 574–581.
8. Rousseau, T.; Cravino, A.; Bura, T.; Ulrich, G.; Ziessel, R.; Roncali, J. BODIPY Derivatives as Donor Materials for Bulk Heterojunction Solar Cells. *Chem. Commun.* **2009**, *13*, 1673–1675.
9. Erten-Ela, S.; Yilmaz, M. D.; Icli, B.; Dede, Y.; Icli, S.; Akkaya, E. U. A Panchromatic Boradiazaindacene (BODIPY) Sensitizer for Dye-Sensitized Solar Cells. *Org. Lett.* **2008**, *10*, 3299–3302.
10. Flavin, K.; Lawrence, K.; Bartelmess, J.; Tasior, M.; Navio, C.; Bittencourt, C.; O'Shea, D. F.; Guldi, D. M.; Giordani, S. Synthesis and Characterization of Boron Azadipyrromethene Single-Wall Carbon Nanotube Electron Donor−Acceptor Conjugates. *ACS Nano* **2011**, *5*, 1198–1206.
11. Ge, Y.; O'Shea, D. F. Azadipyrromethenes: From Traditional Dye Chemistry to Leading Edge Applications. *Chem Soc Rev* **2016**, *45*, 3846–3864.

12. Wu, D.; O'Shea, D. F. Synthesis and Properties of BF_2-3,3′-Dimethyldiarylaza-Dipyrromethene Near-Infrared Fluorophores. *Org. Lett.* **2013**, *15*, 3392–3395.
13. Gao, L.; Senevirathna, W.; Sauvé, G. Azadipyrromethene-Based Conjugated Oligomers with Near-IR Absorption and High Electron Affinity. *Org. Lett.* **2011**, *13*, 5354–5357.
14. Senevirathna, W.; Sauvé, G. Introducing 3D Conjugated Acceptors with Intense Red Absorption: Homoleptic Metal(II) Complexes of Di(Phenylacetylene) Aza-Dipyrromethene. *J. Mater. Chem. C* **2013**, *1*, 6684–6694.
15. Senevirathna, W.; Liao, J.; Mao, Z.; Gu, J.; Porter, M.; Wang, C.; Fernando, R.; Sauvé, G. Synthesis, Characterization and Photovoltaic Properties of Azadipyrromethene-Based Acceptors: Effect of Pyrrolic Substituents. *J. Mater. Chem. A* **2015**, *3*, 4203–4214.
16. Roacho, R. I.; Metta-Magaña, A. J.; Peña-Cabrera, E.; Pannell, K. H. Synthesis, Structural Characterization, and Spectroscopic Properties of the *Ortho*, *Meta*, and *Para* Isomers of 8-($HOCH_2$-C_6H_4)-BODIPY and 8-($MeOC_6H_4$)-BODIPY. *J. Phys. Org. Chem.* **2013**, *26*, 345–351.
17. Roacho, R. I.; Metta-Magaña, A.; Portillo, M. M.; Peña-Cabrera, E.; Pannell, K. H. 8-Amino-BODIPYs: Structural Variation, Solvent-Dependent Emission, and VT NMR Spectroscopic Properties of 8-R_2N-BODIPY. *J. Org. Chem.* **2013**, *78*, 4245–4250.
18. Kim, H. N.; Ren, W. X.; Kim, J. S.; Yoon, J. Fluorescent and Colorimetric Sensors for Detection of Lead, Cadmium, and Mercury Ions. *Chem Soc Rev* **2012**, *41*, 3210–3244.
19. Zeng, L.; Miller, E. W.; Pralle, A.; Isacoff, E. Y.; Chang, C. J. A Selective Turn-On Fluorescent Sensor for Imaging Copper in Living Cells. *J. Am. Chem. Soc.* **2006**, *128*, 10–11.
20. Ozlem, S.; Akkaya, E. U. Thinking Outside the Silicon Box: Molecular AND Logic As an Additional Layer of Selectivity in Singlet Oxygen Generation for Photodynamic Therapy. *J. Am. Chem. Soc.* **2009**, *131*, 48–49.

21. Bozdemir, O. A.; Guliyev, R.; Buyukcakir, O.; Selcuk, S.; Kolemen, S.; Gulseren, G.; Nalbantoglu, T.; Boyaci, H.; Akkaya, E. U. Selective Manipulation of ICT and PET Processes in Styryl-Bodipy Derivatives: Applications in Molecular Logic and Fluorescence Sensing of Metal Ions. *J. Am. Chem. Soc.* **2010**, *132*, 8029–8036.
22. Na, H.; Maity, A.; Teets, T. S. Postsynthetic Systematic Electronic Tuning of Organoplatinum Photosensitizers via Secondary Coordination Sphere Interactions. *Organometallics* **2016**, *35*, 2267–2274.
23. Hansmann, M. M.; López-Andarias, A.; Rettenmeier, E.; Egler-Lucas, C.; Rominger, F.; Hashmi, A. S. K.; Romero-Nieto, C. $B(C_6F_5)_3$: A Lewis Acid That Brings the Light to the Solid State. *Angew. Chem. Int. Ed.* **2016**, *55*, 1196–1199.
24. Ono, T.; Sugimoto, M.; Hisaeda, Y. Multicomponent Molecular Puzzles for Photofunction Design: Emission Color Variation in Lewis Acid–Base Pair Crystals Coupled with Guest-to-Host Charge Transfer Excitation. *J. Am. Chem. Soc.* **2015**, *137*, 9519–9522.
25. Hatanaka, S.; Ono, T.; Hisaeda, Y. Turn-On Fluorogenic and Chromogenic Detection of Small Aromatic Hydrocarbon Vapors by a Porous Supramolecular Host. *Chem. - Eur. J.* **2016**, *22*, 10346–10350.
26. Liu, S.; Shi, Z.; Xu, W.; Yang, H.; Xi, N.; Liu, X.; Zhao, Q.; Huang, W. A Class of Wavelength-Tunable near-Infrared Aza-BODIPY Dyes and Their Application for Sensing Mercury Ion. *Dyes Pigments* **2014**, *103*, 145–153.
27. Coskun, A.; Yilmaz, M. D.; Akkaya, E. U. Bis(2-Pyridyl)-Substituted Boratriaza-Indacene as an NIR-Emitting Chemosensor for Hg(II). *Org. Lett.* **2007**, *9*, 607–609.
28. Quartarolo, A. D.; Russo, N.; Sicilia, E. Structures and Electronic Absorption Spectra of a Recently Synthesised Class of Photodynamic Therapy Agents. *Chem. - Eur. J.* **2006**, *12*, 6797–6803.
29. Le Guennic, B.; Maury, O.; Jacquemin, D. Aza-Boron-Dipyrromethene Dyes: TD-DFT Benchmarks, Spectral Analysis and Design of Original near-IR Structures. *Phys Chem Chem Phys* **2012**, *14*, 157–164.

30. Bartelmess, J.; Weare, W. W.; Latortue, N.; Duong, C.; Jones, D. S. Meso-Pyridyl BODIPYs with Tunable Chemical, Optical and Electrochemical Properties. *New J. Chem.* **2013**, *37*, 2663–2668.

31. Trawny, D.; Vandromme, L.; Rabe, J. P.; Reissig, H.-U. The Side Chain Makes the Difference: Investigation of the 2D Self-Assembly of 1,3,5-Tris[4-(4-Pyridinyl)Phenyl]Benzene Derivatives by Scanning Tunneling Microscopy: 2D Self-Assembly of 1,3,5-Tris[4-(4-Pyridinyl)Phenyl]Benzene Derivatives. *Eur. J. Org. Chem.* **2014**, *2014*, 4985–4992.

32. Wang, Y.-W.; Li, M.; Shen, Z.; You, X.-Z. Meso-Pyridine Substituted Boron-Dipyrromethene (BDP) Dye as a pH Probe: Synthesis, Crystal Structure and Spectroscopic Properties. *Wuji Huaxue Xuebao* **2008**, *24*, 1247–1252.

33. Sheldrake, P. W. The Anion of 4-Dimethoxymethylpyridine. A Convenient Synthesis of Some 4-Pyridyl Ketones A Convienient Synthesis of Some 4-Pyridyl Ketones. *Synth. Commun.* **1993**, *23*, 1967–1971.

34. Bartelmess, J.; Weare, W. W. Preparation and Characterization of Multi-Cationic BODIPYs and Their Synthetically Versatile Precursors. *Dyes Pigments* **2013**, *97*, 1–8.

35. Berhe, S. A.; Rodriguez, M. T.; Park, E.; Nesterov, V. N.; Pan, H.; Youngblood, W. J. Optoelectronic Tuning of Organoborylazadipyrromethenes via Effective Electronegativity at the Metalloid Center. *Inorg. Chem.* **2014**, *53*, 2346–2348.

36. Harriman, A.; Mallon, L. J.; Ulrich, G.; Ziessel, R. Rapid Intersystem Crossing in Closely-Spaced but Orthogonal Molecular Dyads. *ChemPhysChem* **2007**, *8*, 1207–1214.

37. Beringhelli, T.; Maggioni, D.; D'Alfonso, G. ^{1}H and ^{19}F NMR Investigation of the Reaction of $B(C_6F_5)_3$ with Water in Toluene Solution. *Organometallics* **2001**, *20*, 4927–4938.

38. Focante, F.; Mercandelli, P.; Sironi, A.; Resconi, L. Complexes of Tris(Penta-Fluorophenyl)Boron with Nitrogen-Containing Compounds: Synthesis, Reactivity and Metallocene Activation. *Coord. Chem. Rev.* **2006**, *250*, 170–188.

39. Höpfl, H. The Tetrahedral Character of the Boron Atom Newly Defined—a Useful Tool to Evaluate the N→B Bond. *J. Organomet. Chem.* **1999**, *581*, 129–149.

40. Bessette, A.; Hanan, G. S. Design, Synthesis and Photophysical Studies of Dipyrromethene-Based Materials: Insights into Their Applications in Organic Photovoltaic Devices. *Chem Soc Rev* **2014**, *43*, 3342–3405.

41. Alamiry, M. A. H.; Benniston, A. C.; Hagon, J.; Winstanley, T. P. L.; Lemmetyinen, H.; Tkachenko, N. V. The Fluorine Effect: Photophysical Properties of Boron-Dipyrromethene (Bodipy) Dyes Appended at the Meso Position with Fluorinated Aryl Groups. *RSC Adv.* **2012**, *2*, 4944–4950.

Chapter 3. Cyclometalated Iridium-BODIPY Ratiometric O_2 Sensors

3.1. Introduction

Molecular oxygen plays a major role in a large range of chemical and biochemical reactions essential to aerobic metabolism.[1–3] As hypoxia is associated with a variety of diseases in our daily lives and also found in tumor cells,[4] many researchers have worked to develop reliable methods for sensing triplet oxygen in the past several years.[5–10] Accurate O_2 sensors are especially important in cancer biology, where the O_2 level in tumor cells can be used to determine the tumor's metabolic state and guide therapeutic protocols. Ratiometric luminescent oxygen sensors, where the readout is a ratio of two emission signals, provide an advantage over conventional sensors in that they circumvent the need to measure absolute emission intensities as the primary readout. This ratiometric response minimizes detection errors resulting from heterogeneous cellular environments, differences in excitation power, or variations in optical path length, and as such is a considerably more reproducible method for measuring cellular O_2.[11]

Conventional designs for ratiometric oxygen sensors partner a fluorescent molecule or nanomaterial with a molecular phosphor; in the presence of O_2 phosphorescence is quenched whereas fluorescence is unaffected. A schematic of this sensing mechanism is summarized in **Figure 3.1**. The diagram in **Figure 3.1** assumes fluorophore emission which is higher energy (bluer) than the phosphor emission, but the opposite configuration is also possible, provided energy transfer from the phosphor to fluorophore can be minimized. Excitation of the construct could then be followed by energy transfer between the components, although in many cases energy transfer from the fluorophore to the phosphor

is minimal, given the short lifetime of the fluorophore. Nevertheless, if both sites can be excited simultaneously, in the absence of O_2 fluorescence and phosphorescence from the respective sites occur.

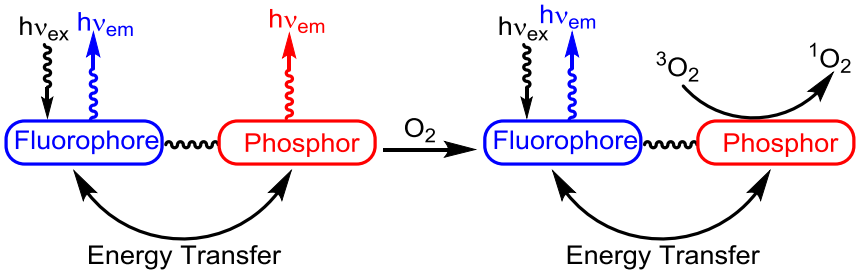

Figure 3.1. Design of ratiometric phosphor-fluorophore conjugates for sensing oxygen.

When O_2 is added, the triplet excited state of the phosphor is quenched, reducing the phosphorescence signal. Important criteria for effective sensor design include fluorescence and phosphorescence wavelengths that are far enough apart to be resolved, and minimal energy transfer between the two components to ensure that both emission signals are observed. Along these lines, recently reported designs for ratiometric O_2 sensors include quantum dots decorated with phosphorescent metal complexes,[12] metal-organic frame-works with both fluorescent and phosphorescent linkers,[13] fluorescent polymers with embedded phosphors,[14] and phosphorescent cyclometalated iridium complexes tethered to coumarin fluorophores.[15] Cyclometalated iridium complexes are especially attractive as the phosphorescent component, offering a combination of color tunability, high photoluminescence quantum yield, and relatively long (ca. μs) lifetimes not found in any other class of molecular phosphor. These attributes of cyclometalated iridium(III) complexes have been outlined in many recent studies[15–24] and have made these compounds prime candidates for a number of optoelectronic applications, including organic light

emitting diodes (OLEDs)[25–28] and sensing applications such as phosphorescent chemosensors[29–41] and singlet oxygen ($^1O_2$) sensitizers.[42–49]

Despite their potential advantages, there are comparatively few reports using cyclometalated iridium complexes in ratiometric O_2 sensor. One recent design which functioned well for intracellular oxygen sensing pairs a red-emitting cyclometalated iridium phosphor with a blue-emitting coumarin fluorophore, tethered to one another via a biologically compatible tetraproline linker.[5] The complex linker was needed to minimize energy transfer between the components and allow simultaneous detection of both emission signals. Although this construct was ultimately effective as a ratiometric oxygen probe, synthesis of this sensor required at least 10 steps to prepare the fluorophore/linker construct, which was then coupled to the cyclometalated iridium fragment in 19% yield. There are some known constructs which combine bis-cyclometalated iridium complexes with BODIPY fluorophores,[50–55] offering the advantages of BODIPY's high fluorescence quantum yields and biological compatibility,[56–59] but these have not been developed as ratiometric oxygen sensors.

Inspired by this previous work, here we introduce a class of ratiometric sensors prepared by a simple, modular approach, offering rapid access to several sensors with a range of emission profiles and ratiometric responses. These constructs pair bis-cyclometalated iridium fragments with BODIPY fluorophores, joined via variable pyridine-based linkers. The BODIPY and iridium precursors are each prepared in 1–3 steps from commercial precursors, and can be coupled to one another in yields ranging from 52% to 93%. This improved synthesis is enabled by a highly reactive cyclometalated iridium synthon recently disclosed by our group, and it is very easy to control the phosphorescence

color by changing the cyclometalating ligand. Furthermore, the linker be-tween the iridium and BODIPY influences the extent of energy transfer between the components, providing additional control over the photoluminescence output. By varying the cyclometalating ligand and linker it is possible to engender some of these compounds with dual luminescence. These dual-emitting compounds function effectively as ratiometric sensors for hypoxic environments, with high sensitivity and a large dynamic range for measuring oxygen partial pressure in abiological medium.

3.2. Experimental Section

3.2.1. Materials

Dry solvents were obtained from a Grubbs Solvent Purification System and deaerated with argon. Starting materials and reagents, unless otherwise specified, were obtained from commercial sources and used without further purification. 4-pyridinyl BODIPY complex **3** was prepared by the published method using 2,4-dimethylpyrrole, pyridine-4-carboxaldehyde, and chloranil.[60,61] 4-phenyl-4-pyridinyl BODIPY complex **4** was prepared by the synthetic procedure previously reported by our group.[62] 4-Pyridinyl-CH_2-BODIPY complex **5** was prepared according to the published synthetic procedure using a palladium-catalyzed Suzuki cross-coupling reaction.[63] The starting materials $Ir(C\hat{}N)_2(CNArdmp)(Cl)$ (**1a**: C^N = F_2ppy; **1b**: C^N = piq) and $Ir(F_2ppy)_2(CNArdmp)$-(FPF_5) (**2a**) were prepared as previously described by our group.[64]

3.2.2. Physical Methods.

^1H, $^{13}C\{^1H\}$, ^{19}F, and ^{11}B NMR spectra were recorded at room temperature using a JEOL ECA-400 or ECA-500 spectrometer. UV-vis absorption spectra were recorded in

screw-capped 1 cm quartz cuvettes using an Agilent Carey 8454 UV-vis spectrophotometer. Steady-state emission spectra were recorded using a Horiba FluoroMax-4 spectrofluorometer. To exclude air, samples for emission spectra were prepared in a nitrogen-filled glove-box using dry, deoxygenated toluene. Emission quantum yields were obtained by a relative method using 4-Pyridinyl BODIPY **3** as the standard(Φ_F = 0.30, λ_{ex} = 310 or 475 nm).[60] The emission spectra of the Ir-BODIPY complexes and the standard were measured with a range of absorbance between 0.01 and 0.1 at the excitation wavelengths mentioned above. The integrated emission intensity was plotted vs. absorbance and the slope of the best-fit line was obtained. The quantum yield of the Ir-BODIPY conjugates (Φ_x) was calculated using Equation 1 below, where Φ_{st} = the quantum yield of the standard, m_x = the slope for the samples, m_{st} = standard compound, η_x and η_{st} are the refractive indexes of the solvents of the sample and standard, respectively).

$$\Phi_x = \Phi_{st}\left[\frac{m_x}{m_{st}}\right]\left[\frac{\eta_x}{\eta_{st}}\right]^2 \quad (1)$$

The high-resolution mass spectrometry (HRMS-ESI) measurements were carried out by the Mass Spectrometry Laboratory at University of Houston, using a Thermo Exactive mass spectrometer and operated in positive ionization mode with a spray voltage at 1.5 kV. ^{1}H and ^{19}F NMR spectra of all new compounds are shown in **Appendix 3**, **Figures A3.1**–**A3.18**, and provide additional evidence for sample purity.

3.2.3. Oxygen Sensing and Stern-Volmer Experiments.

Dichloromethane solutions of Ir-BODIPY conjugates **6a** and **6b**–**8b** were prepared in a nitrogen-filled glovebox. These stock solutions were diluted in a quartz cuvette to concentrations of 5.0−7.0 × 10^{-6} M. Using a microliter syringe, 50−100 μL aliquots of air

were introduced to the cuvette. The lifetimes and emission spectra were measured in the nitrogen atmosphere (pO_2 = 0 mmHg) and following addition of each aliquot of air, up to atmospheric conditions (pO_2 = 160 mmHg). For emission spectra, the samples were excited at 310 nm, and for lifetime decay, 330 nm excitation was used. Using the changes of lifetimes in various oxygen partial pressures, the Stern–Volmer relationship was used to extract Stern–Volmer quenching constants (K_{sv}) and the quenching rate constant (k_q).

3.2.4. General synthetic procedure for [Ir(F$_2$ppy)$_2$(CNAr^{dmp})(BODIPY)](PF$_6$) complexes 6a–8a.

A mixture of Ir(F$_2$ppy)$_2$(CNArdmp)(FPF$_5$) (**1a**) (1 equiv.) and the respective BODIPY compound **3**–**5** (1 equiv.) was dissolved in 10 mL of CH_2Cl_2 in a vial in the glovebox. The solution was stirred at room temperature for 18 h. The solvent was removed under reduced pressure and the resulting solid was washed three times with hexane. The residue was purified by silica gel column chromatography (SiO_2) eluting with ethyl acetate/CH_2Cl_2 (1:4 v/v) to get the desired product, which was further purified by recrystallization (dichloromethane/hexane).

[Ir(F$_2$ppy)$_2$(CNAr^{dmp})(4-pyridinyl-BODIPY)](PF$_6$) (6a). Prepared by the general method using Ir(F$_2$ppy)$_2$(CNArdmp)(FPF$_5$) (**2a**) (54 mg, 0.063 mmol) and 4-pyridinyl-BODIPY (**3**) (20 mg, 0.063 mmol). Yield: 69 mg (93%). ^{1}H NMR (500 MHz, $CDCl_3$) δ: 9.38 (d, J = 5.5 Hz, 1H, Ar*H*), 8.86 (br, s, 2H, Pyridine *H*), 8.41 (dd, J = 21.7, 7.7 Hz, 2H, Ar*H*), 8.22 (d, J = 8.3 Hz, 1H, Ar*H*), 8.04 (t, J = 8.5 Hz, 1H, Ar*H*), 7.93 (t, J = 7.4 Hz, 1H, Ar*H*), 7.51–7.39 (m, 4H, Ar*H*), 7.13 (d, J = 15.3 Hz, 1H, Ar*H*), 7.00 (d, J = 6.4 Hz, 2H, Pyridine *H*), 6.53 (q, J = 11.7 Hz, 2H, Ar*H*), 5.95 (s, 2H, Pyrrole *H*), 5.82 (d, J = 10.4 Hz, 1H, Ar*H*), 5.74–5.63 (m, 1H, Ar*H*), 2.49 (s, 6H, C*H*$_3$), 2.10 (s, 6H, C*H*$_3$), 1.16 (s, 6H, C*H*$_3$).

^{19}F NMR (470 MHz, $CDCl_3$) δ: −72.32 (d, *J* = 713.0 Hz, 6F, PF_6), −103.49 to −104.01 (m, 1F, F_2ppy), −105.11 (q, *J* = 9.0 Hz, 1F, F_2ppy), −107.14 (t, *J* = 11.7 Hz, 1F, F_2ppy), −108.38 (t, *J* = 12.5 Hz, 1F, F_2ppy), −145.75 to −146.02 (m, 2F, BF_2). ^{11}B NMR (160 MHz, $CDCl_3$) δ: −0.38 (t, *J* = 31.2 Hz, 1B, BF_2). HRMS (ESI): m/z calcd. for $C_{49}H_{39}BF_{12}IrN_6P$ [M − PF_6]$^+$: 1029.2863, found: 1029.2996.

[Ir(F_2ppy)$_2$(CNAr^{dmp})(4-phenyl-4-pyridinylBODIPY)](PF_6) (7a). Prepared by the general method using Ir(F_2ppy)$_2$(CNArdmp)(FPF_5) (**2a**) (54 mg, 0.063 mmol) and 4-phenyl-4-pyridinyl-BODIPY (**4**) (25 mg, 0.063 mmol). Yield: 62 mg (79%). ^{1}H NMR (500 MHz, $CDCl_3$) *δ*: 9.41 (d, *J* = 1.4 Hz, 1H, Ar*H*), 8.74 (br, s, 2H, Pyridine *H*), 8.42 (d, *J* = 9.0 Hz, 1H, Ar*H*), 8.34 (d, *J* = 5.9 Hz, 1H, Ar*H*), 8.28 (d, *J* = 10.0 Hz, 1H, Ar*H*), 8.03 (t, *J* = 7.8 Hz, 1H, Ar*H*), 7.96 (t, *J* = 8.1 Hz, 1H, Ar*H*), 7.85 (d, *J* = 8.5 Hz, 2H, Ph*H*), 7.82 (s, 2H, Ar*H*), 7.51 (t, *J* = 7.4 Hz, 1H, Ar*H*), 7.42 (d, *J* = 7.4 Hz, 1H, Ar*H*), 7.39 (d, *J* = 8.4 Hz, 2H, Ph*H*), 7.19–7.13 (m, 1H, Ar*H*), 7.04 (d, *J* = 7.8 Hz, 2H, Pyridine *H*), 6.53 (dd, *J* = 12.4, 7.7 Hz, 2H, Ar*H*), 5.95 (s, 2H, Pyrrole *H*), 5.78 (d, *J* = 8.1 Hz, 1H, Ar*H*), 5.70 (d, *J* = 7.7 Hz, 1H, Ar*H*), 2.53 (s, 6H, C*H*$_3$), 2.13 (s, 6H, C*H*$_3$), 1.33 (s, 6H, C*H*$_3$). ^{19}F NMR (470 MHz, $CDCl_3$) δ: −72.64 (d, *J* = 712.6 Hz, 6F, PF_6), −104.08 to −104.40 (m, 1F, F_2ppy), −105.23 (q, *J* = 8.7 Hz, 1F, F_2ppy), −107.17 (t, *J* = 11.7 Hz, 1F, F_2ppy), −108.48 (d, *J* = 11.9 Hz, 1F, F_2ppy), −146.02 (dd, *J* = 65.7, 31.7 Hz, 2F, BF_2). ^{11}B NMR (160 MHz, $CDCl_3$) δ: −0.21 (t, *J* = 31.8 Hz, 1B, BF_2). HRMS (ESI): m/z calcd. for $C_{55}H_{43}BF_{12}IrN_6P$ [M − PF_6]$^+$: 1105.3176, found: 1105.3590.

[Ir(F_2ppy)$_2$(CNArdmp)(4-pyridinyl-CH_2-BODIPY)](PF_6) (8a). Prepared by the general method using Ir(F_2ppy)2(CNArdmp)(FPF_5) (**2a**) (54 mg, 0.063 mmol) and 4-phenyl-CH_2-BODIPY (**5**) (21 mg, 0.063 mmol). Yield: 57 mg (76%). ^{1}H NMR (400 MHz, $CDCl_3$) δ:

9.27 (d, *J* = 5.6 Hz, 1H, Ar*H*), 8.53 (br, s, 2H, Pyridine *H*), 8.39 (d, *J* = 8.9 Hz, 1H, Ar*H*), 8.29 (d, *J* = 9.6 Hz, 1H, Ar*H*), 8.20 (d, *J* = 5.7 Hz, 1H, Ar*H*), 8.03 – 7.93 (m, 2H, ArH), 7.43 (t, *J* = 6.6 Hz, 2H, Ar*H*), 7.37 (s, 2H, Ar*H*), 7.17 (t, *J* = 7.6 Hz, 1H, Ar*H*), 7.04 (d, *J* = 7.6 Hz, 2H, Pyridine *H*), 6.50 (q, *J* = 9.7 Hz, 2H, Ar*H*), 6.01 (d, *J* = 16.7 Hz, 2H, Pyrrole *H*), 5.69 (d, *J* = 10.0 Hz, 1H, Ar*H*), 5.60 (d, *J* = 9.5 Hz, 1H, Ar*H*), 4.43 (s, 2H, CH_2), 2.49 (s, 6H, C*H*$_3$), 2.18 (s, 3H, C*H*$_3$), 2.10 (s, 9H, C*H*$_3$). ^{19}F NMR (376 MHz, $CDCl_3$) δ: −72.62 (d, *J* = 712.7 Hz, 6F, PF_6), −103.91 (q, *J* = 9.5, 8.4 Hz, 1F, F_2ppy), −105.35 (q, *J* = 9.0 Hz, 1F, F_2ppy), −106.95 (t, *J* = 11.8 Hz, 1F, F_2ppy), −108.49 (t, *J* = 11.6 Hz, 1F, F_2ppy), −145.76 to −146.82 (m, 2F, BF_2). ^{11}B NMR (160 MHz, $CDCl_3$) δ: −0.41 (t, *J* = 34.4 Hz, 1B, BF_2). HRMS (ESI): m/z calcd. for $C_{50}H_{41}BF_{12}IrN_6P$ $[M - PF_6]^+$: 1043.3019, found: 1043.3406.

3.2.5. General procedure to prepare [Ir(piq)$_2$(CNAr^{dmp})(BODIPY)](PF$_6$) complexes 6b–8b.

Ir(piq)$_2$(CNArdmp)(Cl) (**1b**) (1 equiv.) and BODIPY compound **3**–**5** (1 equiv.) were dissolved in 15 mL of CH_2Cl_2 in a 25 mL round-bottom flask in the glovebox and stirred at room temperature for 1 h. $AgPF_6$ (1 equiv.) was added to the orange mixture which was stirred for 24 h at room temperature. The AgCl was filtered off and the solvent was removed under vacuum. The orange solid was washed three times with hexane. The residue was purified by column chromatography, using a silica gel (SiO_2) and 1:4 (v:v) ethyl acetate/CH_2Cl_2 as the eluent, followed by recrystallization (dichloro-methane/hexane).

[Ir(piq)$_2$(CNAr^{dmp})(4-pyridinyl-BODIPY)](PF$_6$) (6b). Prepared by the general procedure using Ir(piq)$_2$(CNArdmp)(Cl) (**1b**) (40 mg, 0.052 mmol), 4-pyridinyl-BODIPY

(**3**) (17 mg, 0.052 mmol), and $AgPF_6$ (14 mg, 0.052 mmol). Yield: 39 mg (65%). ^{1}H NMR (500 MHz, $CDCl_3$) δ: 9.24 (d, J = 6.4 Hz, 1H, Ar*H*), 8.98 (d, J = 8.4 Hz, 1H, Ar*H*), 8.88 (br, s, 2H, Pyridine *H*), 8.78 (d, J = 8.6 Hz, 1H, Ar*H*), 8.25 (dd, J = 16.0, 7.2 Hz, 2H, Ar*H*), 8.15 (d, J = 8.0 Hz, 1H, Ar*H*), 8.09 (d, J = 8.0 Hz, 1H, Ar*H*), 8.04 (d, J = 8.2 Hz, 1H, Ar*H*), 7.90–7.81 (m, 4H, Ar*H*), 7.75 (d, J = 6.6 Hz, 2H, Ar*H*), 7.35 (d, J = 6.0 Hz, 2H, Pyridine *H*), 7.09 (dt, J = 12.5, 6.8 Hz, 3H, Ar*H*), 6.96 (d, J = 7.6 Hz, 3H, Ar*H*), 6.84 (t, J = 7.4 Hz, 1H, Ar*H*), 6.51 (d, J = 7.6 Hz, 1H, Ar*H*), 6.24 (d, J = 7.4 Hz, 1H, Ar*H*), 5.90 (s, 2H, Pyrrole *H*), 2.46 (s, 6H, CH_3), 2.05 (s, 6H, CH_3), 1.04 (s, 6H, CH_3). ^{19}F NMR (470 MHz, $CDCl_3$) δ: −72.69 (d, J = 712.7 Hz, 6F, PF_6), −145.93 (dd, J = 64.4, 30.8 Hz, 2F, BF_2). ^{11}B NMR (160 MHz, $CDCl_3$) δ: −0.43 (t, J = 32.5 Hz, 1B, BF_2). HRMS (ESI): m/z calcd. for $C_{57}H_{47}BF_8IrN_6P$ $[M - PF_6]^+$: 1057.3553, found: 1057.3947.

[Ir(piq)$_2$(CNAr^{dmp})(4-phenyl-4-pyridinyl-BODIPY)](PF$_6$) (7b). Prepared by the general procedure using Ir(piq)$_2$(CNArdmp)(Cl) (**1b**) (40 mg, 0.052 mmol), 4-phenyl-4-pyridinyl-BODIPY (**4**) (21 mg, 0.052 mmol), and $AgPF_6$ (14 mg, 0.052 mmol). Yield: 35 mg (52%). ^{1}H NMR (500 MHz, $CDCl_3$) δ: 9.29 (d, J = 6.4 Hz, 1H, Ar*H*), 8.96 (d, J = 8.5 Hz, 1H, Ar*H*), 8.82 (d, J = 8.6 Hz, 1H, Ar*H*), 8.78 (br, s, 2H, Pyridine *H*), 8.23 (d, J = 6.3 Hz, 2H, Ph*H*), 8.15 (d, J = 8.0 Hz, 1H, Ar*H*), 8.07 (d, J = 8.1 Hz, 1H, Ar*H*), 8.03 (d, J = 8.1 Hz, 1H, Ar*H*), 7.83 (td, J = 16.8, 16.3, 7.1 Hz, 7H, Ar*H*), 7.76 (d, J = 5.6 Hz, 2H, Ph*H*), 7.69 (d, J = 6.4 Hz, 1H, Ar*H*), 7.37 (d, J = 8.0 Hz, 2H, Pyridine *H*), 7.14–7.09 (m, 2H), 7.07–7.02 (m, 1H, Ar*H*), 6.97 (dd, J = 13.8, 7.4 Hz, 3H, Ar*H*), 6.82 (t, J = 7.4 Hz, 1H, Ar*H*), 6.36 (d, J = 7.6 Hz, 1H, Ar*H*), 6.22 (d, J = 7.4 Hz, 1H, Ar*H*), 5.94 (s, 2H, Pyrrole *H*), 2.53 (s, 6H, CH_3), 2.08 (s, 6H, CH_3), 1.32 (s, 6H, CH_3). ^{19}F NMR (470 MHz, $CDCl_3$) δ: −73.04 (d, J = 712.6 Hz, 6F, PF_6), −146.07 (dd, J = 65.8, 31.7 Hz, 2F, BF_2). ^{11}B NMR

(160 MHz, $CDCl_3$) δ: −0.21 (t, *J* = 30.2 Hz, 1B, BF_2). HRMS (ESI): m/z calcd. for $C_{63}H_{51}BF_8IrN_6P$ $[M - PF_6]^+$: 1133.3866, found: 1133.4300.

[Ir(piq)$_2$(CNAr^{dmp})(4-pyridinyl-CH$_2$-BODIPY)](PF$_6$) (8b). Prepared by the general procedure using Ir(piq)$_2$(CNArdmp)(Cl) (**1b**) (33 mg, 0.041 mmol), 4-pyridinyl-CH_2-BODIPY (**5**) (14 mg, 0.041 mmol), and $AgPF_6$ (11 mg, 0.041 mmol). Yield: 39 mg (78%). ^{1}H NMR (500 MHz, CD_2Cl_2) δ: 9.07 (d, *J* = 5.9 Hz, 1H, Ar*H*), 8.96 (d, *J* = 8.4 Hz, 1H, Ar*H*), 8.82 (d, *J* = 8.5 Hz, 1H, Ar*H*), 8.52 (s, 2H, Pyridine *H*), 8.26 (d, *J* = 8.1 Hz, 1H, Ar*H*), 8.18 (d, *J* = 7.7 Hz, 1H, Ar*H*), 8.07–7.98 (m, 3H, Ar*H*), 7.86 (dd, *J* = 17.9, 8.2 Hz, 3H, Ar*H*), 7.78 (t, *J* = 7.4 Hz, 1H, Ar*H*), 7.65 (d, *J* = 5.5 Hz, 1H, Ar*H*), 7.61 (d, *J* = 6.0 Hz, 1H, Ar*H*), 7.21 (s, 2H, Pyridine *H*), 7.17–7.11 (m, 2H, Ar*H*), 7.05 (dd, *J* = 17.1, 7.4 Hz, 3H, Ar*H*), 6.93 (d, *J* = 6.7 Hz, 1H, Ar*H*), 6.81 (t, *J* = 7.2 Hz, 1H, Ar*H*), 6.34 (d, *J* = 7.6 Hz, 1H, Ar*H*), 6.18 (d, *J* = 7.1 Hz, 1H, Ar*H*), 6.02 (d, *J* = 8.0 Hz, 2H, Pyrrole *H*), 4.37 (s, 2H, C*H*$_2$), 2.44 (s, 6H, C*H*$_3$), 2.06 (s, 3H, C*H*$_3$), 2.01 (s, 9H, C*H*$_3$). ^{19}F NMR (376 MHz, CD_2Cl_2) δ: −73.08 (d, *J* = 710.7 Hz, 6F, PF_6), −145.97 to −146.64 (m, 2F, BF_2). ^{11}B NMR (160 MHz, CD_2Cl_2) δ: −0.47 (t, *J* = 32.2 Hz, 1B, BF_2). HRMS (ESI): m/z calcd. for $C_{58}H_{49}BF_8IrN_6P$ $[M - PF_6]^+$: 1071.3709, found: 1071.4089.

3.2.6. X-ray Crystallography Procedures.

Single crystals were grown Single crystals were grown by diffusion of hexane into concentrated CH_2Cl_2 solutions, in air. Crystals were mounted on a Bruker Apex II three-circle diffractometer using MoKα radiation (λ = 0.71073 Å). The data was collected at 123(2) K and was processed and refined within the APEXII software. Structures were solved by direct methods in SHELXS or by intrinsic phasing in SHELXT and refined by standard difference Fourier techniques in the program SHELXL.[65] Hydrogen atoms were

placed in calculated positions using the standard riding model and refined isotropically; all non-hydrogen atoms were refined anisotropically. All three crystals (**6a**–**8a**) were partially desolvated, resulting in large regions of electron density corresponding to disordered and/or partially occupied dichloromethane solvent molecules. In the case of **6a**, the presence of large voids and the heavy disorder of the solvent necessitated the use of the SQUEEZE function in PLATON.[66] For **7a** and **8a**, the disordered solvent could be modeled, but it did result in high checkCIF alerts (Level B for **7a**, Level A and B for **8a**) for abnormally large chlorine ellipsoids. Notwithstanding these checkCIF errors, we concluded that the model which included the disordered solvent was satisfactory, and did not use SQUEEZE for these latter two structures. Distance restraints and rigid-bond restraints (SIMU and DELU) were used on all disordered parts. Crystallographic details of complexes **6a**–**8a** are summarized in **Tables A3.1** in **Appendix 3**.

3.3. Results and Discussion

3.3.1. Synthesis of Ir-BODIPY Constructs.

Scheme 3.1 presents the synthetic method to generate complexes with a phosphorescent $[Ir(C\text{^}N)_2]^+$ center linked to a fluorescent BODIPY chromophore. Pyridyl-substituted BODIPY precursors **3**–**5** with three types of linkers at the meso-position were prepared. Compounds **3** and **4**, with a meso-pyridyl and extended meso-4-pyridylphenyl linker, respectively, were accessed following known procedures,[60,61] and the Lewis acid-base chemistry of these versions have been recently described by our group.[62] Methylene-spaced 4-pyridinyl-CH_2-BODIPY **5**, with an unconjugated linker between the pyridine moiety and the BODIPY core, can be prepared by the previously reported synthetic method

Scheme 3.1. Synthesis of cyclometalated iridium-BODIPY constructs.

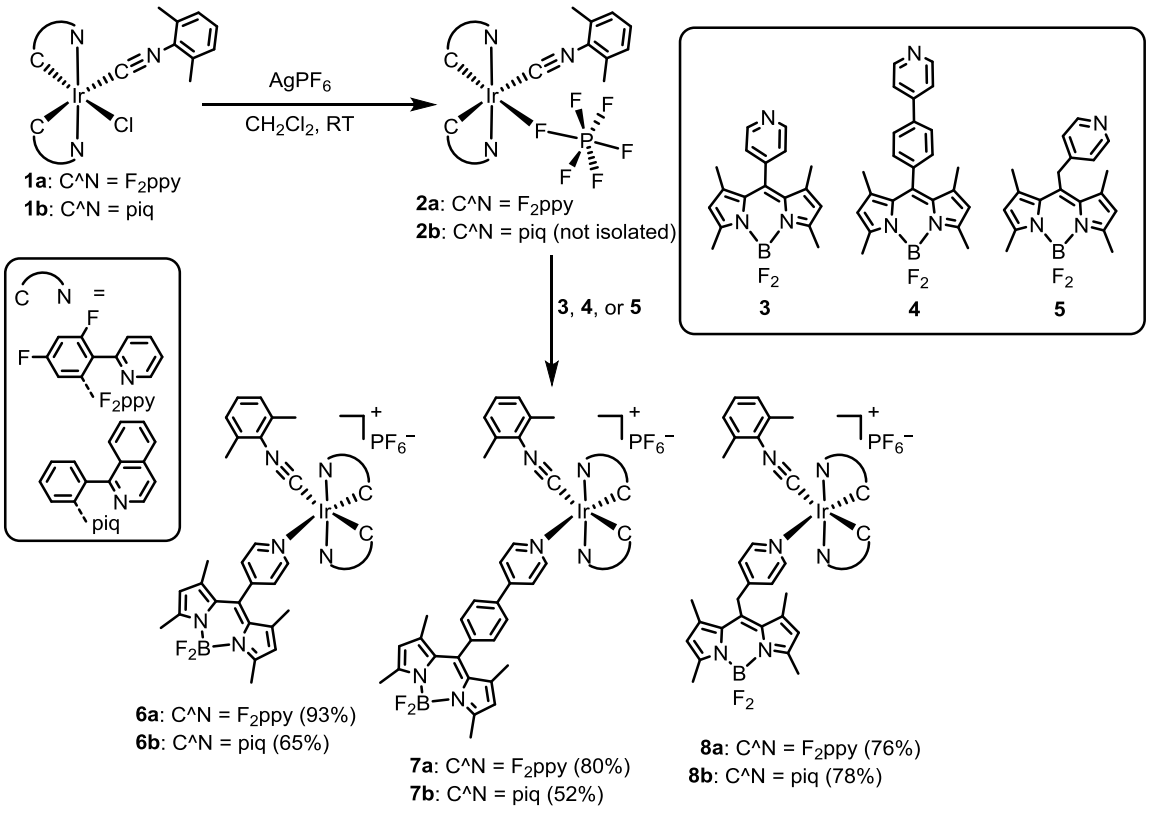

involving a palladium-catalyzed Suzuki cross-coupling reaction.[63] The bis-cyclometalated iridium fragment originates from precursors of the type $Ir(C^N)_2(CNAr^{dmp})(FPF_5)$ (**2a** and **2b**; C^N = cyclometalating ligand, $CNAr^{dmp}$ = 2,6-dimethylphenyl isocyanide), accessed via silver-mediated halide abstraction from the respective chloride-bound precursors **1a** and **1b**.[64] For this study the two cyclometalating ligands 2-(2-,4-difluorophenyl)pyridine (F_2ppy, **1a**/**2a**) and 1-phenylisoquinoline (piq, **1b**/**2b**) were chosen, which are known to engender the complexes with blue or red phosphorescence, respectively. Two slight variations in procedure were used to generate the reactive PF_6^- precursors and combine them with the BODIPY. For the F_2ppy complexes, the isolated precursor $Ir(F_2ppy)_2(CNAr^{dmp})(FPF_5)$ (**2a**) was treated with BODIPYs **3**–**5** in CH_2Cl_2, allowing rapid

room-temperature assembly of adducts **6a**–**8a**, isolated in yields of 76–93%. The same procedure was unsuccessful for the preparation of the piq analogues, so instead a one-pot reaction involving $Ir(piq)_2(CNArdmp)(Cl)$ (**1b**), $AgPF_6$, and the respective BODIPY was carried out to synthesize **6b**–**8b**, isolated in 52–78% yield. Both procedures require silica gel column chromatography and recrystallization to separate small amounts of unreacted BODIPY and unidentified side products, following which the complexes are deemed pure by ^{1}H, ^{19}F, and ^{11}B NMR spectra, shown in **Figures A3.1**–**A3.18** of **Appendix 3**.

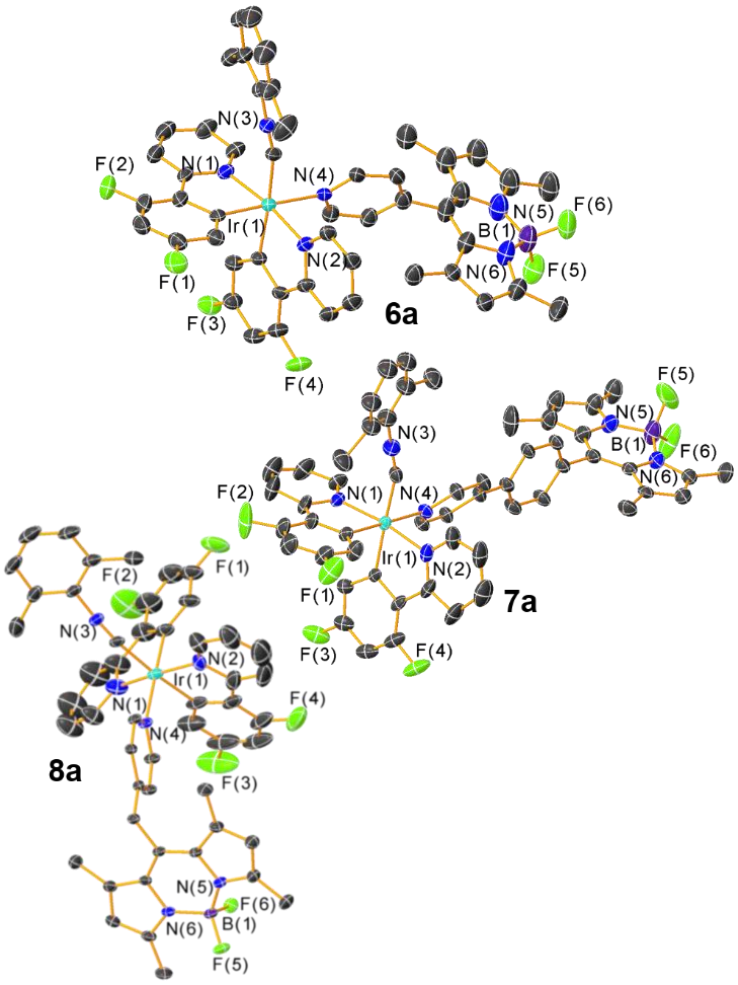

Figure 3.2. X-ray crystal structures of complex **6a**–**8a**. Ellipsoids are drawn at the 50% probability level with counterions, solvent molecules, and hydrogen atoms omitted.

The structures of the [Ir(F_2ppy)($CNAr^{dmp}$)(BODIPY)](PF_6) complexes **6a**–**8a** were ascertained by single-crystal X-ray diffraction and shown in **Figure 3.2**. Diffraction data and refinement details for complexes **6a**–**8a** are summarized in **Table A3.1** of **Appendix 3**. The X-ray structures verify that the BODIPY attaches to the iridium center through a covalent bond with Ir–$N_{pyridyl}$ distances ranging from 2.173(5) Å to 2.222(8) Å. The nature of the linker between the iridium and the BODIPY has measurable effects on the relative orientation of the two components. The internuclear distance between the iridium and boron atoms are similar for **6a** (9.38(1) Å, average of two independent molecules) and methylene-spaced **8a** (9.140(6) Å), whereas the additional phenyl spacer in **7a** results in a substantially longer distance of 13.73(1) Å. The alignment of the BODIPY relative to the iridium fragment also differs considerably in the three structures, as measured by the dihedral angle between the mean plain of the BODIPY and the mean plane of the F_2ppy ligand trans to the BODIPY pyridyl. In complex **7a** this angle is 7.2°, indicating a nearly parallel arrangement of the BODIPY, and it increases to 21.1° in **6a** (average of two crystallographically independent molecules), and with the sp^3 linker in **8a** the angle is 73.9°.

The identities of [Ir($C^{\wedge}N)_2$($CNAr^{dmp}$)(BODIPY)](PF_6) complexes **6**–**8** were also confirmed by high resolution mass spectrometry (ESI), which clearly show the 1:1 combination of the bis-cyclometalated iridium fragment with the pyridyl-substituted BODIPY in each case. For each compound a strong molecular ion peak was located, the mass being a good match for the corresponding $[M–PF_6]^+$ ion. **Figures A3.27–A3.32** of **Appendix 3** show the experimental data for the $[M–PF_6]^+$ ion juxtaposed with the simulated pattern. In each case, the isotope peaks are separated by 1 m/z unit, confirming the +1 charge of the ion, and there is a good match between the experimental and simulated

isotopologue ratios. To summarize the characterization of the Ir-BODIPY constructs, the combination of X-ray crystallography and HRMS confirms the identity of the compounds, whereas multinuclear NMR validates their bulk purity.

3.3.2. Photophysical Properties.

The UV-vis absorption and emission spectra of the free BODIPY complexes **3**–**5**, measured in CH_2Cl_2, are shown in **Figures A3.19** and **A3.20** of **Appendix 3**. To summarize briefly, the UV-vis absorption profiles are dominated by intense visible absorption with λ_{max} = 505 nm (ε = 82 300 M^{-1} cm^{-1}) and λ_{max} = 503 nm (ε = 82 000 M^{-1} cm^{-1}) for **3** and **4**, respectively. The absorption coefficient of methylene-spaced **5** (ε = 163 000 M^{-1} cm^{-1}) at λ_{max} (505 nm) is much larger than that of the analogues with aromatic spacers. All of organic chromophores **3**–**5** are fluorescent at room temperature, and the steady-state and time-resolved emission data are summarized in **Table A3.2** of **Appendix 3**. All three pyridyl-BODPYS have similar photoluminescence spectra, the notable difference being the quantum yields, which for methylene-spaced **5** is observed to be 0.99, compared to 0.30 (**3**) and 0.43 (**4**) for the aromatic pyridyl-BODIPYs. This exceptionally high quantum yield for complex **5** has also been observed in other solvents such as toluene (100%) and ethanol (89%).[63] The fluorescence lifetimes for all of the free BODIPYs are in the ns range, with a slightly longer value for **5** (6.6 ns) when compared with **3** and **4** (1.9 and 2.7 ns, respectively).

The UV-vis absorption spectra of all Ir-BODIPY conjugates **6**–**8** measured at room temperature in dichloromethane are shown in **Figure 3.3** and summarized in **Table A3.3** of **Appendix 3**. The UV-vis absorption spectra of the Ir-BODIPY constructs are dominated in the visible region by strong bands in the range of 504–510 nm originating from the

BODIPY. The wavelengths of these visible absorption bands are very similar to the free BODIPYs, but the molar absorptivities (ε) are attenuated to a significant extent, especially in the piq series. The UV and near-visible regions involve several overlapping bands, attributed to a combination of π→π* transitions involving the BODIPY (compare to **Figure A3.19**), and the expected bands[67] from the $[Ir(C\wedge N)_2]^+$ fragment that include C^N-centered π→π* transitions at higher energy and MLCT transitions at lower energy.

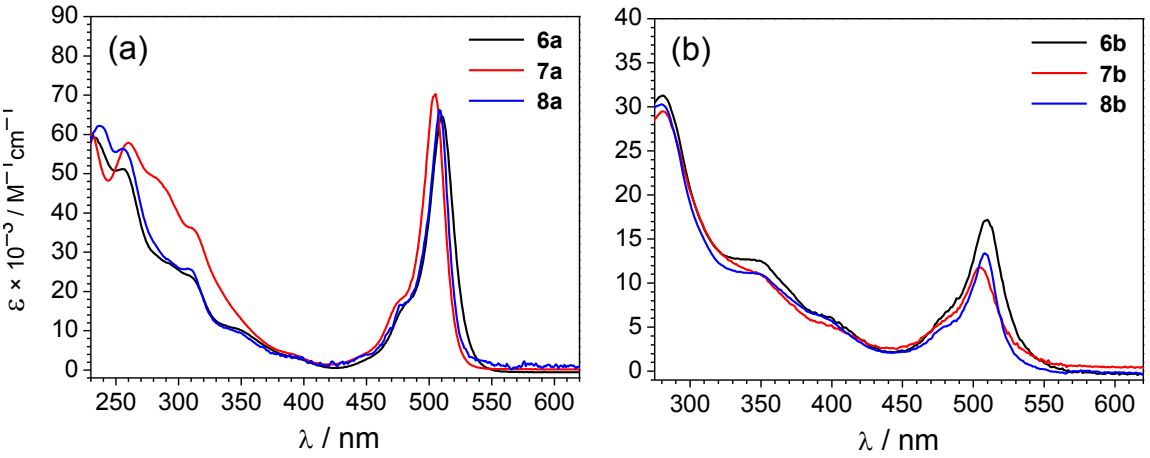

Figure 3.3. Overlaid UV-vis absorption spectra (a) of $[Ir(F_2ppy)_2(CNAr^{dmp})(BODIPY)](PF_6)$ complexes **6a**–**8a** and (b) of $[Ir(piq)_2(CNAr^{dmp})(BODIPY)](PF_6)$ complexes **6b**–**8b**. Absorption spectra were recorded at room temperature in CH_2Cl_2.

Overlaid photoluminescence spectra of complexes **6**–**8** are displayed in **Figure 3.4**. The spectra are excitation-wavelength dependent, and with 475 nm excitation, where only the BODIPY is expected to absorb, only fluorescence coming from the BODIPY fragment is observed. In most cases the fluorescence wave-length is nearly identical to the respective free BODIPY. However in complex **6a**, where the $[Ir(F_2ppy)_2(CNAr^{dmp})]^+$ fragment is linked to the BODIPY via a short pyridyl spacer, the BODIPY fluorescence is significantly

red-shifted to 549 nm, and while not as pronounced the fluorescence in the piq complex with the same linker (**6b**) red-shifts to 528 nm.

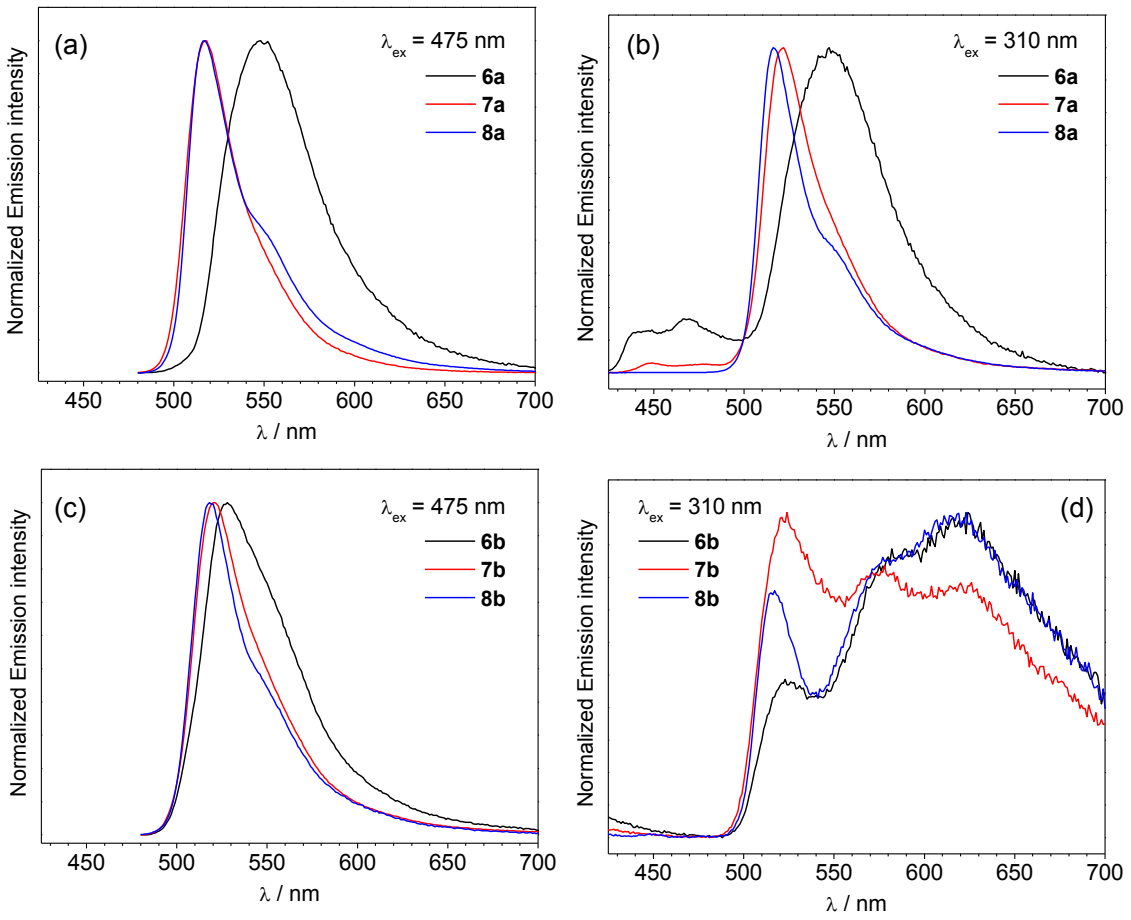

Figure 3.4. Photoluminescence spectra (a) F_2ppy complexes **6a**–**8a**, excited at 475 nm, (b) **6a**–**8a** excited at 310 nm, (c) piq complexes **6b**–**8b** excited at 475 nm, and (d) **6b**–**8b** excited at 310 nm. All spectra were recorded at room temperature in deoxygenated CH_2Cl_2.

This measurable red shift of the fluorescence upon coordination to iridium is similar to the effect we observed previously when Lewis acidic boranes were coordinated to BODIPY **3**.[62] Lifetimes for the fluorescence component are quite similar to the free BODIPYs **3**–**5** (**Table A3.2** in **Appendix 3**). In most cases the fluorescence quantum yields, determined

when the BODIPY is selectively excited at 475 nm, are significantly lower than the free BODIPY and range from 7.4–66% across the series of compounds.

In contrast, with 310 nm excitation, where both the iridium phosphor and the BODIPY fluorophore absorb, two emission bands are observed in most cases. Iridium-centered phosphorescence, with wavelengths that depend on the identity of the cyclometalating ligand, is observed in addition to the BODIPY-centered fluorescence. This vibronically structured band occurs with λ_{max} at ca. 440 and 467 nm in F_2ppy complexes **6a** and **7a**, and λ_{max} at ca. 575 and 623 nm for piq complexes **6b**–**8b**. No phosphorescence is observed in complex **8a**, where C^N = F_2ppy and the BODIPY includes a methylene spacer, suggesting that in this case there is efficient energy transfer from the $[Ir(F_2ppy)_2]^{2+}$ fragment to the BODIPY, and only BODIPY-centered fluorescence is observed at either excitation wavelength. Energy transfer from BODIPY to Ir does not appear to occur, since the red phosphorescence in piq complexes **6b**–**8b** is only observed when the Ir center is excited directly, and does not occur when only the BODIPY is excited at 475 nm.

The photoluminescence quantum yields (Φ_{PL}) of the Ir-BODIPY conjugates tend to be somewhat lower when both the Ir and the BODIPY are simultaneously excited at 310 nm, ranging between 6.0 and 65%. The one exception is complex **8a**, which only exhibits fluorescence at both excitation wavelengths and has the same quantum yield in each case, again consistent with efficient energy transfer from Ir to BODIPY for this compound. For the rest of the compounds, the wavelength-dependence of the quantum yield suggests that phosphorescence from the iridium center is inherently less efficient than fluorescence from the BODIPY. In **6a** and **7a** it is difficult to evaluate whether excited-state energy transfer

between the $[Ir(F_2ppy)_2]^{2+}$ center and the BODIPY is occurring, though we presume there is some degree of energy transfer since the phosphorescence quantum yield in these

Table 3.1. Summary of photophysical properties of Ir-BODIPY complexes **6**–**8**. Emission spectra were measured in CH_2Cl_2 at 293 K.

	λ_{em}/nm[a]	λ_{em}/nm[b]	Φ_{PL}[a]	Φ_{PL}[b]	τ/ns[d]	τ/μs[e]
6a	549	438, 465, 550	0.074	0.060	1.4	6.8
7a	517	448, 472(sh), 521	0.30	0.13	2.7	5.6
8a	516	517[c]	0.66	0.65	5.2	N.D.[c]
6b	528	527, 585(sh), 621	0.089	0.041	2.5	6.0
7b	521	520, 576, 620	0.16	0.063	1.5	6.9
8b	518	515, 574, 619	0.13	0.052	5.2	7.3

[a] Fluorescence only, excited at 475 nm. [b] Fluorescence and phosphorescence excited at 310 nm. [c] No phosphorescence for this compound. [d] Fluorescence lifetimes, excited at 455 nm. [e] Phosphorescence lifetime, excited at 330 nm.

compounds is much lower than we typically observe for isocyanide-bound $[Ir(F_2ppy)_2]^+$ complexes.[67,68] The phosphorescence lifetimes of all complexes (except **8a**, which doesn't phosphoresce) fall in the narrow range of 5.6–7.3 μs. The apparent dual emission with UV excitation persists and is identical in samples of the Ir-BODIPY complexes that have been purified multiple times by silica gel column chromatography and recrystallization, suggesting it is not a result of minor impurities. In addition, the excitation spectra for **6**–**8** (**Figures A3.21**–**A3.26** in **Appendix 3**) overlay very well with the UV-vis absorption,

indicating that both emission bands arise from the Ir-BODIPY conjugate. These investigations suggest that the orientation of the BODIPY chromophore relative to the iridium center, controlled by the nature of the linker between the fluorophore component and phosphor fragment, can play a role in the energy-transfer dynamics and photolumine-

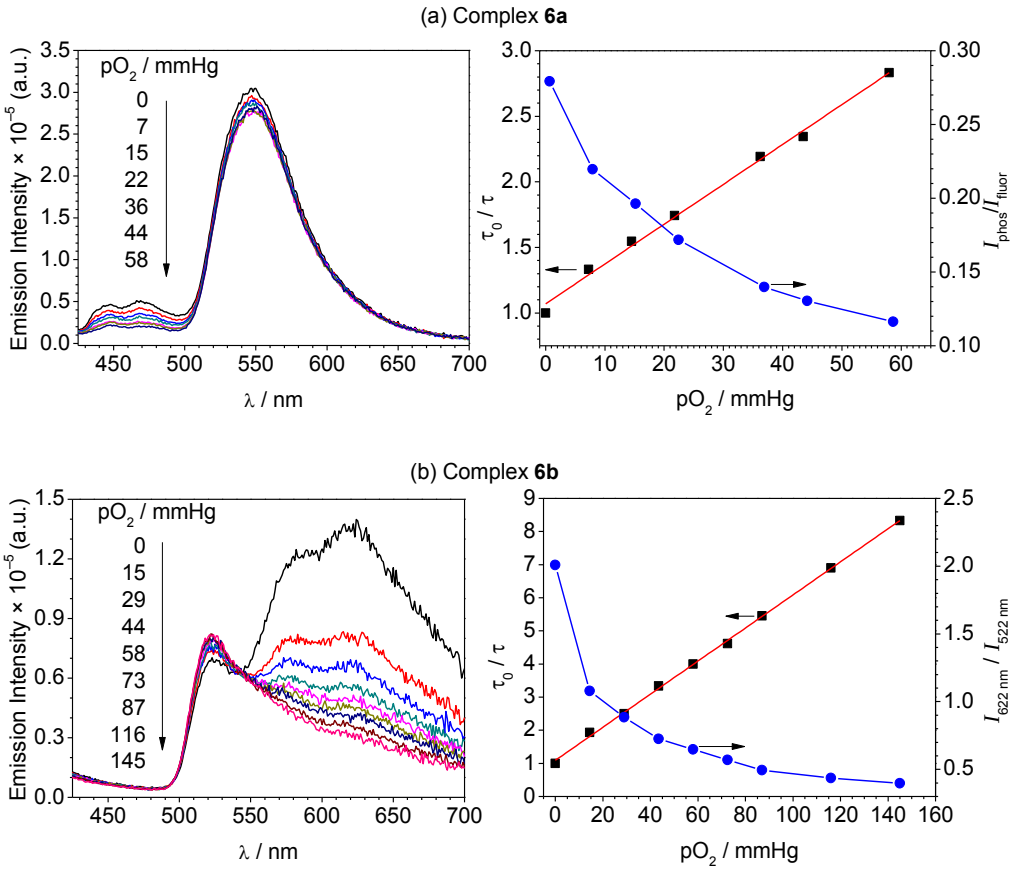

Figure 3.5. Oxygen sensing data for complexes **6a** (a), **6b** (b). The left-hand plots show photoluminescence spectra (λ_{ex} = 310 nm) of the respective Ir-BODIPY complex (5 μM) measured in CH_2Cl_2 at room temperature under various oxygen partial pressures. The right-hand plots overlay the ratiometric response (blue circles) and Stern-Volmer plot (black squares, with linear fit) as a function of oxygen partial pressure. For the ratiometric data, the solid line is drawn merely as a guide, and the ratio was determined from integrated emission intensities below 500 nm (phosphorescence) and above 500 nm (fluorescence) for complex **6a**, and for emission signal at the peak wavelengths for complex **6b**.

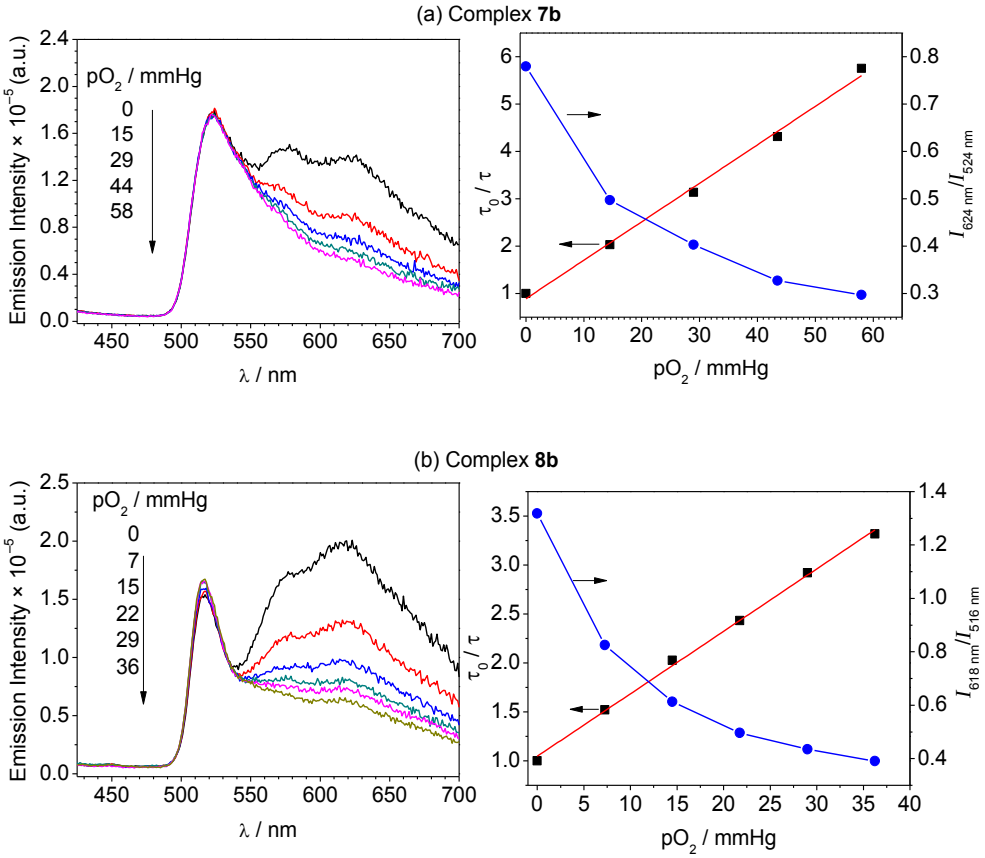

Figure 3.6. Oxygen sensing data for complexes **7b** (a), **8b** (b). The left-hand plots show photoluminescence spectra (λ_{ex} = 310 nm) of the respective Ir-BODIPY complex (5 μM) measured in CH_2Cl_2 at room temperature under various oxygen partial pressures. The right-hand plots overlay the ratiometric response (blue circles) and Stern-Volmer plot (black squares, with linear fit) as a function of oxygen partial pressure. For the ratiometric data, the solid line is drawn merely as a guide, and the ratio was determined from emission signal at the peak wavelengths for complexes **7b** and **8b**.

scence properties. In general, when C^N = F_2ppy energy transfer can occur such that predominantly BODIPY fluorescence is observed, whereas when C^N = piq there is minimal energy transfer and dual emission occurs when both sites are excited. The relative amounts of phosphorescence and fluorescence do vary somewhat across the series as a

function of the linker, although the ratio of phosphorescence to fluorescence is also excitation-wavelength dependent.

Whereas complexes **7a** and **8a** have very weak or negligible phosphorescence and are not good candidates for ratiometric oxygen sensing, the remaining four compounds have comparable levels of phosphorescence and fluorescence and were evaluated as ratiometric O_2 sensors. To qualitatively investigate their response to O_2, samples photoluminescence spectra were collected in deoxygenated solutions, prepared in a nitrogen-filled glovebox, and compared to spectra for air-equilibrated samples. As shown in **Figure A3.33** in **Appendix 3**, after air exposure the signal arising from iridium-centered phosphorescence, which occurs in the blue region for **6a** and in the red for **6b**–**8b**, disappears completely. The fluorescence signal from the BODIPY is minimally altered.

To more quantitatively evaluate the sensing response, photoluminescence measurements were carried out at varying pO_2 levels, until the point when the phosphorescence signal no longer changed appreciably. These results are summarized in **Figure 3.5** and **Figure 3.6**, which shows the spectral evolution for each compound as pO_2 is gradually increased. All four of the complexes are able to sense low levels of oxygen below atmospheric content ($pO_2 \leq 160$ mmHg), indicating they are suitable for hypoxic environments. The right-hand plots of **Figure 3.5** (blue circles) show the sensing response plotted as the ratio of phosphorescence to fluorescence signal, vs. pO_2. For **6a** where the phosphorescence and fluorescence are well-separated, this ratio was determined by integrating the two spectral bands, below 500 nm for phosphorescence and above 500 nm for fluorescence. In **6b**–**8b** the fluorescence and phosphorescence overlap, and the ratio was determined by taking the signal at the respective peak wavelengths for the

phosphorescence and fluorescence bands. These plots demonstrate that the ratiometric response spans a >3-fold range in each case, i.e. the signal ratio changes by more than a factor of three over the range of pO_2 values tested.

To gain further insight into the oxygen sensing response, Stern-Volmer analysis on the phosphorescence lifetime was conducted. Equation 2 shows the Stern–Volmer relationship,[69,70] where K_{sv} is the Stern–Volmer constant, pO_2 is the oxygen partial pressure, k_q is the quenching rate constant, and τ_0 and τ are the lifetimes in the absence and presence of oxygen, respectively.

$$\frac{\tau_0}{\tau} = 1 + K_{SV} pO_2 = 1 + k_q \tau_0 pO_2 \quad (2)$$

The Stern–Volmer plots and linear fits are overlaid with the ratiometric sensing data in in **Figure 3.5** and **Figure 3.6**, and the Stern-Volmer parameters extracted from this data are summarized in **Table 3.2**. The Stern–Volmer constant K_{sv} can be obtained from the slope of the linear fit. Also, the quenching rate constant k_q can be determined by using K_{sv} and τ_0. The Stern–Volmer constants (K_{sv}) for bis-cyclometalated iridium-BODIPY complexes **6a**, and **6b**–**8b** were determined to be 3.0–8.1 × 10^{-2} $mmHg^{-1}$, and from these values quenching rate constants (k_q) were determined to vary from 4.4 × 10^3 s^{-1} $mmHg^{-1}$ to 1.2 × 10^4 s^{-1} $mmHg^{-1}$. To convert the unit of the quenching rate constant to s^{-1} M^{-1}, which is more conventional for bimolecular quenching rate constants, we adopted the previously reported literature[71] regarding to the solubility of oxygen into organic solvents. The solubility value of oxygen into dichloromethane at 298.2 K and 101.33 kPa (1 atm) is 7.09 × 10^{-4} M, and using this conversion factor k_q ranges from 4.7 × 10^9 s^{-1} M^{-1} to 1.3 × 10^{10} $s^{-1}M^{-1}$ in the four Ir-BODIPY conjugates evaluated as sensors.

Table 3.2. Stern–Volmer constants (K_{sv}) and the quenching rate constants (k_q) for complexes **6a** and **6b**–**8b**.

Entry	K_{sv} / $mmHg^{-1}$	k_q / s^{-1} $mmHg^{-1}$	k_q / s^{-1} M^{-1}
6a	3.0×10^{-2}	4.4×10^{3}	4.7×10^{9}
6b	5.0×10^{-2}	8.3×10^{3}	8.9×10^{9}
7b	8.1×10^{-2}	1.2×10^{4}	1.3×10^{10}
8b	6.4×10^{-2}	8.8×10^{3}	9.4×10^{9}

To contextualize these results, we see that all four sensors presented here are efficiently quenched by O_2, with k_q values approaching the diffusion limit. The Stern-Volmer kinetics seem to depend slightly on the C^N ligand, with the complexes in the piq series (**6b**–**8b**) quenching more efficiently than F_2ppy complex **6a**. For **6b**–**8b** there are slight differences in Stern-Volmer parameters, indicating there may be a small dependence on the nature of the BODIPY spacer, but all three behave quite similarly overall. Comparing to previously described ratiometric oxygen sensors, the K_{sv} values for the Ir-BODIPY constructs described here are intermediate between those of a recently described MOF-based nanosensor ($K_{sv} = 1.7 \times 10^{-2}$ $mmHg^{-1}$)[13] and a cyclometalated iridium-coumarin sensor ($K_{sv} = 6.4 \times 10^{-2}$ $mmHg^{-1}$)[5]. Comparing to sensors with reported quenching rate constants, the complexes described here have k_q values that exceed those of a nano-crystal sensor decorated with osmium phosphors ($k_q = 1.8 \times 10^{9}$ s^{-1} M^{-1})[12] and proto-porphyrin IX ($k_q = 4.0 \times 10^{2}$ s^{-1} $mmHg^{-1}$)[72], which functions as an endogenous turn-off O_2 sensor. These comparisons demonstrate that the new ratiometric oxygen sensors described here compare

favorably with well-known examples of biological oxygen sensors, with good sensitivity (k_q up to 1.3×10^{10} s^{-1} M^{-1}) and dynamic ranges suitable for hypoxic measurements (< 160 mmHg).[73,74]

3.4. Conclusions

In summary, we have developed two-component assemblies with a phosphorescent metal center ($[Ir(C\text{^}N)_2(CNAr^{dmp})]^+$) linked to the well-known fluorophore BODIPY and demonstrated their utility as ratiometric O_2 sensors. The constructs are very simple to prepare in high yields using a modular approach where the synthetic linchpin is a labile cyclometalated iridium precursor with a loosely bound PF_6^- anion. These Ir-BODIPY conjugates exhibit dual luminescence where fluorescence originates from the organic chromophore and phosphorescence comes from the iridium center, and the spectral profile is dependent on the identity of the C^N ligand as well as the nature of the linker between the iridium center and the BODIPY. Complexes with C^N = F_2ppy in general do not function well as sensors, since energy transfer from the long-lived iridium-centered excited state to the BODIPY is favorable and efficient, resulting in very weak phosphorescence signal.

By contrast, for complexes with C^N = piq, where the triplet excited state is lower in energy than the BODIPY singlet state, energy transfer is shut down and comparable amounts of luminescence from both sites are observed, the precise ratio varying slightly with the nature of the linker between BODIPY and iridium. Evaluation of the oxygen-dependent photoluminescence, in concert with Stern-Volmer quenching analysis of the phosphorescence lifetime, demonstrates that four compounds described here function as

effective ratiometric O_2 sensors with sensitivities and dynamic ranges suitable for hypoxic environments. This conceptually simple design, where the fluorophore and phosphor are linked via a modular and simple synthetic strategy, should be applicable to a range of next-generation oxygen sensors. Specific future improvements include the design of sensors with greater brightness (higher quantum yields) and larger spectral separation between the fluorescence and phosphorescence signal, both of which should improve sensitivity and dynamic range.

3.5. References

1. Aragonés, J.; Fraisl, P.; Baes, M.; Carmeliet, P. Oxygen Sensors at the Crossroad of Metabolism. *Cell Metab.* **2009**, *9*, 11–22.
2. Pecher, J.; Mecking, S. Nanoparticles of Conjugated Polymers. *Chem. Rev.* **2010**, *110*, 6260–6279.
3. Wu, C.; Chiu, D. T. Highly Fluorescent Semiconducting Polymer Dots for Biology and Medicine. *Angew. Chem. Int. Ed.* **2013**, *52*, 3086–3109.
4. Hockel, M.; Vaupel, P. Tumor Hypoxia: Definitions and Current Clinical, Biologic, and Molecular Aspects. *JNCI J. Natl. Cancer Inst.* **2001**, *93*, 266–276.
5. Yoshihara, T.; Yamaguchi, Y.; Hosaka, M.; Takeuchi, T.; Tobita, S. Ratiometric Molecular Sensor for Monitoring Oxygen Levels in Living Cells. *Angew. Chem. Int. Ed.* **2012**, *51*, 4148–4151.
6. Wu, C.; Bull, B.; Christensen, K.; McNeill, J. Ratiometric Single-Nanoparticle Oxygen Sensors for Biological Imaging. *Angew. Chem. Int. Ed.* **2009**, *48*, 2741–2745.
7. Zhang, S.; Hosaka, M.; Yoshihara, T.; Negishi, K.; Iida, Y.; Tobita, S.; Takeuchi, T. Phosphorescent Light–Emitting Iridium Complexes Serve as a Hypoxia-Sensing Probe for Tumor Imaging in Living Animals. *Cancer Res.* **2010**, *70*, 4490–4498.
8. Pistner, A. J.; Pupillo, R. C.; Yap, G. P. A.; Lutterman, D. A.; Ma, Y.-Z.; Rosenthal, J. Electrochemical, Spectroscopic, and $^1O_2$ Sensitization Characteristics of 10,10-

Dimethylbiladiene Complexes of Zinc and Copper. *J. Phys. Chem. A* **2014**, *118*, 10639–10648.

9. Lincoln, R.; Kohler, L.; Monro, S.; Yin, H.; Stephenson, M.; Zong, R.; Chouai, A.; Dorsey, C.; Hennigar, R.; Thummel, R. P.; et al. Exploitation of Long-Lived ^{3}IL Excited States for Metal–Organic Photodynamic Therapy: Verification in a Metastatic Melanoma Model. *J. Am. Chem. Soc.* **2013**, *135*, 17161–17175.
10. McDonnell, S. O.; Hall, M. J.; Allen, L. T.; Byrne, A.; Gallagher, W. M.; O'Shea, D. F. Supramolecular Photonic Therapeutic Agents. *J. Am. Chem. Soc.* **2005**, *127*, 16360–16361.
11. Ma, J.; Chen, J.-Y.; Idowu, M.; Nyokong, T. Generation of Singlet Oxygen via the Composites of Water-Soluble Thiol-Capped CdTe Quantum DotsSulfonated Aluminum Phthalocyanines. *J. Phys. Chem. B* **2008**, *112*, 4465–4469.
12. McLaurin, E. J.; Greytak, A. B.; Bawendi, M. G.; Nocera, D. G. Two-Photon Absorbing Nanocrystal Sensors for Ratiometric Detection of Oxygen. *J. Am. Chem. Soc.* **2009**, *131*, 12994–13001.
13. Xu, R.; Wang, Y.; Duan, X.; Lu, K.; Micheroni, D.; Hu, A.; Lin, W. Nanoscale Metal–Organic Frameworks for Ratiometric Oxygen Sensing in Live Cells. *J. Am. Chem. Soc.* **2016**, *138*, 2158–2161.
14. Shi, H.; Ma, X.; Zhao, Q.; Liu, B.; Qu, Q.; An, Z.; Zhao, Y.; Huang, W. Ultrasmall Phosphorescent Polymer Dots for Ratiometric Oxygen Sensing and Photodynamic Cancer Therapy. *Adv. Funct. Mater.* **2014**, *24*, 4823–4830.
15. Kando, A.; Hisamatsu, Y.; Ohwada, H.; Itoh, T.; Moromizato, S.; Kohno, M.; Aoki, S. Photochemical Properties of Red-Emitting Tris(Cyclometalated) Iridium(III) Complexes Having Basic and Nitro Groups and Application to pH Sensing and Photoinduced Cell Death. *Inorg. Chem.* **2015**, *54*, 5342–5357.
16. Cao, R.; Jia, J.; Ma, X.; Zhou, M.; Fei, H. Membrane Localized Iridium(III) Complex Induces Endoplasmic Reticulum Stress and Mitochondria-Mediated Apoptosis in Human Cancer Cells. *J. Med. Chem.* **2013**, *56*, 3636–3644.

17. Wang, W.; Mao, Z.; Wang, M.; Liu, L.-J.; Kwong, D. W. J.; Leung, C.-H.; Ma, D.-L. A Long Lifetime Luminescent Iridium(III) Complex Chemosensor for the Selective Switch-on Detection of Al^{3+} Ions. *Chem. Commun.* **2016**, *52*, 3611–3614.
18. Tamayo, A. B.; Alleyne, B. D.; Djurovich, P. I.; Lamansky, S.; Tsyba, I.; Ho, N. N.; Bau, R.; Thompson, M. E. Synthesis and Characterization of Facial and Meridional Tris-Cyclometalated Iridium(III) Complexes. *J. Am. Chem. Soc.* **2003**, *125*, 7377–7387.
19. Dedeian, K.; Djurovich, P. I.; Garces, F. O.; Carlson, G.; Watts, R. J. A New Synthetic Route to the Preparation of a Series of Strong Photoreducing Agents: Fac-Tris-Ortho-Metalated Complexes of Iridium(III) with Substituted 2-Phenylpyridines. *Inorg. Chem.* **1991**, *30*, 1685–1687.
20. Lowry, M. S.; Bernhard, S. Synthetically Tailored Excited States: Phosphorescent, Cyclometalated Iridium(III) Complexes and Their Applications. *Chem. - Eur. J.* **2006**, *12*, 7970–7977.
21. You, Y.; Park, S. Y. Phosphorescent Iridium(III) Complexes: Toward High Phosphorescence Quantum Efficiency through Ligand Control. *Dalton Trans* **2009**, *8*, 1267–1282.
22. You, Y.; Nam, W. Photofunctional Triplet Excited States of Cyclometalated Ir(III) Complexes: Beyond Electroluminescence. *Chem. Soc. Rev.* **2012**, *41*, 7061–7084.
23. Wong, W.-Y.; Ho, C.-L. Functional Metallophosphors for Effective Charge Carrier Injection/Transport: New Robust OLED Materials with Emerging Applications. *J. Mater. Chem.* **2009**, *19*, 4457–4482.
24. Ulbricht, C.; Beyer, B.; Friebe, C.; Winter, A.; Schubert, U. S. Recent Developments in the Application of Phosphorescent Iridium(III) Complex Systems. *Adv. Mater.* **2009**, *21*, 4418–4441.
25. Sasabe, H.; Kido, J. Multifunctional Materials in High-Performance OLEDs: Challenges for Solid-State Lighting†. *Chem. Mater.* **2011**, *23*, 621–630.
26. Baldo, M. A.; O'Brien, D. F.; You, Y.; Shoustikov, A.; Sibley, S.; Thompson, M. E.; Forrest, S. R. Highly Efficient Phosphorescent Emission from Organic Electroluminescent Devices. *Nature* **1998**, *395*, 151–154.

27. Farinola, G. M.; Ragni, R. Electroluminescent Materials for White Organic Light Emitting Diodes. *Chem. Soc. Rev.* **2011**, *40*, 3467–3482.
28. *Highly Efficient OLEDs with Phosphorescent Materials*; Yersin, H., Ed.; WILEY-VCH: Weinheim, 2008.
29. Ho, M.-L.; Hwang, F.-M.; Chen, P.-N.; Hu, Y.-H.; Cheng, Y.-M.; Chen, K.-S.; Lee, G.-H.; Chi, Y.; Chou, P.-T. Design and Synthesis of Iridium(III) Azacrown Complex: Application as a Highly Sensitive Metal Cation Phosphorescence Sensor. *Org. Biomol. Chem.* **2006**, *4*, 98–103.
30. Konishi, K.; Yamaguchi, H.; Harada, A. Synthesis of a Water-Soluble Iridium(III) Complex with pH and Metal Cation Sensitive Photoluminescence. *Chem. Lett.* **2006**, *35*, 720–721.
31. Schmittel, M.; Lin, H. Luminescent Iridium Phenanthroline Crown Ether Complex for the Detection of Silver(I) Ions in Aqueous Media. *Inorg. Chem.* **2007**, *46*, 9139–9145.
32. Zhao, Q.; Cao, T.; Li, F.; Li, X.; Jing, H.; Yi, T.; Huang, C. A Highly Selective and Multisignaling Optical−Electrochemical Sensor for Hg^{2+} Based on a Phosphorescent Iridium(III) Complex. *Organometallics* **2007**, *26*, 2077–2081.
33. Zhao, Q.; Li, F.; Huang, C. Phosphorescent Chemosensors Based on Heavy-Metal Complexes. *Chem. Soc. Rev.* **2010**, *39*, 3007–3030.
34. Araya, J. C.; Gajardo, J.; Moya, S. A.; Aguirre, P.; Toupet, L.; Williams, J. A. G.; Escadeillas, M.; Le Bozec, H.; Guerchais, V. Modulating the Luminescence of an Iridium(III) Complex Incorporating a Di(2-Picolyl)Anilino-Appended Bipyridine Ligand with Zn^{2+} Cations. *New J Chem* **2010**, *34*, 21–24.
35. Brandel, J.; Sairenji, M.; Ichikawa, K.; Nabeshima, T. Remarkable Mg^{2+}-Selective Emission of an Azacrown Receptor Based on Ir(III) Complex. *Chem. Commun.* **2010**, *46*, 3958–3960.
36. You, Y.; Han, Y.; Lee, Y.-M.; Park, S. Y.; Nam, W.; Lippard, S. J. Phosphorescent Sensor for Robust Quantification of Copper(II) Ion. *J. Am. Chem. Soc.* **2011**, *133*, 11488–11491.

37. Woo, H.; Cho, S.; Han, Y.; Chae, W.-S.; Ahn, D.-R.; You, Y.; Nam, W. Synthetic Control Over Photoinduced Electron Transfer in Phosphorescence Zinc Sensors. *J. Am. Chem. Soc.* **2013**, *135*, 4771–4787.

38. Lu, F.; Yamamura, M.; Nabeshima, T. A Highly Selective and Sensitive Ratiometric Chemodosimeter for Hg^{2+} Ions Based on an Iridium(III) Complex via Thioacetal Deprotection Reaction. *Dalton Trans.* **2013**, *42*, 12093–12100.

39. Tang, Y.; Yang, H.-R.; Sun, H.-B.; Liu, S.-J.; Wang, J.-X.; Zhao, Q.; Liu, X.-M.; Xu, W.-J.; Li, S.-B.; Huang, W. Rational Design of an 'OFF-ON' Phosphorescent Chemodosimeter Based on an Iridium(III) Complex and Its Application for Time-Resolved Luminescent Detection and Bioimaging of Cysteine and Homocysteine. *Chem. - Eur. J.* **2013**, *19*, 1311–1319.

40. Ru, J.-X.; Guan, L.-P.; Tang, X.-L.; Dou, W.; Yao, X.; Chen, W.-M.; Liu, Y.-M.; Zhang, G.-L.; Liu, W.-S.; Meng, Y.; et al. Turn-on Phosphorescent Chemodosimeter for Hg^{2+} Based on a Cyclometalated Ir(III) Complex and Its Application in Time-Resolved Luminescence Assays and Live Cell Imaging. *Inorg. Chem.* **2014**, *53*, 11498–11506.

41. Kang, J. H.; Kim, H. J.; Kwon, T.-H.; Hong, J.-I. Phosphorescent Sensor for Phosphorylated Peptides Based on an Iridium Complex. *J. Org. Chem.* **2014**, *79*, 6000–6005.

42. Maggioni, D.; Galli, M.; D'Alfonso, L.; Inverso, D.; Dozzi, M. V.; Sironi, L.; Iannacone, M.; Collini, M.; Ferruti, P.; Ranucci, E.; et al. A Luminescent Poly(Amidoamine)–Iridium Complex as a New Singlet-Oxygen Sensitizer for Photodynamic Therapy. *Inorg. Chem.* **2015**, *54*, 544–553.

43. Xue, F.; Lu, Y.; Zhou, Z.; Shi, M.; Yan, Y.; Yang, H.; Yang, S. Two in One: Luminescence Imaging and 730 Nm Continuous Wave Laser Driven Photodynamic Therapy of Iridium Complexes. *Organometallics* **2015**, *34*, 73–77.

44. Ye, R.-R.; Tan, C.-P.; He, L.; Chen, M.-H.; Ji, L.-N.; Mao, Z.-W. Cyclometalated Ir(III) Complexes as Targeted Theranostic Anticancer Therapeutics: Combining HDAC Inhibition with Photodynamic Therapy. *Chem. Commun.* **2014**, *50*, 10945–10948.

45. Ashen-Garry, D.; Selke, M. Singlet Oxygen Generation by Cyclometalated Complexes and Applications. *Photochem. Photobiol.* **2014**, *90*, 257–274.

46. Li, S. P.-Y.; Lau, C. T.-S.; Louie, M.-W.; Lam, Y.-W.; Cheng, S. H.; Lo, K. K.-W. Mitochondria-Targeting Cyclometalated Iridium(III)–PEG Complexes with Tunable Photodynamic Activity. *Biomaterials* **2013**, *34*, 7519–7532.

47. Takizawa, S.; Aboshi, R.; Murata, S. Photooxidation of 1,5-Dihydroxynaphthalene with Iridium Complexes as Singlet Oxygen Sensitizers. *Photochem. Photobiol. Sci.* **2011**, *10*, 895–903.

48. Djurovich, P. I.; Murphy, D.; Thompson, M. E.; Hernandez, B.; Gao, R.; Hunt, P. L.; Selke, M. Cyclometalated Iridium and Platinum Complexes as Singlet Oxygen Photosensitizers: Quantum Yields, Quenching Rates and Correlation with Electronic Structures. *Dalton Trans.* **2007**, *34*, 3763–3770.

49. Gao, R.; Ho, D. G.; Hernandez, B.; Selke, M.; Murphy, D.; Djurovich, P. I.; Thompson, M. E. Bis-Cyclometalated Ir(III) Complexes as Efficient Singlet Oxygen Sensitizers. *J. Am. Chem. Soc.* **2002**, *124*, 14828–14829.

50. Rachford, A. A.; Ziessel, R.; Bura, T.; Retailleau, P.; Castellano, F. N. Boron Dipyrromethene (Bodipy) Phosphorescence Revealed in $[Ir(Ppy)_2(Bpy\text{-}C{\equiv}C\text{-}Bodipy)]^+$. *Inorg. Chem.* **2010**, *49*, 3730–3736.

51. Sun, J.; Zhong, F.; Yi, X.; Zhao, J. Efficient Enhancement of the Visible-Light Absorption of Cyclometalated Ir(III) Complexes Triplet Photosensitizers with Bodipy and Applications in Photooxidation and Triplet–Triplet Annihilation Upconversion. *Inorg. Chem.* **2013**, *52*, 6299–6310.

52. Majumdar, P.; Yuan, X.; Li, S.; Le Guennic, B.; Ma, J.; Zhang, C.; Jacquemin, D.; Zhao, J. Cyclometalated Ir(III) Complexes with Styryl-BODIPY Ligands Showing near IR Absorption/Emission: Preparation, Study of Photophysical Properties and Application as Photodynamic/Luminescence Imaging Materials. *J Mater Chem B* **2014**, *2*, 2838–2854.

53. Wang, J.; Lu, Y.; McGoldrick, N.; Zhang, C.; Yang, W.; Zhao, J.; Draper, S. M. Dual Phosphorescent Dinuclear Transition Metal Complexes, and Their

Application as Triplet Photosensitizers for TTA Upconversion and Photodynamic Therapy. *J. Mater. Chem. C* **2016**, *4*, 6131–6139.

54. Palao, E.; Sola-Llano, R.; Tabero, A.; Manzano, H.; Agarrabeitia, A. R.; Villanueva, A.; López-Arbeloa, I.; Martínez-Martínez, V.; Ortiz, M. J. Acetylacetonate BODIPY-Biscyclometalated Iridium(III) Complexes: Effective Strategy towards Smarter Fluorescent Photosensitizer Agents. *Chem. - Eur. J.* **2017**, *23*, 10139–10147.
55. Tabrizi, L.; Chiniforoshan, H. New Cyclometalated Ir(III) Complexes with NCN Pincer and Meso-Phenylcyanamide BODIPY Ligands as Efficient Photodynamic Therapy Agents. *RSC Adv.* **2017**, *7*, 34160–34169.
56. Bröring, M.; Krüger, R.; Link, S.; Kleeberg, C.; Köhler, S.; Xie, X.; Ventura, B.; Flamigni, L. Bis(BF_2)-2,2′-Bidipyrrins (BisBODIPYs): Highly Fluorescent BODIPY Dimers with Large Stokes Shifts. *Chem. - Eur. J.* **2008**, *14*, 2976–2983.
57. Xu, J.; Sun, S.; Li, Q.; Yue, Y.; Li, Y.; Shao, S. A Rapid Response 'Turn-On' Fluorescent Probe for Nitroreductase Detection and Its Application in Hypoxic Tumor Cell Imaging. *The Analyst* **2015**, *140*, 574–581.
58. Erten-Ela, S.; Yilmaz, M. D.; Icli, B.; Dede, Y.; Icli, S.; Akkaya, E. U. A Panchromatic Boradiazaindacene (BODIPY) Sensitizer for Dye-Sensitized Solar Cells. *Org. Lett.* **2008**, *10*, 3299–3302.
59. Flavin, K.; Lawrence, K.; Bartelmess, J.; Tasior, M.; Navio, C.; Bittencourt, C.; O'Shea, D. F.; Guldi, D. M.; Giordani, S. Synthesis and Characterization of Boron Azadipyrromethene Single-Wall Carbon Nanotube Electron Donor−Acceptor Conjugates. *ACS Nano* **2011**, *5*, 1198–1206.
60. Bartelmess, J.; Weare, W. W.; Latortue, N.; Duong, C.; Jones, D. S. Meso-Pyridyl BODIPYs with Tunable Chemical, Optical and Electrochemical Properties. *New J. Chem.* **2013**, *37*, 2663–2668.
61. Bartelmess, J.; Weare, W. W. Preparation and Characterization of Multi-Cationic BODIPYs and Their Synthetically Versatile Precursors. *Dyes Pigments* **2013**, *97*, 1–8.

62. Choung, K. S.; Teets, T. S. Lewis Acid Modulation of Meso-Pyridyl BODIPY Chromophores. *ChemPhotoChem* **2019**, *3*, 86–92.

63. Chong, H.; Fron, E.; Liu, Z.; Boodts, S.; Thomas, J.; Harvey, J. N.; Hofkens, J.; Dehaen, W.; Van der Auweraer, M.; Smet, M. Acid-Sensitive BODIPY Dyes: Synthesis through Pd-Catalyzed Direct C(Sp^3)−H Arylation and Photophysics. *Chem. - Eur. J.* **2017**, *23*, 4687–4699.

64. Maity, A.; Kölsch, J. C.; Na, H.; Teets, T. S. Room Temperature Transmetallation from Tris(Pentafluorophenyl)Borane to Cyclometallated Iridium(III). *Dalton Trans.* **2017**, *46*, 11757–11767.

65. Sheldrick, G. M. A Short History of *SHELX*. *Acta Crystallogr. A* **2008**, *64*, 112–122.

66. Spek, A. L. Structure Validation in Chemical Crystallography. *Acta Crystallogr. D Biol. Crystallogr.* **2009**, *65*, 148–155.

67. Maity, A.; Le, L. Q.; Zhu, Z.; Bao, J.; Teets, T. S. Steric and Electronic Influence of Aryl Isocyanides on the Properties of Iridium(III) Cyclometalates. *Inorg. Chem.* **2016**, *55*, 2299–2308.

68. Na, H.; Maity, A.; Teets, T. S. Bis-Cyclometalated Iridium Complexes with Electronically Modified Aryl Isocyanide Ancillary Ligands. *Dalton Trans.* **2017**, *46*, 5008–5016.

69. Valeur, B. *Molecular Fluorescence: Principles and Applications*; Wiley-VCH: Weinheim; New York, 2002.

70. Turro, N. J.; Ramamurthy, V.; Scaiano, J. C. *Modern Molecular Photochemistry of Organic Molecules*; University Science Books: Sausalito, Calif, 2010.

71. Sato, T.; Hamada, Y.; Sumikawa, M.; Araki, S.; Yamamoto, H. Solubility of Oxygen in Organic Solvents and Calculation of the Hansen Solubility Parameters of Oxygen. *Ind. Eng. Chem. Res.* **2014**, *53*, 19331–19337.

72. Mik, E. G.; Stap, J.; Sinaasappel, M.; Beek, J. F.; Aten, J. A.; van Leeuwen, T. G.; Ince, C. Mitochondrial pO_2 Measured by Delayed Fluorescence of Endogenous Protoporphyrin IX. *Nat. Methods* **2006**, *3*, 939–945.

73. Helmlinger, G.; Yuan, F.; Dellian, M.; Jain, R. K. Interstitial $_{P}$H and pO_2 Gradients in Solid Tumors in Vivo: High-Resolution Measurements Reveal a Lack of Correlation. *Nat. Med.* **1997**, *3*, 177–182.

74. Finikova, O. S.; Lebedev, A. Y.; Aprelev, A.; Troxler, T.; Gao, F.; Garnacho, C.; Muro, S.; Hochstrasser, R. M.; Vinogradov, S. A. Oxygen Microscopy by Two-Photon-Excited Phosphorescence. *ChemPhysChem* **2008**, *9*, 1673–1679.

Chapter 4. NHC Iridium(III) Pincer Complexes for Alkane Dehydrogenation

4.1. Introduction

Alkanes are a major fraction of naturally occurring petroleum resources, and are also significant products in catalytic cracking and Fischer-Tropsch synthesis. Whereas certain alkane fractions, particularly those with $C_{n>4}$ are valuable as transportation fuels (gasoline, diesel, and jet fuel), lighter fractions are frequently burned during the extraction or refining processes.

Catalytic C–H bond activation of alkanes is a central challenge in organometallic chemistry. The dehydrogenation of alkanes is one of the most important applications in industry because the resulting alkenes can be useful resources for commodity chemicals. The development of methodologies for C–H bond catalyzed by transition-metal complexes has expanded in the past 16 years.[1] Moreover, chemical transformations which could selectively upgrade these alkanes into value-added products would be both economically and environmentally beneficial.

Many well-known homogeneous catalysts for alkane dehydrogenation and other C–H activation schemes involve tridentate ligands known as "pincer" ligands. Since the seminal reports by Shaw and co-workers in the mid-1970s,[2] the chemistry of pincer ligated metal complexes has been developed and applied to a variety of fields ranging from stoichiometric and catalytic chemical transformation to sensors, switches, and supramolecular chemistry. The term pincer ligand was used in Van Koten's paper[3] in 2001 and referred to species of the form 2,6-*E*$CH_2C_6H_3$, where *E* is a neutral two electron donor.

To be specific, tertiary phosphines (E = PR_2) are the most common donor groups, giving PCP pincer ligands. Usage of the term pincer[4] has broadened in recent years to include other ligand types (see **Figure 4.1**).

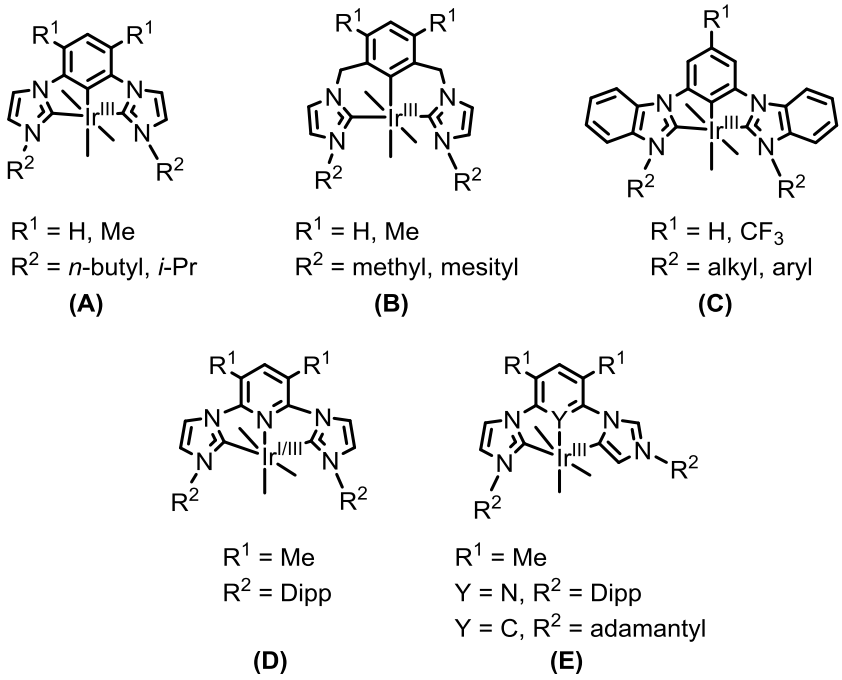

Figure 4.1. Various Pincer NHC complexes with 2,6-disubstituted benzene-1-ide backbone and pyridine backbone.

The pincer ligand has proven to be especially useful for C–H bond activation and functionalization reactions catalyzed by iridium. Iridium PCP-pincer complexes[5] can be active as catalysts for the dehydrogenation of alkanes either with or without a hydrogen acceptor,[6] and iridium PCP and PNP pincer complexes have been introduced as homogeneous catalysts for the dehydrogenation of alkanes[7], alkane metathesis[8], and amine borane dehydrogenation,[9] among other catalytic applications with the most well-known catalysts utilizing electron-rich, air-sensitive supporting ligands and requiring intermediacy of a reactive 14-electron Ir(I) species. It may be possible that replacement of

the P-donor moiety in phosphine-based pincer ligands with *N*-heterocyclic carbene (NHC) donors will improve thermal and oxidative stability of iridium catalysts in high-temperature alkane dehydrogenation reactions, with recent precedents showing that iridium(III) complexes with aerobically stable pincer ligands can promote stoichiometric alkane dehydrogenation in the presence of oxygen.[10–12]

The currently known structural frameworks of $C_{NHC}CC_{NHC}$ and $C_{NHC}NC_{NHC}$ pincer iridium complexes are shown in **Figure 4.1**. Also, the alternative ligands with methyl substitution at the 3- and 5-positions of the central arene were developed to suppress cyclometallation side reactions.[13] Other *N*-heterocyclic carbene-based pincers currently being used as robust supporting ligands for catalysts include CNC[14], CNN[15], PCP[16], SCS[17], and CSC[18] types. Due to the utility of the PCP motif an analogous framework with a CCC motif can be an attractive target molecule as a catalyst for dehydrogenation of alkanes. Two classes of most reported CCC-pincer complexes are shown in **Figure 4.2**.

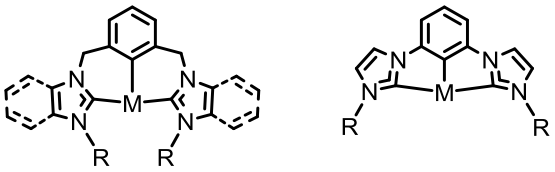

Figure 4.2. Known CCC ligand classes.

In class **A**, the central aryl fragment is connected to two benzimidazole- or imidazole-based *N*-heterocyclic carbenes through CH_2 linkers. These ligands form two six-membered and boat-shaped chelate rings.[19] The Cui group reported the preparation of the xylene-bridged CCC-pincer complexes based on various rare-earth metal centers.[20] Goldberg and Heinekey prepared iridium pincer complexes of the form $(CCC^{Mes})IrCl_2$

containing methylene bridges.[21] In class **B**, this pincer complex has no CH_2 linker, which is expected to be a rigid, flat backbone with two five-membered chelate rings. Hollis and co-workers initially prepared class **B** ligand as precursors[22] and later reported their metalation to zirconium.[23] Also, they described transmetalation from zirconium to rhodium[24] and iridium[25], and catalytic applications including hydrosilylation[26] and hydroamination[25]. The groups of Chianese[19] and Braunstein[27] have reported the metalation of class **B** ligands from imidazolium salt precursors directly to iridium, by refluxing with $[Ir(COD)Cl]_2$, Cs_2CO_3, and KI in acetonitrile. The resulting octahedral complexes of the formula Ir(CCC)(H)(I)(MeCN) were isolated in good yield. These pincer complexes are similar to five-coordinate Ir(PCP)(H)(Cl) complexes that have already been known to form active catalysts for dehydrogenation of alkane and can be expected to do reactivity similarly.

This chapter describes iridium precatalysts with *N*-heterocyclic carbene (NHC) pincer ligands, which are strongly coordinating, oxidatively robust, and thermally stable supporting ligands. These complexes are targeted as next-generation iridium(III) catalysts which can promote aerobic functionalization of alkanes. Specifically, we describe the synthesis of robust and rigid CCC- and CNC-pincer ligands with *n*-butyl or mesityl substituents and pincer complexes of the types $Ir(C^{n\text{-}Bu}CC^{n\text{-}Bu})(X)(I)(MeCN)$ (X = H, I) and $Ir(C^{R}NC^{R})(Cl)$ (R = *n*-butyl, mesityl). We also examined their reactivity for the dehydrogenation of cyclooctane to cyclootene. Initial experiments using $Ir(CCC)(I)_2(MeCN)$ indicate that this iridium pincer complex can be active as a catalyst for the dehydrogenation of cyclooctane.

4.2. Experimental Section

4.2.1. Materials and Physical Methods.

Dry solvents were obtained from a Grubbs Solvent Purification System and degassed with argon. Starting materials and reagents, unless otherwise specified, were obtained from commercial sources and used without further purification. [$IrI_2{}^{n\text{-}Bu}(C_{NHC}CC_{NHC})(NCMe)$] types of iridium pincer complexes[27] were prepared with a previously described the literature procedure. Bis(imidazolium) pyridine derivatives dibromide compounds were prepared by known synthetic procedures.[28] ^{1}H NMR spectra were recorded at room temperature using a JEOL ECA-400.

4.2.2. Synthesis of phenyl bis(imidazolium) carbene precursor ($C_{NHC}CC_{NHC}$ type).

Synthesis of 1,5-dibromo-2,4-dimethylbenzene (1b). To an ice-cooled solution of iodine (0.10 g, 0.4 mmol) in neat *m*-xylene (10 mL, 0.8 mol) was added bromine (27.3 g, 0.17 mol) dropwise over 2 h in the absence of light. After 16 h at room temperature, 20% aqueous KOH (100 mL) was added. The mixture was shaken under slight warming until the disappearance of the yellow color and was then allowed to cool. The aqueous layer was decanted, and the remaining solids were washed with water to give a white solid. Yield: 15.1 g (72%). ^{1}H NMR (400 MHz, $CDCl_3$) δ: 7.67 (s, 1H, Ar*H*), 7.10 (s, 1H, Ar*H*), 2.30 (s, 6H, CH_3).

4.2.3. General synthetic procedure for bis(imidazolyl) benzene derivatives 2a and 2b.

A mixture of 1,3-dibromobenzene derivatives (1 equiv.), imidazole (2.5 equiv.), K_2CO_3 (2.5 equiv.), CuO (25 mol%), and DMSO (20 mL). The solution was heated at 150 °C for 48 h. The reaction was cooled, and the DMSO was evaporated in vacuo, giving

a white solid. The residue was purified by column chromatography on silica gel eluting with 10:1 (v:v) CH_2Cl_2/MeOH.

1,3-Bis(imidazolyl) Benzene (2a). Prepared by the general procedure using 1,3-dibromobenzene (2.5 g, 21 mmol), imidazole (3.5 g, 52 mmol), K_2CO_3 (7.2 g, 52 mmol), and CuO (0.4 g, 5.2 mmol). Yield: 3.3 g (77%). ^{1}H NMR (400 MHz, $CDCl_3$) δ: 7.91 (s, 2H, imidazole *H*), 7.61 (t, *J* = 8.2 Hz, 1H, Ar*H*), 7.42 (s, 2H, Ar*H*), 7.40 (s, 1H, Ar*H*), 7.33 (t, *J* = 1.3 Hz, 2H, imidazole *H*), 7.25 (d, *J* = 3.4 Hz, 2H, imidazole *H*).

1,3-Bis(imidazolyl)-4,6-dimethylbenzene (2b). Prepared by the general procedure using 1,5-dibromo-2,4-dimethylbenzene (5.0 g, 21 mmol), imidazole (3.5 g, 52 mmol), K_2CO_3 (7.2 g, 52 mmol), and CuO (0.4 g, 5.2 mmol). Yield: 2.2 g (48%). ^{1}H NMR (400 MHz, $CDCl_3$) δ: 7.58 (s, 2H, imidazole *H*), 7.31 (s, 1H, Ar*H*), 7.20 (s, 2H, imidazole *H*), 7.14 (s, 1H, Ar*H*), 7.05 (s, 2H, imidazole *H*), 2.21 (s, 6H, CH_3).

4.2.4. General synthetic procedure for bis(imidazolium) benzene salts 3a and 3b.

1,3-Bis-(imidazolyl) benzene derivatives (1 equiv.), butyl iodide (20 equiv.) and MeCN (50 mL) were combined. The resulting mixture was stirred at reflux overnight. After cooling to room temperature, the reaction mixture was concentrated in vacuo to get product.

1,3-Bis(3-butylimidazolium-1-yl)benzene diiodide (3a). Prepared by the general procedure using 1,3-bis-(imidazolyl) benzene (1.1 g, 5.0 mmol) and butyl iodide (11.3 mL, 99.0 mmol). Yield: 2.8 g (99%). ^{1}H NMR (400 MHz, $CDCl_3$) δ: 11.13 (s, 2H, imidazolium *H*), 8.91 (t, *J* = 2.1 Hz, 1H, Ar*H*), 8.74 (t, *J* = 1.8 Hz, 2H, imidazolium *H*), 8.29 (dd, *J* = 8.3, 2.1 Hz, 2H, Ar*H*), 7.77 (t, *J* = 8.3 Hz, 1H, Ar*H*), 7.49 (t, *J* = 1.7 Hz, 2H, imidazolium *H*), 4.47 (t, *J* = 7.4 Hz, 4H, CH_2), 2.11 – 1.59 (m, 4H, CH_2), 1.46 (dq, *J* = 14.8, 7.4 Hz, 4H, CH_2), 1.01 (t, *J* = 7.4 Hz, 6H, CH_3).

(4,6-Dimethyl-1,3-phenylene)bis(1-butylimidazolium) diiodide (3b). Prepared by the general procedure using 1,3-bis(imidazolyl)-4,6-dimethylbenzene (1.0 g, 4.0 mmol) and butyl iodide (10.2 mL, 90.0 mmol). Yield: 2.8 g (99%). ^{1}H NMR (400 MHz, $CDCl_3$) δ: 10.57 (s, 2H, imidazolium *H*), 8.13 (d, J = 1.7 Hz, 2H, imidazolium *H*), 8.02 (s, 1H, Ar*H*), 7.58 (d, J = 1.7 Hz, 2H, imidazolium *H*), 7.46 (s, 1H, Ar*H*), 4.45 (t, J = 7.4 Hz, 4H, CH_2), 2.40 (s, 6H, ArCH_3), 2.14 – 1.89 (m, 4H, CH_2), 1.44 (dq, J = 14.8, 7.4 Hz, 4H, CH_2), 1.00 (t, J = 7.4 Hz, 6H, CH_3).

4.2.5. General synthetic procedure for Iridium(III) pincer monohydride complexes 4a and 4b.

A mixture of (1,3-phenylene)bis(1-butylimidazolium) diiodide (2.0 equiv.), $[Ir(COD)Cl]_2$ (1.0 equiv.), and Cs_2CO_3 (4.4 equiv.) in MeCN (20 mL) was refluxed under argon gas for 18 h. The resulting orange suspension was filtered, and the solvent was removed in vacuo. The solid residue was dissolved in approximately acetonitrile (2 mL) and diethyl ether (10 mL) was added dropwise until the desired product precipitated as a pale yellow solid.

(1,3-Phenylene-κC^2)bis(1-butylimidazol-2-ylidene)(acetonitrile)(hydrido)(iodo)iridium(III), [Ir(H)(I)($^{n\text{-Bu}}$-($C_{NHC}CC_{NHC}$)(NCMe)] (4a). Prepared by the general procedure using complex **3a** (0.35 g, 0.60 mmol), $[Ir(COD)Cl]_2$ (0.20 g, 0.30 mmol), and Cs_2CO_3 (0.45 g, 1.32 mml). Yield: 0.31 g (68%). ^{1}H NMR (400 MHz, CD_3CN) δ: 7.69 (d, J = 2.1 Hz, 2H, imidazolium *H*), 7.23 (d, J = 2.0 Hz, 2H, imidazolium *H*), 7.14 (d, J = 7.8 Hz, 2H, Ar*H*), 6.91 (d, J = 3.1 Hz, 1H, Ar*H*), 4.37 (t, J = 7.3 Hz, 4H, CH_2), 1.92 (dt, J = 5.1, 2.5 Hz, 4H, CH_2), 1.46 – 1.40 (m, 4H, CH_2), 0.98 (t, J = 7.4 Hz, 6H, CH_3), –22.71 (s, 1H, Ir–*H*). The CH_3CN ligand is displaced by CD_3CN.

(4,6-Dimethyl-1,3-phenylene-κC^2)bis(1-butylimidazol-2-ylidene)(acetonitrile)(hydrido)(iodo)iridium(III), [Ir(H)(I)($^{n\text{-Bu}}$)($C_{NHC}^{Me}CC_{NHC}$)(NCMe)] (4b). Prepared by the general procedure using complex **3b** (0.40 g, 0.60 mmol), $[Ir(COD)Cl]_2$ (0.20 g, 0.30 mmol), and Cs_2CO_3 (0.45 g, 1.32 mmol). Yield: 0.38 g (81%). ^{1}H NMR (400 MHz, CD_3CN) δ: 7.85 (d, *J* = 2.4 Hz, 2H, imidazolium *H*), 7.21 (d, *J* = 2.3 Hz, 2H, imidazolium *H*), 6.44 (s, 1H, Ar*H*), 4.36 (t, *J* = 7.3 Hz, 4H, CH_2), 2.69 (s, 6H, ArCH_3), 2.09 – 2.00 (m, 4H, CH_2), 1.47 – 1.37 (m, 4H, CH_2), 0.98 (t, *J* = 7.3 Hz, 6H, CH_3), –22.60 (s, 1H, Ir–*H*). The CH_3CN ligand is displaced by CD_3CN.

4.2.6. General synthetic procedure for Iridium(III) pincer diiodide complexes 5a and 5b.

Iridum(III) pincer monohydride complexes (1 equiv.) and $[HNEt_3]^+I^-$ (11 equiv.) were refluxed in MeCN (15 mL) for 18 h. The reaction mixture was then allowed to cool to room temperature and the solvent was removed in vacuo. The crude solid was triturated with deionized water (15 mL), washed with diethyl ether (10 mL) and dried overnight under vacuum.

(1,3-Phenylene-κC^2)bis(1-butylimidazol-2-ylidene)(acetonitrile)bis(iodo)iridium(III), [IrI_2($^{n\text{-Bu}}$)($C_{NHC}CC_{NHC}$)(NCMe)] (5a). Prepared by the general procedure using complex **4a** (0.03 g, 0.04 mmol) and $[HNEt_3]^+I^-$ (0.10 g, 0.44 mmol). Yield: 0.02 g (68%). ^{1}H NMR (400 MHz, CD_3CN) δ: 7.69 (d, *J* = 2.1 Hz, 2H, imidazolium *H*), 7.23 (d, *J* = 2.0 Hz, 2H, imidazolium *H*), 7.14 (d, *J* = 7.8 Hz, 2H, Ar*H*), 6.90 (d, *J* = 8.0 Hz, 1H, Ar*H*), 4.36 (t, *J* = 7.3 Hz, 4H, CH_2), 2.05 (dt, *J* = 15.1, 7.6 Hz, 4H, CH_2), 1.43 (dq, *J* = 14.9, 7.4 Hz, 4H, CH_2), 0.98 (t, *J* = 7.4 Hz, 6H, CH_3). The CH_3CN ligand is displaced by CD_3CN.

(4,6-Dimethyl-1,3-phenylene-κC^2)bis(1-butylimidazol-2-ylidene)(acetonitrile)bis(iodo)iridium(III), [$IrI_2{}^{n\text{-}Bu}(C_{NHC}{}^{Me}CC_{NHC})(NCMe)$] (5b). Prepared by the general procedure using complex **4b** (0.03 g, 0.04 mmol) and $[HNEt_3]^+I^-$ (0.10 g, 0.44 mmol). Yield: 0.02 g (76%). ^{1}H NMR (400 MHz, CD_3CN) δ: 7.85 (s, 2H, imidazolium *H*), 7.20 (s, 2H, imidazolium *H*), 6.44 (s, 1H, Ar*H*), 4.36 (t, J = 7.3 Hz, 4H, CH_2), 2.55 (s, 6H, ArCH_3), 2.07 – 2.00 (m, 4H, CH_2), 1.43 (dt, J = 14.7, 7.3 Hz, 4H, CH_2), 0.97 (t, J = 7.3 Hz, 6H, CH_3). The CH_3CN ligand is displaced by CD_3CN.

4.2.7. Synthesis of pyridyl bis(imidazolium) carbene precursor ($C_{NHC}NC_{NHC}$ type).

Synthesis of 1-(2,4,6-Trimethylphenyl)-1H-imidazole (6b). A mixture of glacial acetic acid (10 mL), 37% aqueous formaldehyde (3 mL) and 37% aqueous glyoxal (4.6 mL) was heated to 70 °C. A solution of 2,4,6-trimethylaniline (5.4 g, 40.0 mmol), ammonium acetate (3.1 g, 40.0 mmol) in 2 mL water and glacial acetic acid (10 mL) was added dropwise after which the reaction mixture was heated at 70 °C for 18 hours. After cooling to room temperature the resulting brown solution was added very slowly to a stirred solution of 29.4 g $NaHCO_3$ in 300 mL water. Brownish solid was precipitated and filtered. Yield: 5.2 g (70%). ^{1}H NMR (400 MHz, $CDCl_3$) δ: 7.43 (s, 1H, imidazole *H*), 7.22 (s, 1H, imidazole *H*), 6.96 (s, 2H, Ar*H*), 6.88 (s, 1H, imidazole *H*), 2.33 (s, 3H, CH_3), 1.98 (s, 6H, CH_3).

4.2.8. General synthetic procedure for bis(imidazolium) pyridine derivatives salts 7a and 7b.

A sealed glass ampule immersed in an oil bath containing a mixture of 2,6-dibromopyridine (1.0 equiv.) and imidazole derivatives (2.5 equiv.) was heated to 150 °C for 5 days. After cooling to room temperature, the brown residue was triturated with Et_2O (15 mL) and filtered. The resulting light brown solid was stirred overnight in Et_2O (300

mL) to remove soluble impurities. The remaining solid was isolated via vacuum filtration to afford the product.

2,6-Bis[(3-butyl)imidazolium]pyridine dibromide (7a). Prepared by the general procedure using 2,6-dibromopyridine (1.5 g, 6.3 mmol) and 1-(butyl)imidazole (2.2 g, 15.8 mmol). Yield: 2.2 g (94%). ^{1}H NMR (400 MHz, $CDCl_3$) δ: 11.92 (s, 2H, imidazolium *H*), 9.28 (s, 2H, imidazolium *H*), 8.78 (d, *J* = 7.9 Hz, 2H, Ar*H*), 8.29 (t, *J* = 7.9 Hz, 1H, Ar*H*), 7.54 (s, 2H, imidazolium *H*), 4.60 (t, *J* = 7.2 Hz, 4H, CH_2), 2.00 (dt, *J* = 15.0, 7.4 Hz, 4H, CH_2), 1.44 (dq, *J* = 14.7, 7.4 Hz, 4H, CH_2), 0.98 (t, *J* = 7.3 Hz, 6H, CH_3).

2,6-Bis[(3-mesityl)imidazolium]pyridine dibromide (7b). Prepared by the general procedure using 2,6-dibromopyridine (1.5 g, 6.3 mmol) and 1-(mesityl)imidazole (2.9 g, 15.8 mmol). Yield: 3.7 g (95%). ^{1}H NMR (400 MHz, $CDCl_3$) δ: 11.89 (s, 2H, imidazolium *H*), 9.85 (s, 2H, imidazolium *H*), 9.10 (d, *J* = 8.1 Hz, 2H, Ar*H*), 8.24 (t, *J* = 8.1 Hz, 1H, Ar*H*), 7.31 (t, *J* = 1.7 Hz, 2H, imidazolium *H*), 7.00 (s, 4H, Mesityl Ar*H*), 2.31 (s, 6H, Mesityl CH_3), 2.16 (s, 12H, Mesityl CH_3).

4.2.9. General synthetic procedure for Iridium(I) pincer chloride complexes 9a and 9b.

The respective (1,3-pyridylene)bis(imidazolium) dibromide (1.0 equiv.) was suspended in THF (10 mL) in a schlenk flask, and cooled to –78 °C. A solution of potassium bis(trimethylsilyl)amide (KHMDS) (2.2 equiv.) in THF (2 mL) was cooled to –78 °C and added to the salt suspension. The reaction mixture was warmed to room temperature overnight, the solvent evaporated and the residue dissolved in toluene (10 mL). The dark-brown solution was filtered through a Celite, and the volume reduced by vacuum pump. And suspension of $[Ir(COE)_2Cl]_2$ (0.5 equiv.) in THF (5 mL) was added to the

Schlenk flask which contained the carbene ligand. The resulting suspension was stirred for 18 h, and the solvent was removed in vacuo. The crude product was dissolved in acetonitrile (5 mL) and filtered through a Celite. The filtrate was concentrated in vacuo and washed with hexane, affording the desired product.

(1,3-Pyridylene-κC^2)bis(1-butylimidazol-2-ylidene)(iodo)iridium(I), [IrCl$^{n\text{-Bu}}$(C_{NHC}-NC$_{NHC}$)] (9a). Prepared by the general procedure using bis(imidazolium) salt (*n*-butyl)($C_{NHC}NC_{NHC}$)Br_2 (50 mg, 0.10 mmol), KHMDS (43 mg, 0.22 mmol), and $[Ir(COE)_2Cl]_2$ (25 mg, 0.05 mmol). Yield: 8.3 mg (15%). ^{1}H NMR (400 MHz, CD_3CN) δ: 8.20 (d, J = 8.1 Hz, 2H, Ar*H*), 7.89 – 7.84 (m, 1H, Ar*H*), 7.34 (d, J = 3.2 Hz, 2H, , imidazolium *H*), 6.51 (d, J = 3.2 Hz, 2H, , imidazolium *H*), 3.59 (t, J = 7.1 Hz, 4H, CH_2), 1.63 (dt, J = 14.6, 7.3 Hz, 4H, CH_2), 1.37 – 1.27 (m, 4H, CH_2), 0.91 (t, J = 7.4 Hz, 6H, CH_3).

(1,3-Pyridylene-κC^2)bis(1-mesitylimidazol-2-ylidene)(iodo)iridium(I), [IrCl^{Mes}(C_{NHC}-NC$_{NHC}$)] (9b). Prepared by the general procedure using bis(imidazolium) salt (mesityl)($C_{NHC}NC_{NHC}$)Br_2 (68 mg, 0.10 mmol), KHMDS (43 mg, 0.22 mmol), and $[Ir(COE)_2Cl]_2$ (25 mg, 0.05 mmol). Yield: 14.2 mg (21%). ^{1}H NMR (500 MHz, CD_3CN) δ: 8.19 (d, J = 8.2 Hz, 2H, Ar*H*), 7.92 (t, J = 8.0 Hz, 1H, Ar*H*), 7.18 (s, 4H, Mesityl Ar*H*), 7.03 (s, 2H, imidazolium *H*), 6.87 (s, 2H, imidazolium *H*), 2.21 (s, 6H, Mesityl CH_3), 2.11 (s, 12H, Mesityl CH_3).

4.2.10. General procedure for catalytic dehydrogenation of cyclooctane.

In a nitrogen-filled glovebox, a 15 mL high-pressure screw-cap tube was charged with CCC/CNC-iridium pincer complexes (2 mol%), 0.1 mL of cyclooctane, and a stir-bar. The tube was capped, and then brought out from the glovebox. The mixture was stirred and

heated to 200 ℃ for reaction time. After the mixture was cooled to room temperature, mesitylene (140 μL, 1.00 mmol) as an internal standard was added to the reaction mixture in $CDCl_3$. Cyclooctene and unconsumed cyclooctane were quantified by integrating the ^1H NMR signals against the standard of mesitylene.

4.3. Results and Discussion

4.3.1. Synthesis of $C_{NHC}CC_{NHC}$ precursor ligands and iridium pincer complexes.

Scheme 4.1. Synthesis of bis(imidazolium) benzene derivatives salts **3a**, **3b**.

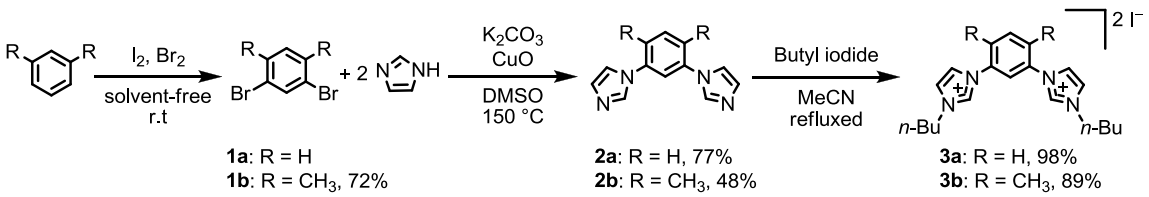

In this work, we have targeted precatalysts with N-heterocyclic carbene (NHC) pincer ligands, which are oxidatively robust, thermally stable, and easy to synthetically modify. Synthesis of the *n*-butyl-substituted CCC-pincer ligand precursors **3a**, **3b** was achieved as shown in **Scheme 4.1**. Initial electrophilic bromination of *m*-xylene using the method of Schlüter smoothly afforded the dibromoxylene **1b**;[29] whereas **1a** is commercially available. 1,3-di-*N*-imidazolylbenzene derivatives **2a** and **2b** were then prepared. In order to get high yield we used an one-step synthesis from 1,3-dibromobenzene and imidazole to the bis(imidazolium) salts with copper oxide catalyst and potassium carbonate base. The reaction is based on precedent from the preparation of the **2a** analogue.[30] The imidazolium salts were prepared by combining the bis(imidazole) **2a**/**2b** with 1-iodobutane and heating as outlined in **Scheme 4.1**.[31] These facile syntheses

provided efficient access to the requisite imidazolium salt **3a**, **3b** and are amenable to combinatorial synthesis of carbene ligands.

Scheme 4.2. Synthesis of iridium CCC-*N*- heterocyclic carbene pincer complexes **4a**, **4b**, **5a**, and **5b**.

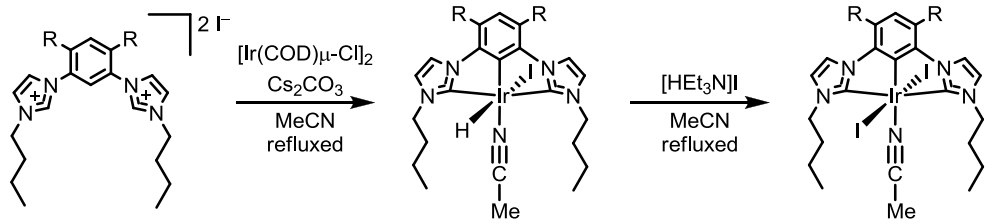

3a: R = H
3b: R = CH_3

4a: R = H, 68%
4b: R = CH_3, 81%

5a: R = H, 68%
5b: R = CH_3, 76%

The use of excess amount of Cs_2CO_3 as a base in the reaction of **3a**, **3b** with $[Ir(COD)(\mu\text{-}Cl)]_2$ (COD = cyclooctadiene) gave a crude product of the iridium(III) $C_{NHC}CC_{NHC}$ pincer hydride compounds **4a**, **4b** via three based-promoted C–H addition reactions.[27] To purify the crude products recrystallization was done with MeCN/Et_2O, which afforded pure **4a** and **4b** in good yield (**Scheme 4.2**). The next step is conversion of monohydride to diiodide substituted iridium pincer complexes which can serve as precatalysts for dehydrogenation of cylcooctane.

4.3.2. Synthesis of $C_{NHC}NC_{NHC}$ precursor ligands and iridium pincer complexes.

Scheme 4.3. Synthesis of bis(imidazolium) pyridine derivatives salts **7a**, **7b**.

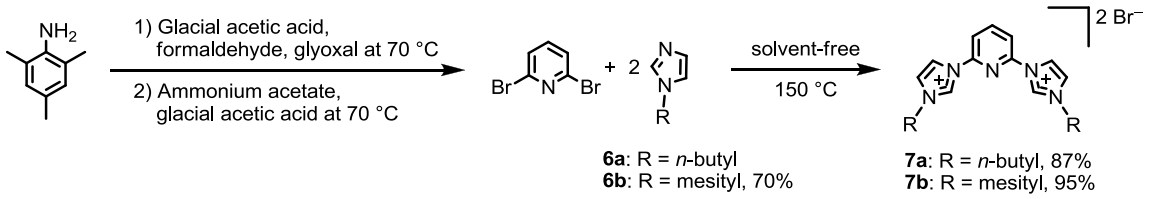

6a: R = *n*-butyl
6b: R = mesityl, 70%

7a: R = *n*-butyl, 87%
7b: R = mesityl, 95%

With the weak acid [HNEt$_3$]I the iridium $C_{NHC}CC_{NHC}$ pincer complexes **5a**/**5b** were formed in good yield, which have been characterized by ^{1}H NMR spectroscopy.

The CNC precursor ligands are generated via a slightly differently route, with uncatalyzed nucleophilic aromatic substitution between 2,6-dibromopyridine and the alkyl or aryl imidazole producing the desired product. We also have investigated the synthesis of novel iridium pincer complexes based on pyridine bis-*N*-heterocyclic carbene ligands, to evaluate their potential in homogeneous catalysis. 1-(2,4,6-Trimethylphenyl)-1*H*-imidazole (**6b**) was prepared the synthetic procedure reported previously.[32] The mixture of 2,6-dibromo-3,5-lutidine with **6a**/**6b** resulted in good yield of the pyridinyl substituted imidazolium dibromide **7a**/**7b** as outlined in **Scheme 4.3**.

Scheme 4.4. Synthesis of iridium CNC-*N*- heterocyclic carbene pincer complexes **9a**, and **9b**.

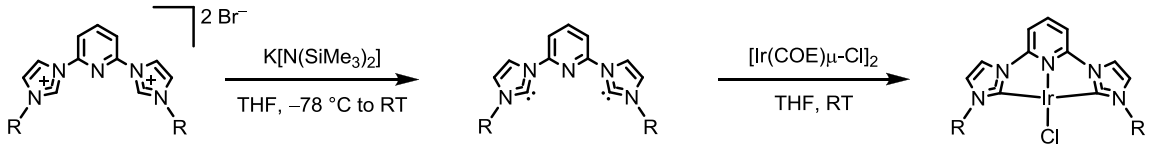

7a: R = *n*-butyl
7b: R = mesityl

8a: R = *n*-butyl (not isolated)
8b: R = mesityl (not isolated)

9a: R = *n*-butyl, 15%
9b: R = mesityl, 21%

The CNC pincer complexes were not accessible using [Ir(COD)(μ-Cl)]$_2$ in the presence of cesium carbonate. Instead, the free $C_{NHC}NC_{NHC}$ carbene ligand was prepared by an adaptation of the previously reported literature using KN(SiMe$_3$)$_2$ (KHMDS) as a strong base for the double deprotonation of the pyridinyl substituted imidazolium dibromide **7a**/**7b**. In an attempt to prepare CNC-iridium(I) pincer complexes **9a**/**9b**, the $C_{NHC}NC_{NHC}$-free carbene ligands **8a**/**8b** formed by KHMDS at –78 °C were not isolated

and directly reacted with $[Ir(COE)(\mu\text{-}Cl)]_2$ at room temperature *in situ* as shown in **Scheme 4.4**.

4.3.3. Catalytic dehydrogenation of cylooctane by C–H bond activation at Ir(III).

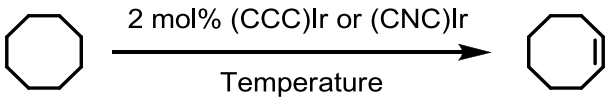

Table 4.1. Acceptorless dehydrogenation of cyclooctane at CCC/CNC-pincer Ir(III). [a]

Entry	Ir catalysts	T[°C]	time[h]	TON
1	**5a**	200	12	< 1
2	**5a**	200	24	2
3	**5a**	200	72	13
4	**5a**	150	72	5
5	**5b**	200	12	0
6	**5b**	200	24	1
7	**5b**	200	72	8
8	**5b**	150	72	2
9	**9a**	200	72	[b]
10	**9b**	200	72	[b]

[a] Standard conditions: CCC/CNC-Ir cat. (2 mol%), 0.1 mL of cyclooctane. The yield of cyclooctene was calculated by ^{1}H NMR. [b] No dehydrogenation of cyclooctane.

The catalytic dehydrogenation of alkanes can be used to produce value-added alkenes from relatively abundant saturated petroleum feedstocks. In general, the tridentate coordination mode of pincers results in strong binding to the metal center and results in high stability of the pincer complex. Also, the rigidity of the framework tends to inhibit cyclometallation at the terminal group. Although various catalysts based on transition-metal systems have been reported, the highest catalytic activities have been achieved with iridium PCP-pincer complexes including bis(phosphine)[6] or bis(phosphinite)[33] ligands.

Also, the neutral CCC type-iridium(III) pincer complexes consist of bis-benzimidazole backbones have been reported to be catalytically activity for the transfer and acceptorless dehydrogenation of cyclooctane in the presence of NaO-*t*-Bu.[19]

In this work, $C_{NHC}CC_{NHC}$-iridium pincer complexes **5a**/**5b** as well as $C_{NHC}NC_{NHC}$-iridium pincer complexes **9a**/**9b** having both thermally and oxidatively stable supporting ligands are targeted as precatalysts for alkane dehydrogenation. We have examined the potential catalytic activity of **5a** and **5b** for the dehydrogenation of cyclooctane through C–H bond activation at Ir(III) oxidation state in the proposed catalytic cycle. It is worth mentioning that Braunstein reported a lack of catalytic activity for the transfer dehydrogenation of cyclooctane with **4a**, *tert*-butylethylene, and NaO*t*-Bu at 150 °C.[27] The results of the catalytic studies with **5a**/**5b** are shown in **Table 4.1**. For the dehydrogenation of cyclooctane at Ir(III), we found **5a** was a weakly effective precatalyst giving almost 1 turnover estimated by ^{1}H NMR at 200 °C in 12 h period (entry 1). Changing to a longer time (e.g. 3 days) could improve the TON up to 13 (entries 2 and 3). On the other hand, initial experiments conducted with **5b** did not yield the expected dehydrogenation product as a cyclootene at 200 °C in 12 h period (entry 5). However, with longer reaction times, 72 hours, the TON increased to 8 (entries 6 and 7). With reaction temperatures of 150 °C, we found **5a** and **5b** exhibited modest catalytic activity for the dehydrogenation of cyclooctane with lower turnovers (entries 4 and 8). Thus, *n*-butyl-substituted CCC-pincer iridium(III) complexes **5a** and **5b** could be applied to the dehydrogenation of cyclooctane as catalysts. On the other hand, CNC-pincer iridium(I) complexes **9a** and **9b** showed the lack of catalytic behavior for the dehydrogenation of alkane (**Table 4.1**).

Table 4.2. Catalytic dehydrogenation of cyclooctane using CCC-pincer Ir(III).

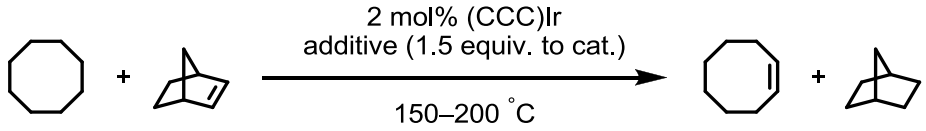

Entry	CCC-Ir catalysts	additive	T[℃]	Product detection
1	**4a**	*t*-BuOK	200	Yes
2	**4b**	*t*-BuOK	200	Yes
3	**4a**	*t*-BuOK	150	No
4	**4b**	*t*-BuOK	150	No

In addition, we found that **4a** and **4b** would be effective at 200 °C for the transfer dehydrogenation of cyclooctane using norbornene as a hydrogen acceptor, although we have yet to quantify the reactivity. On the other hand, **4a** and **4b** catalysts did not give the desired product at 150 °C. Having established the reactivity of **4a** and **4b** under these conditions, we need to examine other strong bases such as *t*-BuONa, *t*-BuOLi, LiTMP, and KHMDS.

In analogy to the previously reported PCP-pincer Ir complexes[7] a possible mechanism for transfer hydrogenation of cyclooctane is shown in **Scheme 4.5**. The reaction of **5a** with KO*t*-Bu would give the active 14-electron species **10**. Oxidative addition of cyclooctane to **10** would form cyclooctyl-iridium hydride complex **11** through C–H bond activation. And then β-hydride reductive elimination would generate iridium dihydride complex **12**, releasing cyclooctene as a product. Norbornene would insert into the Ir–H bond of **12** complex in order to generate alkyl-iridium hydride complex **13**. The reductive elimination from **13** would afford norbornane to regenerate the 14-electron active species **10**.

Scheme 4.5. Possible catalytic cycle for transfer dehydrogenation of cyclooctane.

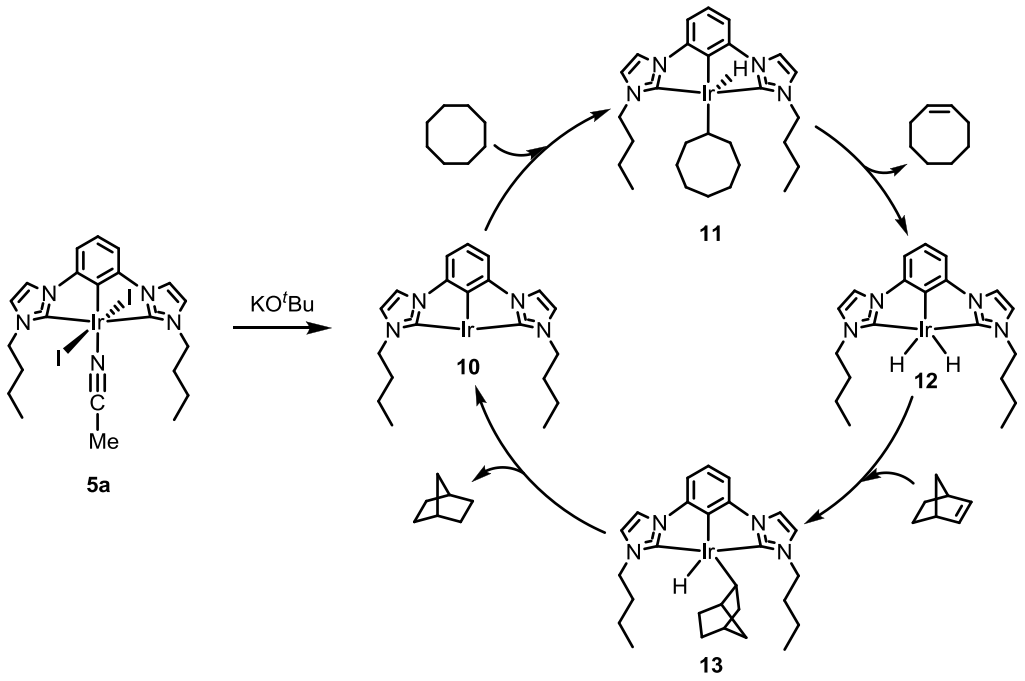

4.4. Future work

4.4.1. Modification of Ir CCC-pincer complexes.

Scheme 4.6. New acetate-bound precatalyst targets.

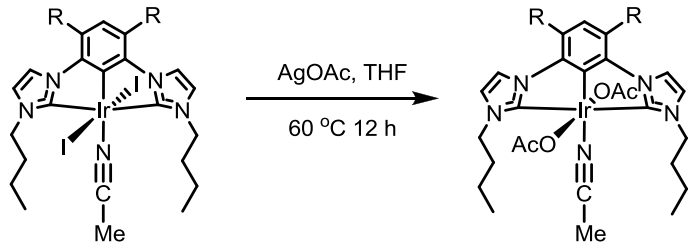

Several years ago, Nishiyama reported that the Rh(III) complex (^{dm}Phebox)Rh(OAc)$_2$(H$_2$O) (^{dm}Phebox = 2,6-bis(4,4-dimethyloxazolinyl)-3,5-dimethyl-phenyl) activated C–H bonds substituted arenes to form Rh(III)–aryl complexes.[34] This

group also described that the Ir(III) analogue (^{dm}Phebox)Ir(OAc)$_2$ (H_2O) activates arene and alkane C–H bonds to give Ir(III)–aryl and –alkyl complexes.[10] We may expect to generate a faster-activating catalyst with acetates for the C–H bond activation because our preliminary data seems to indicate that the rate is slower at the beginning (see **Table 4.1**). The preparation of Ir(CCC)(OAc)$_2$(MeCN) by metathesis reaction of Ir(CCC)(I)$_2$(MeCN) with AgOAc, described in **Scheme 4.6**, could be a possible route to prepare acetate-ligated analogues of **5a**/**5b**.

4.4.2. Catalytic Oxidation of Alkanes to Ketones.

The overall reaction is shown in **Scheme 4.7**, and involves the combination of a linear or cyclic alkane with O_2 to generate a ketone. Ketones are important as precursors for polymers or pharmaceuticals.

Scheme 4.7. Two-stage catalytic aerobic oxidation of alkanes.

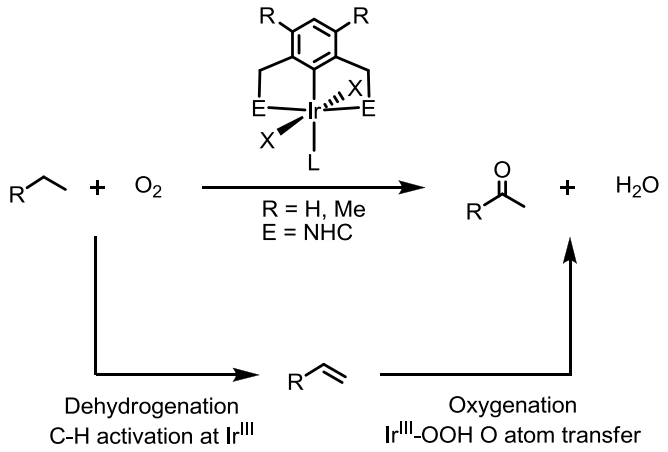

In **Scheme 4.7**, ketones are synthesized directly from alkanes, with no sacrificial hydrogen acceptor required and water as the only byproduct. Ir(CCC)I$_2$(MeCN) complexes **5a**/**5b** with oxidatively robust, electron-rich NHC-based pincer ligands will be used as

precatalysts. The transformation can occur through two stages including C–H activation and β-hydride elimination to generate an olefin and then be followed to produce a ketone. C–H activation occurs via an electrophilic mechanism, avoiding the intermediacy of highly reactive Ir(I) fragments. Once formed, the alkene can be trapped by reaction with O_2, which doubles as the hydrogen acceptor.

4.5. Conclusions

The Ir(III) pincer complexes including **4a**/**4b**, **5a**/**5b**, and **9a**/**9b** with robust pincer ligands were prepared and used to dehydrogenate cyclooctane to yield cyclootene. Iridium pincer complexes were formed on the bench top and shown to be active catalysts for the dehydrogenation of cycloocatane through the C–H activation. Further studies including catalysts optimization for much higher active catalysts and application to two-stage catalytic aerobic oxidation of alkanes are in progress.

4.6. References

1. Dobereiner, G. E.; Crabtree, R. H. Dehydrogenation as a Substrate-Activating Strategy in Homogeneous Transition-Metal Catalysis. *Chem. Rev.* **2010**, *110*, 681–703.
2. Moulton, C. J.; Shaw, B. L. Transition Metal–Carbon Bonds. Part XLII. Complexes of Nickel, Palladium, Platinum, Rhodium and Iridium with the Tridentate Ligand 2,6-Bis[(Di-*t*-Butylphosphino)Methyl]Phenyl. *J. Chem. Soc. Dalton Trans.* **1976**, *11*, 1020–1024.
3. Albrecht, M.; van Koten, G. Platinum Group Organometallics Based on 'Pincer' Complexes: Sensors, Switches, and Catalysts. *Angew. Chem. Int. Ed.* **2001**, *40*, 3750–3781.
4. Segawa, Y.; Yamashita, M.; Nozaki, K. Syntheses of PBP Pincer Iridium Complexes: A Supporting Boryl Ligand. *J. Am. Chem. Soc.* **2009**, *131*, 9201–9203.

5. Van der Boom, M. E.; Milstein, D. Cyclometalated Phosphine–Based Pincer Complexes: Mechanistic Insight in Catalysis, Coordination, and Bond Activation. *Chem. Rev.* **2003**, *103*, 1759–1792.
6. Kundu, S.; Choliy, Y.; Zhuo, G.; Ahuja, R.; Emge, T. J.; Warmuth, R.; Brookhart, M.; Krogh-Jespersen, K.; Goldman, A. S. Rational Design and Synthesis of Highly Active Pincer–Iridium Catalysts for Alkane Dehydrogenation. *Organometallics* **2009**, *28*, 5432–5444.
7. Choi, J.; MacArthur, A. H. R.; Brookhart, M.; Goldman, A. S. Dehydrogenation and Related Reactions Catalyzed by Iridium Pincer Complexes. *Chem. Rev.* **2011**, *111*, 1761–1779.
8. Nawara-Hultzsch, A. J.; Hackenberg, J. D.; Punji, B.; Supplee, C.; Emge, T. J.; Bailey, B. C.; Schrock, R. R.; Brookhart, M.; Goldman, A. S. Rational Design of Highly Active 'Hybrid' Phosphine–Phosphinite Pincer Iridium Catalysts for Alkane Metathesis. *ACS Catal.* **2013**, *3*, 2505–2514.
9. Denney, M. C.; Pons, V.; Hebden, T. J.; Heinekey, D. M.; Goldberg, K. I. Efficient Catalysis of Ammonia Borane Dehydrogenation. *J. Am. Chem. Soc.* **2006**, *128*, 12048–12049.
10. Ito, J.; Kaneda, T.; Nishiyama, H. Intermolecular C–H Bond Activation of Alkanes and Arenes by NCN Pincer Iridium(III) Acetate Complexes Containing Bis(Oxazolinyl)Phenyl Ligands. *Organometallics* **2012**, *31*, 4442–4449.
11. Allen, K. E.; Heinekey, D. M.; Goldman, A. S.; Goldberg, K. I. Regeneration of an Iridium(III) Complex Active for Alkane Dehydrogenation Using Molecular Oxygen. *Organometallics* **2014**, *33*, 1337–1340.
12. Allen, K. E.; Heinekey, D. M.; Goldman, A. S.; Goldberg, K. I. Alkane Dehydrogenation by C–H Activation at Iridium(III). *Organometallics* **2013**, *32*, 1579–1582.
13. Jagenbrein, M.; Danopoulos, A. A.; Braunstein, P. Bis-*N*-Heterocyclic Carbene 'Pincer' Ligands and Iridium Complexes with CF_3–Substituted Phenylene Backbone. *J. Organomet. Chem.* **2015**, *775*, 169–172.

14. Danopoulos, A. A.; Pugh, D.; Wright, J. A. 'Pincer' Pyridine–Dicarbene–Iridium Complexes: Facile C–H Activation and Unexpected η^2-Imidazol-2-Ylidene Coordination. *Angew. Chem. Int. Ed.* **2008**, *47*, 9765–9767.

15. Gu, S.; Chen, W. Pincer Complexes of Palladium- and Nickel-Containing 3-Butyl-1-(1,10-Phenanthrolin-2-Yl)Imidazolylidene as Efficient Aqueous Sonogashira and Kumada Coupling Reactions. *Organometallics* **2009**, *28*, 909–914.

16. Steinke, T.; Shaw, B. K.; Jong, H.; Patrick, B. O.; Fryzuk, M. D. Synthesis and Coordination Chemistry of a Tridentate *o*-Phenylene-Bridged Diphosphine−NHC System. *Organometallics* **2009**, *28*, 2830–2836.

17. Iglesias-Sigüenza, J.; Ros, A.; Díez, E.; Magriz, A.; Vázquez, A.; Álvarez, E.; Fernández, R.; Lassaletta, J. M. C_2-Symmetric SCS Ligands Based on *N*-Heterocyclic Carbenes: A New Ligand Architecture for Asymmetric Catalysis. *Dalton Trans.* **2009**, *40*, 8485–8488.

18. Huynh, H. V.; Yuan, D.; Han, Y. Syntheses and Catalytic Activities of Pseudo-Pincer and CSC Pincer–Type Pd(II) Complexes Derived from Benzannulated *N*-Heterocyclic Carbenes. *Dalton Trans.* **2009**, *35*, 7262–7268.

19. Chianese, A. R.; Mo, A.; Lampland, N. L.; Swartz, R. L.; Bremer, P. T. Iridium Complexes of CCC-Pincer *N*-Heterocyclic Carbene Ligands: Synthesis and Catalytic C−H Functionalization. *Organometallics* **2010**, *29*, 3019–3026.

20. Lv, K.; Cui, D. Tridentate CCC-Pincer Bis(Carbene)-Ligated Rare-Earth Metal Dibromides. Synthesis and Characterization. *Organometallics* **2008**, *27*, 5438–5440.

21. Schultz, K. M.; Goldberg, K. I.; Gusev, D. G.; Heinekey, D. M. Synthesis, Structure, and Reactivity of Iridium NHC Pincer Complexes. *Organometallics* **2011**, *30*, 1429–1437.

22. Vargas, V. C.; Rubio, R. J.; Hollis, T. K.; Salcido, M. E. Efficient Route to 1,3-Di-*N*-Imidazolylbenzene. A Comparison of Monodentate vs Bidentate Carbenes in Pd-Catalyzed Cross Coupling. *Org. Lett.* **2003**, *5*, 4847–4849.

23. Rubio, R. J.; Andavan, G. T. S.; Bauer, E. B.; Hollis, T. K.; Cho, J.; Tham, F. S.; Donnadieu, B. Toward a General Method for CCC *N*-Heterocyclic Carbene Pincer

Synthesis: Metallation and Transmetallation Strategies for Concurrent Activation of Three C–H Bonds. *J. Organomet. Chem.* **2005**, *690*, 5353–5364.

24. Bauer, E. B.; Andavan, G. T. S.; Hollis, T. K.; Rubio, R. J.; Cho, J.; Kuchenbeiser, G. R.; Helgert, T. R.; Letko, C. S.; Tham, F. S. Air- and Water-Stable Catalysts for Hydroamination/Cyclization. Synthesis and Application of CCC−NHC Pincer Complexes of Rh and Ir. *Org. Lett.* **2008**, *10*, 1175–1178.
25. Cho, J.; Hollis, T. K.; Helgert, T. R.; Valente, E. J. An Improved Method for the Synthesis of Zirconium (CCC-*N*-Heterocyclic Carbene) Pincer Complexes and Applications in Hydroamination. *Chem. Commun.* **2008**, *40*, 5001–5003.
26. Andavan, G. T. S.; Bauer, E. B.; Letko, C. S.; Hollis, T. K.; Tham, F. S. Synthesis and Characterization of a Free Phenylene Bis(*N*-Heterocyclic Carbene) and Its Di-Rh Complex: Catalytic Activity of the Di-Rh and CCC–NHC Rh Pincer Complexes in Intermolecular Hydrosilylation of Alkynes. *J. Organomet. Chem.* **2005**, *690*, 5938–5947.
27. Raynal, M.; Pattacini, R.; Cazin, C. S. J.; Vallée, C.; Olivier-Bourbigou, H.; Braunstein, P. Reaction Intermediates in the Synthesis of New Hydrido, *N*-Heterocyclic Dicarbene Iridium(III) Pincer Complexes. *Organometallics* **2009**, *28*, 4028–4047.
28. Serra, D.; Cao, P.; Cabrera, J.; Padilla, R.; Rominger, F.; Limbach, M. Development of Platinum(II) and -(IV) CNC Pincer Complexes and Their Application in a Hydrovinylation Reaction. *Organometallics* **2011**, *30*, 1885–1895.
29. Bonifacio, M. C.; Robertson, C. R.; Jung, J.-Y.; King, B. T. Polycyclic Aromatic Hydrocarbons by Ring-Closing Metathesis. *J. Org. Chem.* **2005**, *70*, 8522–8526.
30. So, Y. H. Novel Thermoset Polyimidazole Amides. *Macromolecules* **1992**, *25*, 516–520.
31. Cho, J.; Hollis, T. K.; Valente, E. J.; Trate, J. M. CCC-*N*-Heterocyclic Carbene Pincer Complexes: Synthesis, Characterization and Hydroamination Activity of a Hafnium Complex. *J. Organomet. Chem.* **2011**, *696*, 373–377.
32. Zhao, Y.; Gilbertson, S. R. Synthesis of Proline-Based N-Heterocyclic Carbene Ligands. *Org. Lett.* **2014**, *16*, 1033–1035.

33. Huang, Z.; Brookhart, M.; Goldman, A. S.; Kundu, S.; Ray, A.; Scott, S. L.; Vicente, B. C. Highly Active and Recyclable Heterogeneous Iridium Pincer Catalysts for Transfer Dehydrogenation of Alkanes. *Adv. Synth. Catal.* **2009**, *351*, 188–206.

34. Ito, J.; Nishiyama, H. Carbon–Hydrogen Bond Activation of Arenes by a [Bis(Oxazolinyl)Phenyl]Rhodium(III) Acetate Complex. *Eur. J. Inorg. Chem.* **2007**, *2007*, 1114–1119.

Chapter 5. Conclusions

This thesis covers four different topics: 1) monometallic and bimetallic platinum complexes with fluorinated β-diketiminate ligands; 2) Lewis acid modulation of aza-BODIPY and *meso*-Pyridyl BODIPY chromophores; 3) cyclometalated iridium-BODIPY ratiometric O_2 sensors; and 4) dehydrogenation of alkanes with iridium(III) pincer complexes. The following are summaries for the research projects reported in this dissertation.

Chapter 1 provided a series of platinum complexes of fluorinated β-diketiminate ligands and two different coordination modes which can be prepared by slight variation of the reaction temperature. A series of bimetallic platinum complexes, featuring a previously unobserved NacNac binding mode, were investigated and structurally characterized. Moreover, monometallic Pt(C^N)(NacNac) bis-chelate species were generated by increasing the reaction temperature and adding excess amount of NacNac precursor. All of the monometallic and bimetallic platinum complexes exhibited redox and optical properties derived from the NacNac ligands, revealing reversible reductions at mild potentials ($E > –1.65$ V vs. Fc^+/Fc) and intense visible absorptions covering much of the visible spectrum. The monoplatinum complexes exhibit luminescence in the red and near-infrared regions involving NacNac-centered frontier orbitals.

Chapter 2 described the synthesis of two BODIPY compounds with pendant pyridine donors and a sterically unhindered aza-BODIPY molecule. Two different types of pyridyl BODIPYs have been investigated for their interactions with Lewis acids in the secondary coordination sphere, resulting in significant changes to the optical properties.

Addition of $B(C_6F_5)_3$ to pyridyl substituted BODIPYs results in bathochromic shifts in the UV-vis absorption and emission bands. The Lewis acid functions as an electron-withdrawing group and lowers the S_1 excited-state energy, giving rise to the red-shifted absorption and emission bands. The coordination of $B(C_6F_5)_3$ to the bridgehead nitrogen of aza-BODIPY can be sterically accessible to Lewis acids was also studied. The binding of aza-BODIPY compound with Lewis acids resulted in a substantial red shift in the UV-vis absorption spectrum even though the adducts of aza-BODIPY with $B(C_6F_5)_3$ is accompanied by nonspecific decomposition.

Chapter 3 introduced the development of two-component assemblies with a phosphorescent metal center ($[Ir(C\text{^}N)_2(CNAr^{dmp})]^+$) linked to the well-known fluorophore BODIPY, applied as ratiometric O_2 sensors. The constructs were successfully synthesized by a modular approach using a cyclometalated iridium precursor with a loosely bound PF_6^- anion. These Ir-BODIPY conjugates exhibit dual luminescence where phosphorescence originates from the iridium fragment and fluorescence comes from BODIPY component, and the absorption and emission properties are dependent on the identity of the linker between the iridium center and the BODIPY compound as well as the C^N ligand. Since energy transfer from the long-lived iridium-centered excited state to the BODIPY is favorable and efficient, complexes with C^N = F_2ppy do not function well as sensors. In contrast, for complexes with C^N = piq, where the triplet excited state is lower in energy than the BODIPY singlet state, energy transfer is shut down and comparable amounts of luminescence from both sites are observed, the precise ratio varying slightly with the nature of the linker between BODIPY and iridium. Evaluation of the oxygen-dependent photoluminescence, in concert with Stern-Volmer quenching analysis of the

phosphorescence lifetime, demonstrates that four compounds described here function as effective ratiometric O_2 sensors with sensitivities and dynamic ranges suitable for hypoxic environments. This simple synthetic strategy, where the fluorophore and phosphor are linked via a modular strategy, can be applicable to a range of next-generation oxygen sensors.

Chapter 4 described the synthesis of CCC- and CNC-iridium pincer complexes as precatalysts for dehydrogenation of alkanes and the preliminary results of C–H bond activation. The pincer iridium(III) hydride complexes were prepared by the reaction of $[Ir(COD)(\mu\text{-}Cl)_2]_2$ with bis(imidazolium) benzene derivatives diiodide in the presence of Cs_2CO_3 in refluxing acetonitrile. Diiodide substituted iridium pincer complexes were successfully prepared in high yield using the weak acid $[HNEt_3]I$, and these complexes can serve as precatalysts for dehydrogenation of cylcooctane. In order to generate CNC-iridium(I) pincer complexes, we adopted the slightly differently route via free carbene ligand using $KN(SiMe_3)_2$ as the strong base for the double dehydrogenation of the pyridinyl substituted imidazolium dibromide. The free carbene ligands were not isolated and directly reacted with $[Ir(COE)(\mu\text{-}Cl)]_2$ at room temperature in situ, generating CNC-iridium(I) pincer complexes. We examined the four kinds of iridium pincer complexes as precatalysts for dehydrogenation of cyclooctane. Iridium(III) pincer complexes $[IrI_2{}^{n\text{-}Bu}(C_{NHC}CC_{NHC})\text{-}(NCMe)]$ resulted in little catalytic activity for cyclooctane dehydrogenation using either norbornene as a hydrogen acceptor or under acceptorless conditions.

Appendix 1. Monometallic and Bimetallic Platinum Complexes with Fluorinated β-Diketiminate Ligands

A1.1. X-ray crystal structures

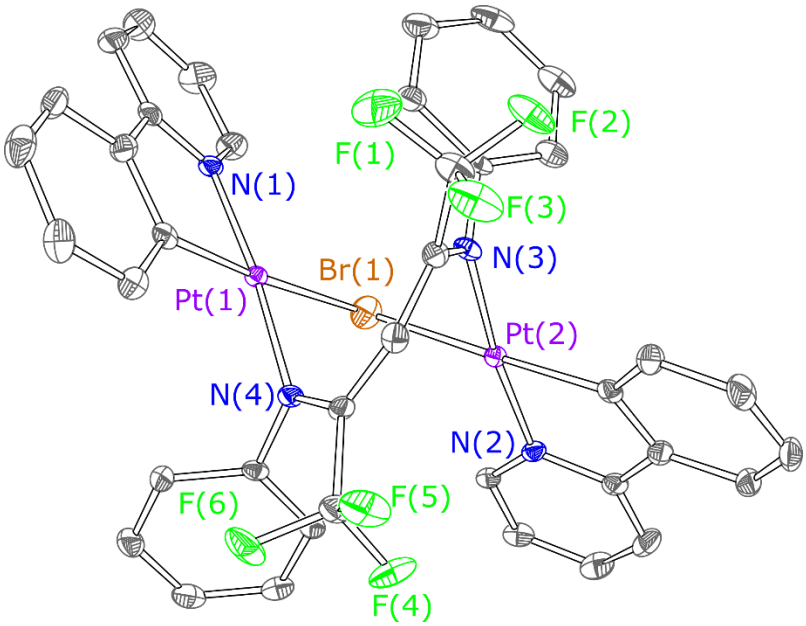

Figure A1.1. X-ray crystal structure of complex **2**. Ellipsoids are drawn at the 50% probability level with solvent molecules and hydrogen atoms omitted.

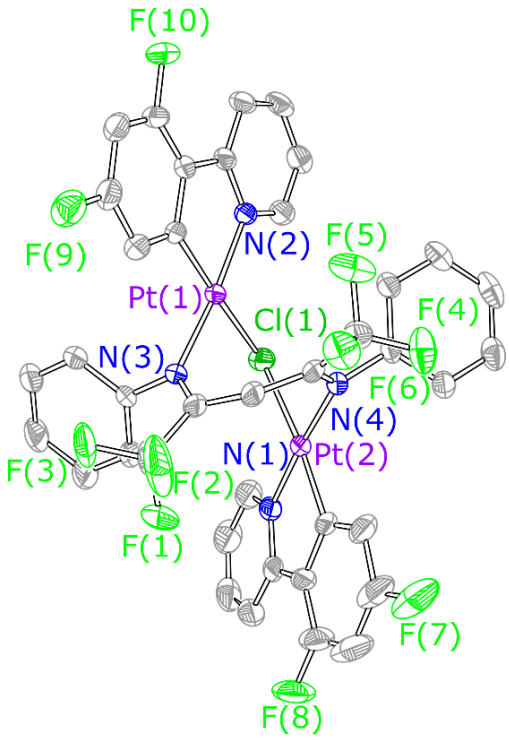

Figure A1.2. X-ray crystal structure of complex **3**. Ellipsoids are drawn at the 50% probability level with solvent molecules and hydrogen atoms omitted.

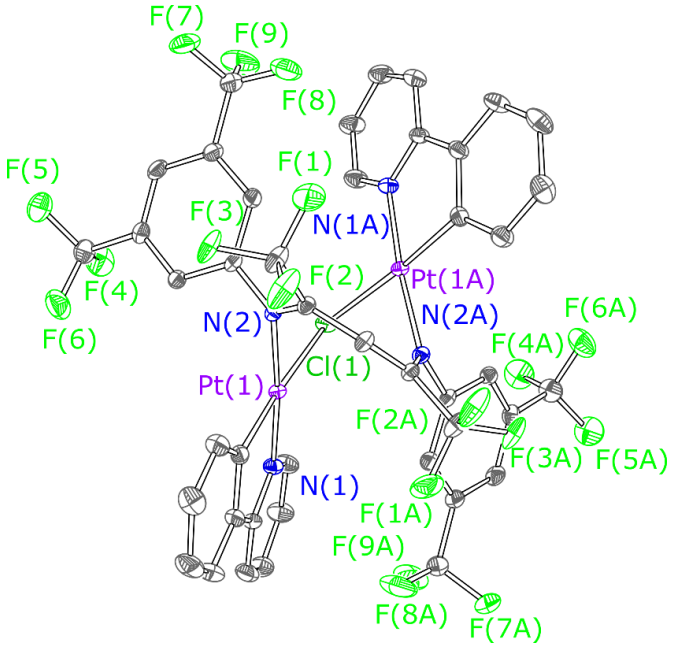

Figure A1.3. X-ray crystal structure of complex **4**. Ellipsoids are drawn at the 50% probability level with hydrogen atoms omitted.

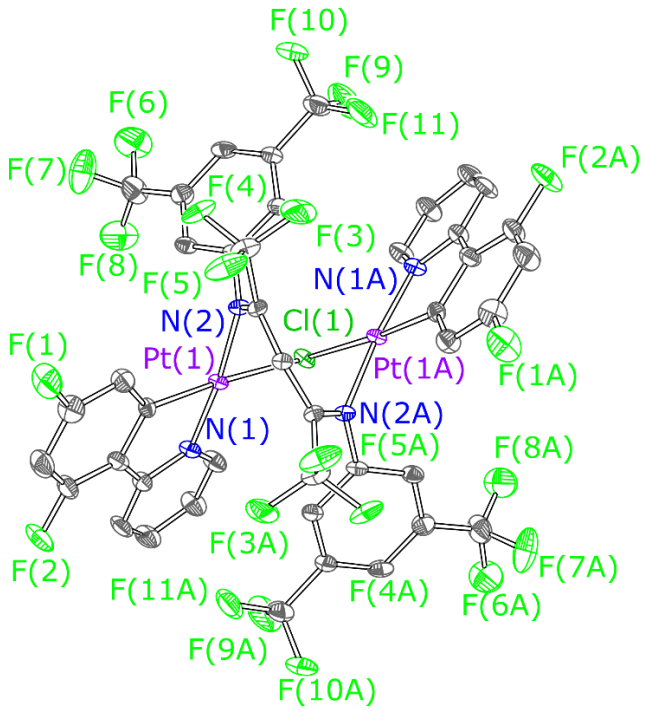

Figure A1.4. X-ray crystal structure of complex **5**. Ellipsoids are drawn at the 50% probability level with hydrogen atoms omitted.

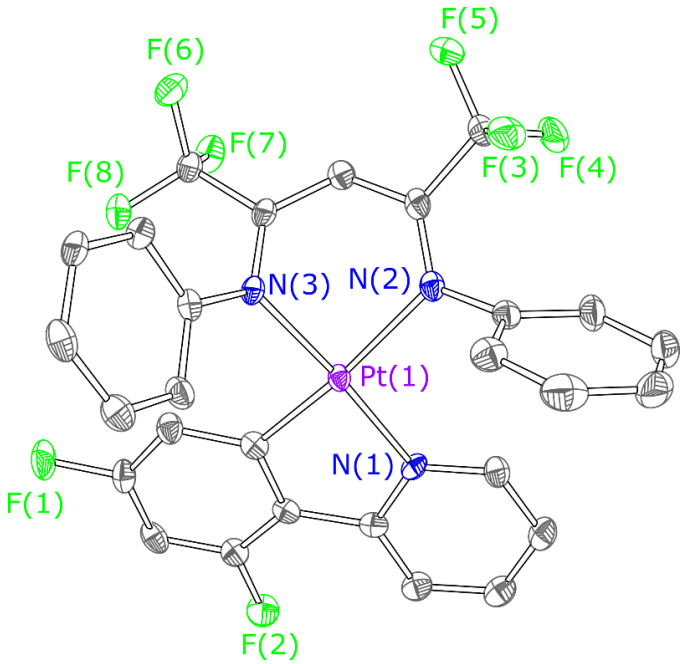

Figure A1.5. X-ray crystal structure of complex **7**. Ellipsoids are drawn at the 50% probability level with hydrogen atoms omitted.

A1.2. X-ray crystallography summary tables

Table A1.1. Summary of X-ray crystallographic data for **1**–**3**.

	1•2THF	**2**•1.5CH_2Cl_2	**3**•2THF
CCDC	1565320	1565321	1565322
Crystal data			
Chemical formula	$C_{47}H_{43}ClF_6N_4O_2Pt_2$	$C_{40.50}H_{29}BrCl_3F_6N_4Pt_2$	$C_{47}H_{38}ClF_{10}N_4O_2Pt_2$
M_r	1235.48	1262.12	1306.44
Crystal system, space group	Monoclinic, $P2_1/c$	Monoclinic, $P2_1/c$	Monoclinic, $P2_1/c$
Temperature (K)	123	296	123
a, b, c (Å)	18.598 (12), 13.252 (9), 19.172 (12)	18.556 (4), 12.490 (3), 19.242 (4)	18.640 (7), 12.391 (5), 19.008 (7)
α, β, γ (°)	90, 113.316 (8), 90	90, 113.200 (2), 90	90, 95.164 (5), 90
V (Å^3)	4339 (5)	4098.9 (15)	4372 (3)
Z	4	4	4
μ (mm^{-1})	6.57	8.05	6.54
Crystal size (mm)	0.45 × 0.32 × 0.12	0.35 × 0.34 × 0.22	0.39 × 0.12 × 0.06
Data collection			
T_{min}, T_{max}	0.399, 0.746	0.497, 0.746	0.451, 0.746
No. of measured, independent and observed [$I > 2\sigma(I)$] reflections	26101, 9801, 8734	25231, 9446, 8718	26617, 10090, 8752
R_{int}	0.039	0.025	0.024
$(\sin\theta/\lambda)_{max}$ (Å^{-1})	0.649	0.651	0.652
Refinement			
$R[F^2 > 2\sigma(F^2)]$, $wR(F^2)$, S	0.029, 0.076, 1.04	0.030, 0.086, 1.05	0.024, 0.059, 1.07
No. of reflections	9801	9446	10090
No. of parameters	584	523	652
No. of restraints	165	0	338
	$w = 1/[\sigma^2(F_o^2) + (0.0358P)^2 + 3.722P]$ where $P = (F_o^2 + 2F_c^2)/3$	$w = 1/[\sigma^2(F_o^2) + (0.043P)^2 + 30.6598P]$ where $P = (F_o^2 + 2F_c^2)/3$	$w = 1/[\sigma^2(F_o^2) + (0.019P)^2 + 8.3592P]$ where $P = (F_o^2 + 2F_c^2)/3$
$\Delta\rho_{max}$, $\Delta\rho_{min}$ (e Å^{-3})	1.74, -2.27	2.11, -3.39	1.00, -1.13

Table A1.2. Summary of X-ray crystallographic data for **4**–**6**.

	4	**5**	**6**
CCDC	1565323	1565324	1565325
Crystal data			
Chemical formula	$C_{43}H_{23}ClF_{18}N_4Pt_2$	$C_{43}H_{19}ClF_{22}N_4Pt_2$	$C_{28}H_{19}F_6N_3Pt$
M_r	1363.28	1435.25	706.55
Crystal system, space group	Monoclinic, *P*2/*n*	Monoclinic, *P*2/*n*	Monoclinic, $P2_1/n$
Temperature (K)	123	123	123
a, *b*, *c* (Å)	14.524 (5), 8.381 (3), 17.682 (6)	14.519 (7), 8.448 (4), 17.901 (8)	17.3823 (8), 14.6397 (7), 20.7366 (9)
α, β, γ (°)	90, 94.386 (5), 90	90, 92.563 (6), 90	90, 110.6249 (6), 90
V (Å^3)	2146.1 (13)	2193.6 (17)	4938.7 (4)
Z	2	2	8
μ (mm^{-1})	6.69	6.56	5.75
Crystal size (mm)	0.37 × 0.36 × 0.34	0.46 × 0.31 × 0.31	0.42 × 0.24 × 0.10
Data collection			
T_{min}, T_{max}	0.644, 0.746	0.520, 0.746	0.523, 0.746
No. of measured, independent and observed [$I > 2\sigma(I)$] reflections	12998, 4907, 4667	12526, 4998, 4520	30428, 11347, 9984
R_{int}	0.023	0.026	0.018
$(\sin\theta/\lambda)_{max}$ (Å^{-1})	0.650	0.649	0.651
Refinement			
$R[F^2 > 2\sigma(F^2)]$, $wR(F^2)$, *S*	0.020, 0.050, 1.15	0.032, 0.086, 1.05	0.016, 0.039, 1.03
No. of reflections	4907	4998	11347
No. of parameters	318	345	685
No. of restraints	114	96	0
	$w = 1/[\sigma^2(F_o^2) + (0.0178P)^2 + 2.6548P]$ where $P = (F_o^2 + 2F_c^2)/3$	$w = 1/[\sigma^2(F_o^2) + (0.048P)^2 + 9.0073P]$ where $P = (F_o^2 + 2F_c^2)/3$	$w = 1/[\sigma^2(F_o^2) + (0.0158P)^2 + 2.4862P]$ where $P = (F_o^2 + 2F_c^2)/3$
$\Delta\rho_{max}$, $\Delta\rho_{min}$ (e Å^{-3})	1.03, -0.84	2.29, -2.60	0.79, -0.52

Table A1.3. Summary of X-ray crystallographic data for **7** and **8**.

	7	**8**
CCDC	1565326	1565327
Crystal data		
Chemical formula	$C_{28}H_{17}F_8N_3Pt$	$C_{24}H_{12}F_{12}N_2OPt$
M_r	742.53	767.45
Crystal system, space group	Triclinic, $P\bar{1}$	Triclinic, $P\bar{1}$
Temperature (K)	123	123
a, *b*, *c* (Å)	10.102 (3), 11.553 (3), 12.922 (3)	8.942 (6), 12.728 (9), 20.463 (14)
α, β, γ (°)	65.226 (3), 73.453 (3), 66.354 (3)	84.68 (1), 83.782 (9), 77.173 (9)
V (Å^3)	1242.0 (5)	2252 (3)
Z	2	4
μ (mm^{-1})	5.73	6.36
Crystal size (mm)	0.43 × 0.29 × 0.24	0.38 × 0.22 × 0.16
Data collection		
T_{min}, T_{max}	0.556, 0.746	0.475, 0.746
No. of measured, independent and observed [$I > 2\sigma(I)$] reflections	21160, 5729, 5297	13980, 10097, 8915
R_{int}	0.036	0.033
$(\sin\theta/\lambda)_{max}$ (Å^{-1})	0.653	0.649
Refinement		
$R[F^2 > 2\sigma(F^2)]$, $wR(F^2)$, *S*	0.043, 0.120, 1.07	0.036, 0.100, 1.01
No. of reflections	5729	10097
No. of parameters	361	721
No. of restraints	0	0
	$w = 1/[\sigma^2(F_o^2) + (0.0926P)^2 + 2.111P]$ where $P = (F_o^2 + 2F_c^2)/3$	$w = 1/[\sigma^2(F_o^2) + (0.0611P)^2]$ where $P = (F_o^2 + 2F_c^2)/3$
$\Delta\rho_{max}$, $\Delta\rho_{min}$ (e Å^{-3})	5.75, -2.56	3.61, -3.37

A1.3. Crude ^{19}F NMR spectrum of complex 8

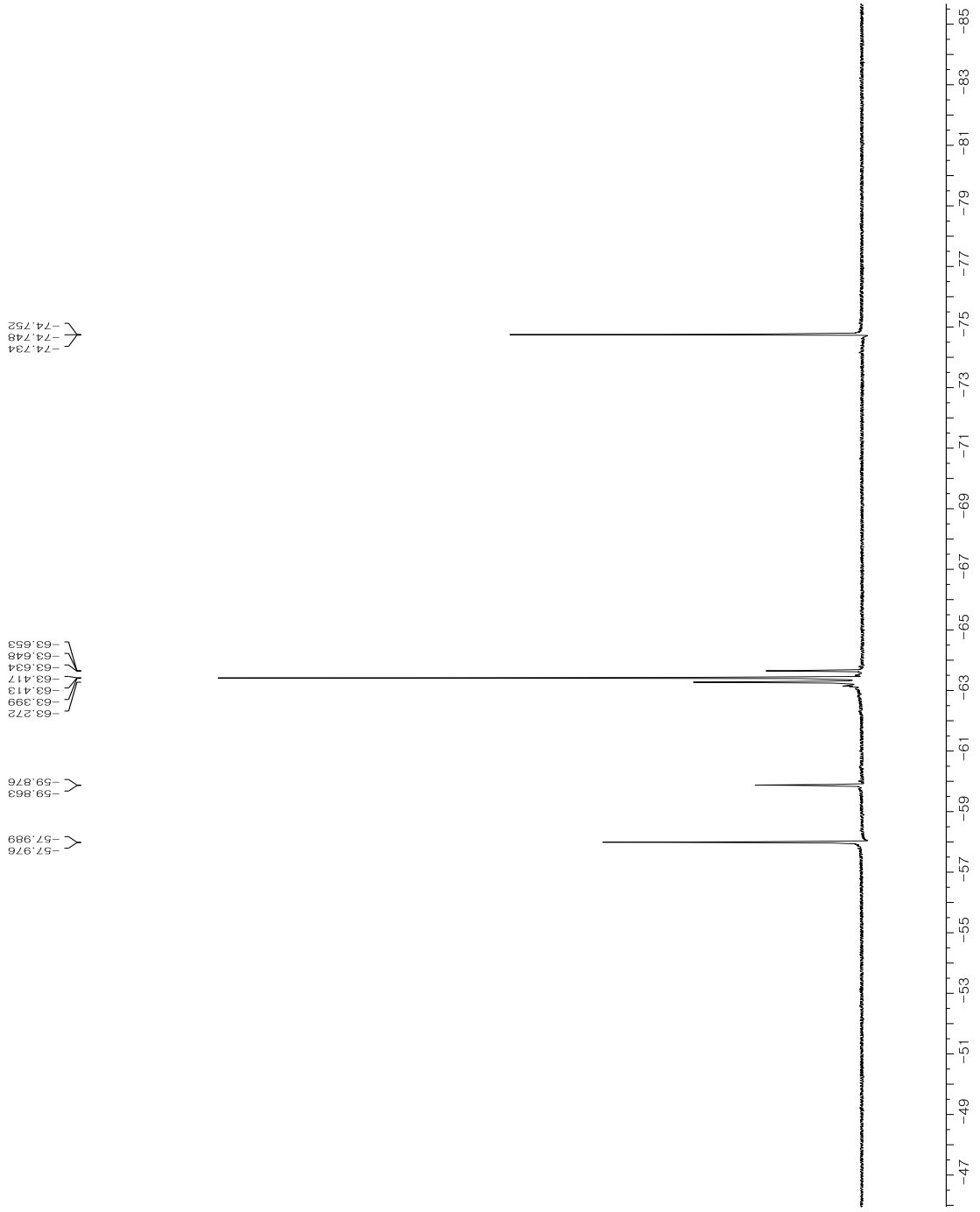

Figure A1.6. ^{19}F NMR spectrum obtained during attempted preparation of Pt(ppy)(NacNac^{F18}), following filtration of the crude product through alumina. The most upfield peak (ca. –75 ppm) is characteristic of the hydrolyzed Pt(ppy)(acNac^{F12}) (**8**) product. The spectrum was recorded in $CDCl_3$ at 376 MHz.

A1.4. Cyclic voltammograms

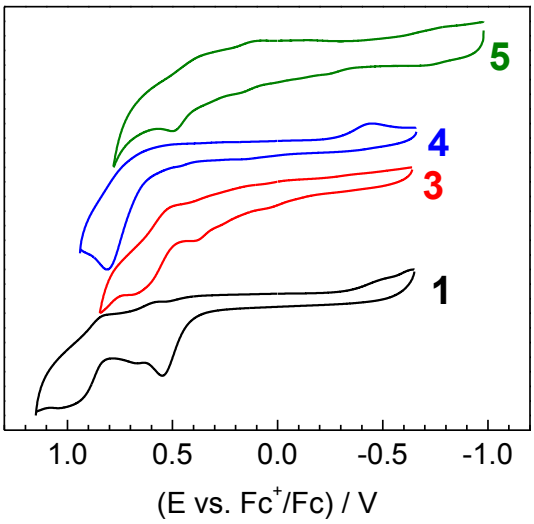

Figure A1.7. Overlaid cyclic voltammograms of chloride-bridged diplatinum complexes **1**, **3**, **4**, and **5**, showing anodic (positive) sweeps only. The voltammograms were recorded in MeCN (**1**, **3**, and **4**) or THF (**5**) with 0.1 M $TBAPF_6$ supporting electrolyte, a glassy carbon working electrode, a platinum wire counter electrode, and a silver wire pseudo-reference electrode. Potentials are referenced to the ferrocenium/ferrocene couple. Currents are normalized to bring the plots onto the same scale.

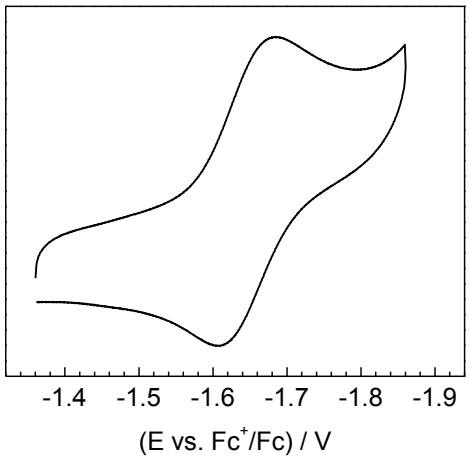

Figure A1.8. Cyclic voltammogram of complex **2**, recorded in MeCN with 0.1 M $TBAPF_6$ supporting electrolyte, a glassy carbon working electrode, a platinum wire counter electrode, and a silver wire pseudo-reference electrode. Potentials are referenced to the ferrocenium/ferrocene couple.

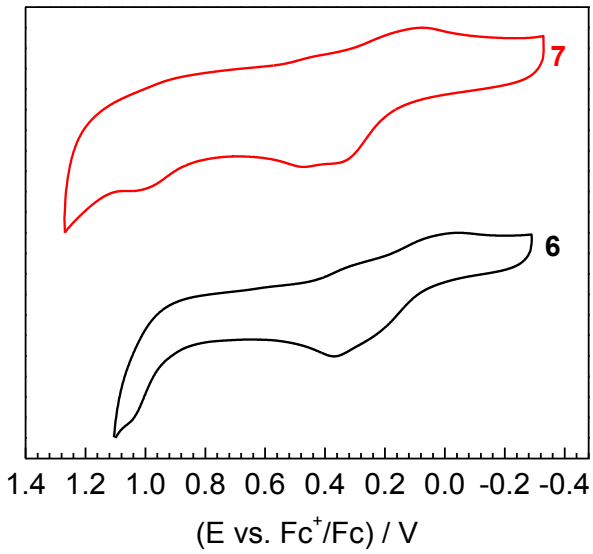

Figure A1.9. Overlaid cyclic voltammograms of monoplatinum complexes **6** and **7**, showing anodic (positive) sweeps only. The voltammograms were recorded in MeCN with 0.1 M $TBAPF_6$ supporting electrolyte, a glassy carbon working electrode, a platinum wire counter electrode, and a silver wire pseudo-reference electrode. Potentials are referenced to the ferrocenium/ferrocene couple. Currents are normalized to bring the plots onto the same scale.

A1.5. Solvatochromic UV-vis absorption spectra

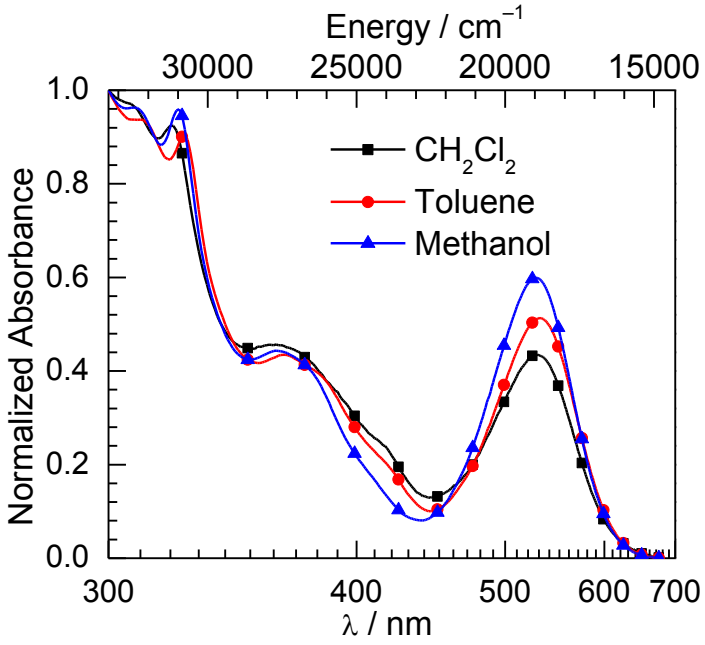

Figure A1.10. Overlaid, normalized UV-vis absorption spectra of complex **3** recorded in CH_2Cl_2, toluene, and methanol at room temperature.

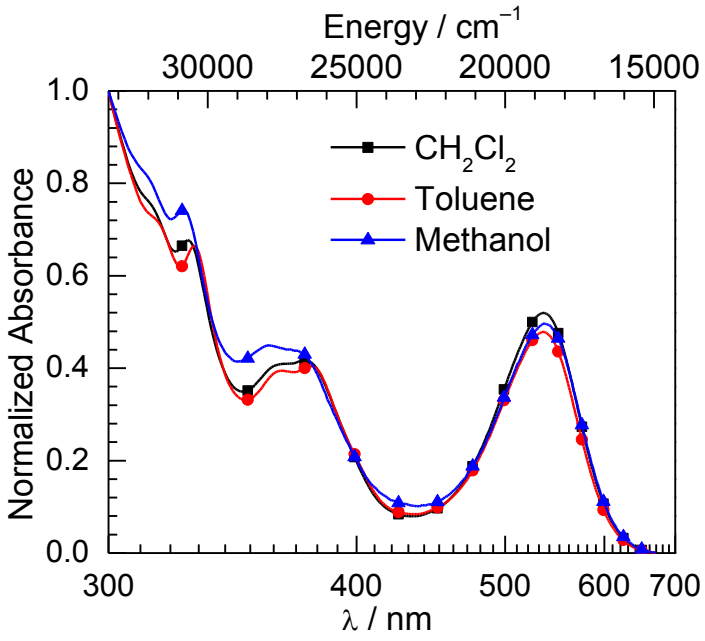

Figure A1.11. Overlaid, normalized UV-vis absorption spectra of complex **4** recorded in CH_2Cl_2, toluene, and methanol at room temperature.

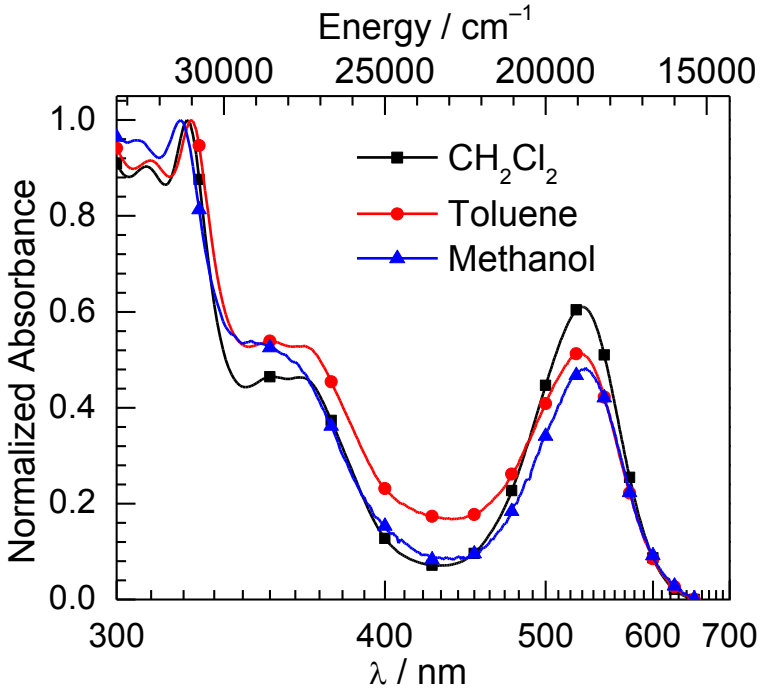

Figure A1.12. Overlaid, normalized UV-vis absorption spectra of complex **5** recorded in CH_2Cl_2, toluene, and methanol at room temperature.

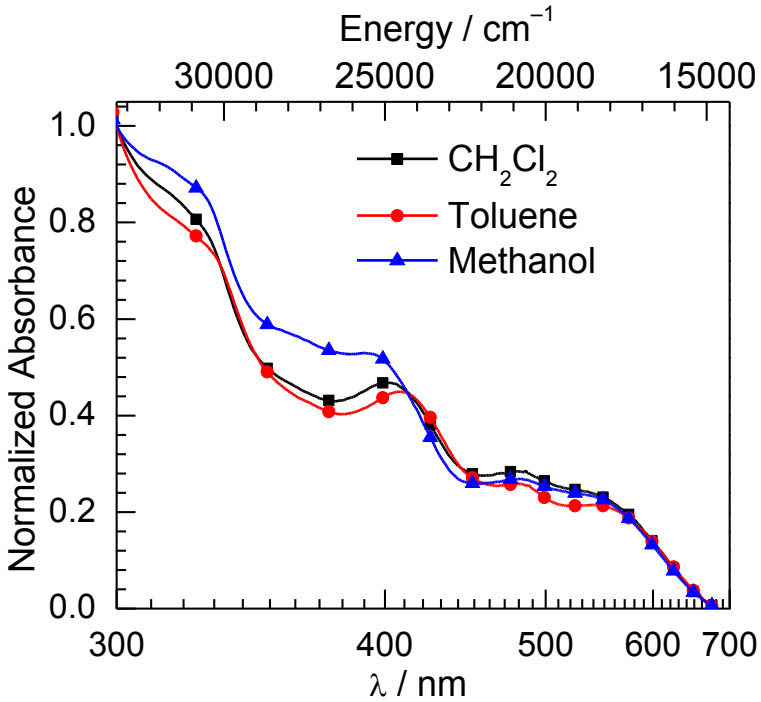

Figure A1.13. Overlaid, normalized UV-vis absorption spectra of complex **6** recorded in CH_2Cl_2, toluene, and methanol at room temperature.

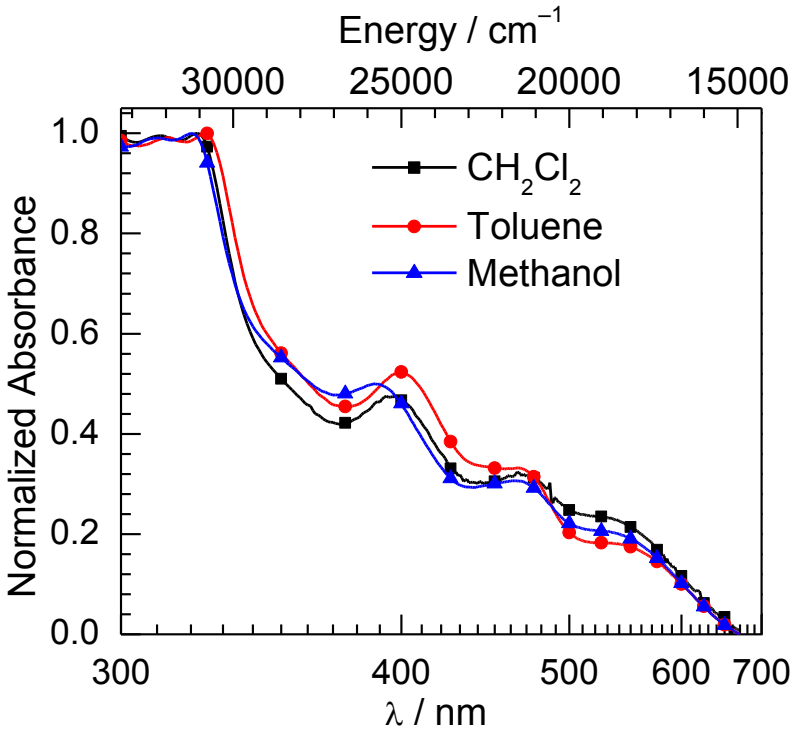

Figure A1.14. Overlaid, normalized UV-vis absorption spectra of complex **7** recorded in CH_2Cl_2, toluene, and methanol at room temperature.

A1.6. NMR spectra of all new complexes

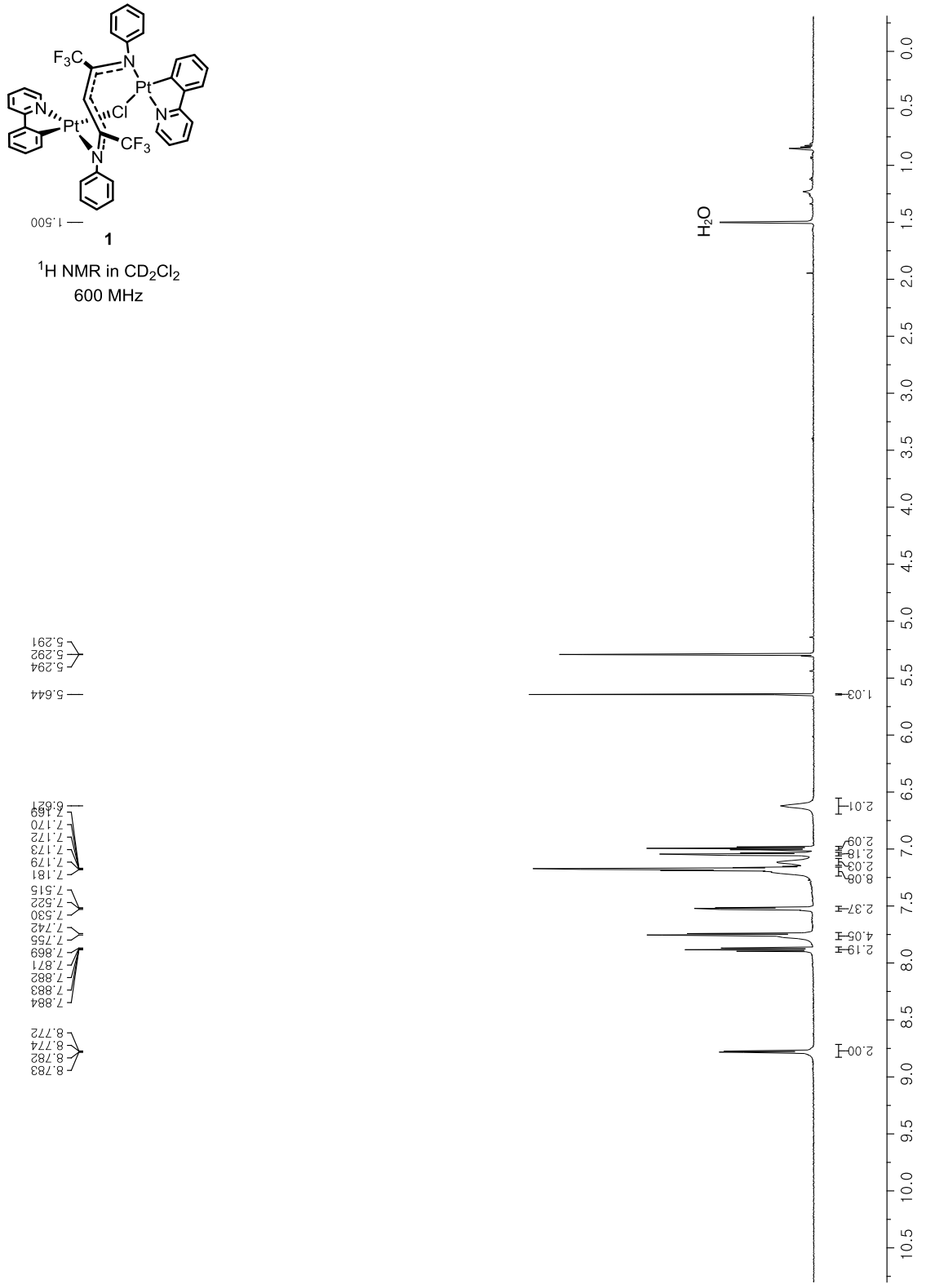

Figure A1.15. ^{1}H NMR spectrum of complex **1**, recorded at 600 MHz in CD_2Cl_2.

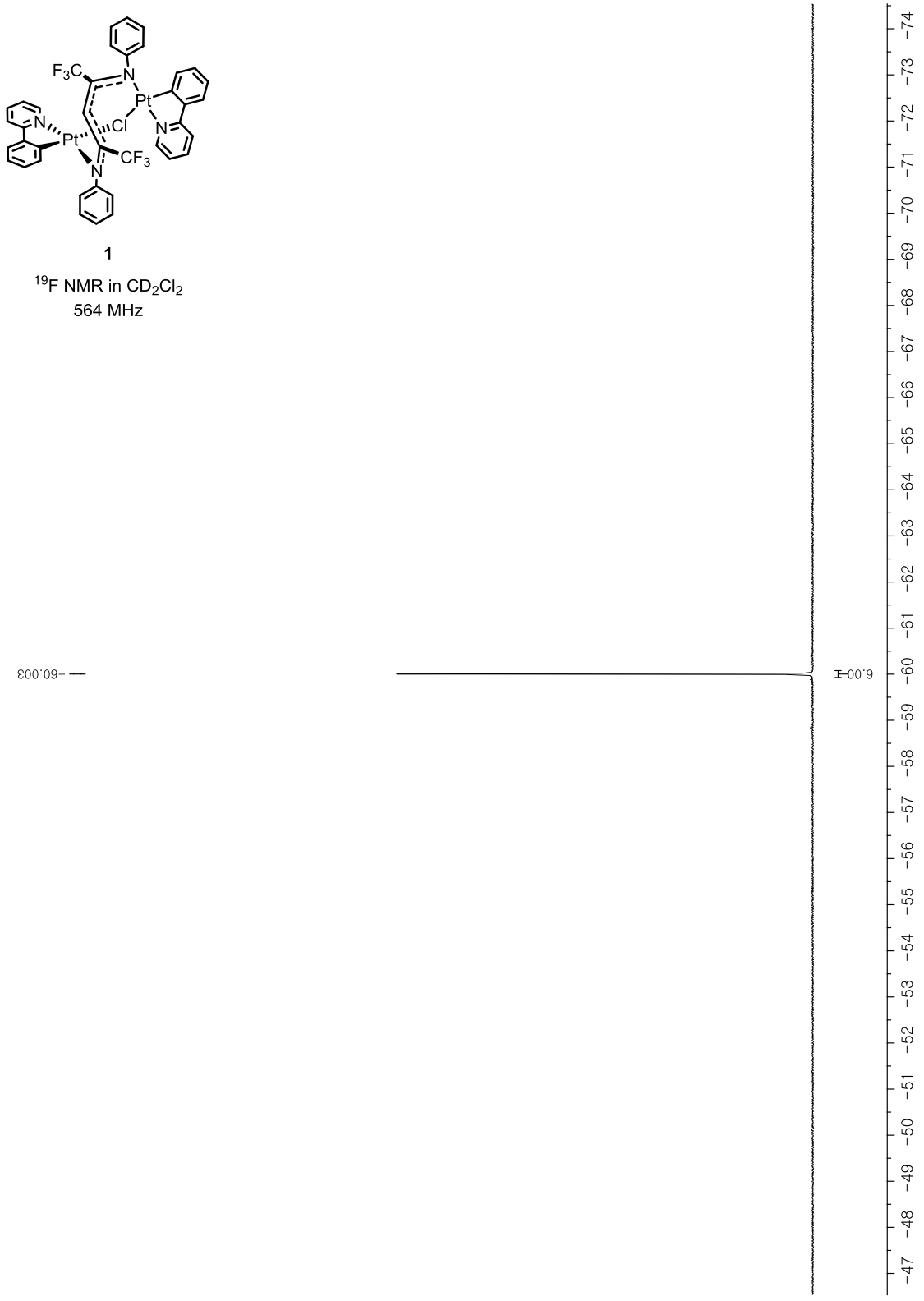

Figure A1.16. ^{19}F NMR spectrum of complex **1**, recorded at 564 MHz in CD_2Cl_2.

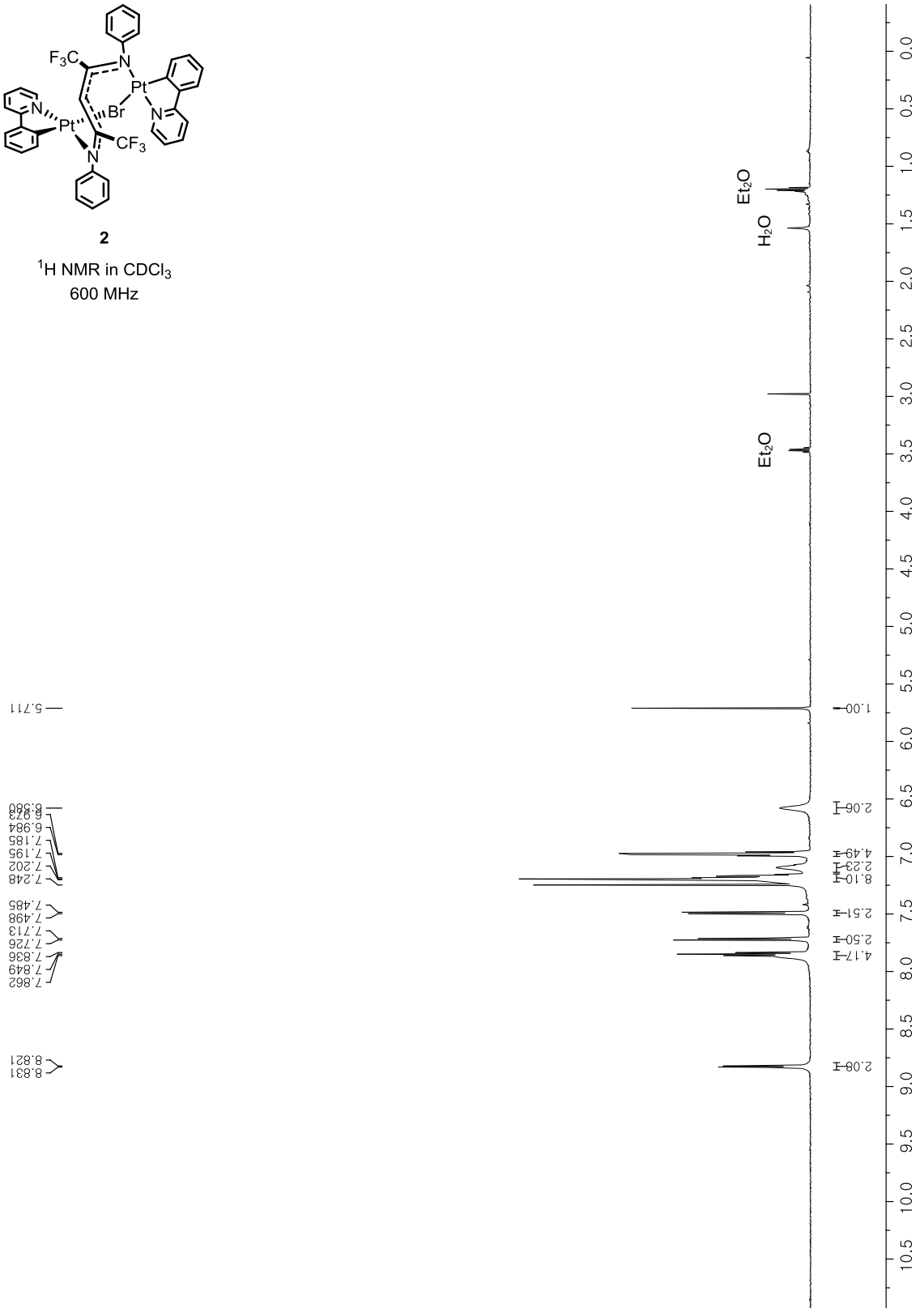

Figure A1.17. ^{1}H NMR spectrum of complex **2**, recorded at 600 MHz in $CDCl_3$.

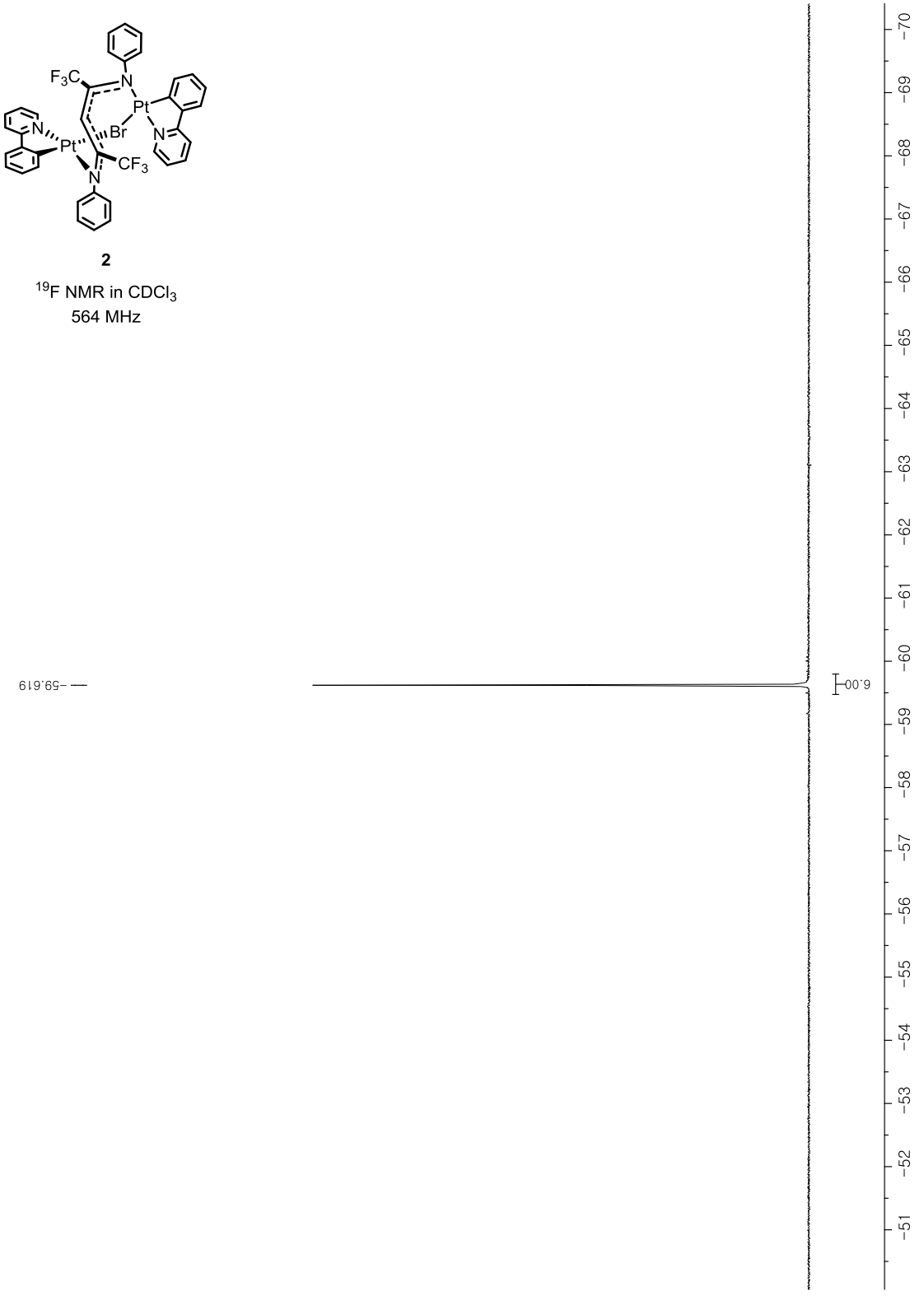

Figure A1.18. ^{19}F NMR spectrum of complex **2**, recorded at 564 MHz in $CDCl_3$.

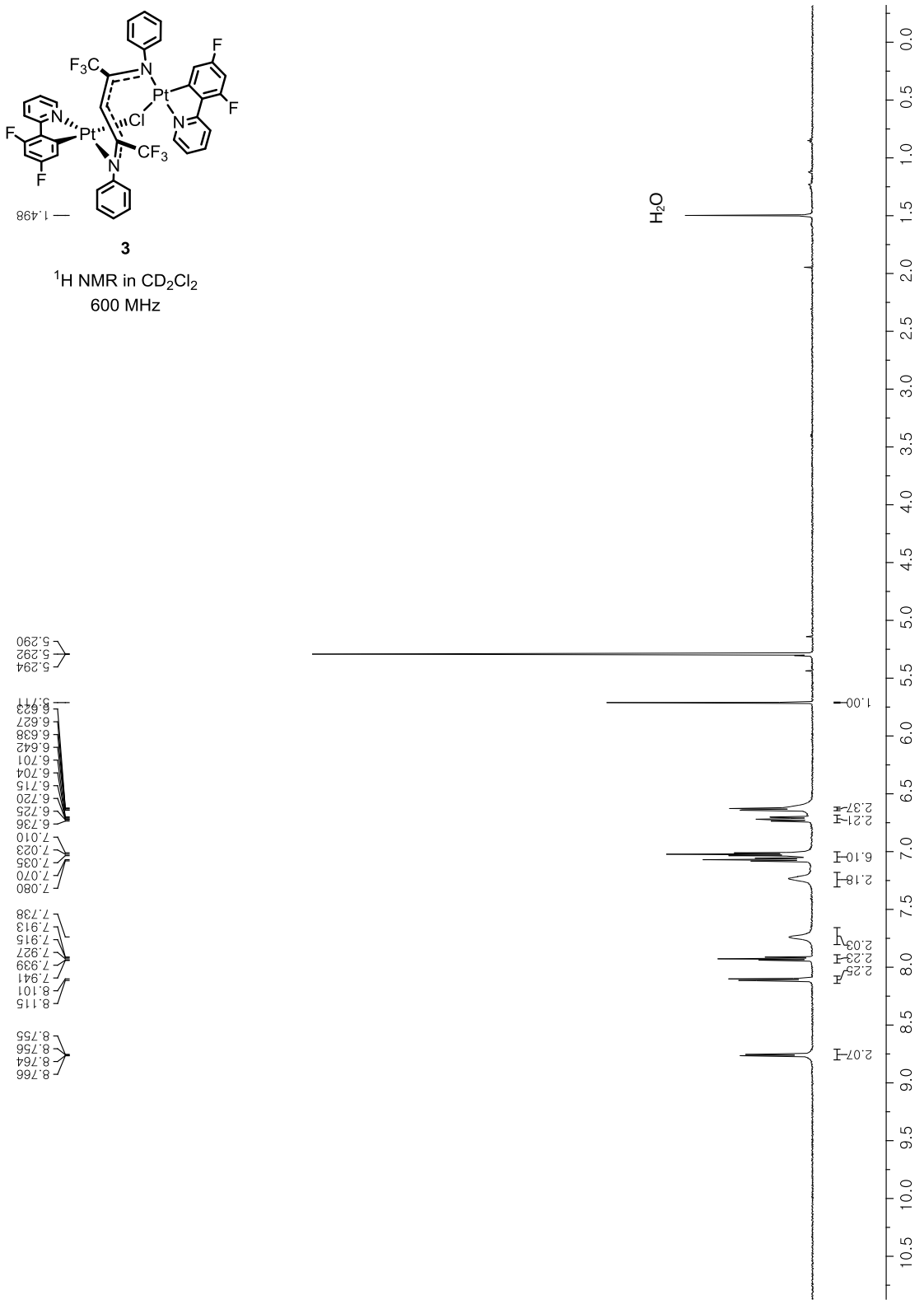

Figure A1.19. ^{1}H NMR spectrum of complex **3**, recorded at 600 MHz in CD_2Cl_2.

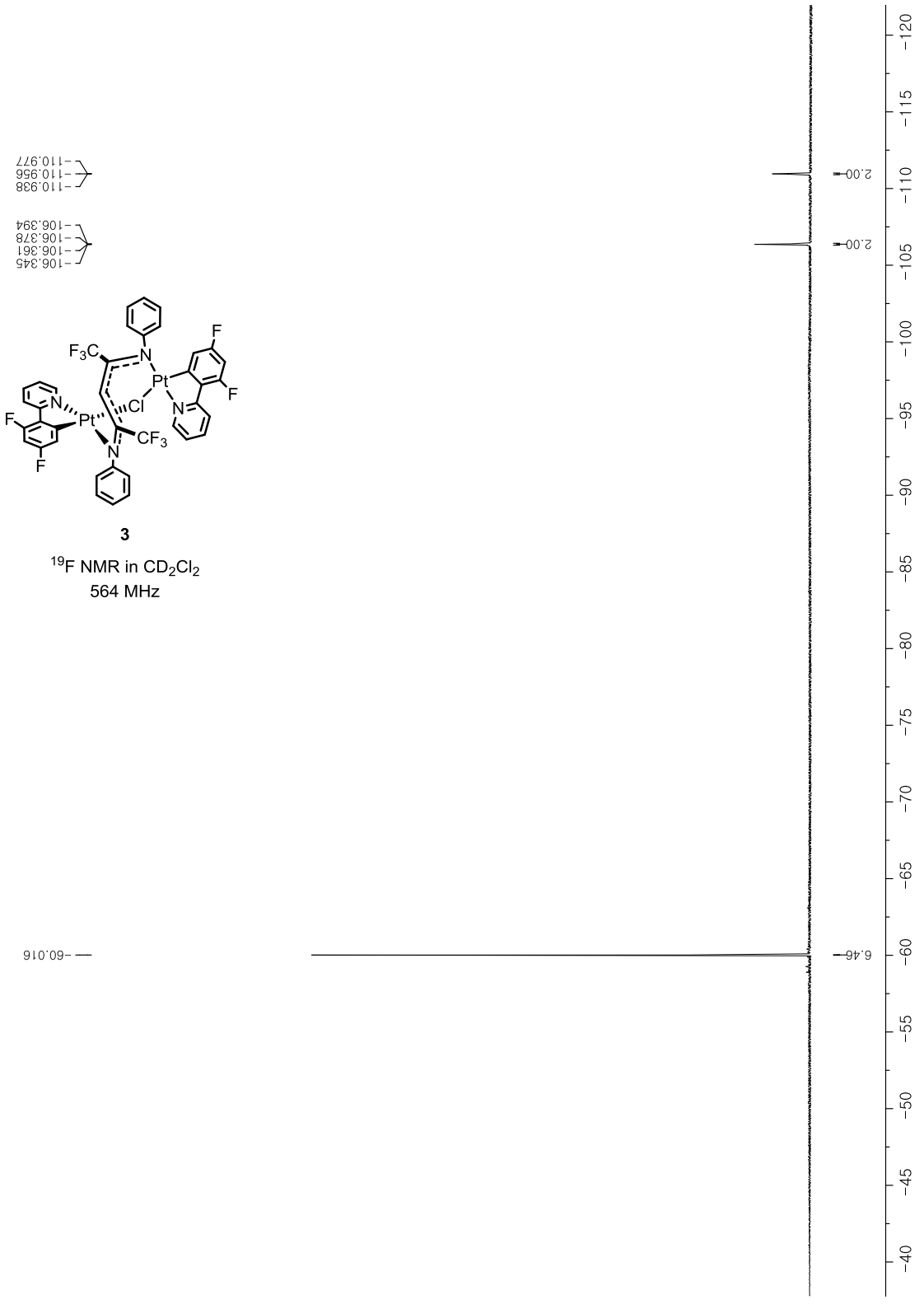

Figure A1.20. ^{19}F NMR spectrum of complex **3**, recorded at 564 MHz in CD_2Cl_2.

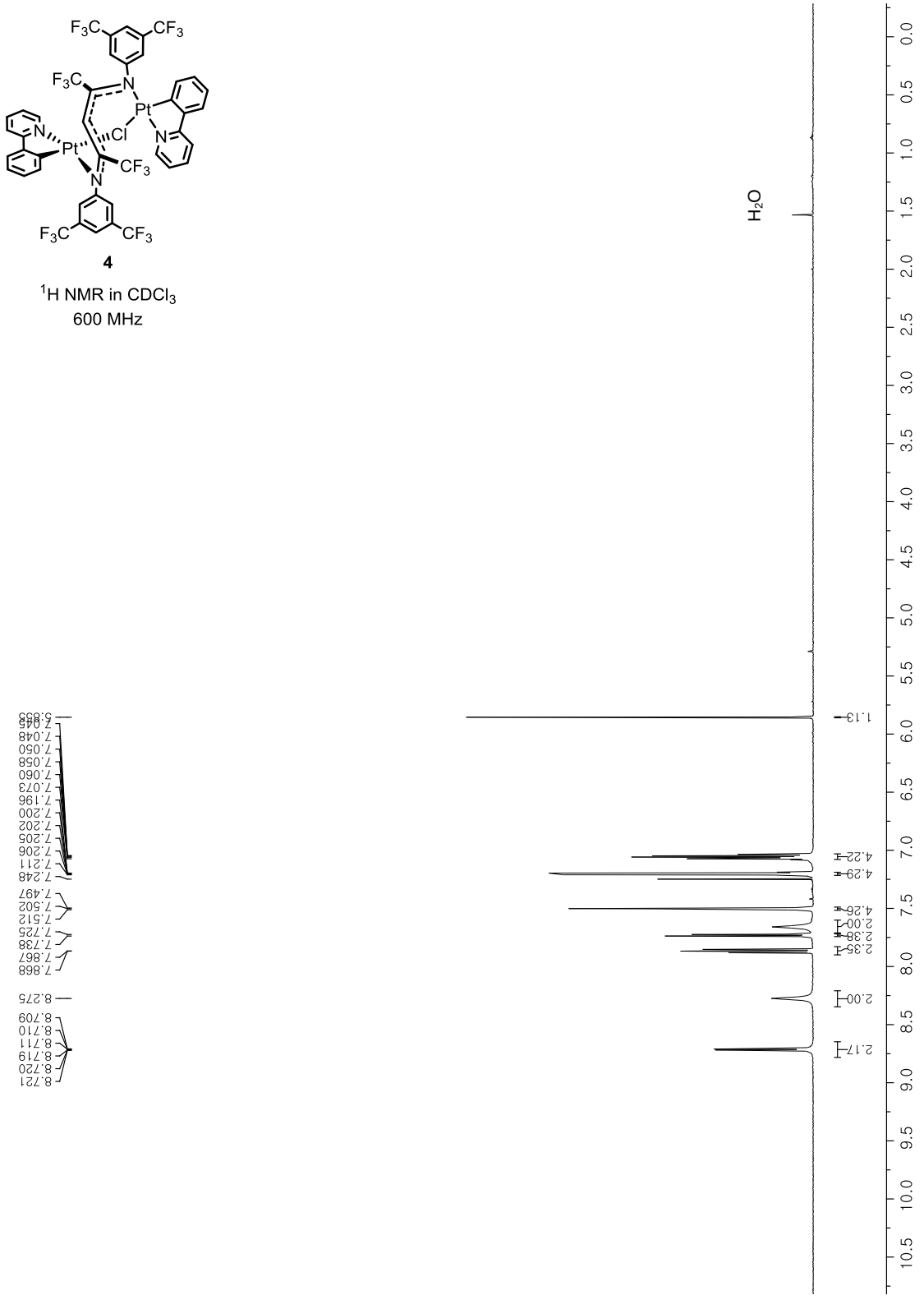

Figure A1.21. ^{1}H NMR spectrum of complex **4**, recorded at 600 MHz in $CDCl_3$.

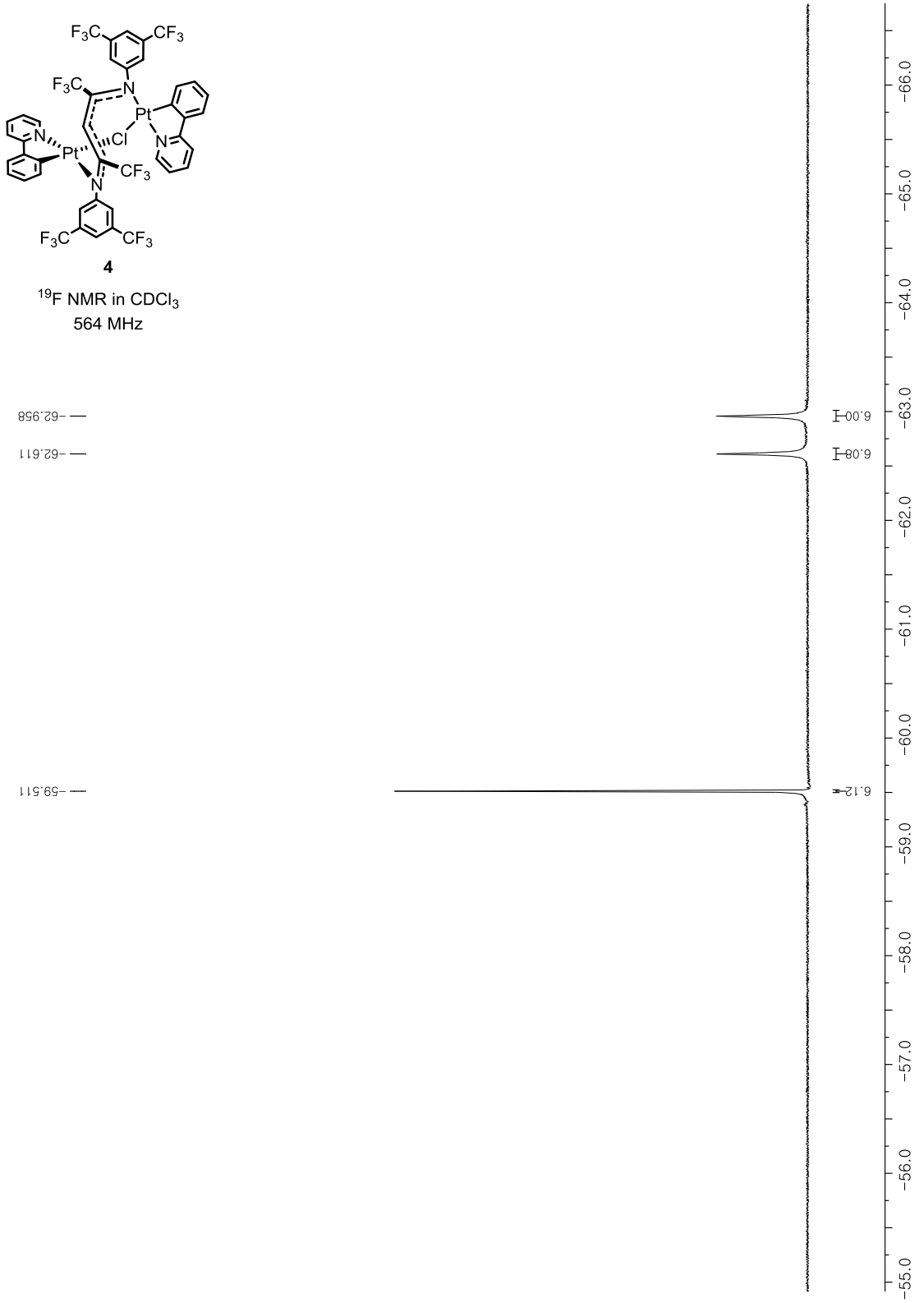

Figure A1.22. ^{19}F NMR spectrum of complex **4**, recorded at 564 MHz in $CDCl_3$.

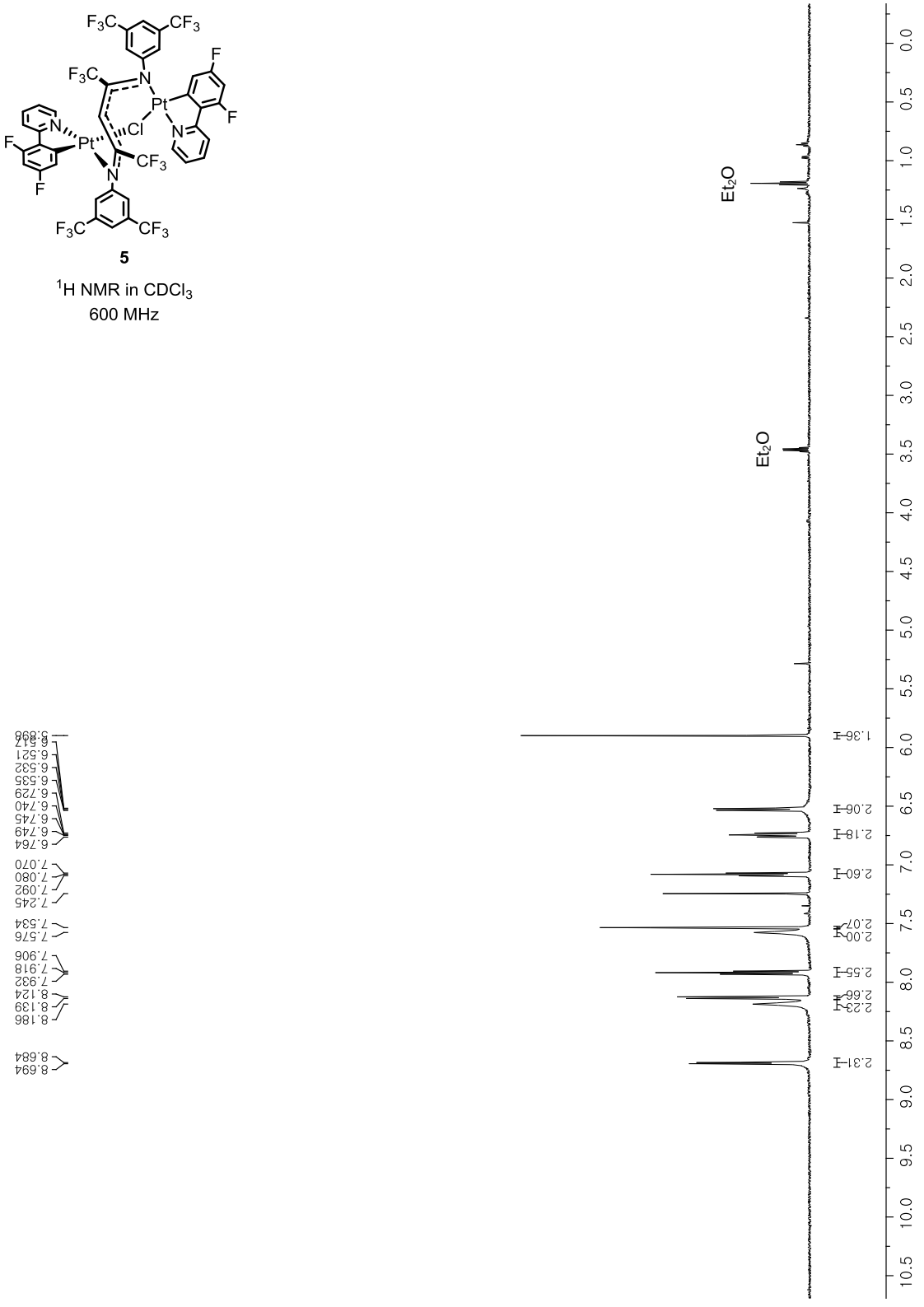

Figure A1.23. ^{1}H NMR spectrum of complex **5**, recorded at 600 MHz in $CDCl_3$.

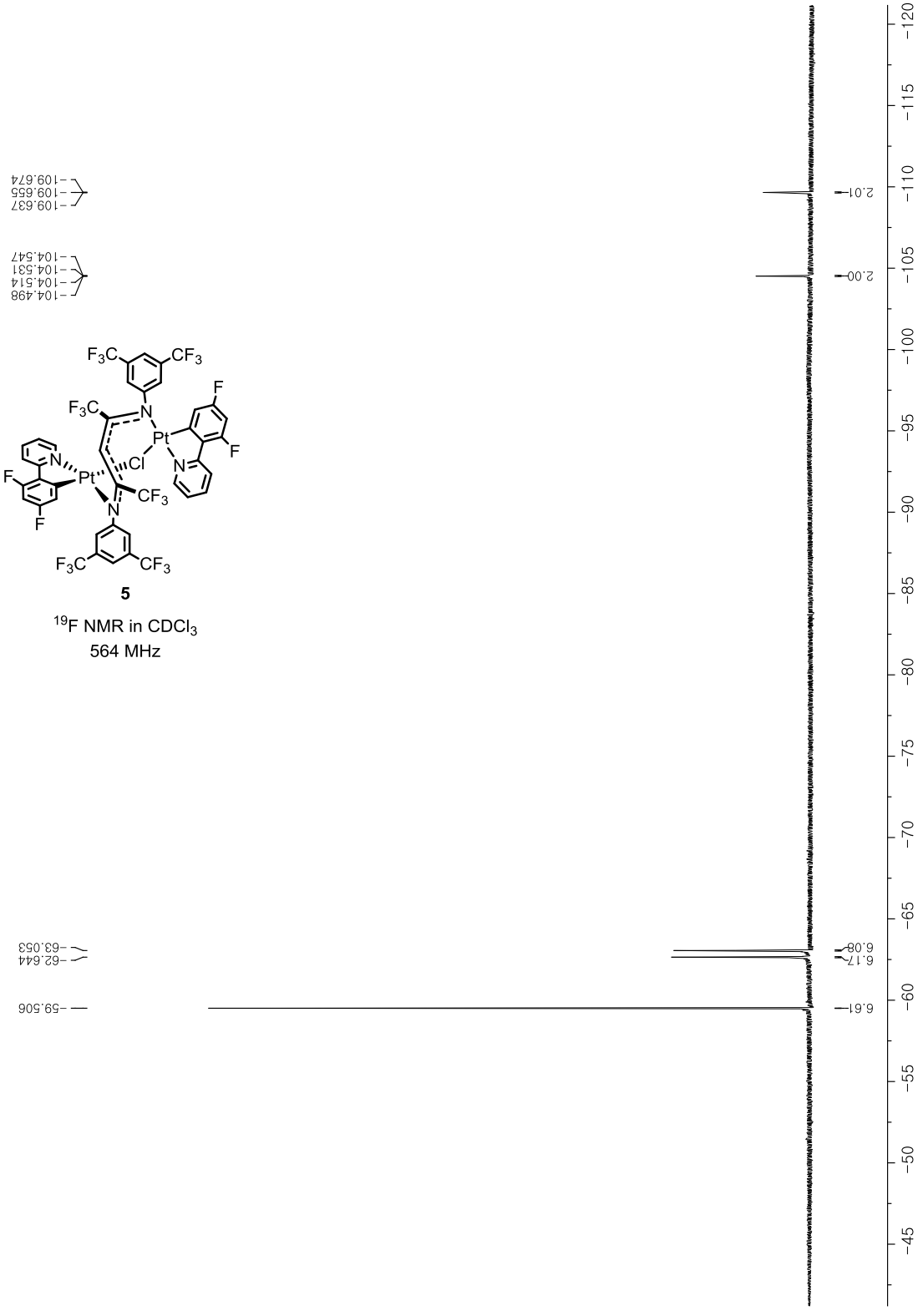

Figure A1.24. ^{19}F NMR spectrum of complex **5**, recorded at 564 MHz in $CDCl_3$.

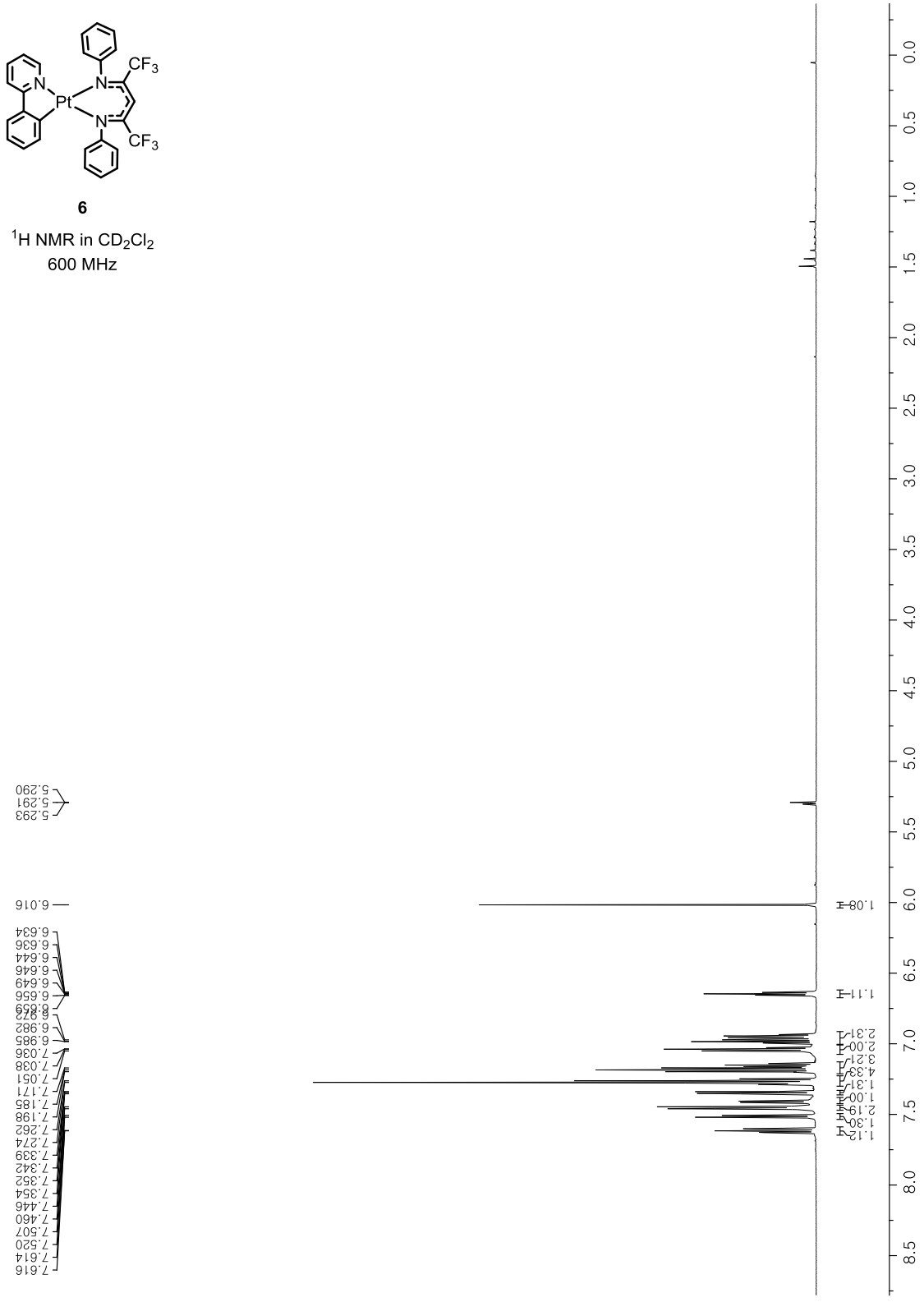

Figure A1.25. ^{1}H NMR spectrum of complex **6**, recorded at 600 MHz in CD_2Cl_2.

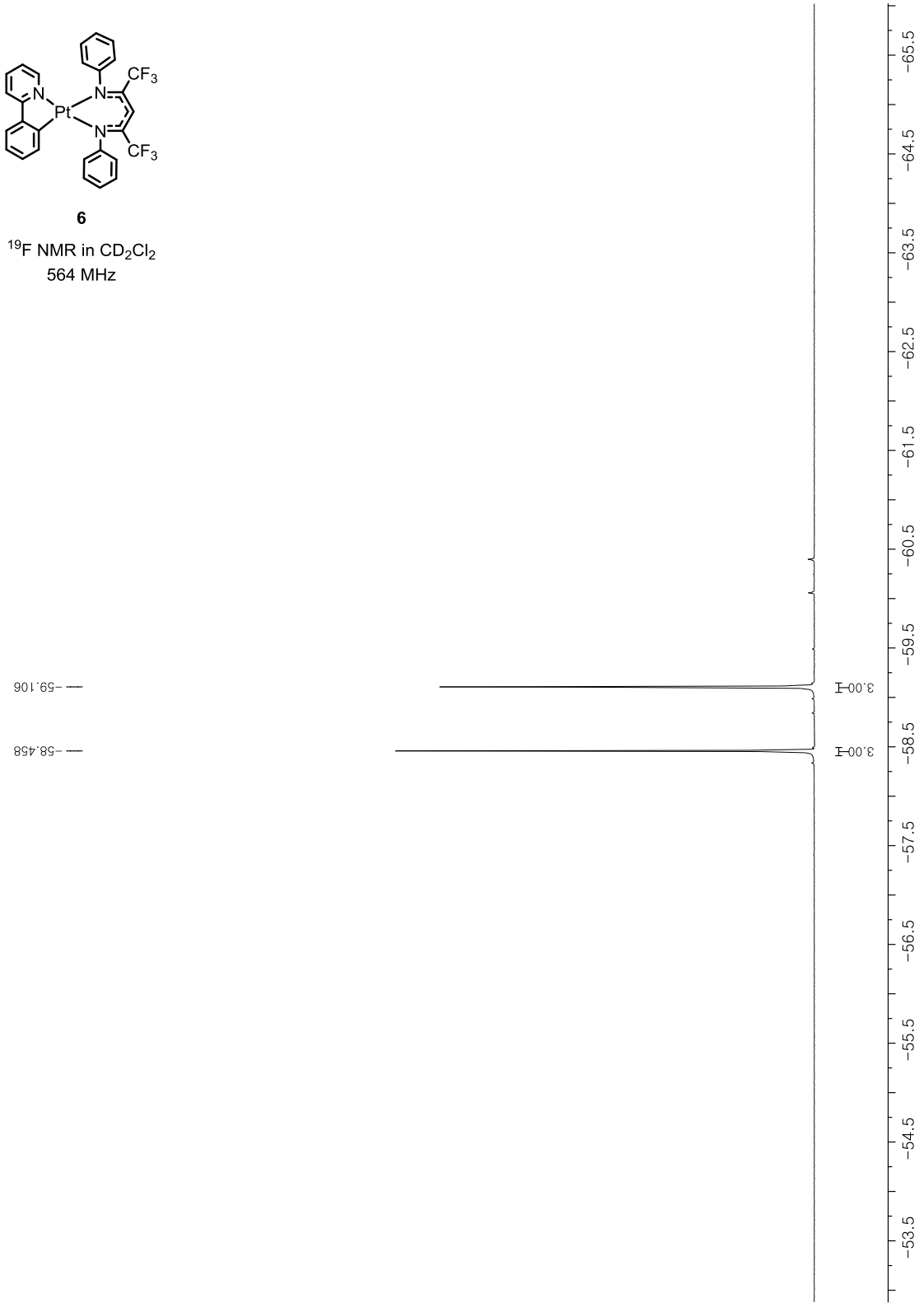

Figure A1.26. ^{19}F NMR spectrum of complex **6**, recorded at 564 MHz in $CDCl_3$.

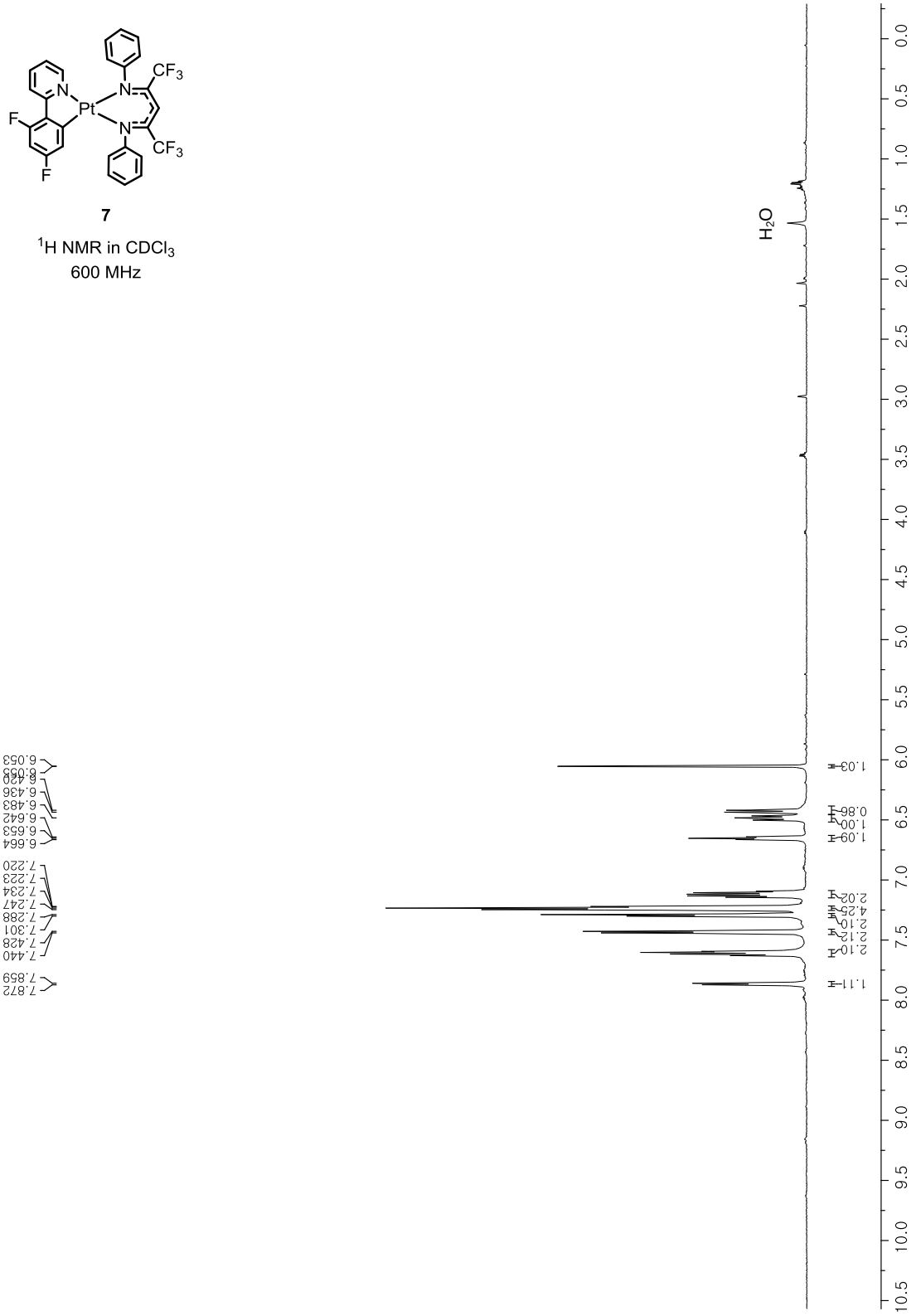

Figure A1.27. ^{1}H NMR spectrum of complex **7**, recorded at 600 MHz in $CDCl_3$.

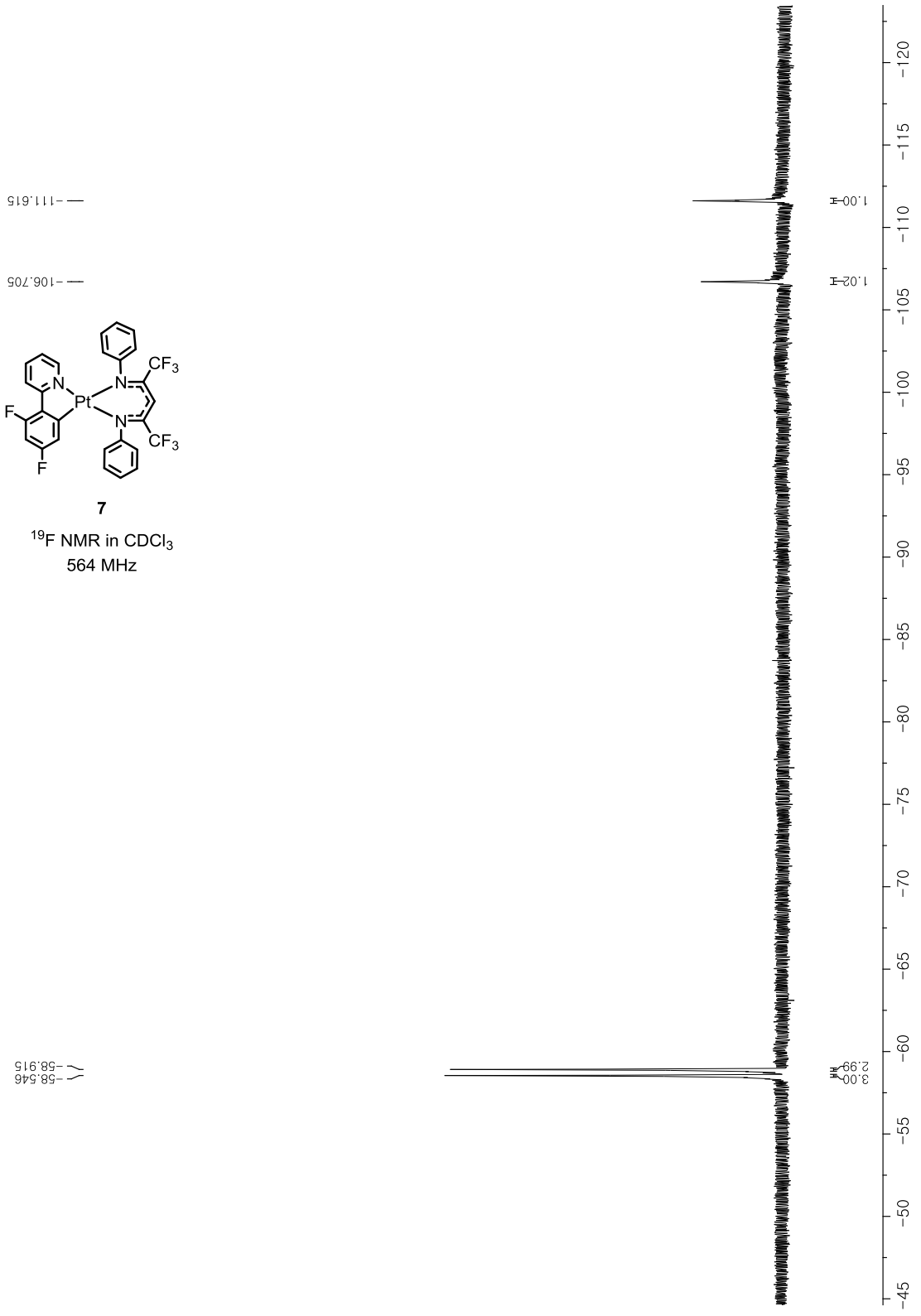

Figure A1.28. ^{19}F NMR spectrum of complex **7**, recorded at 564 MHz in $CDCl_3$.

Appendix 2. Lewis Acid Modulation of aza-BODIPY and *meso*-Pyridyl BODIPY Chromophores

A2.1. Stacked NMR spectra of $B(C_6F_5)_3$ adducts of 1

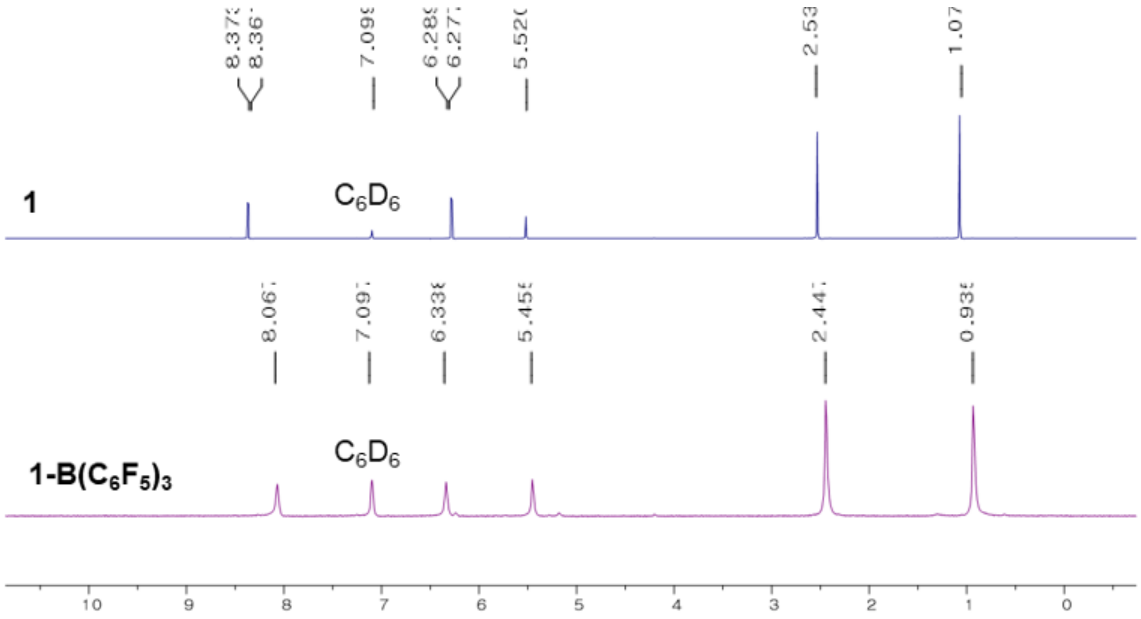

Figure A2.1. Stacked ^{1}H NMR spectra of complex **1** and its $B(C_6F_5)_3$ adduct in C_6D_6 at room temperature.

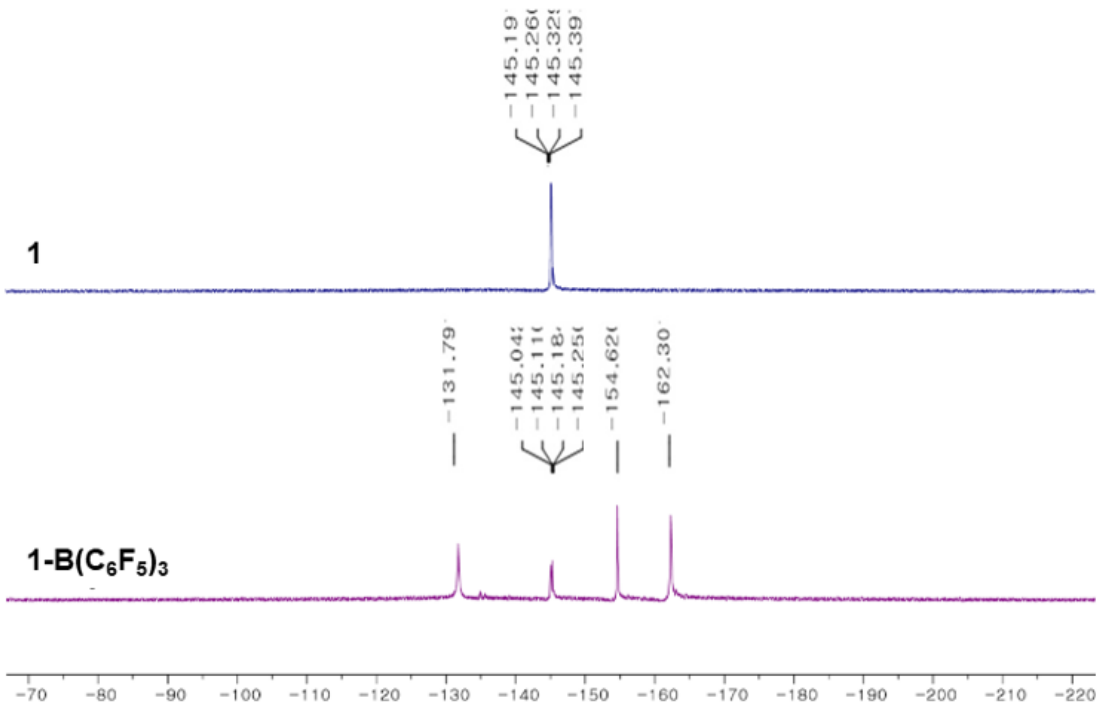

Figure A2.2. Stacked ^{19}F NMR spectra of complex **1** and its $B(C_6F_5)_3$ adduct in C_6D_6 at room temperature.

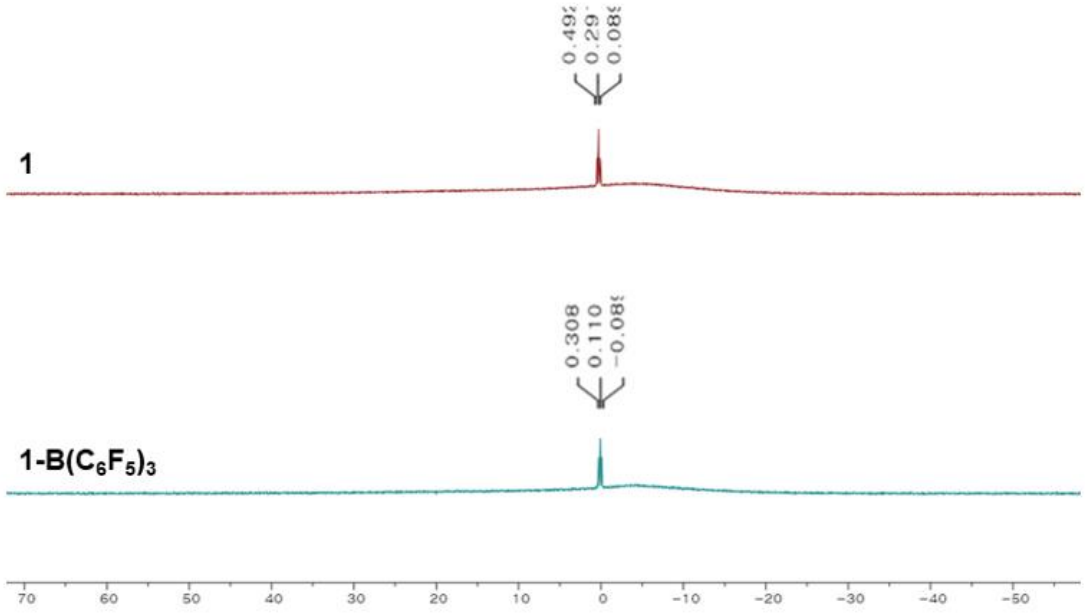

Figure A2.3. Stacked ^{11}B NMR spectra of complex **1** and its $B(C_6F_5)_3$ adduct in C_6D_6 at room temperature.

A2.2. Stacked NMR spectra of $B(C_6F_5)_3$ adducts of 2

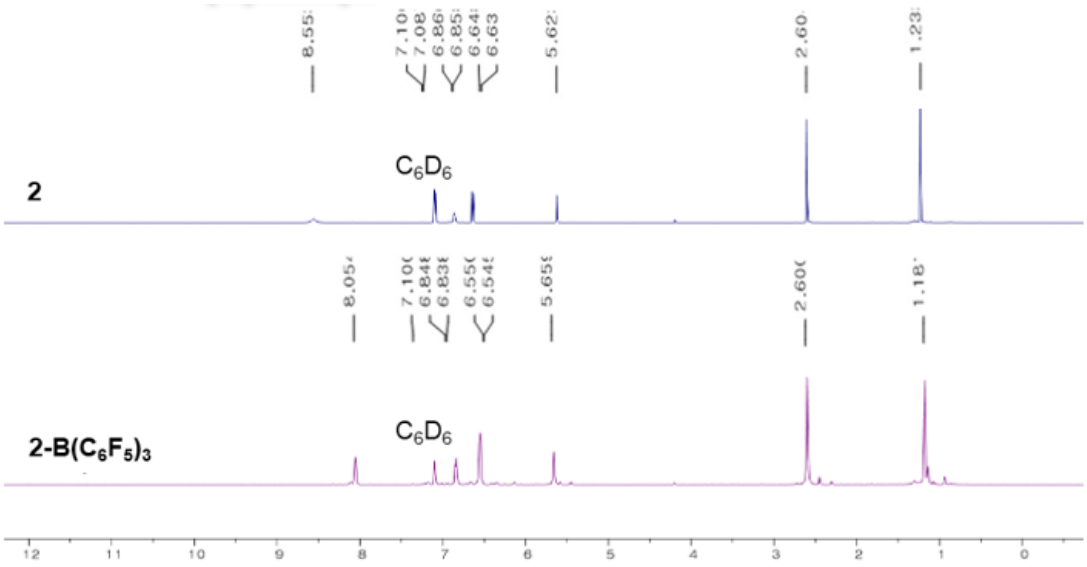

Figure A2.4. Stacked ^{1}H NMR spectra of complex **2** and its $B(C_6F_5)_3$ adduct in C_6D_6 at room temperature.

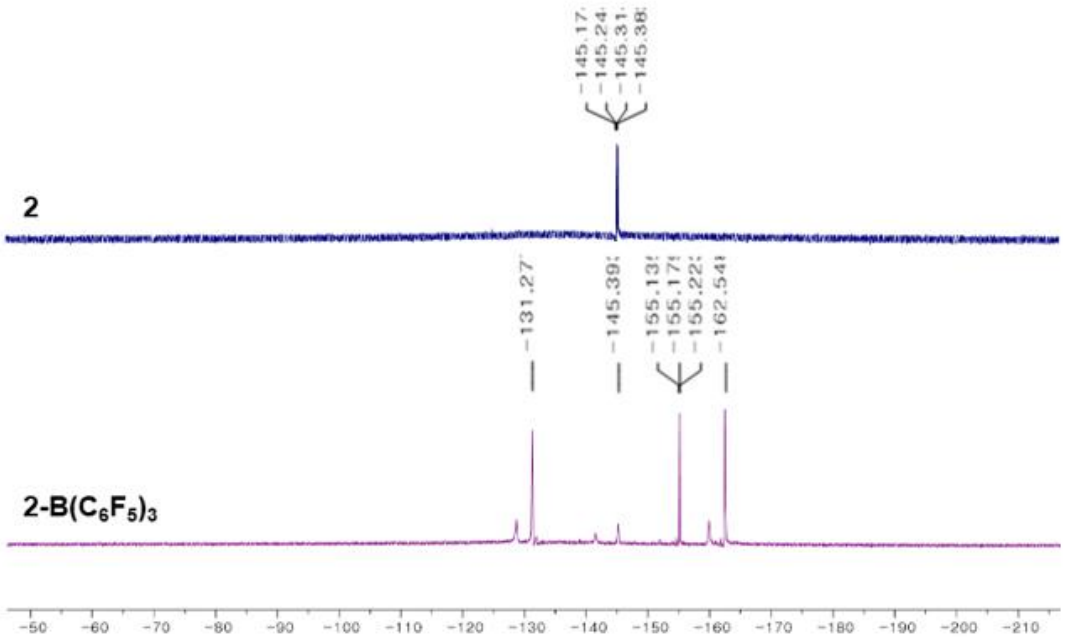

Figure A2.5. Stacked ^{19}F NMR spectra of complex **2** and its $B(C_6F_5)_3$ adduct in C_6D_6 at room temperature.

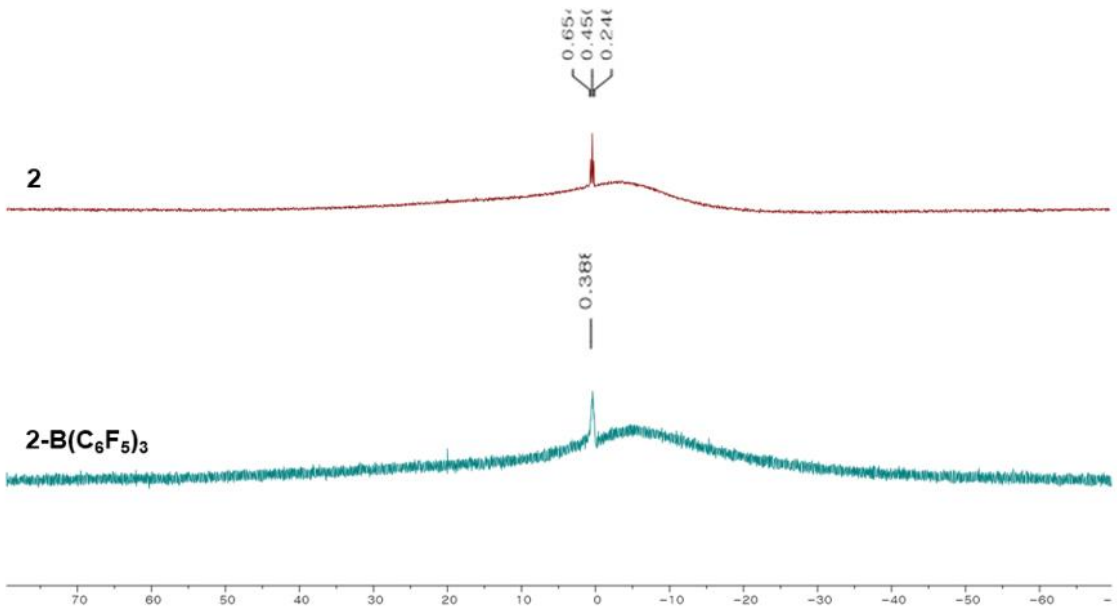

Figure A2.6. Stacked ^{11}B NMR spectra of complex **2** and its $B(C_6F_5)_3$ adduct in C_6D_6 at room temperature.

A2.3. Stacked NMR spectra of $B(C_6F_5)_3$ adducts of 4

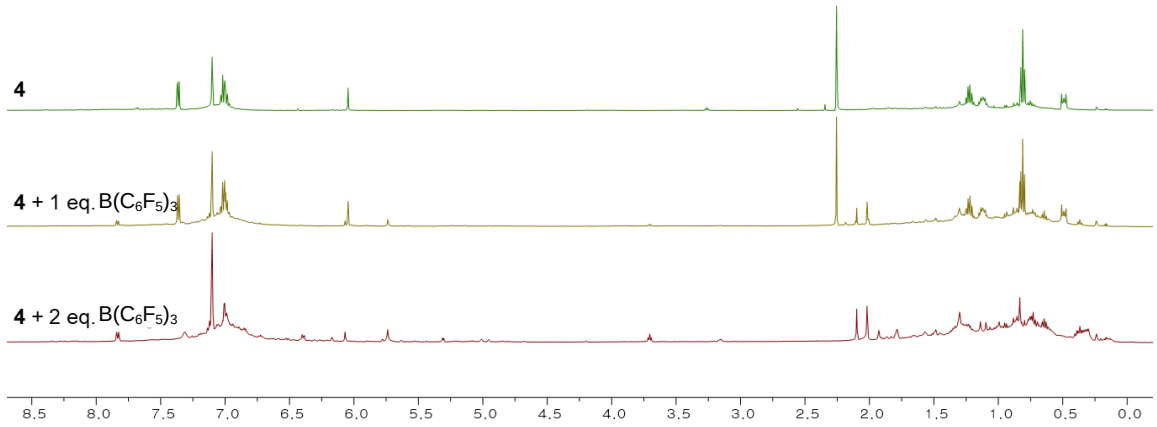

Figure A2.7. Stacked ^{1}H NMR spectra of complex **4** and $B(C_6F_5)_3$ adducts in C_6D_6 at room temperature.

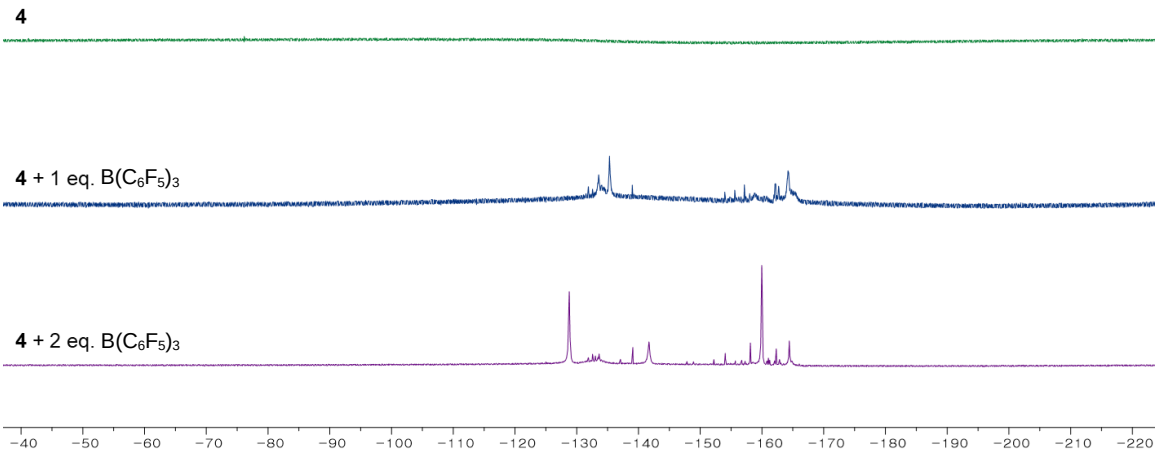

Figure A2.8. Stacked ^{19}F NMR spectra of complex **4** and $B(C_6F_5)_3$ adducts in C_6D_6 at room temperature.

A2.4. X-ray crystallography summary tables

Table A2.1. Summary of X-ray crystallographic data for **2** and **2**-B(C_6F_5)$_3$.

	2	**2**-B(C_6F_5)$_3$
Crystal data		
Chemical formula	$C_{24}H_{22}BF_2N_3$	$C_{43}H_{24}B_2Cl_2F_{17}N_3$
M_r	401.25	998.17
Crystal system, space group	Monoclinic, $P2_1/c$	Triclinic, $P\bar{1}$
Temperature (K)	123	123
a, b, c (Å)	12.156 (2), 10.483 (2), 16.454 (3)	11.0247 (17), 12.8448 (19), 15.084 (2)
α, β, γ (°)	111.218 (3)	79.630 (2), 79.138 (2), 87.039 (2)
V (Å ^{3})	1954.8 (7)	2063.2 (5)
Z	4	2
μ (mm^{-1})	0.09	0.27
Crystal size (mm)	0.36 × 0.10 × 0.01	0.30 × 0.26 × 0.12
Data collection		
T_{min}, T_{max}	0.700, 0.746	0.716, 0.746
No. of measured, independent and observed [$I > 2\sigma(I)$] reflections	18225, 3714, 2827	37515, 9496, 7595
R_{int}	0.033	0.017
(sin θ/λ)$_{max}$ (Å $^{-1}$)	0.610	0.651
Refinement		
$R[F^2 > 2\sigma(F^2)]$, $wR(F^2)$, S	0.037, 0.092, 1.01	0.073, 0.226, 1.04
No. of reflections	3714	9496
No. of parameters	275	622
No. of restraints	0	41
	$w = 1/[\sigma^2(F_o^2) + (0.0416P)^2 + 0.7276P]$ where $P = (F_o^2 + 2F_c^2)/3$	$w = 1/[\sigma^2(F_o^2) + (0.1268P)^2 + 2.7185P]$ where $P = (F_o^2 + 2F_c^2)/3$
$\Delta\rho_{max}$, $\Delta\rho_{min}$ (e Å $^{-3}$)	0.23, −0.18	1.74, −0.60

A2.5. Emission spectra for titration of 4 with $B(C_6F_5)_3$ in C_6H_6

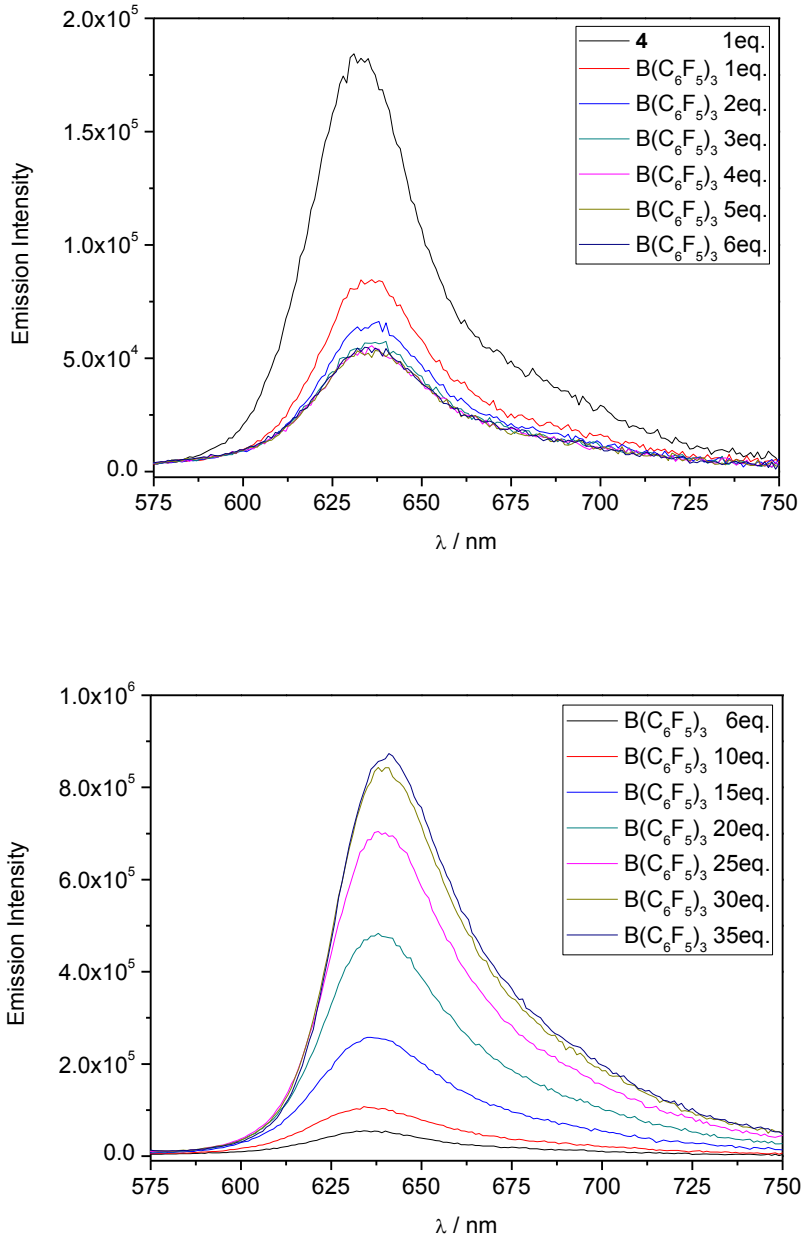

Figure A2.9. Emission spectra for aza-BODIPY **4** (7.7×10^{-5} M) on titration with increasing $B(C_6F_5)_3$ up to 35 equivalents upon excitation at 520 nm. The upper graph shows titration with $B(C_6F_5)_3$ up to 6 equivalents (4.6×10^{-4} M), whereas the bottom shows titration from 6 equivalents to 35 equivalents (2.7×10^{-3} M) in benzene.

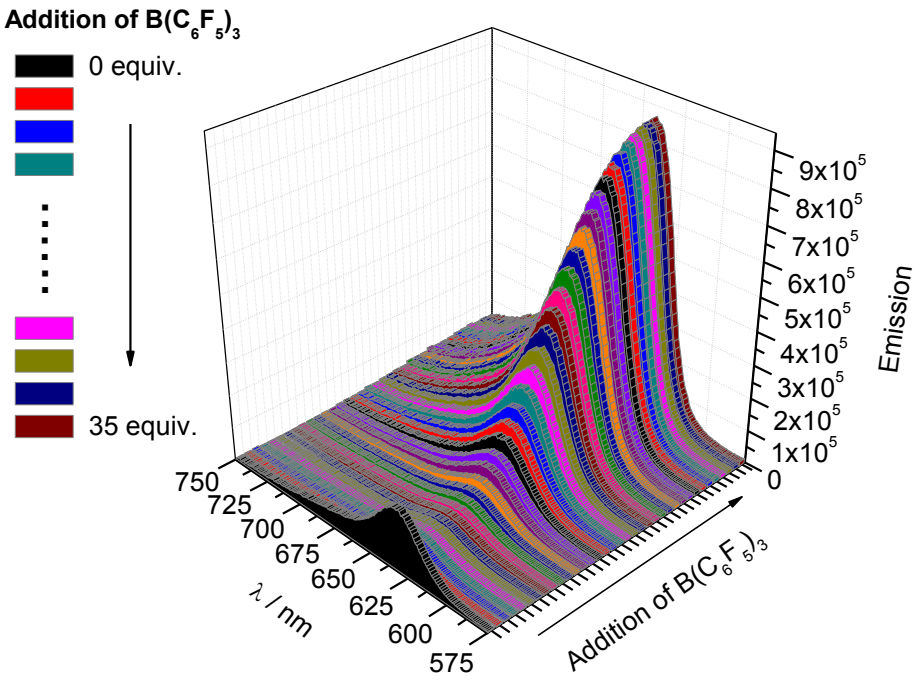

Figure A2.10. Emission spectra (3D version) for aza-BODIPY **4** (7.7×10^{-5} M) when titrated with $B(C_6F_5)_3$ (1–35 equivalents) in benzene at room temperature. Excitation for emission spectra was at 520 nm.

A2.6. NMR spectra of complex 2

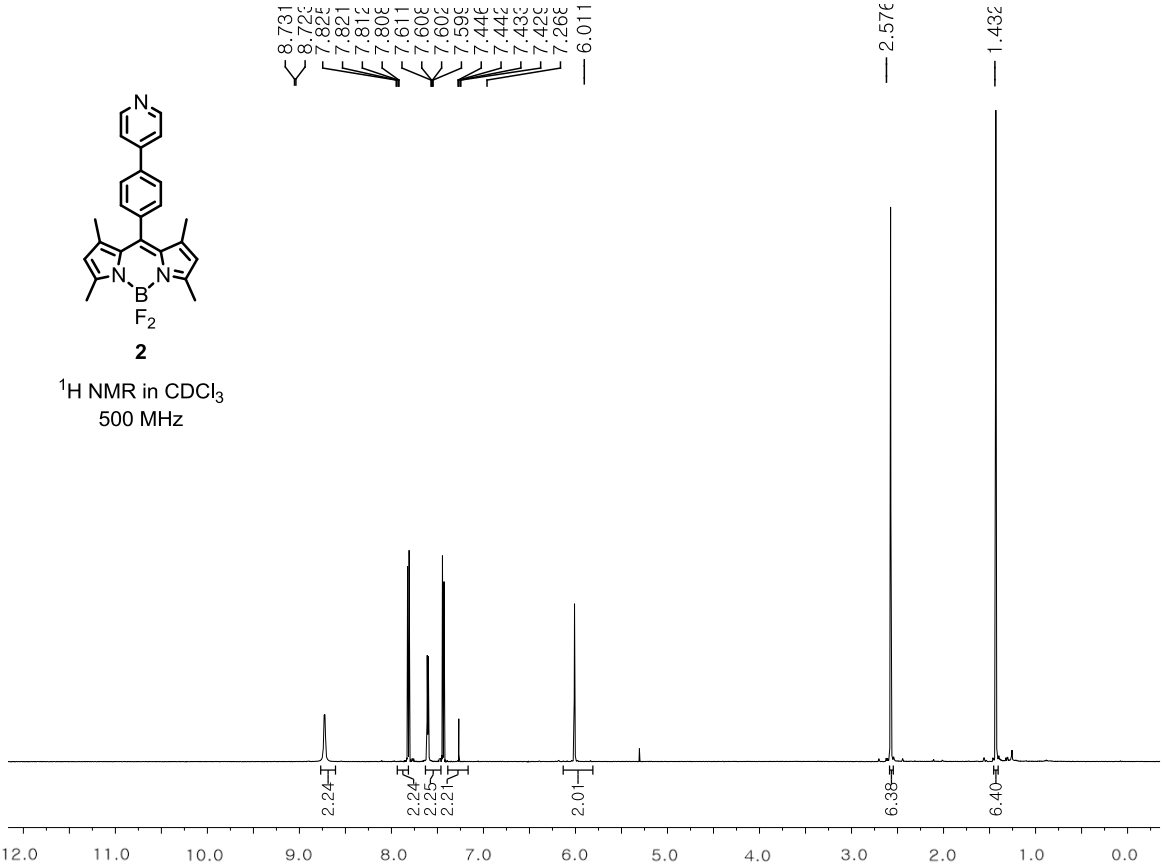

Figure A2.11. ^{1}H NMR spectrum of complex **2**, recorded at 500 MHz in $CDCl_3$.

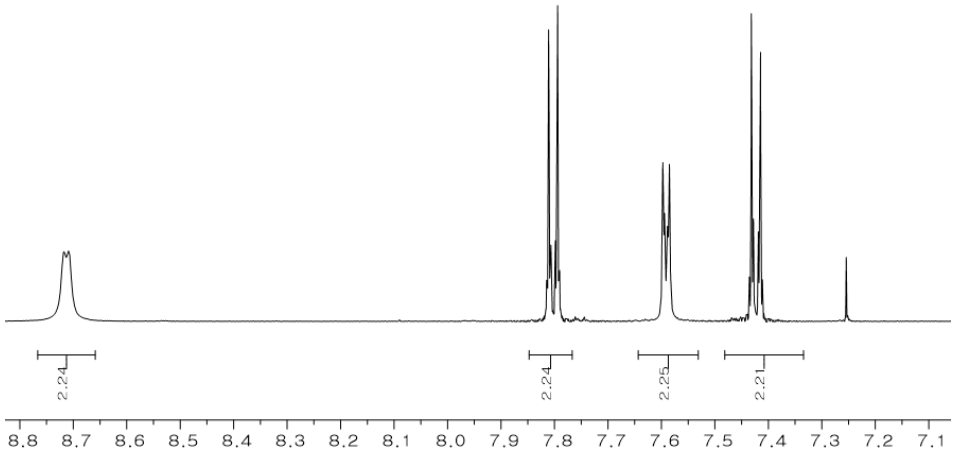

Figure A2.12. ^{1}H NMR spectrum inset for complex **2**, showing the aromatic region. Spectrum was recorded at 500 MHz in $CDCl_3$.

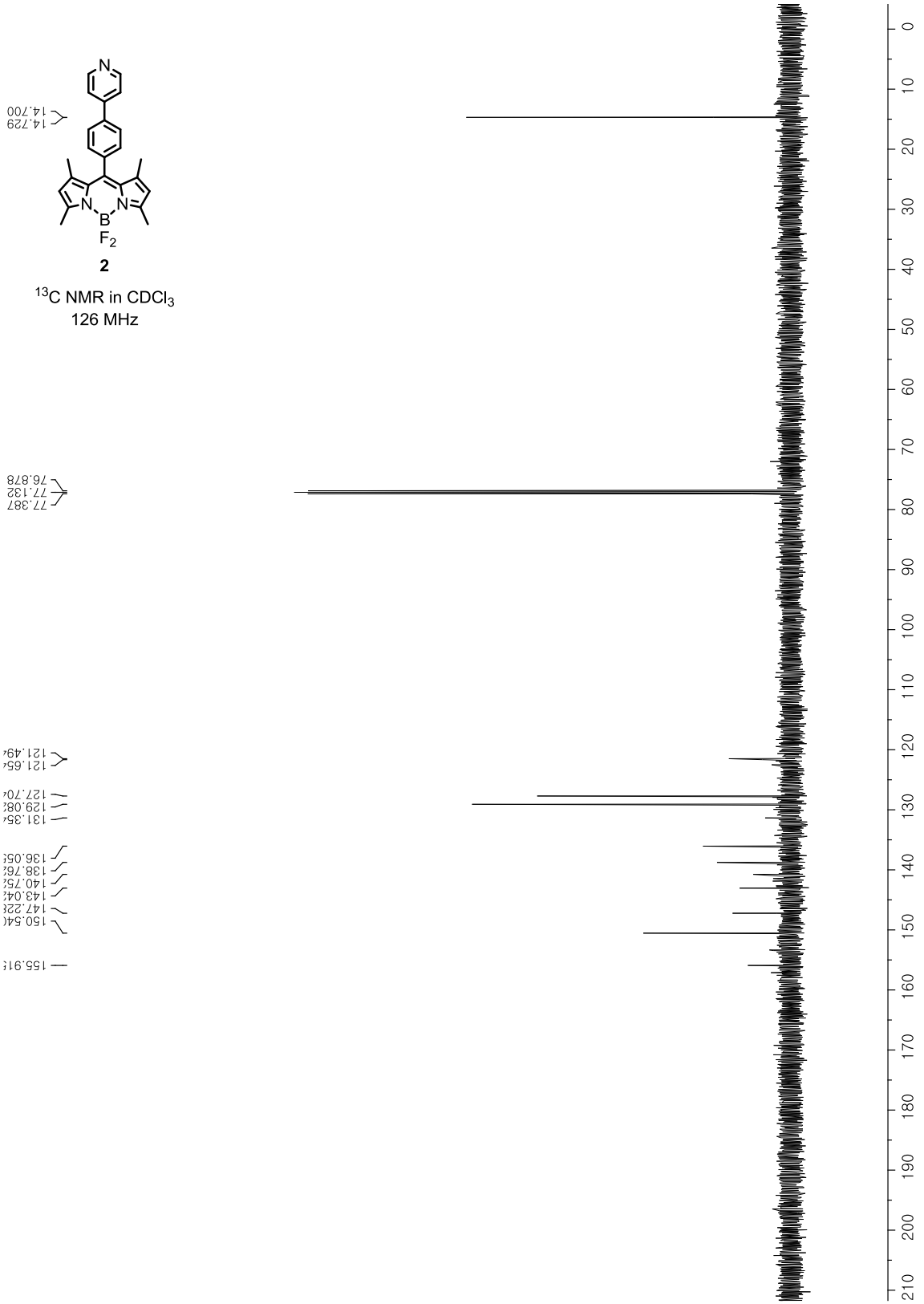

Figure A2.13. $^{13}C\{^{1}H\}$ NMR spectrum of complex **2**, recorded at 126 MHz in $CDCl_3$.

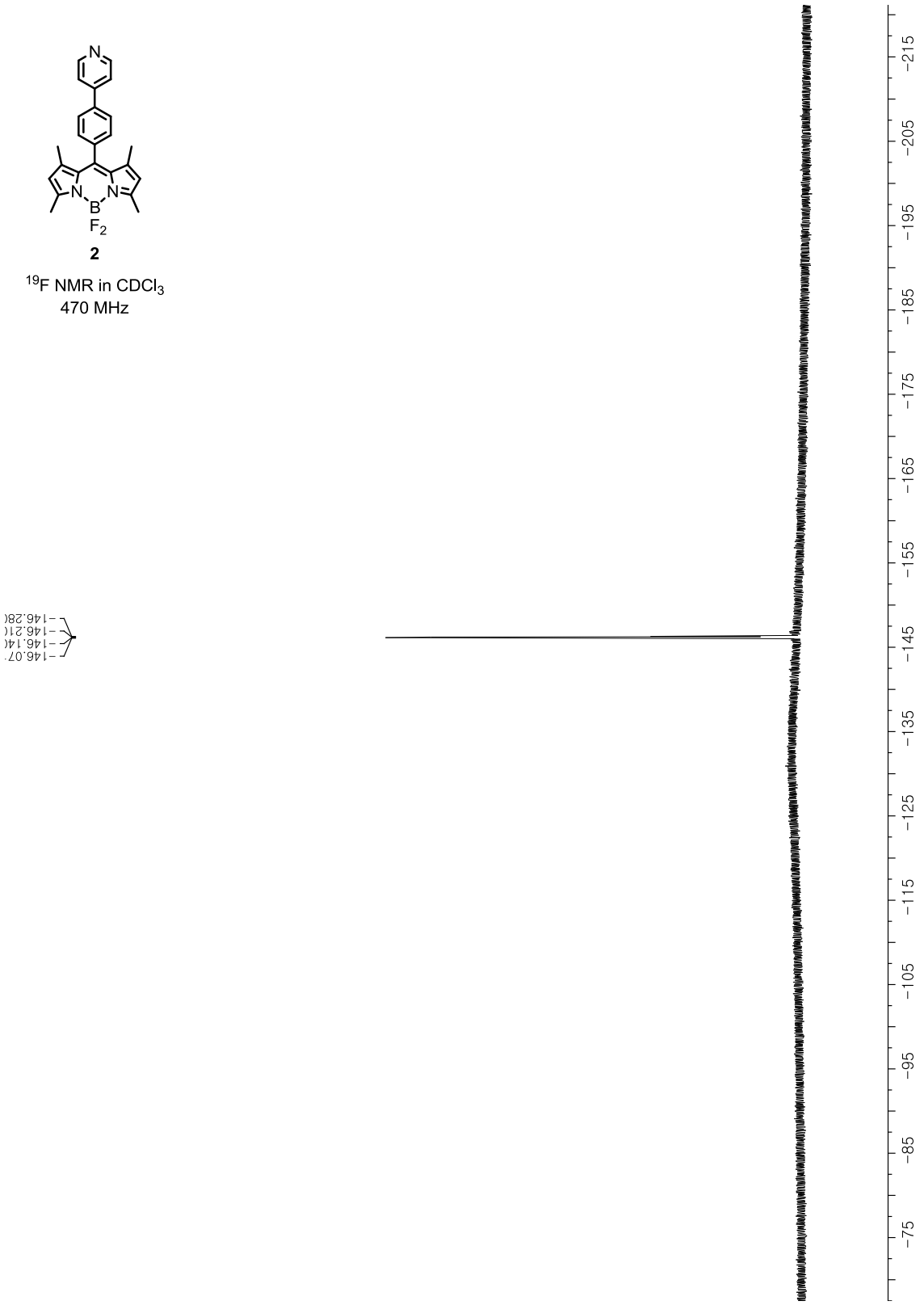

Figure A2.14. ^{19}F NMR spectrum of complex **2**, recorded at 470 MHz in $CDCl_3$.

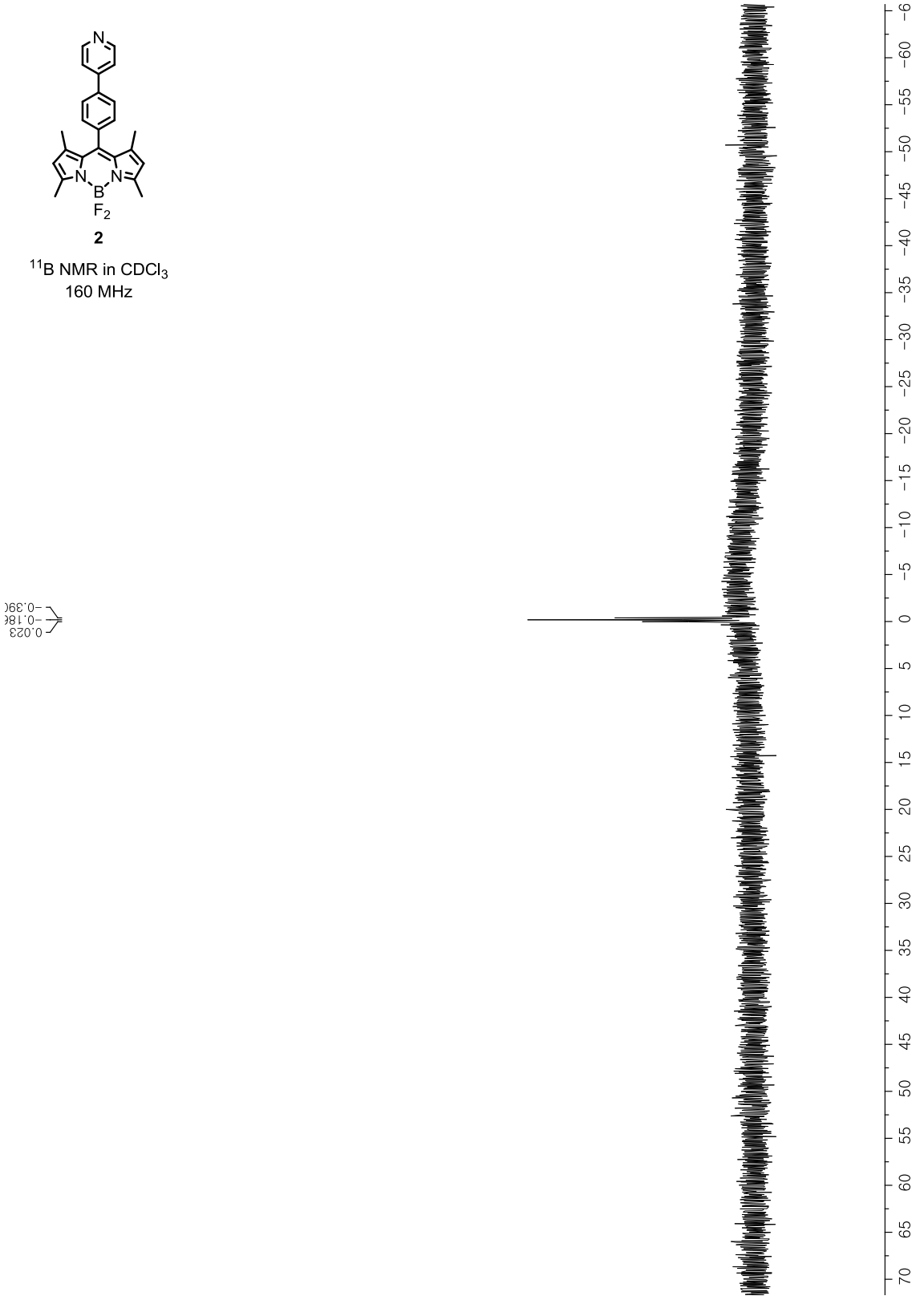

Figure A2.15. ^{11}B NMR spectrum of complex **2**, recorded at 160 MHz in $CDCl_3$.

A2.7. NMR spectra of complex 4

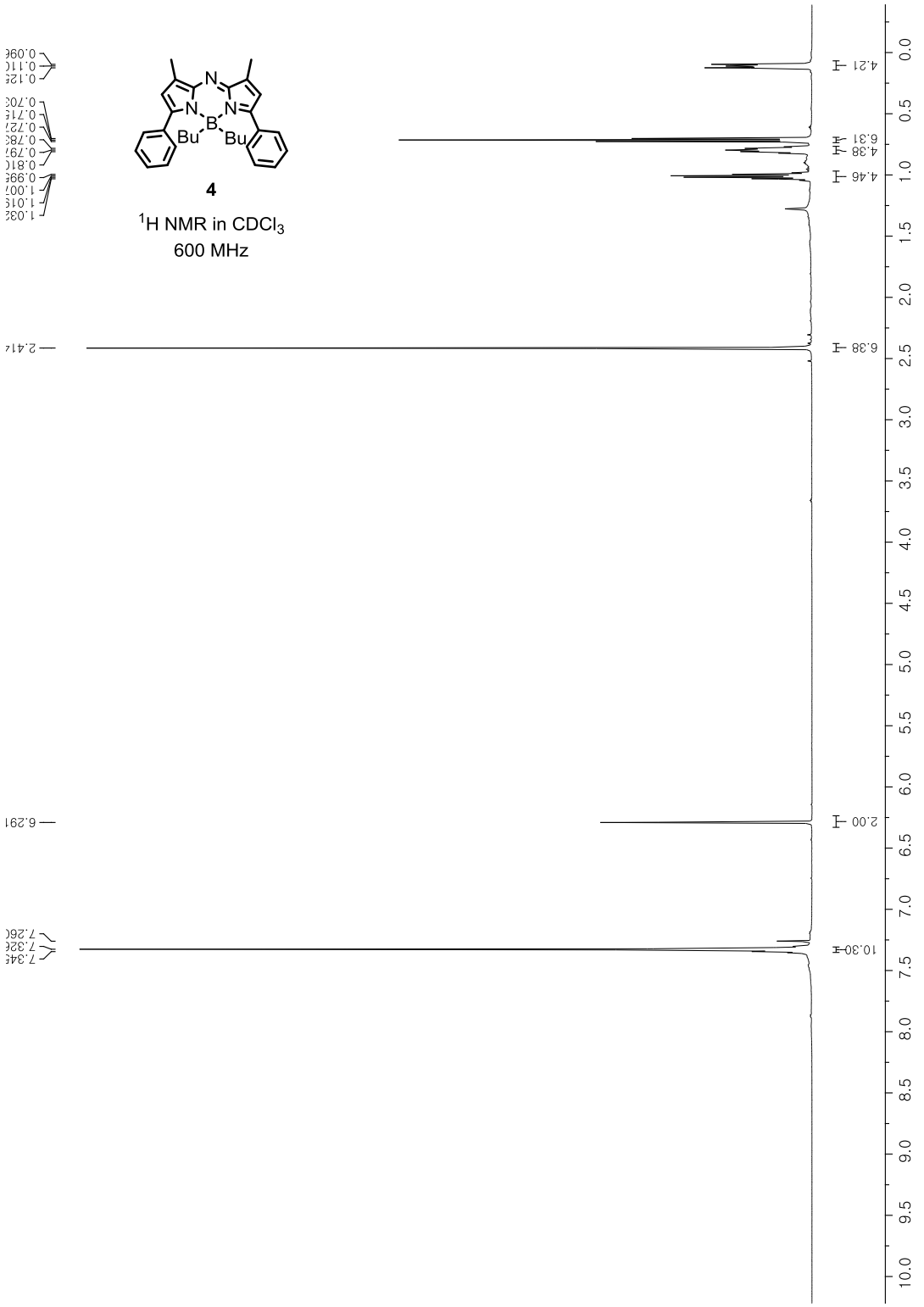

Figure A2.16. ^{1}H NMR spectrum of complex **4**, recorded at 600 MHz in $CDCl_3$.

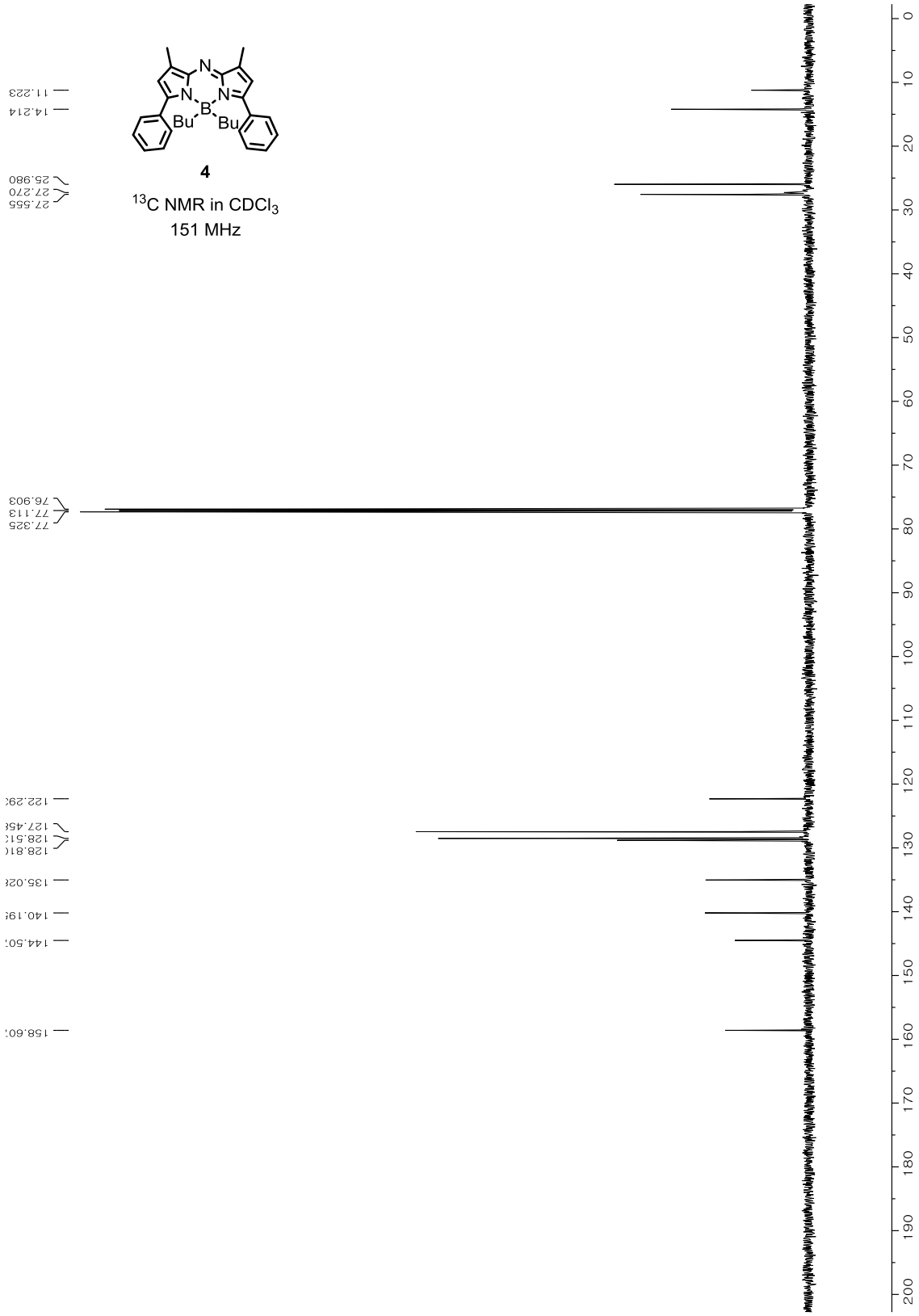

Figure A2.17. $^{13}C\{^{1}H\}$ NMR spectrum of complex **4**, recorded at 151 MHz in $CDCl_3$.

A2.8. Excitation spectra of complexes 1 and 2

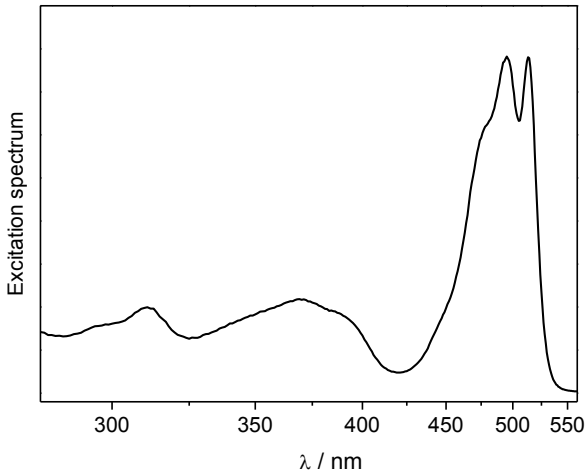

Figure A2.18. Excitation spectrum of complex **1**, recorded in dichloromethane at room temperature. For the excitation spectrum, λ_{em} = 570 nm.

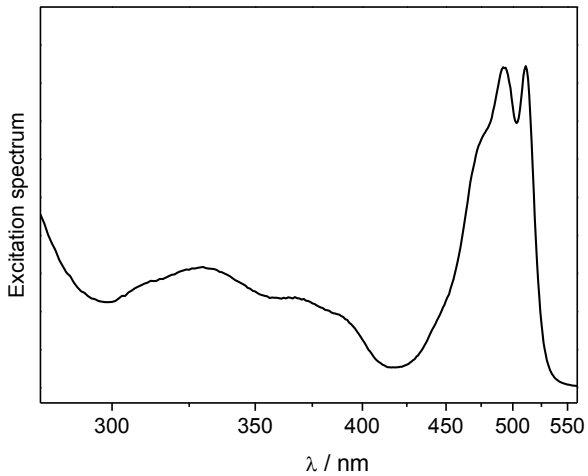

Figure A2.19. Excitation spectrum of complex **2**, recorded in dichloromethane at room temperature. For the excitation spectrum, λ_{em} = 570 nm.

Appendix 3. Cyclometalated Iridium-BODIPY Ratiometric O_2 Sensors

A3.1. NMR spectra of all new complexes

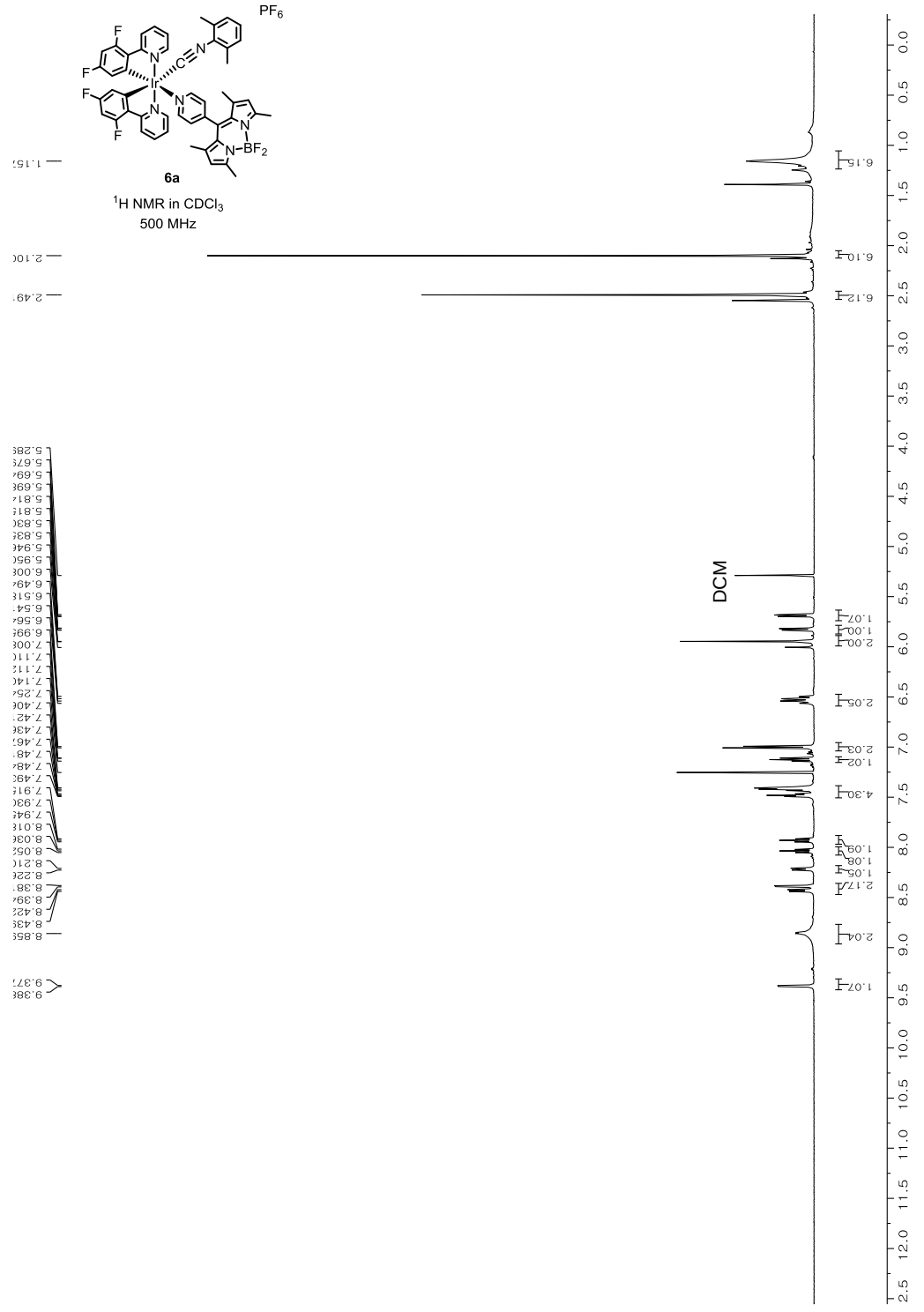

Figure A3.1. ^{1}H NMR spectrum of complex **6a**, recorded at 500 MHz in $CDCl_3$.

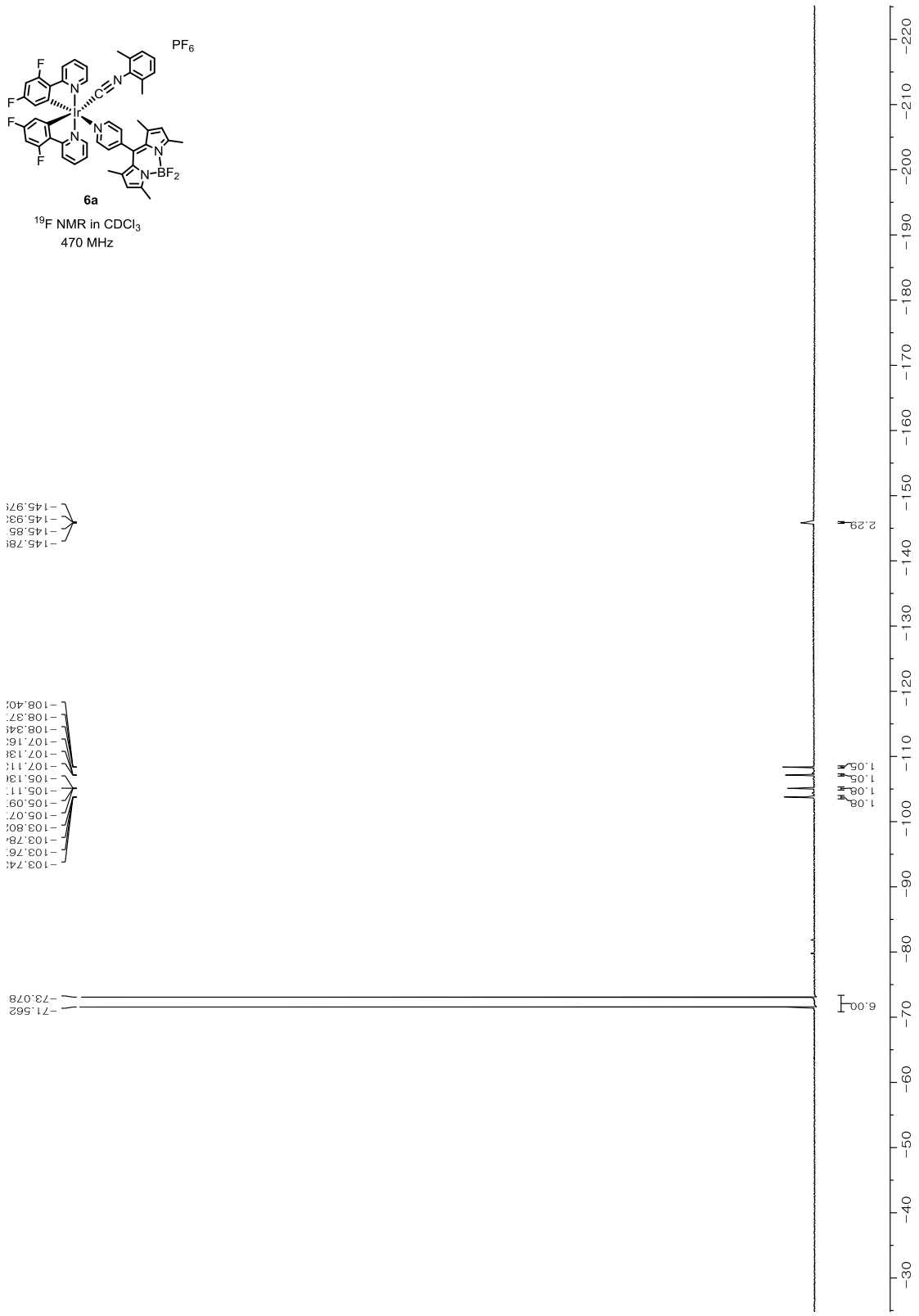

Figure A3.2. ^{19}F NMR spectrum of complex **6a**, recorded at 470 MHz in $CDCl_3$.

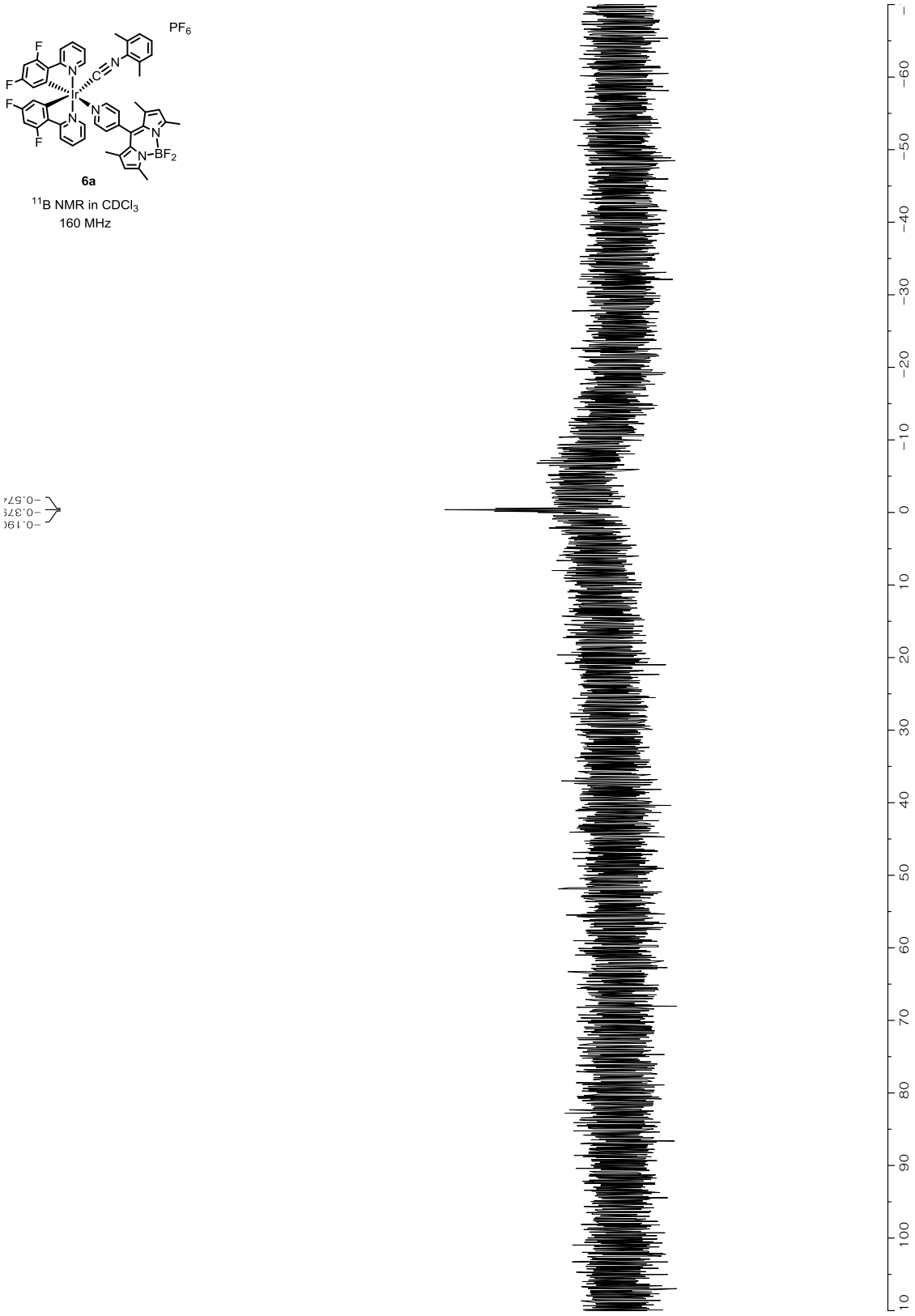

Figure A3.3. ^{11}B NMR spectrum of complex **6a**, recorded at 160 MHz in $CDCl_3$.

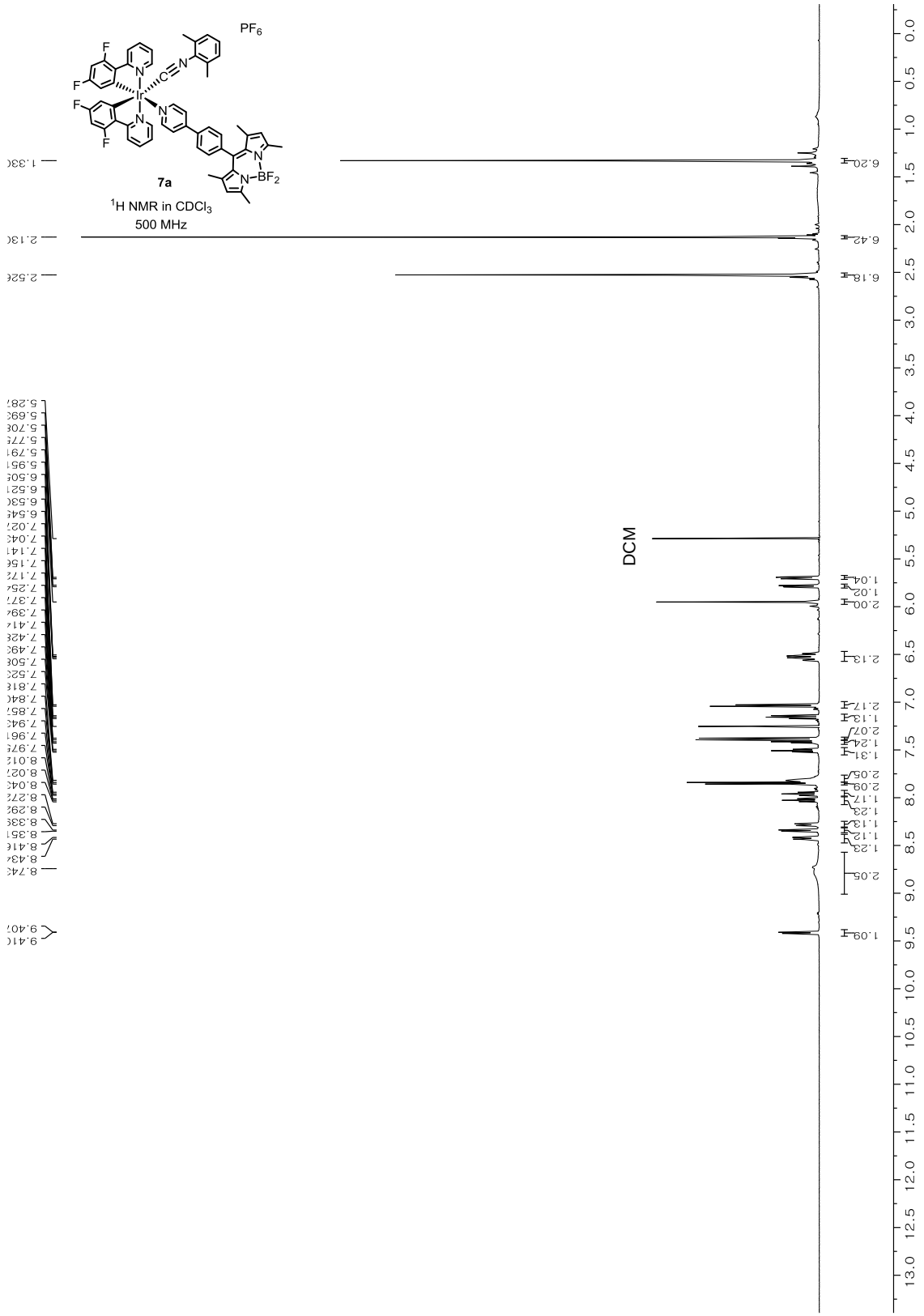

Figure A3.4. ^{1}H NMR spectrum of complex **7a**, recorded at 500 MHz in $CDCl_3$.

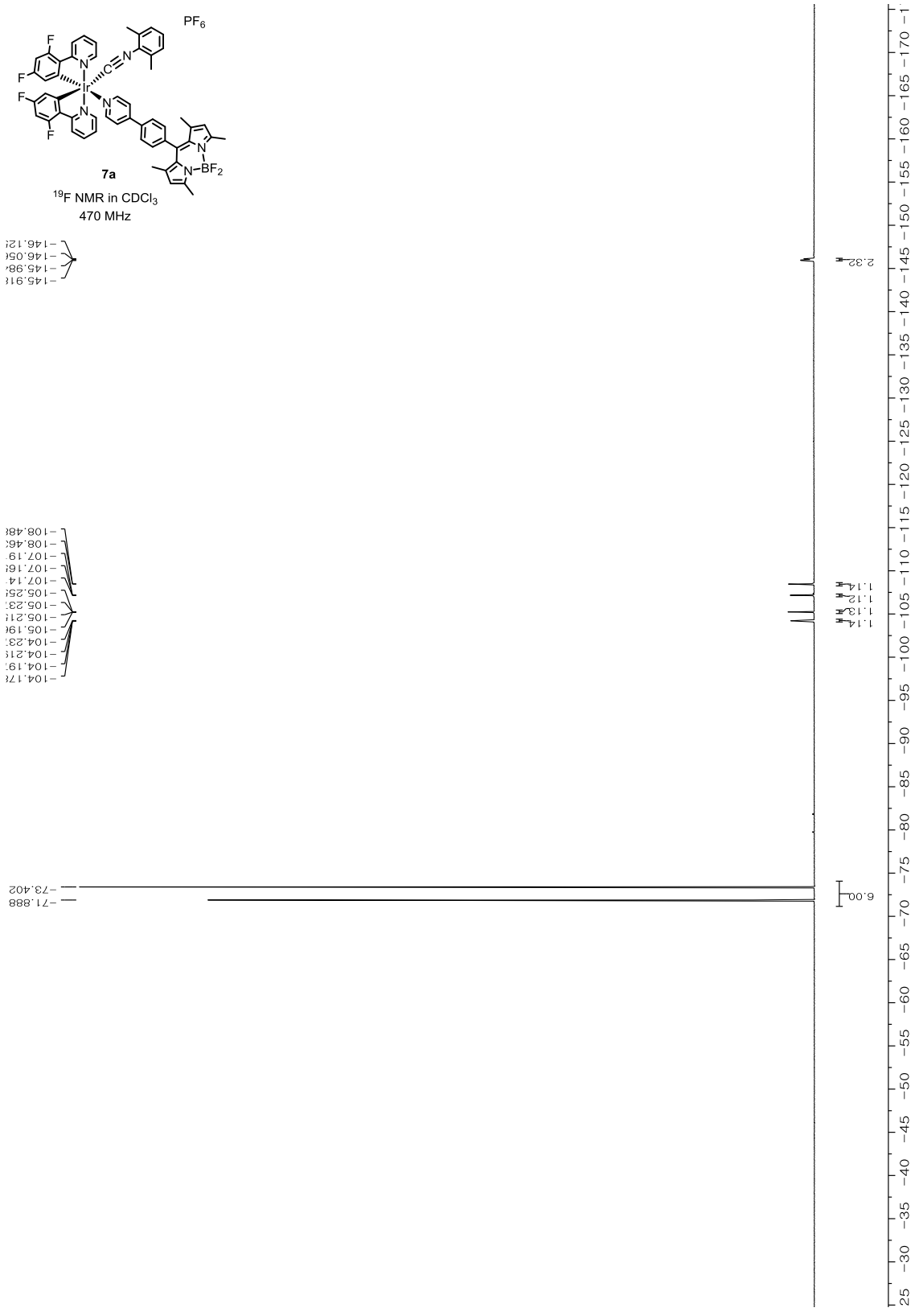

Figure A3.5. ^{19}F NMR spectrum of complex **7a**, recorded at 470 MHz in $CDCl_3$.

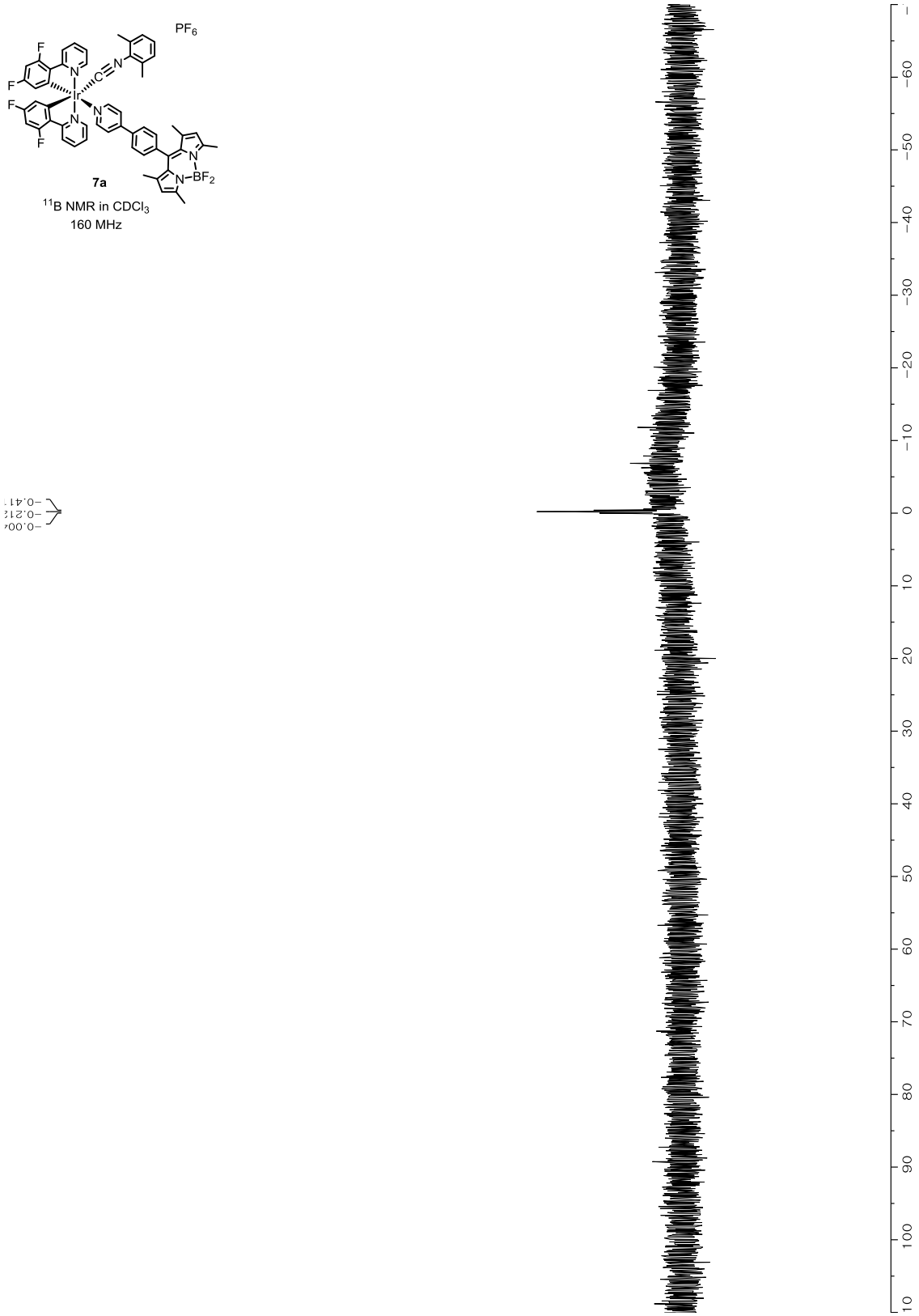

Figure A3.6. ^{11}B NMR spectrum of complex **7a**, recorded at 160 MHz in $CDCl_3$.

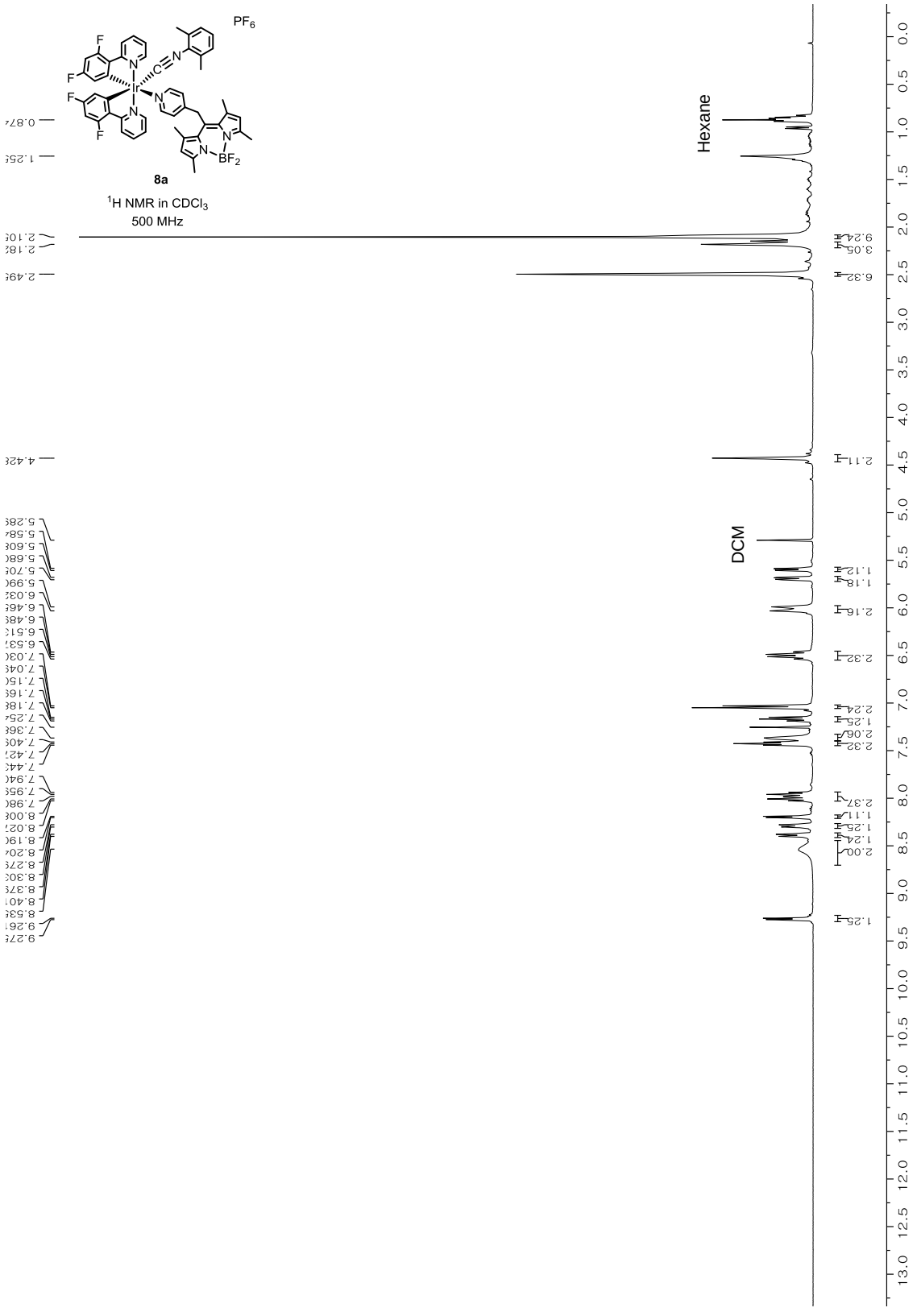

Figure A3.7. ^{1}H NMR spectrum of complex **8a**, recorded at 400 MHz in $CDCl_3$.

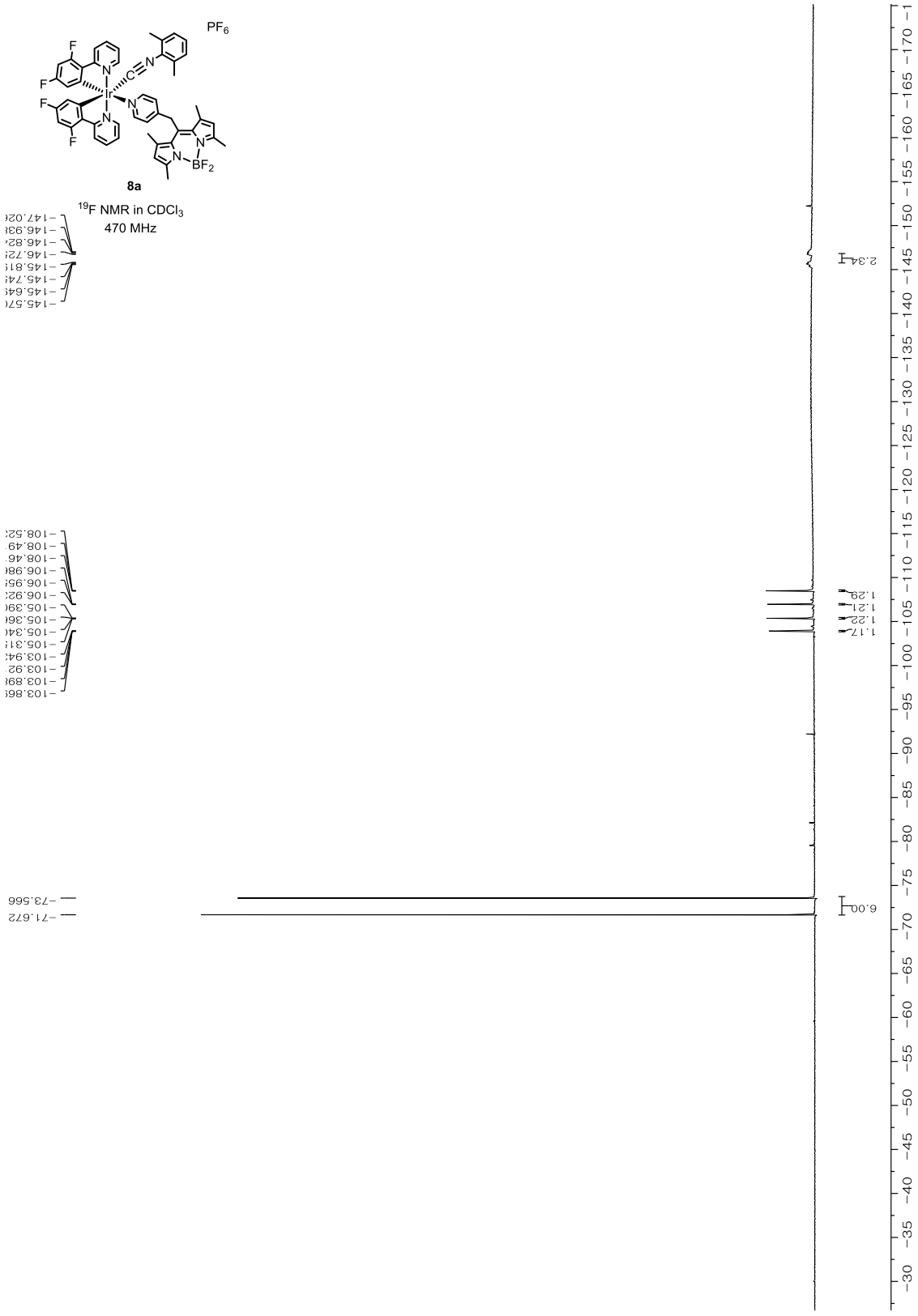

Figure A3.8. ^{19}F NMR spectrum of complex **8a**, recorded at 376 MHz in $CDCl_3$.

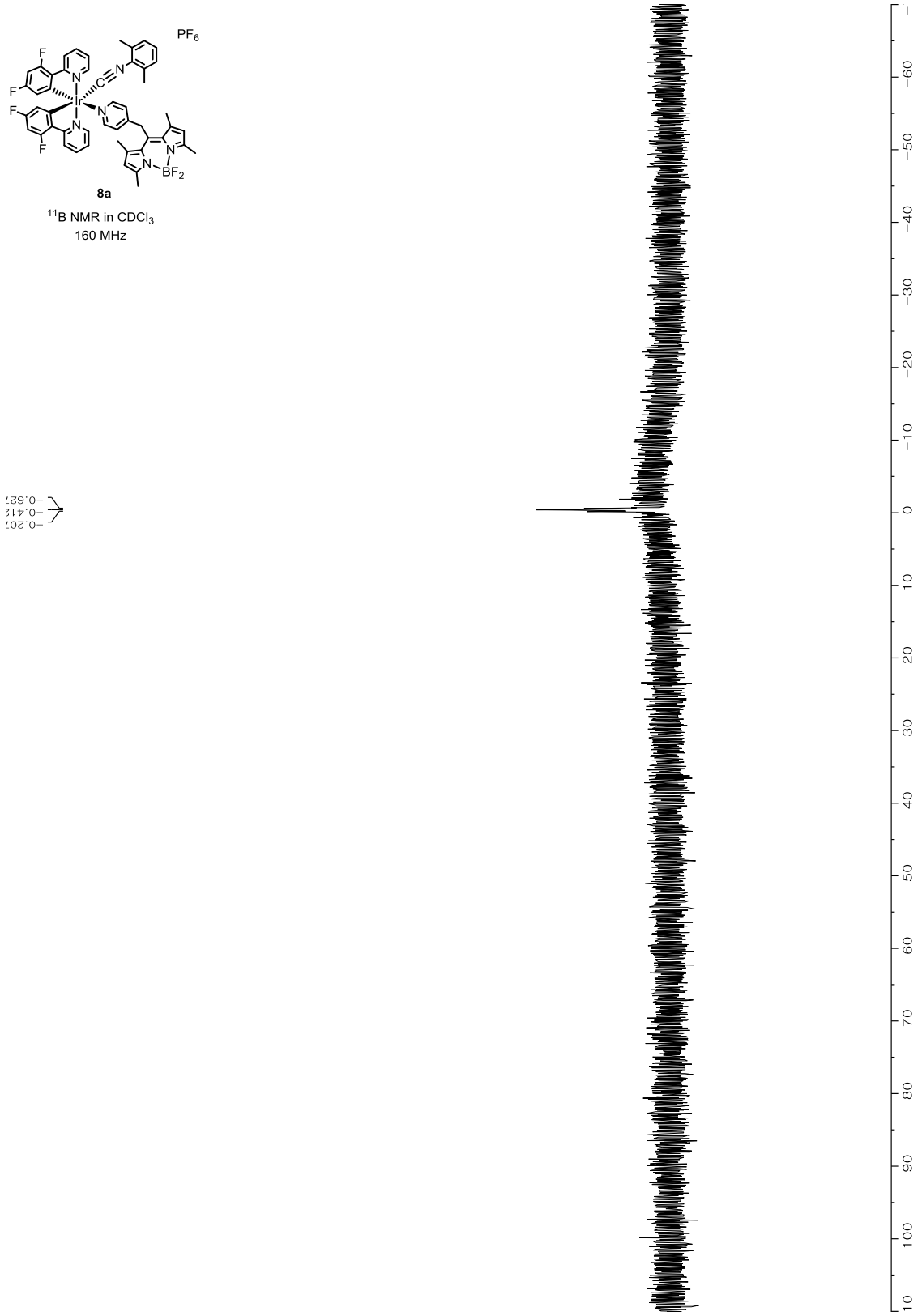

Figure A3.9. ^{11}B NMR spectrum of complex **8a**, recorded at 160 MHz in $CDCl_3$.

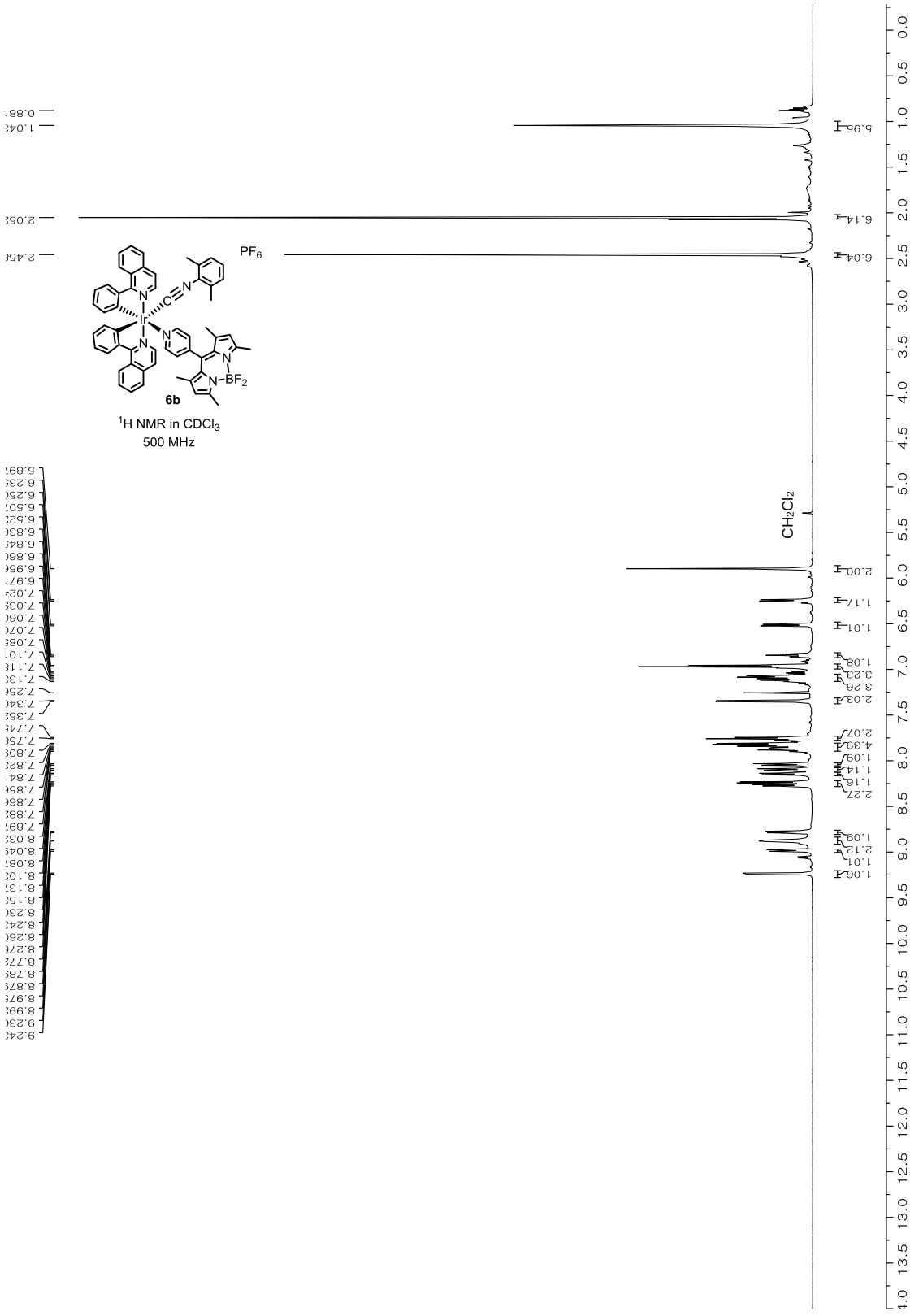

Figure A3.10. ^{1}H NMR spectrum of complex **6b**, recorded at 500 MHz in $CDCl_3$.

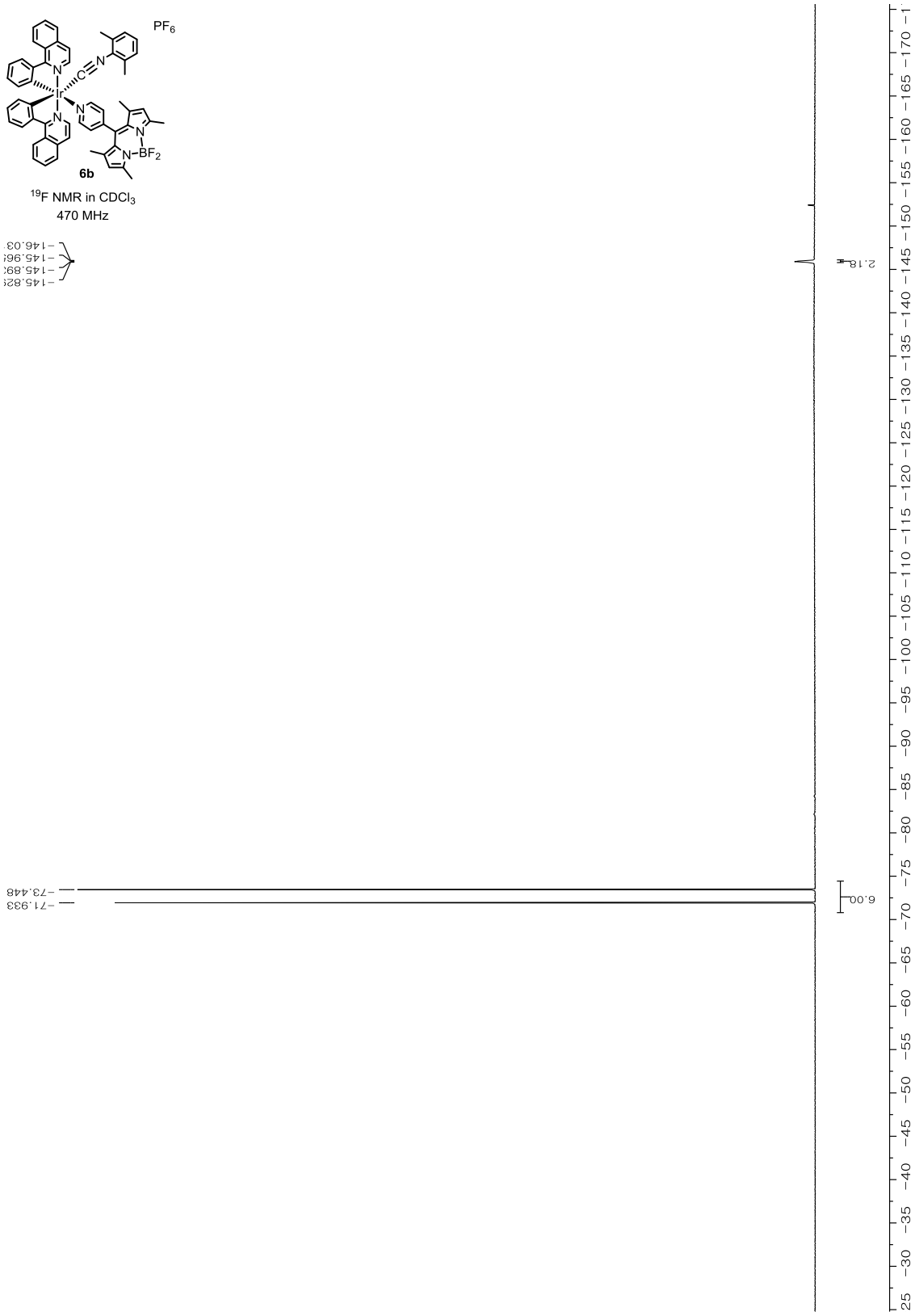

Figure A3.11. ^{19}F NMR spectrum of complex **6b**, recorded at 470 MHz in $CDCl_3$.

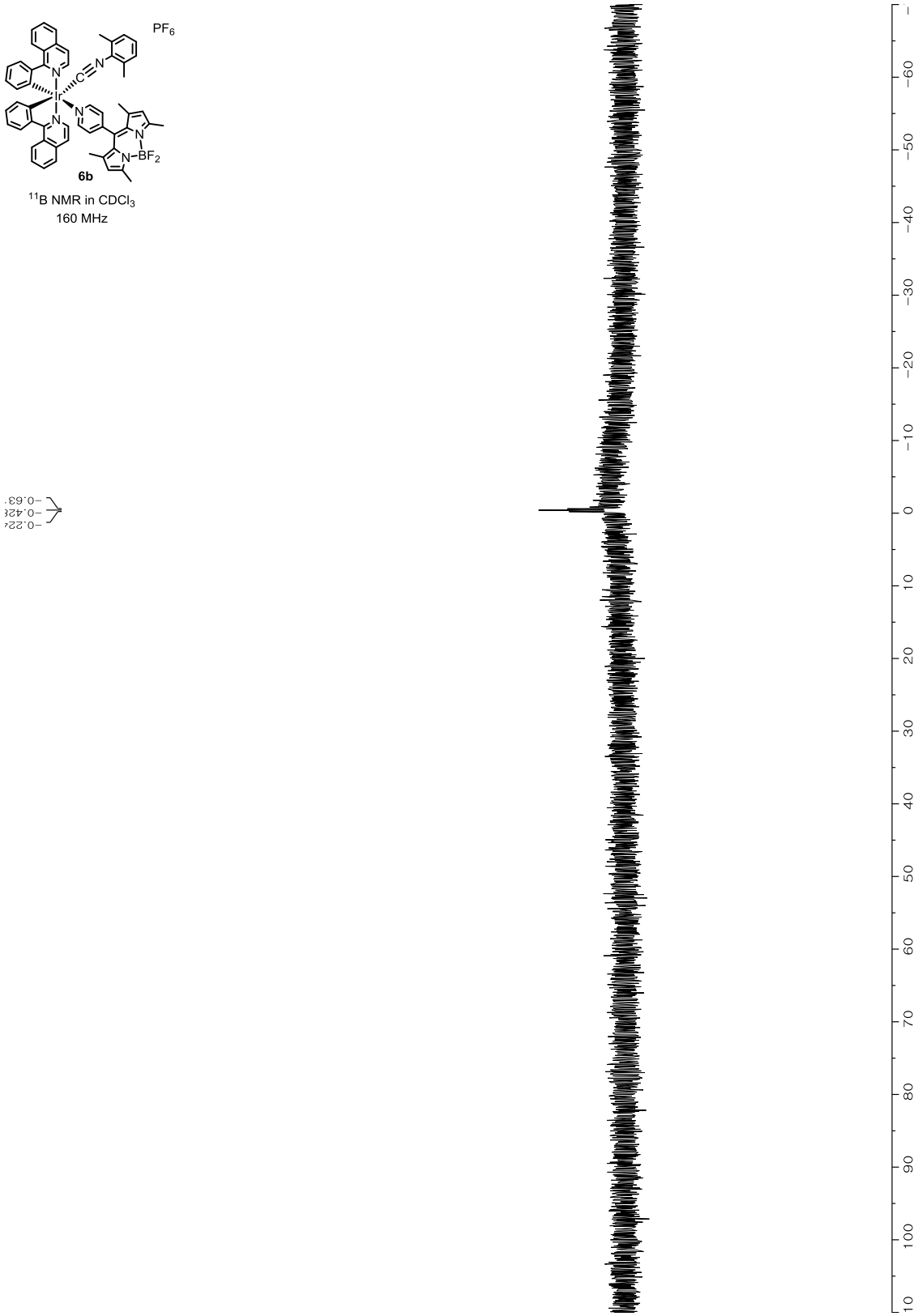

Figure A3.12. ^{11}B NMR spectrum of complex **6b**, recorded at 160 MHz in $CDCl_3$.

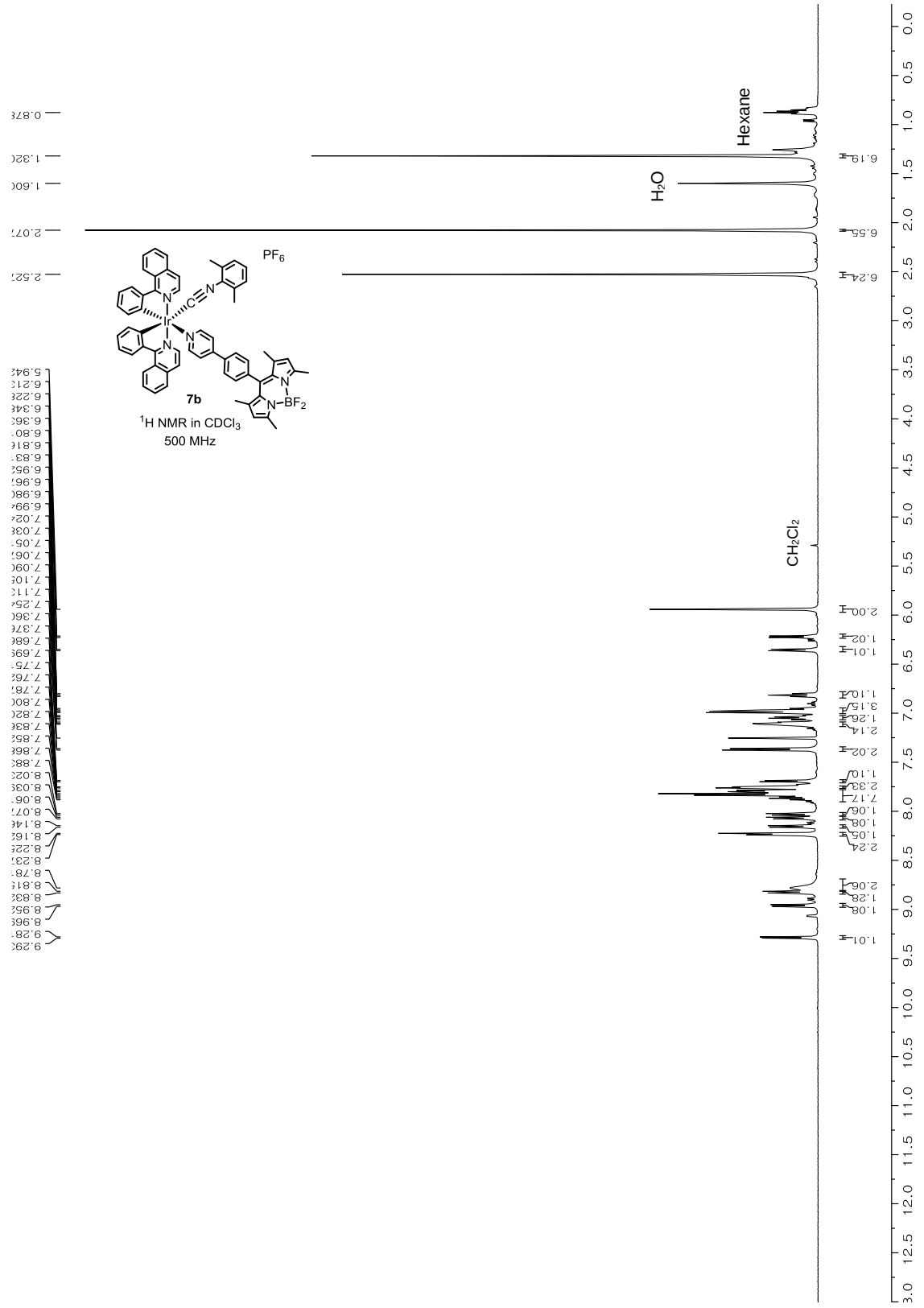

Figure A3.13. ^{1}H NMR spectrum of complex **7b**, recorded at 500 MHz in $CDCl_3$.

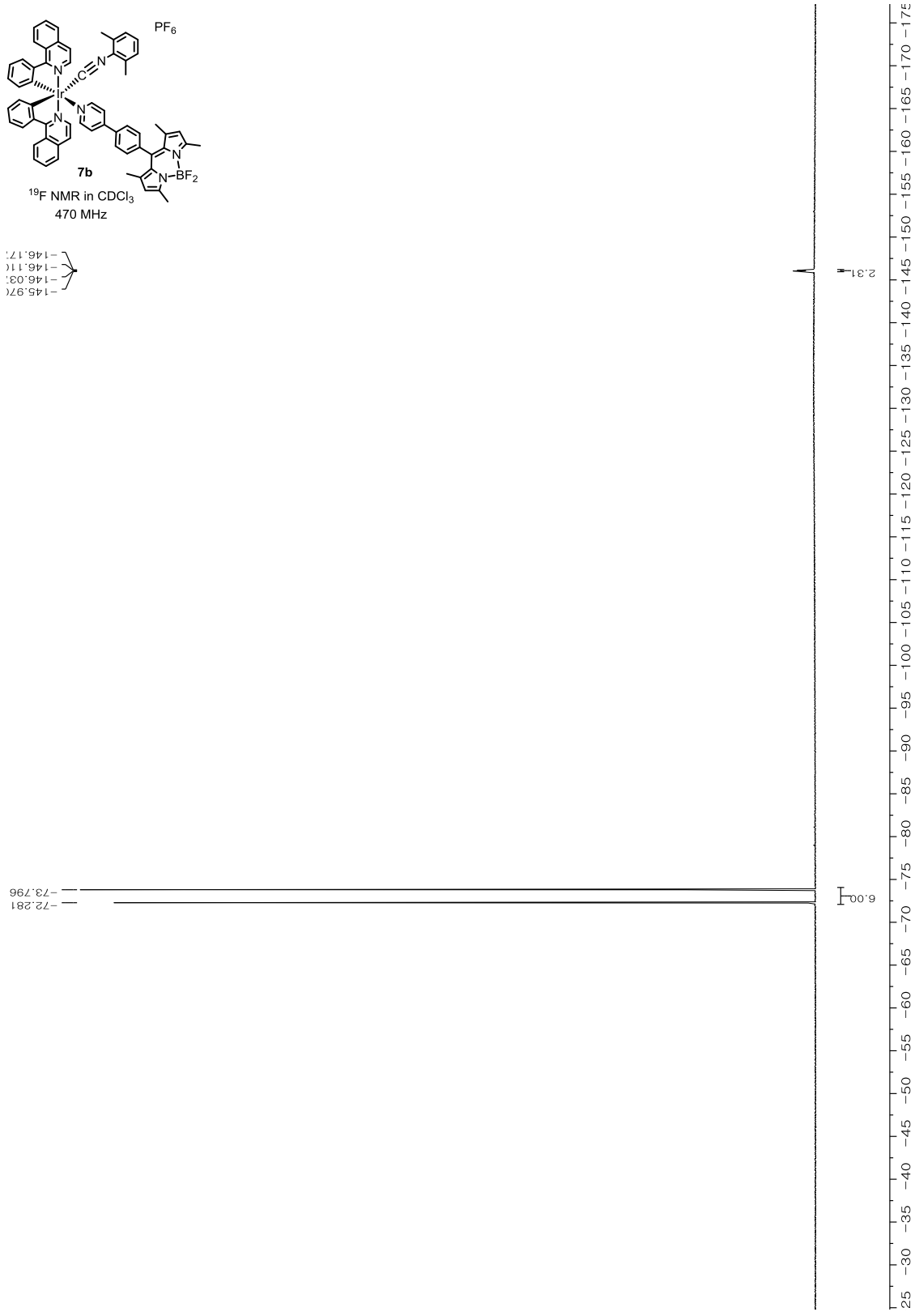

Figure A3.14. ^{19}F NMR spectrum of complex **7b**, recorded at 470 MHz in $CDCl_3$.

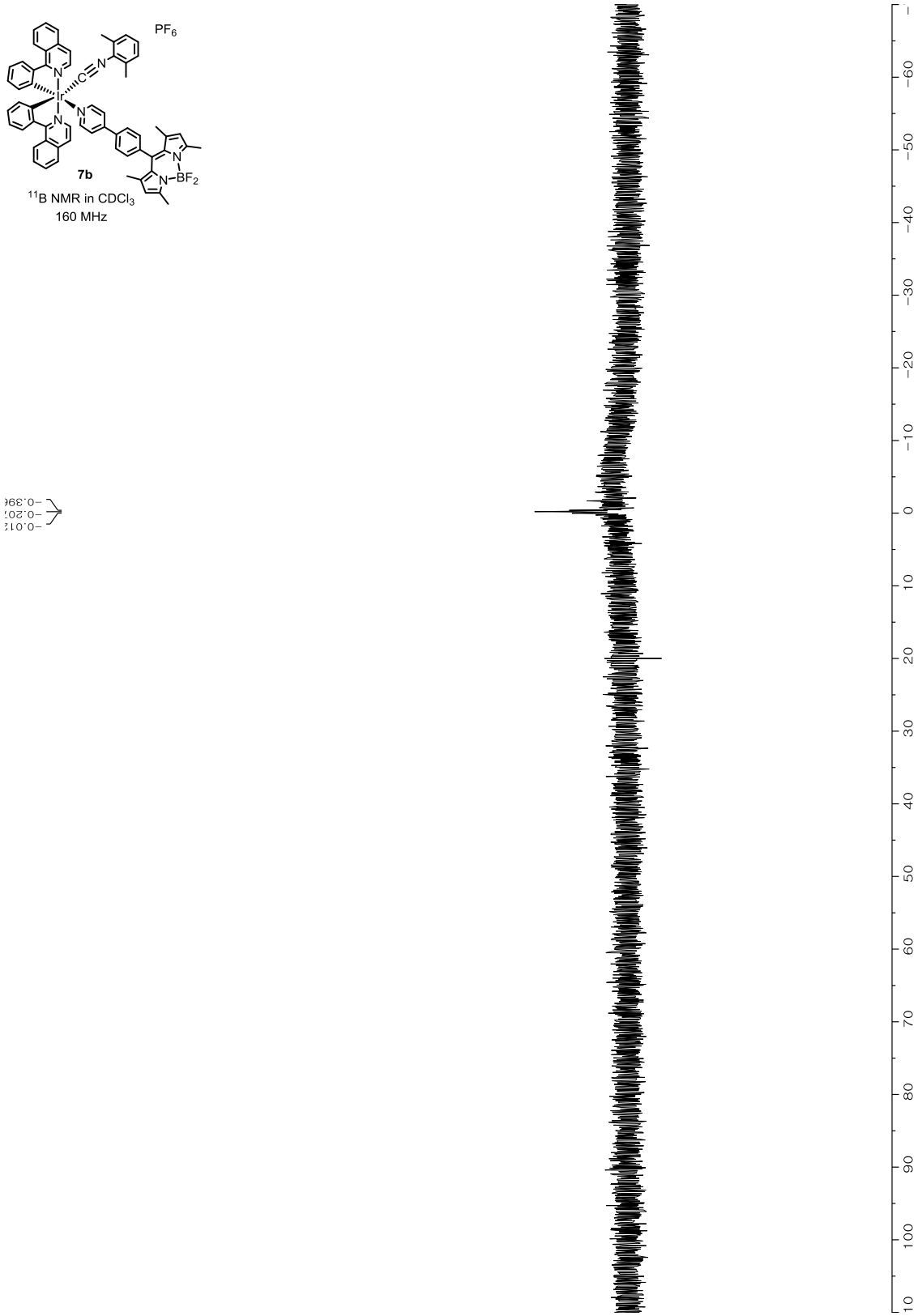

Figure A3.15. ^{11}B NMR spectrum of complex **7b**, recorded at 160 MHz in $CDCl_3$.

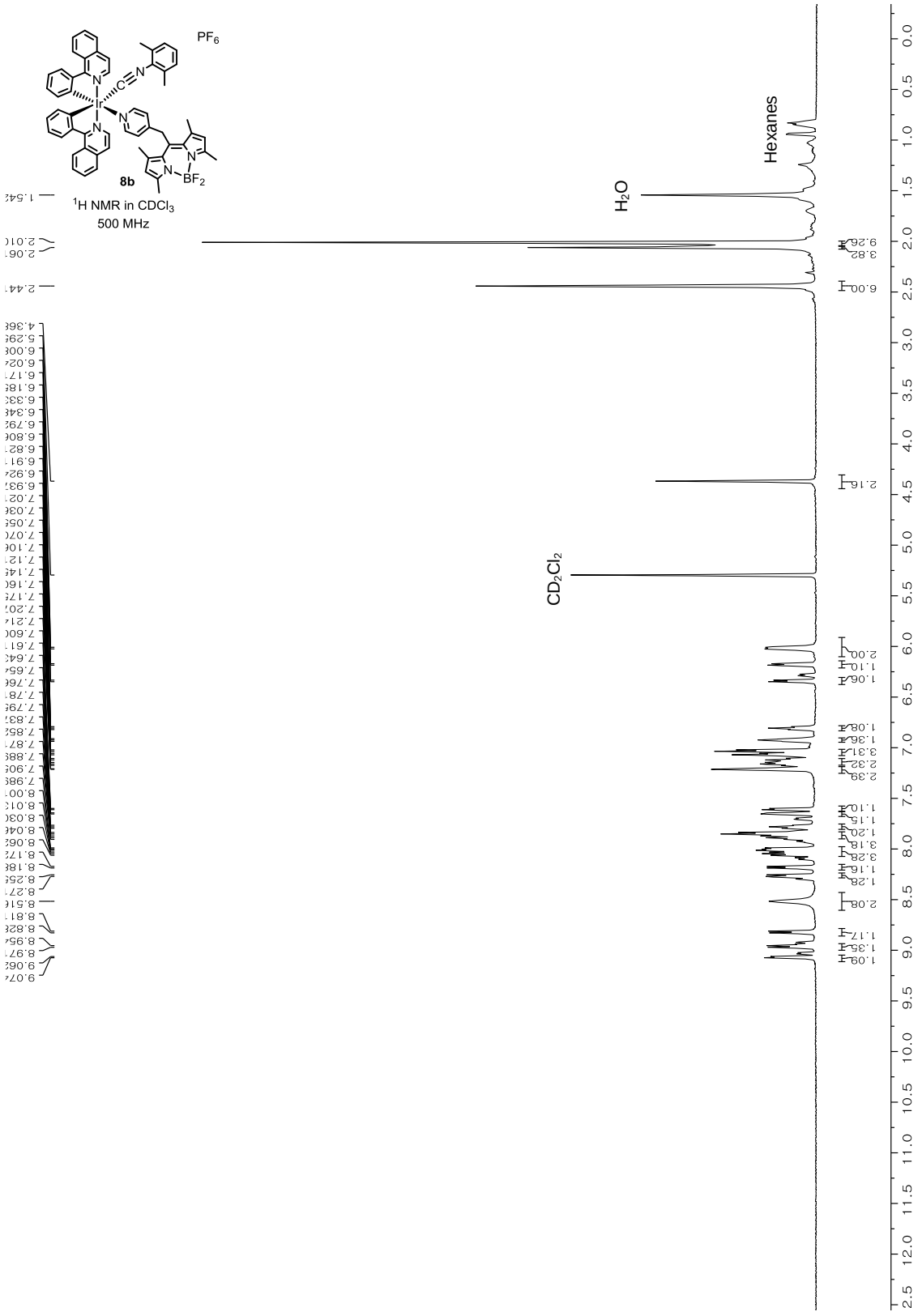

Figure A3.16. ^{1}H NMR spectrum of complex **8b**, recorded at 500 MHz in CD_2Cl_2.

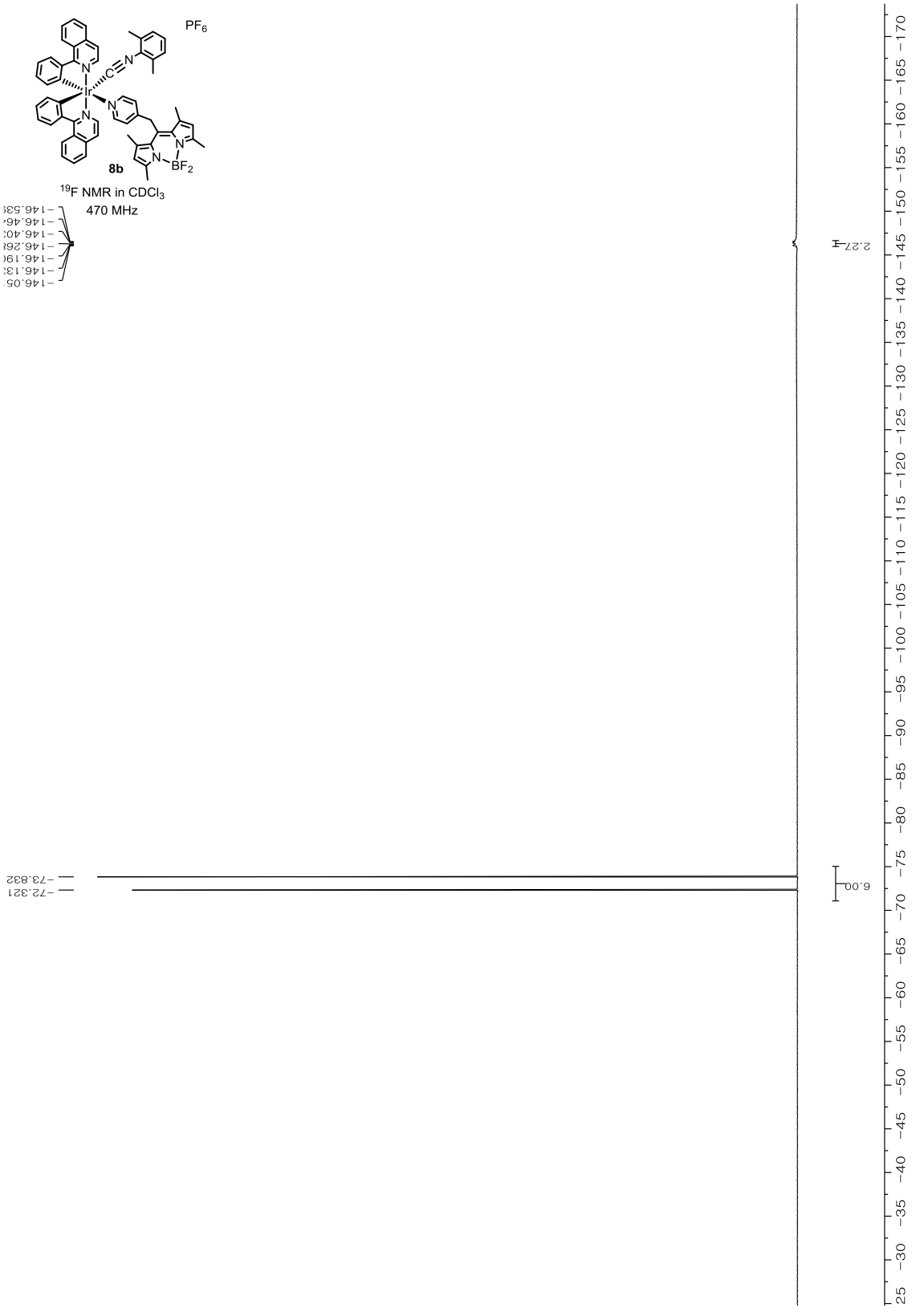

Figure A3.17. ^{19}F NMR spectrum of complex **8b**, recorded at 470 MHz in $CDCl_3$.

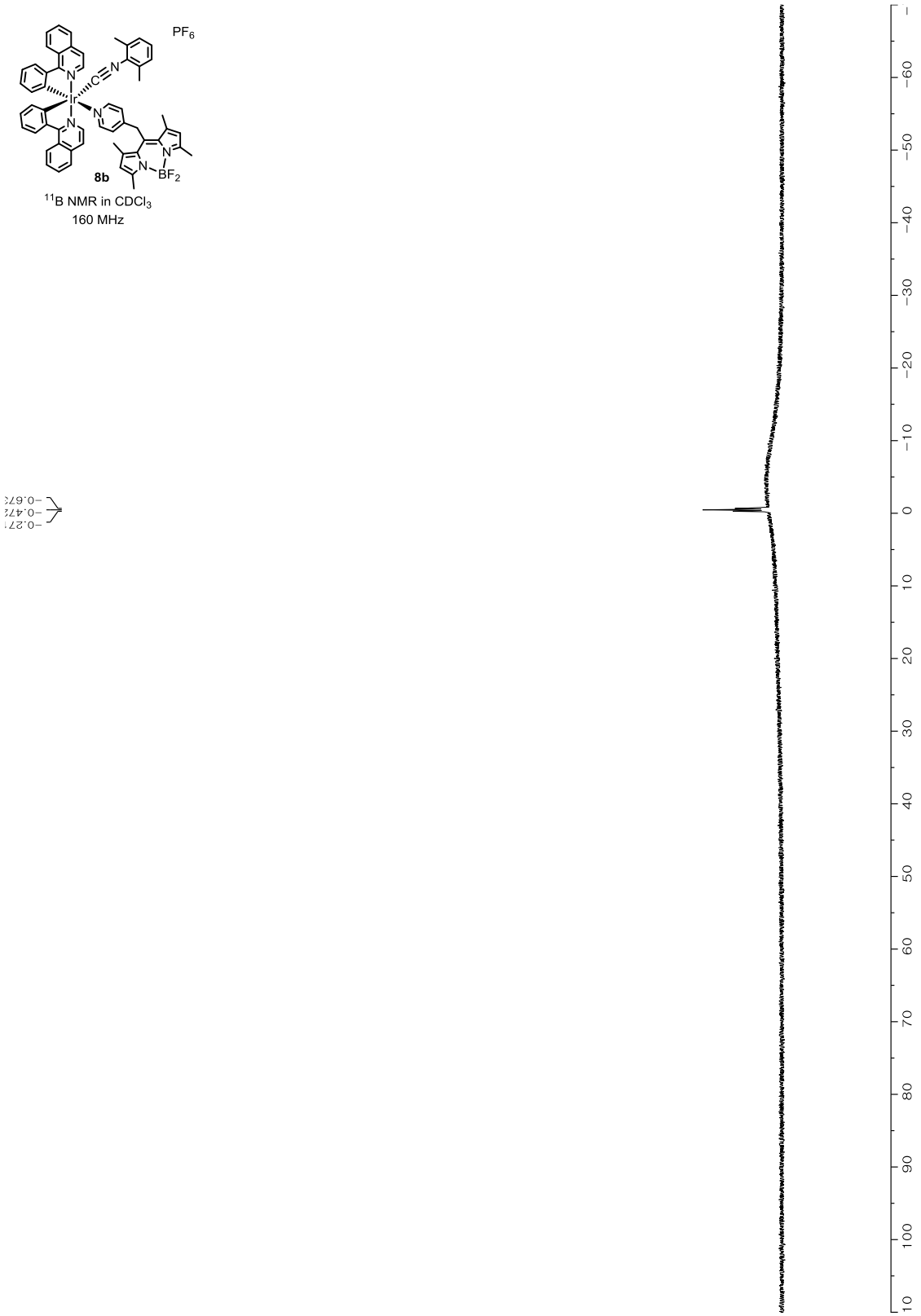

Figure A3.18. ^{11}B NMR spectrum of complex **8b**, recorded at 160 MHz in $CDCl_3$.

A3.2. X-ray crystallography summary table

Table A3.1. Summary of X-ray crystallographic data for **6a**, **7a**, and **8a**.

	6a	**7a**•1.5CH_2Cl_2	**8a**•CH_2Cl_2
CCDC	1883526	1883527	1883528
Crystal data			
Chemical formula	$C_{49}H_{39}BF_{12}IrN_6P$	$C_{56.50}H_{46}BCl_3F_{12}IrN_6P$	$C_{51}H_{43}BCl_2F_{12}IrN_6P$
M_r	1173.84	1377.32	1272.79
Crystal system, space group	Monoclinic, $P2_1/c$	Triclinic, $P\bar{1}$	Monoclinic, $C2/c$
Temperature (K)	123	123	123
a, b, c (Å)	18.512 (5), 18.686 (5), 32.097 (8)	10.868 (3), 14.021 (3), 20.638 (5)	45.386 (6), 11.4399 (14), 20.573 (3)
α, β, γ (°)	91.307 (3)	105.005 (3), 92.613 (3), 95.539 (3)	102.781 (1)
V (Å^3)	11100 (5)	3015.1 (13)	10417 (2)
Z	8	2	8
μ (mm^{-1})	2.51	2.45	2.78
Crystal size (mm)	0.29 × 0.17 × 0.04	0.19 × 0.16 × 0.08	0.35 × 0.27 × 0.12
Data collection			
T_{min}, T_{max}	0.516, 0.746	0.562, 0.746	0.561, 0.746
No. of measured, independent and observed [$I > 2\sigma(I)$] reflections	56882, 23916, 17632	16782, 12744, 10915	54925, 11935, 10920
R_{int}	0.055	0.020	0.025
$(\sin\theta/\lambda)_{max}$ (Å^{-1})	0.641	0.641	0.650
Refinement			
$R[F^2 > 2\sigma(F^2)]$, $wR(F^2)$, S	0.076, 0.242, 1.11	0.084, 0.311, 1.39	0.062, 0.154, 1.23
No. of reflections	23916	12744	11935
No. of parameters	1328	853	730
No. of restraints	2337	1261	756
	$w = 1/[\sigma^2(F_o^2) + (0.1031P)^2 + 138.2186P]$ where $P = (F_o^2 + 2F_c^2)/3$		$w = 1/[\sigma^2(F_o^2) + (0.0507P)^2 + 171.0678P]$ where $P = (F_o^2 + 2F_c^2)/3$
$\Delta\rho_{max}$, $\Delta\rho_{min}$ (e Å^{-3})	3.30, −3.20	5.85, −3.61	4.52, −3.43

A3.3. UV-vis absorption and emission spectra of BODIPYs 3–5

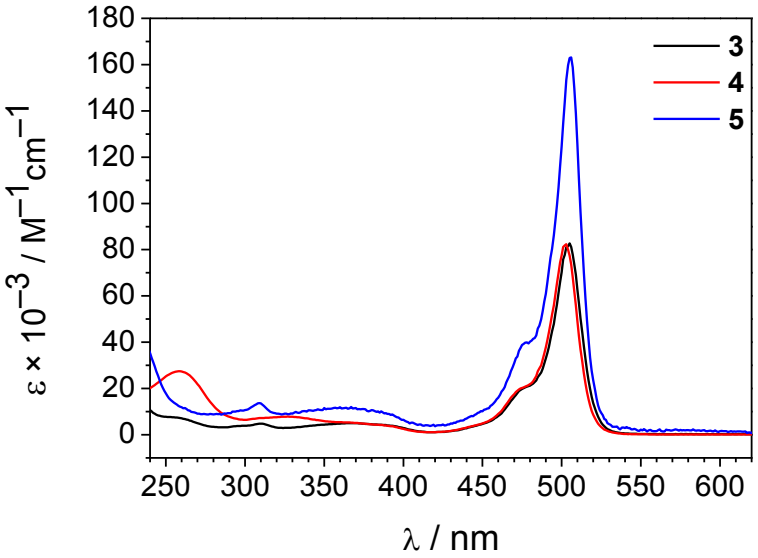

Figure A3.19. Overlaid UV-vis absorption spectra of BODIPYs **3**–**5**. Absorption spectra were recorded at room temperature in CH_2Cl_2.

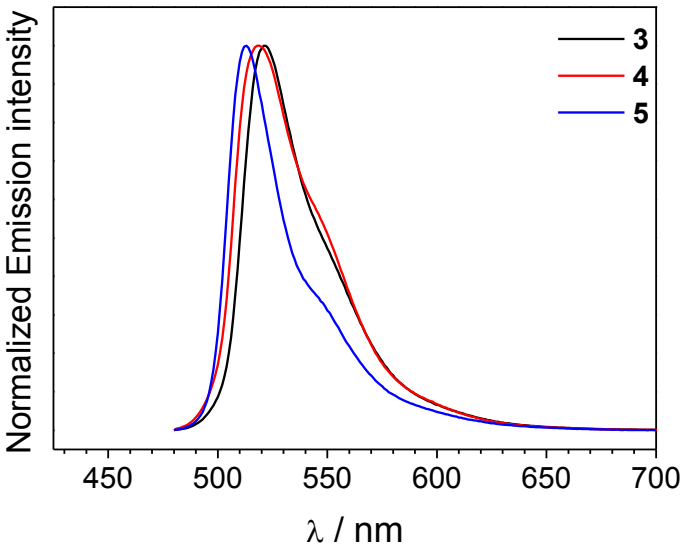

Figure A3.20. Overlaid emission spectra of BODIPYs **3**–**5** were recorded at room temperature in CH_2Cl_2. Excitation for the emission spectra was at 475 nm.

A3.4. Summary of UV-vis absorption and emission data

Table A3.2. Summary of absorption and emission data for BODIPYs **3**–**5**.

	λ_{abs}/nm ($\varepsilon \times 10^{-3}$ /M^{-1} cm^{-1})	λ_{em}/nm	Φ	τ/ns	$k_r \times 10^{-8}/s^{-1}$	$k_{nr} \times 10^{-8}/s^{-1}$
3	505 (82.3)	521	0.30	1.9	160	370
4	503 (82.0)	518	0.43	2.7	160	210
5	505 (163)	514	0.99	6.6	150	1.5

The UV-vis absorption and emission spectra were measured in CH_2Cl_2 at 293 K, and the samples were excited at 475 nm for steady-state measurements and 455 nm for lifetimes.

Table A3.3. Summary of UV-vis absorption data for Ir-BODIPY constructs **6**–**8**.

	λ_{abs}/nm ($\varepsilon \times 10^{-3}$ /M^{-1} cm^{-1})
6a	255 (51.2), 311 (sh) (23.7), 351 (sh) (10.1), 510 (64.7)
7a	260 (57.9), 314 (sh) (35.6), 504 (70.0)
8a	256 (56.4), 309 (26.0), 349 (sh) (9.4), 508 (66.0)
6b	280 (31.3), 352 (12.4), 400 (sh) (6.1), 509 (17.1)
7b	281 (29.4), 350 (sh) (11.0), 401 (sh) (5.1), 504 (11.8)
8b	280 (30.3), 351 (11.0), 399 (sh) (5.9), 508 (13.4)

UV-vis absorption spectra were measured in CH_2Cl_2 at 293 K.

A3.5. UV-vis absorption and excitation spectra of complexes 6–8

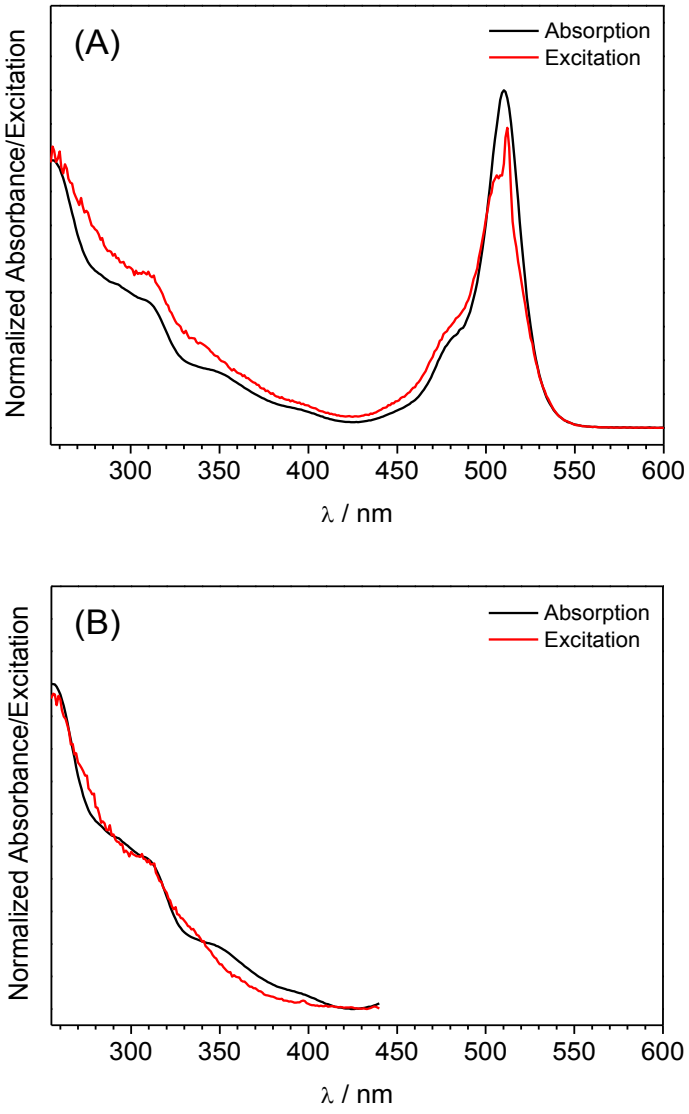

Figure A3.21. Overlaid UV-vis absorption and excitation spectra of complex **6a**, recorded in CH_2Cl_2 at room temperature. For the excitation spectrum, (A) λ_{em} = 510 nm, (B) λ_{em} = 450 nm.

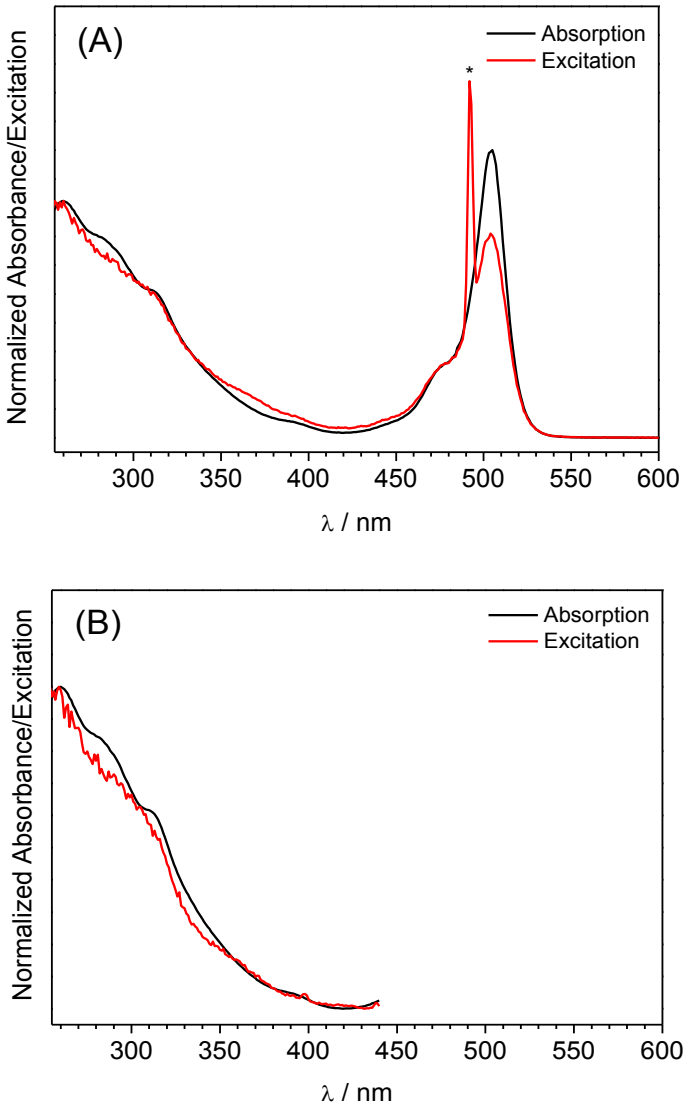

Figure A3.22. Overlaid UV-vis absorption and excitation spectra of complex **7a**, recorded in CH_2Cl_2 at room temperature. For the excitation spectrum, (A) λ_{em} = 490 nm, (B) λ_{em} = 450 nm. The * marks a feature caused by scattered excitation light at the detection wavelength.

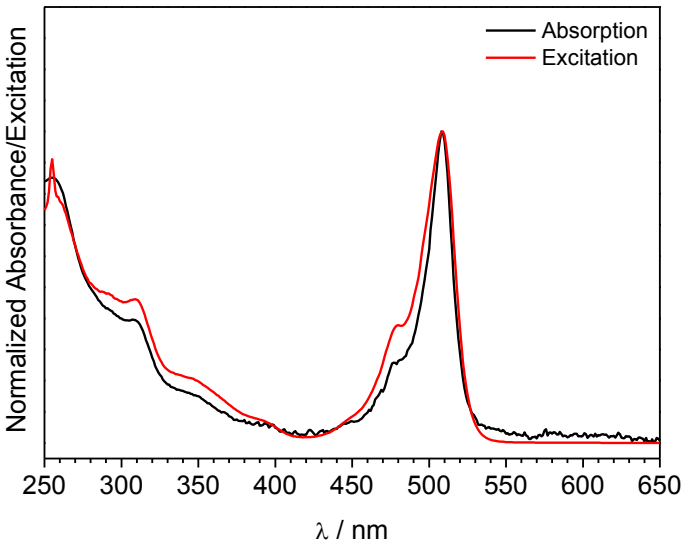

Figure A3.23. Overlaid UV-vis absorption and excitation spectra of complex **8a**, recorded in CH_2Cl_2 at room temperature. For the excitation spectrum, λ_{em} = 510 nm.

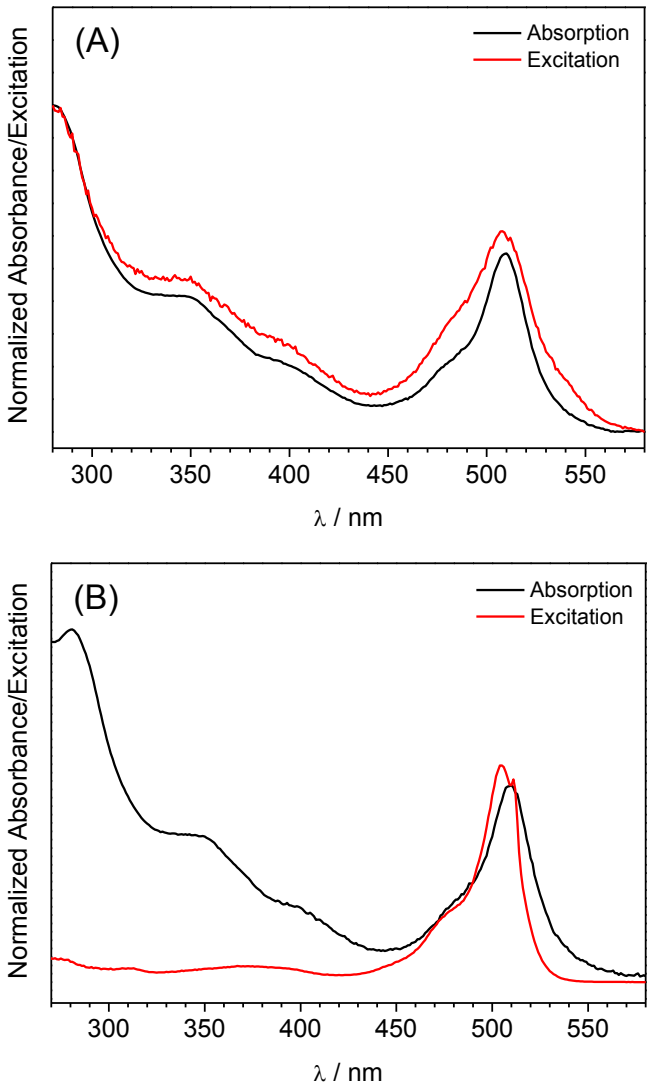

Figure A3.24. Overlaid UV-vis absorption and excitation spectra of complex **6b**, recorded in CH_2Cl_2 at room temperature. For the excitation spectrum, (A) λ_{em} = 600 nm, (B) λ_{em} = 510 nm.

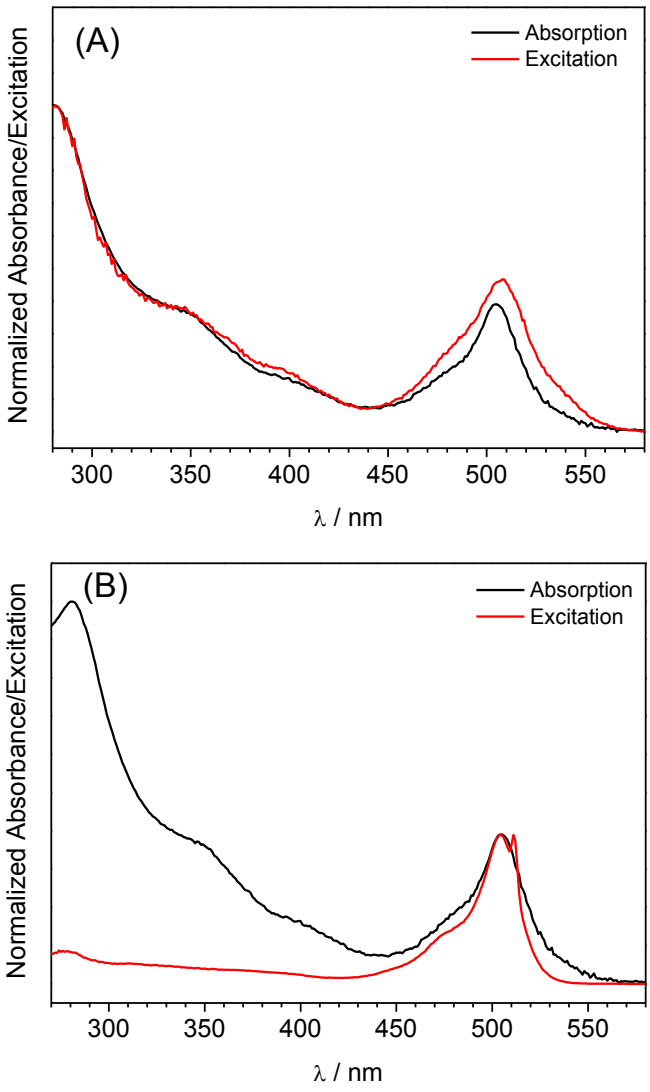

Figure A3.25. Overlaid UV-vis absorption and excitation spectra of complex **7b**, recorded in CH_2Cl_2 at room temperature. For the excitation spectrum, (A) λ_{em} = 600 nm, (B) λ_{em} = 510 nm.

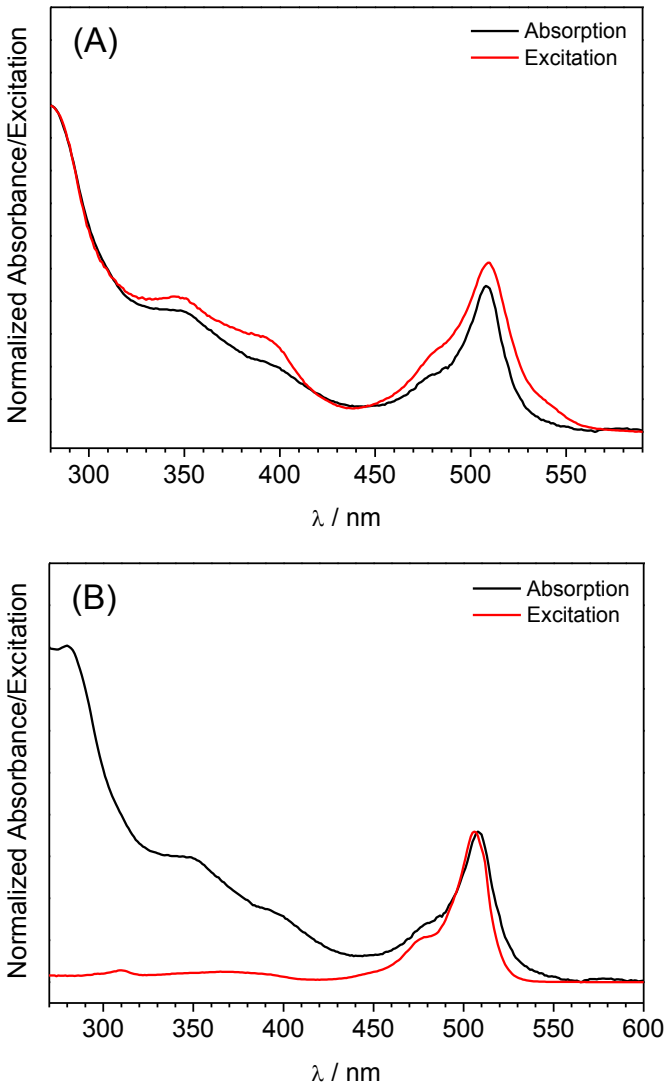

Figure A3.26. Overlaid UV-vis absorption and excitation spectra of complex **8b**, recorded in CH_2Cl_2 at room temperature. For the excitation spectrum, (A) λ_{em} = 600 nm, (B) λ_{em} = 510 nm.

A3.6. High resolution mass spectrometric analysis of complexes 6–8

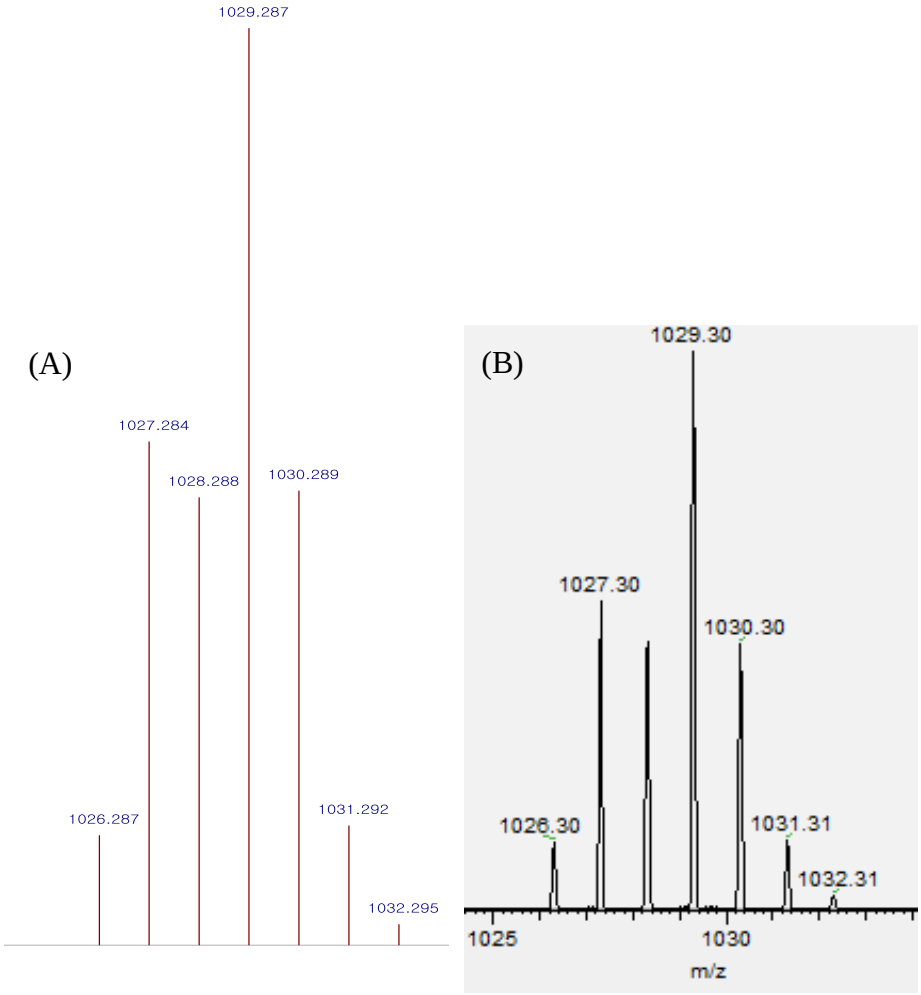

Figure A3.27. Simulated (A) and experimental (B) isotropic distribution patterns of complex **6a**: the molecular ion peak ($[M - PF_6]^+$).

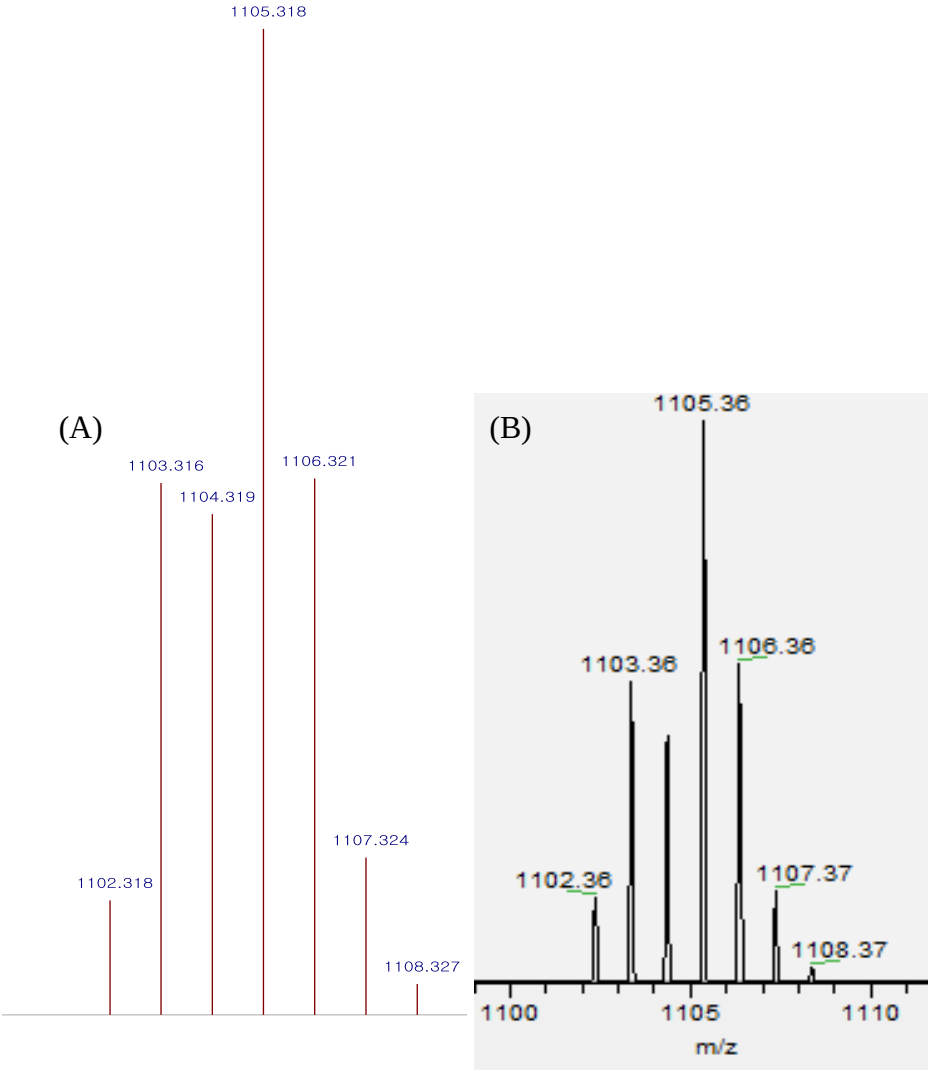

Figure A3.28. Simulated (A) and experimental (B) isotropic distribution patterns of complex **7a**: the molecular ion peak ($[M - PF_6]^+$).

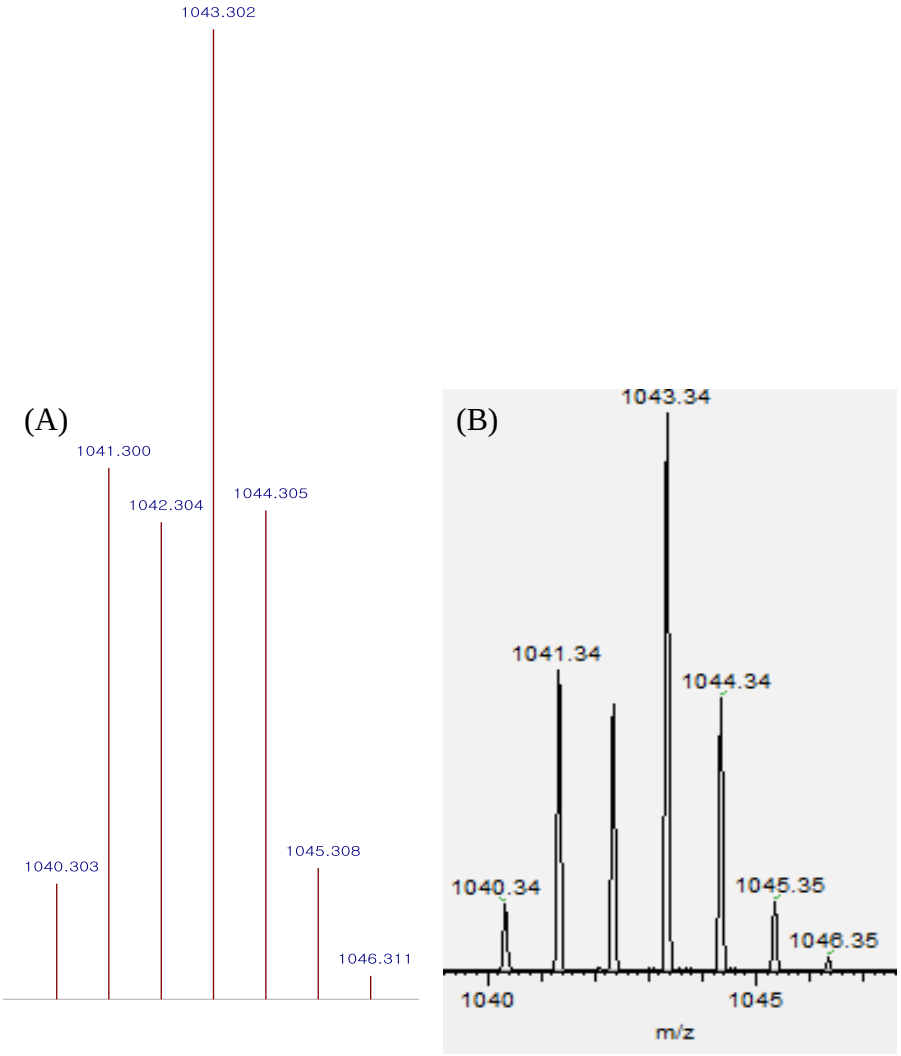

Figure A3.29. Simulated (A) and experimental (B) isotropic distribution patterns of complex **8a**: the molecular ion peak ($[M - PF_6]^+$).

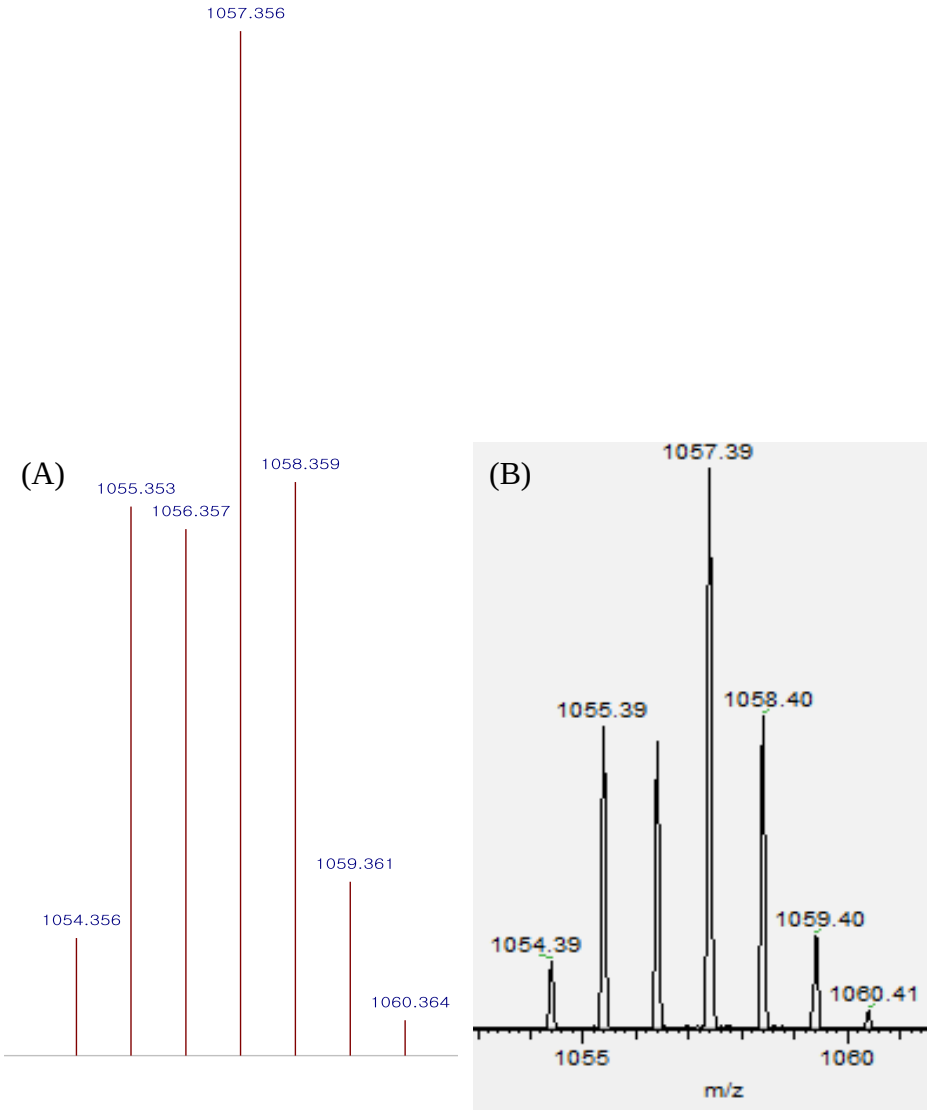

Figure A3.30. Simulated (A) and experimental (B) isotropic distribution patterns of complex **6b**: the molecular ion peak ($[M - PF_6]^+$).

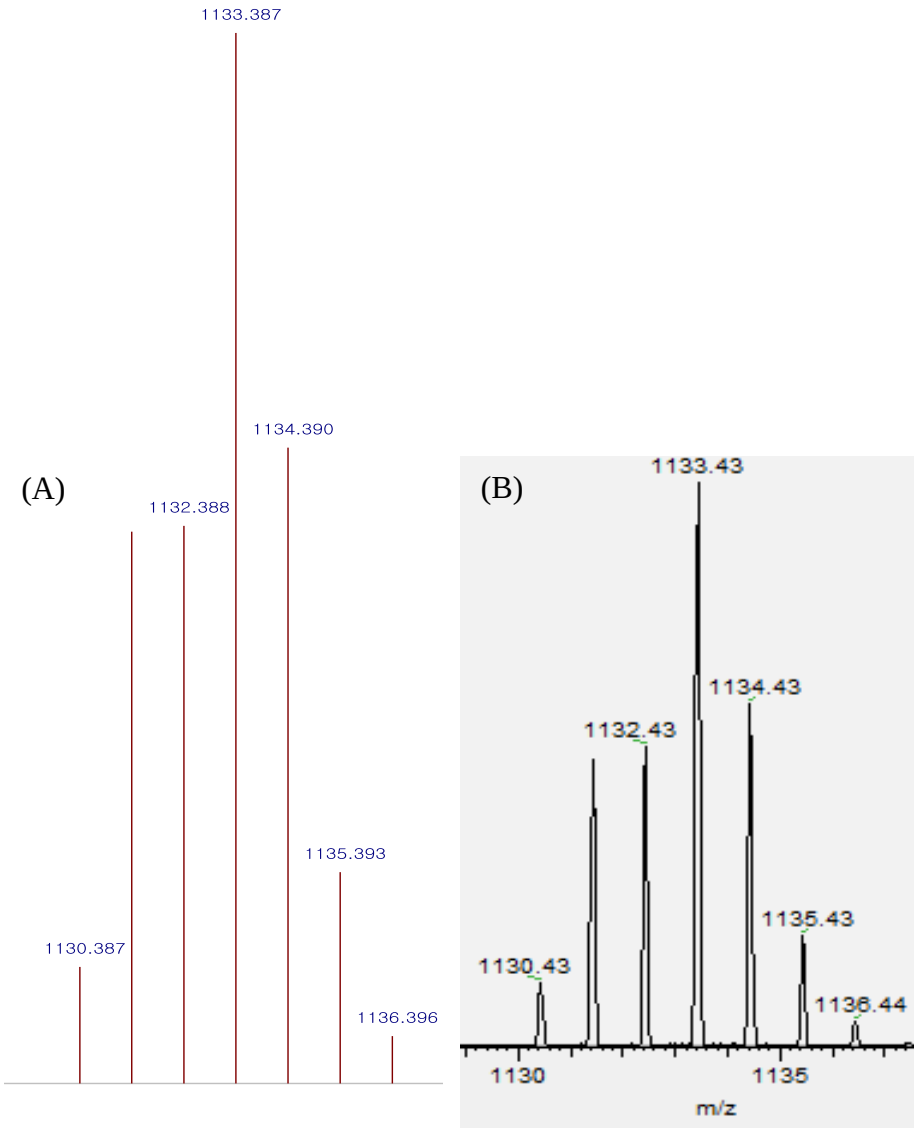

Figure A3.31. Simulated (A) and experimental (B) isotropic distribution patterns of complex **7b**: the molecular ion peak ($[M - PF_6]^+$).

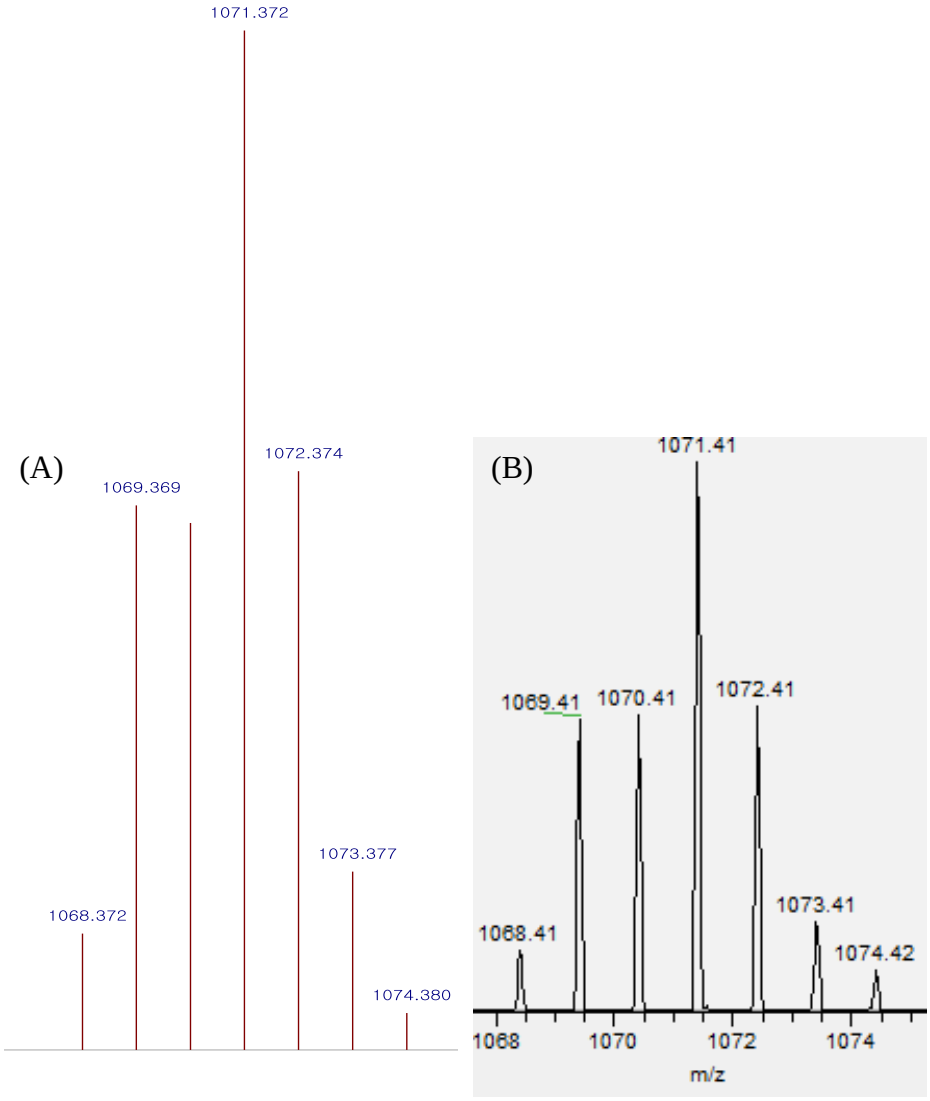

Figure A3.32. Simulated (A) and experimental (B) isotropic distribution patterns of complex **8b**: the molecular ion peak ($[M - PF_6]^+$).

A3.7. Emission spectra of complexes 6a and 6b–8b under inert and aerobic atmospheres.

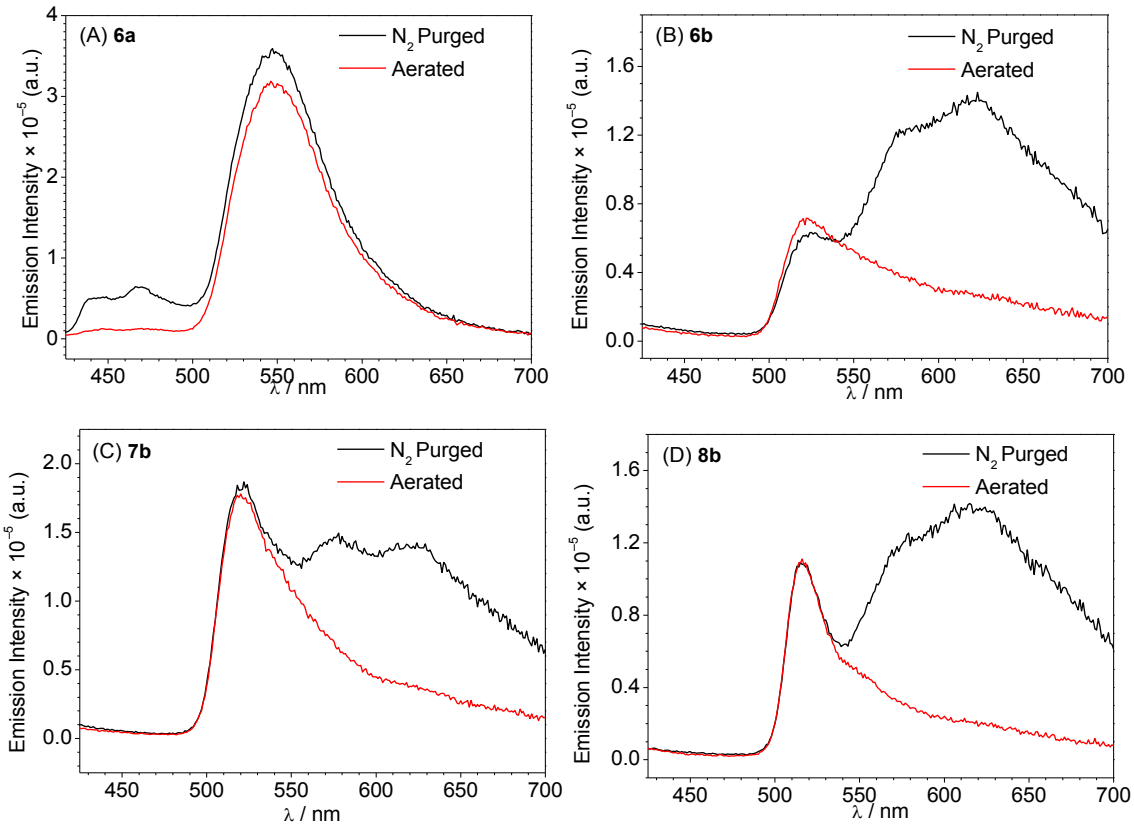

Figure A3.33. Emission spectra of complexes **6a** (A), **6b** (B), **7b** (C), and **8b** (D), were measured at room temperature in CH_2Cl_2 under N_2-purged and aerated conditions (λ_{ex} = 310 nm).